ISSN (online): 3059-9725

JOURNAL OF NEPAL HYDROGEOLOGICAL ASSOCIATION (JNHA)

Volume 2 September 2025

Published by
Nepal Hydrogeological Association
Babarmahal, Kathmandu, Nepal
Estd. 2011 A.D. (2067 B.S.)
Email : info@nha.org.np
Website : www.nha.org.np

Editorial Board of Journal-Nepal Hydrogeological Association
(2023-2025)

SEVENTH EXECUTIVE COMMITTEE

(2023-2025)

Prof. Dr. Dinesh Pathak

President

Central Department of Geology, Tribhuvan University

Email: dpathaktu@gmail.com

Mr. Khila Nath Dahal

Vice President

Department of Water Resources and Irrigation

Email: kndahal@gmail.com

Mr. Anil Khatri

General Secretary

Department of Water Resources and Irrigation

Email: khatrianil01@yahoo.com

Mr. Bala Ram Upadhyaya

Secretary

Water Resources Research and Development Centre,
Pulchowk, Lalitpur, Nepal
Email: brupadhyaya1@gmail.com

Mr. Om Kumar Khadka

Treasurer

Nir Drilling and Construction P.Ltd.

Email: geologist.omk@gmail.com

Mr. Moti Bahadur Kuwar

Immediate Past President

Former Joint Secretary, Ministry of Energy, GON

Email: motikunwar2018@gmail.com

Mr. Pushpa Raj Dahal

Executive Member

Prosperous Terai Madhesh Irrigation Special Program

Email: pushpardahal@gmail.com

Mr. Subash Acharya

Executive Member

Tri-Chnadra College, TU

Email: subashacharya045@gmail.com

Ms. Manjari Acharya

Executive Member

Central Department of Geology, TU

Email: acharya11.manjari@gmail.com

Mr. Govinda Ojha

Executive Member

Freelancer

Email: geo.ojha05@gmail.com

Mr. Nabin Parajuli

Executive Member

KUKL

Email: icenabin@gmail.com

Journal of Nepal Hydrogeological Association (JNHA), Vol (2), 1-15 (2025)
ISSN: 3059-9725 (Online)
https://doi.org/10.3126/jnha.v2i1.85371

RESEARCH ARTICLE

River terraces mapping and assessment of their characteristics along the middle section of the Madi River, Western Nepal, Lesser Himalaya

***Ashok Dhakal, Sunil Lamsal and Kabi Raj Paudyal**
Central Department of Geology, Tribhuvan University, Kirtipur, Nepal
**Corresponding author: ashok.01dhakal7@gmail.com*
***(Submission Date**: 29 April, 2025; **Accepted Date:** 8 June, 2025)*

ABSTRACT

The Madi River, a major tributary of the Sapta Gandaki River in west-central Nepal, exhibits well-developed fluvial terraces that provide insights into Late Quaternary landscape evolution in the Lesser Himalaya. This study focuses on the middle section of the Madi River, from Duipiple to Rudi Dhoban, where three distinct terrace levels higher, middle, and lower were identified along both banks. Six representative sites (Mohoriyatar, Dihi, Dargau, Syastri, Bhatbesi, and Tallobesi) were examined from south to north. The higher terrace, measuring approximately 80 m in height and 46 m in width relative to the modern channel, is composed predominantly of large boulders of gneiss, quartzite, garnet schist, and metasandstone, and is interpreted as the product of glaciofluvial deposition. The middle terrace is widely distributed at around 40 m above the active channel and extends up to 90 m in width, consisting of unsorted, consolidated boulders, cobbles, pebbles, and granules derived from gneiss, quartzite, schist, phyllite, and metasandstone. The lower terrace is the youngest unit, lies ~20 m above the modern river and extends ~120 m in width, containing rounded to sub-rounded sediments sourced from the Higher and Lesser Himalaya. Tributary inputs contribute angular clasts of phyllite and metasandstone to the middle and lower terraces. Sediment provenance analysis indicates transport from both the Higher Himalaya and Lesser Himalaya zones. The terrace stratigraphy and sedimentology suggest that the higher terrace formed under glaciofluvial conditions, while the middle and lower terraces are products of purely fluvial processes.

Keywords: ***River terraces mapping, Higher terrace, Sediment provenance, Glaciofluvial deposition***

INTRODUCTION

Most major rivers in Nepal originate within the Higher Himalaya and Tethys Himalaya zones, exhibiting a range of geomorphological and geological features such as valleys, terraces, and gorges. The evolution of river channels, controlled by flow direction and sediment transport dynamics, has varied significantly from ancient to modern times. River terraces are key geomorphic markers, serving not only as sources of construction aggregates but also as archives of hydrogeological conditions, flood regimes, and sediment supply histories.

The Madi River, a glaciofluvial tributary of the Sapta Gandaki River, originates from Kapuche Lake (Fig. 1) and joins the Seti River near Damauli. It traverses the Higher Himalaya and Lesser Himalaya, with its headwaters in the Tethys Himalaya (Fig. 1). The Tethys Himalaya sequence comprises Paleozoic (Cambrian–Permian) sedimentary rocks, including limestone, sandstone, and shale. The Higher Himalayan Crystalline consists predominantly of Precambrian high-grade metamorphic rocks such as gneiss, quartzite, and marble, with migmatite, granite, and gneiss dominating the upper structural levels (DMG, 2020). The Main Central Thrust (MCT) demarcates the contact between the Higher Himalayan Crystalline and the Lesser Himalaya.

Within the Lesser Himalaya, three lithostratigraphic units are recognized in the study area, arranged from oldest to youngest: the Ranimatta Formation, Naudanda Formation, and Ghan Pokhara Formation (DMG, 2020). The Ranimatta Formation comprises grey to greenish shale, phyllite, slate, garnetiferous phyllite, greyish-white quartzite with carbonate interbeds, and amphibolite. The Naudanda Formation is characterized by fine- to medium-grained white quartzite with ripple marks and thin intercalations of green chlorite phyllite. The Ghan Pokhara Formation, the youngest unit, consists primarily of black to grey carbonaceous slate and green shale.

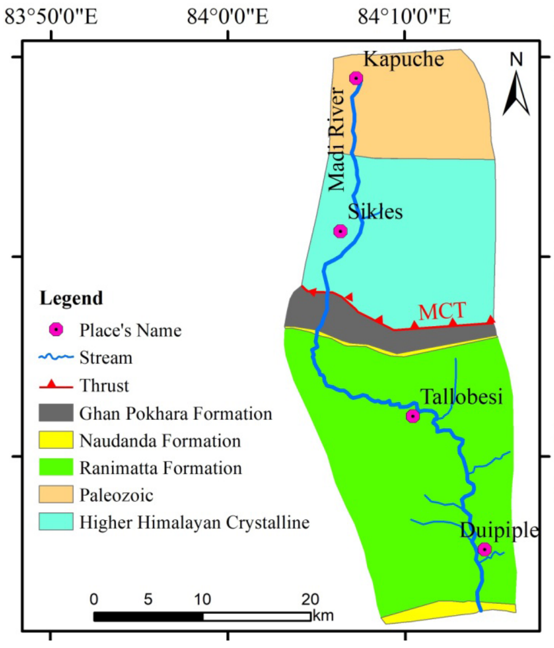

Fig. 1: Geological map of Madi River section from the Duipiple to Kapuche Lake, Modified after (DMG, 2020)

Hiroshima (1972) divided the river terraces into higher, middle, and lower terraces of the Marsyangdi River. According to him, the middle and lower terraces are distributed along the middle terraces. The middle terraces rise 70 to 80 meters above the riverbed and the lower 15 to 20 meters, and both terraces are accumulation ones. Sharma et al. (1980) gave the names of the terraces as T_1, T2, and T_3, which were studied along the middle Kali Gandaki between Kusma and Behadi. According to them, the T_1 terrace is 400 to 300 meters above the riverbed, and the T_2 is 25 to 60 meters lower than the $T_{1.}$ A poorly sorted, non-stratified consolidated conglomerate is present in T_1 and T_2. The T_3 terrace rises 10 to 15 meters above the riverbed, and it is made up of younger, unconsolidated deposits.

Iwata et al. (1982) studied the glacial landform and river terraces in the Thakkhola region, central Nepal. The study clarifies the relationship between the river terrace and glacial landform with the deformation of the Kaligandaki river terraces. A series of field surveys were carried out in the upper course of the Kaligandaki. In the Thakkhola region, the two stages of glacial morines, which fall possibly into the late glacial age. They divided the river terrace into higher, middle, and lower terraces. The higher terrace is denoted by H, the middle terraces (M_1–MM_4) and the lower terrace is L. The higher terraces consist of conglomerates and are about 360–400 meters above the flood plain. The Middle Terrace (M_1, M_2, M3, and M_4) is above the riverbed at about 260 m, 200 m, 150 m, and 110 m, respectively. The Lower Terrace is composed of non-consolidated fluvial gravels.

River terraces along the Middle Kali Gandaki and the Marsyandi River are all valleys filled with deposits formed by glacial fluvial sediments (Yamanaka and Iwata, 1982). The formation of terraces along both rivers was controlled by local and accidental geomorphic events. The tectonic movements along the Kaligandaki resulted in the northern and southern regions being comparatively uplifted during the late quaternary. (Yamanaka and Iwata, 1982) classified the Kaligandaki river terraces into 3 groups, i.e., higher, middle (M_1–M_5) and lower terraces.

Yamanaka and Iwata (1982) also discussed the geomorphological development in the Kaligandaki River. They conclude that the Kaligandaki is deepening and has reached the present level. The Kaligandaki started downcutting and eroded the deposit. They studied the river terraces along the Marsyandi, from Nayagaon to Dumre. The terraces are divided into six groups: Highest (HH), Higher (H), and Middle Terrace (M), Intermediate-Level Terrace (m), between the middle and lower terraces, and Lower (L) and Lowest Terrace (L') terraces are too limited. The Higher Terrace is about 150 meters thick and composed of pebble- and cobble-sized gravels and silty materials. Middle Terrace is about 70 m and consists of angular to sub-angular gneiss gravels and gray silty materials. It is unsorted and not stratified. Lower Terrace has a maximum width of 500 meters and consists of sub-angular to sub-rounded gneiss gravel and sandy deposits in general. Mapping the river terrace level within the Upper Pindar River determines the current and historic hydrogeology, along with the present terrain characteristics of the area (Nandy et al., 2021). The whole region has gone through polycyclic landform development to form steps like river terraces. The wide altitudinal spacing of the river terrace levels indicates the relative change of base level due to the combined effect of tectonic instability. Meikle et al. (2010) mentioned the importance of river terraces. River terraces are important landform as they can provide i) sources of aggregate for construction (Smith and Collis, 2001), ii) information about hydrology for flood management and planning purposes (Carney and Napier, 2004) and iii) archives of longer – term environmental changes that are driven by combinations of climate or anthropogenic related changes in flood regime and sediment supply (Bridgland, 2000) or by tectonic and eustatic changes in base- level (Cunha et al., 2008).

Madi River creates a straight, meandering, and braided channel from beginning to end. The middle section of the Madi River consists of terrace deposits, which are dominantly present in the meandering pattern of the river flow channel. The main aim of the study is to figure out the fundamental characteristics of terraces. This study demonstrates the sequence as well as the development of river terraces in response to the terrace genesis process.

Study Area

The study area lies within Gandaki Province, Nepal, encompassing parts of Kaski, Lamjung, and Tanahun districts, and is accessible via the Prithvi Highway. It is situated approximately 15 km north of Damauli. The middle section of the Madi River, investigated in this study, extends for ~20 km between the Duipiple, Lamjung, in the south and Rudi Doban in the north. The southern and northern boundaries are demarcated by the confluences of the Risti Khola and Rudi Khola, respectively (Fig. 2). The Madi River channel forms the district boundary between Kaski and Lamjung. River terraces are distributed along the Rupa Rural Municipality (Kaski District) and the Madhya Nepal Municipality (Lamjung District). Geographically, the study area extends from 28°04'43" N, 84°13'57" E in the south to 28°12'17" N, 84°20'18" E in the north. Channel elevations range from approximately 378 m at the southern end to 550 m at the northern end.

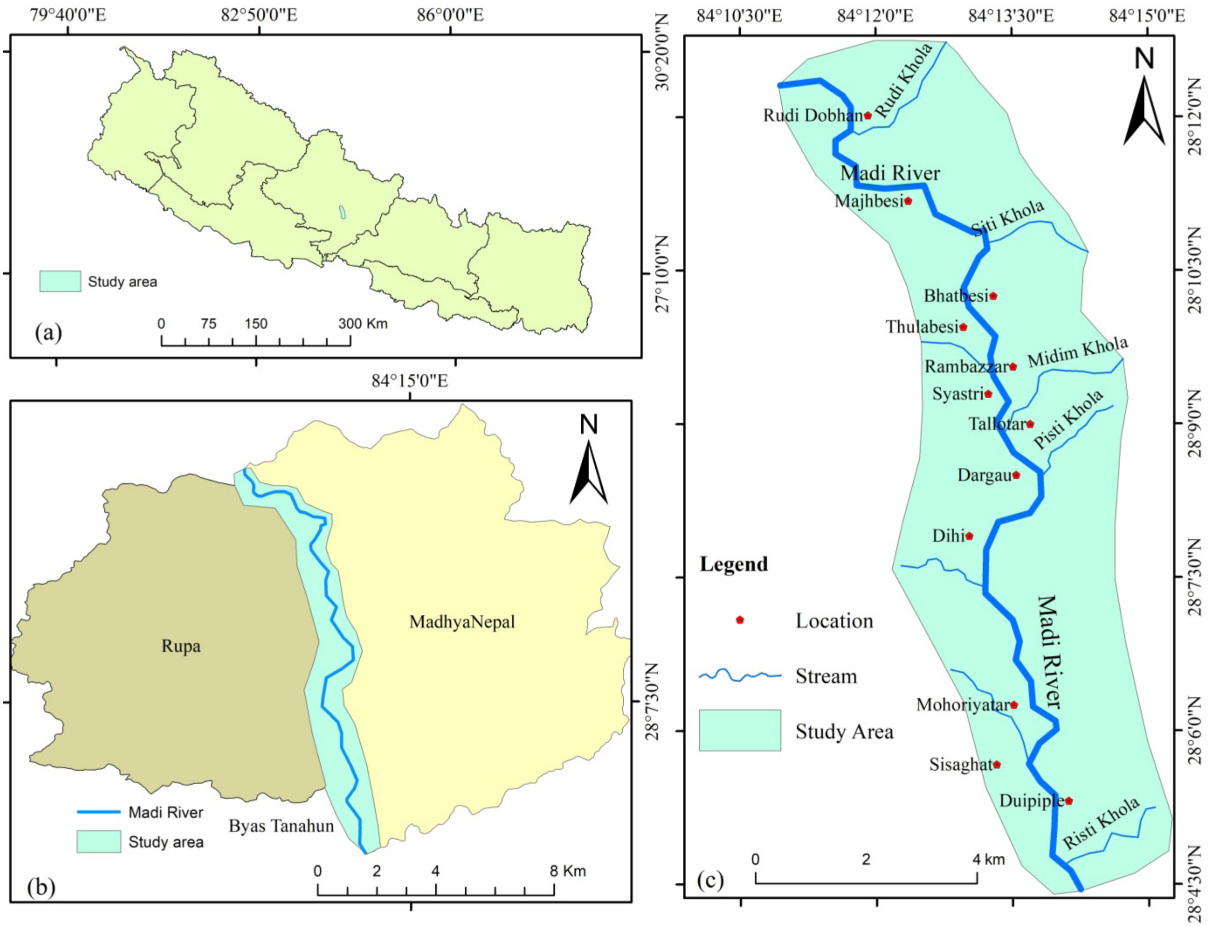

Fig. 2: Location map of the study area (a) Location in map of Nepal, belongs to Gandaki province, (b) Study area showing the Madi River, flows in between Rupa and Madhya Nepal Municipality and (c) Details information about the location of the researched area

METHODOLOGY

The study employed a combination of field investigations, desk-based analysis, and detailed observations of terrace deposits within the basin. Bedrock lithology and composition were also documented during fieldwork. Secondary data were obtained from published journal articles, reports, and relevant geological maps. River terrace analysis involved systematic field observations, detailed geomorphic mapping, and outcrop description (Fig. 3). Columnar sections were prepared for representative terrace exposures, accompanied by systematic photographic documentation. Terrace height and width were measured in the field using measuring tapes and altimeters; for inaccessible sites, Google Earth Pro was used to estimate dimensions. Geographic Information System (GIS) software was employed to prepare geomorphic maps, and CorelDRAW was used for drafting cross-sections and final illustrations. For classification, terraces were designated sequentially as T0, T1, T2, T3, and so forth, where T0 represents the present-day active river channel, T1 is the first terrace above T0, T2 is the second terrace above T1, and T3 lies above T2.

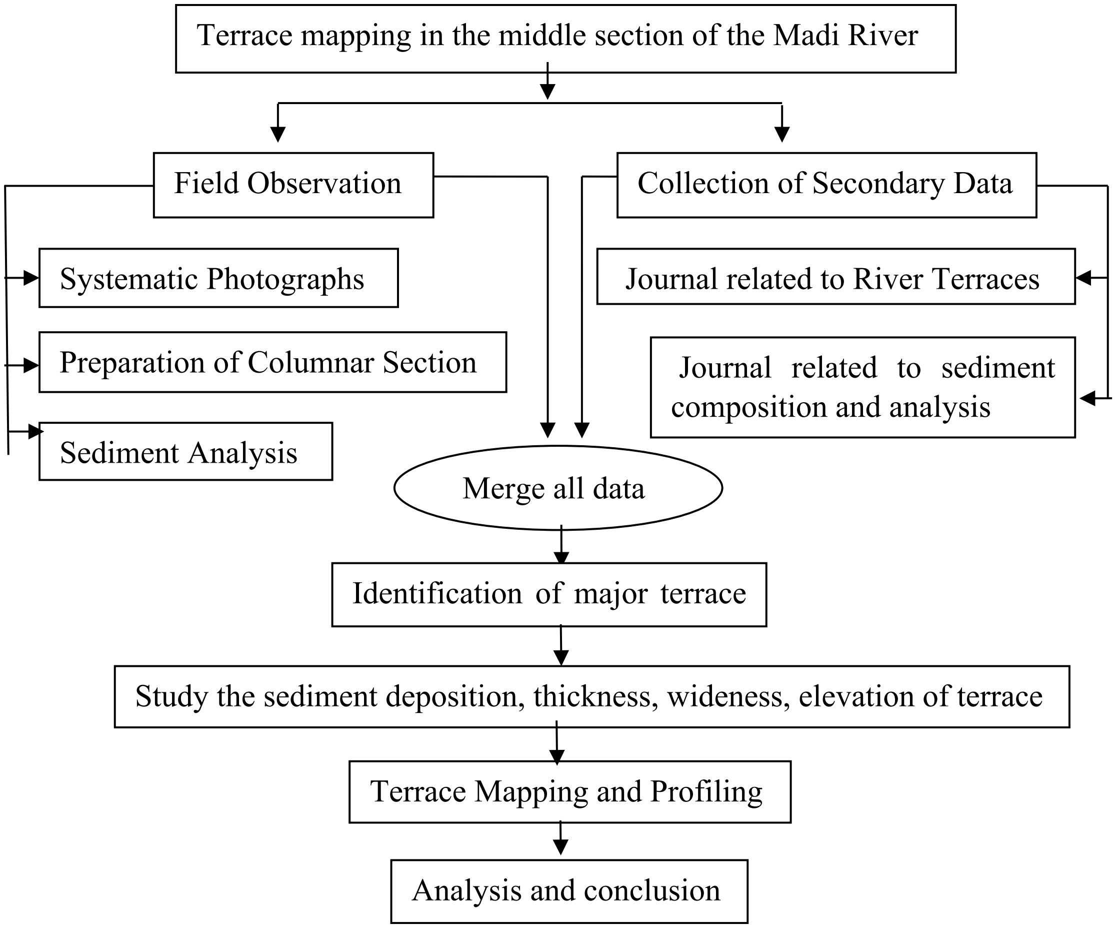

Fig. 3: Methodology flowchart showing the study and analysis of Madi river terrace and their characteristics

RESULTS AND DISCUSSIONS

Detailed geological investigation combined with terrace mapping provided a comprehensive understanding of the study area. River sedimentary deposits are sharply bounded against the underlying bedrock, indicating a distinct depositional gap and the presence of an unconformity. The bedrock in the study area is predominantly assigned to the Ranimatta Formation of the Lesser Himalaya. Based on relative elevation, morphology, and sedimentological characteristics, the river terraces are classified into three distinct levels: higher terrace, middle terrace, and lower terrace.

Ranimatta Formation

The middle reach of the Madi River flows across bedrock exposures belonging to the Ranimatta Formation (Fig. 4). This formation comprises grey, thin- to medium-bedded, fine- to medium-grained metasandstone interlayered with light grey, thinly foliated muscovite–biotite phyllite. River terrace deposits overlie these bedrock exposures, a relationship clearly visible at the Dargau Terrace site (Fig. 8). The bedrock strata in this section generally dips southward.

Higher Terrace

The higher terrace (T3) is distributed across the Dihi (Fig. 5 b), Dargau, Syastri and Bhatbeshi areas (Fig. 4) and rises approximately 130 m above the present Madi River channel (Table 1). At Dargau, T3 forms a well-preserved flat surface with a width of ~80 m. The terrace deposits consist of unsorted and unstratified, sub-rounded to sub-angular large boulders, cobbles, pebbles, and granules composed of augen gneiss, banded gneiss, garnetiferous schist, metasandstone, granite, quartzite, and phyllite. Boulder dimensions reach up to ~5 m × 2 m × 1.5 m. In many areas, the original terrace surface has been modified by colluvial accumulation and agricultural activities, producing a gentle slope. On the opposite bank near the confluence of the Madi River and Pisti Khola, a conglomerate exposure is interpreted as a remnant of the higher terrace (T3).

Middle Terrace

Middle Terrace (T_2) is distributed all over the study area from Duipiple to Rudi Doban (Fig. 4). It is well deposited on the right bank of Madi River. It rises about 40 meters above the riverbed of the Madi River (Table 1). The Middle Terrace is flat terrace of about 70 – 110 meters width with diverse composition (Fig. 6). It is further classified into type a) and type b) according to the sediment type and association. Type a) consists of unconsolidated, unsorted deposit of sub – angular to sub - rounded large boulder, cobble, and pebble with granules association of granite, gneiss, garnet schist, quartzite and metasandstone. In Dihi (Fig. 9), Dargau and Syastri, type a) composition is observed (Fig. 5b, 5c and 5d). This terrace turns into gentle slope and is used for agriculture and settlement. Type b) is composed of firmly consolidated, unsorted, sub – rounded boulder, cobble, pebble, granules and coarse brown sand matrix supported sediment. The Mohoriyatar and Duipiple terraces are type b) of Middle Terraces (Fig. 5a).

Lower Terrace

Lower Terrace (T_1) is distributed all over the study area from Duipiple to Rudi Doban (Fig. 4). It is well deposited on the bank of Madi River. It rises about 20 meters above the riverbed of the Madi River. The Middle Terrace is flat terrace of about 110 – 190 meters width with diverse composition (Table 1). Lower Terrace consists of relatively fine sediments than the Middle and Higher Terraces. Duipiple, Mohoriyatar, Dihi, Dargau, Syastri, Bhatbesi, Majhbesi and Tallobesi area dominantly occupied by the Lower Terrace (Fig.4 and 5). It consists of unconsolidated and moderately sorted boulder, cobble, pebble, granules with coarse to fine sand, silt and clay matrix (Fig. 6). Sub- rounded to round sediment of granite, gneiss, quartzite, garnet schist, pegmatite, metasandstone and phyllite are deposited which is observable throughout the study area (Fig.7, 8 and 10). Sand, silt and clay materials are deposited with alternation of pebble, cobble deposition.

Recent Deposition

Recent Deposition (T_0) is the latest deposition by Madi River which lies in the current flow channels and its bars (Fig. 4). The height of T0 is about 2-7 meters from the current riverbeds. The widening of rivers makes more width of the T0 which is around 60-130 meters at now (Table 1). The Recent Deposition consists of poorly sorted, consolidated, rounded – sub – rounded boulders, cobble, pebble, granules with sandy matrix (Fig. 6). The compositions of these sediments are granite, gneiss, quartzite, pegmatite, and metasandstone (Fig. 5).

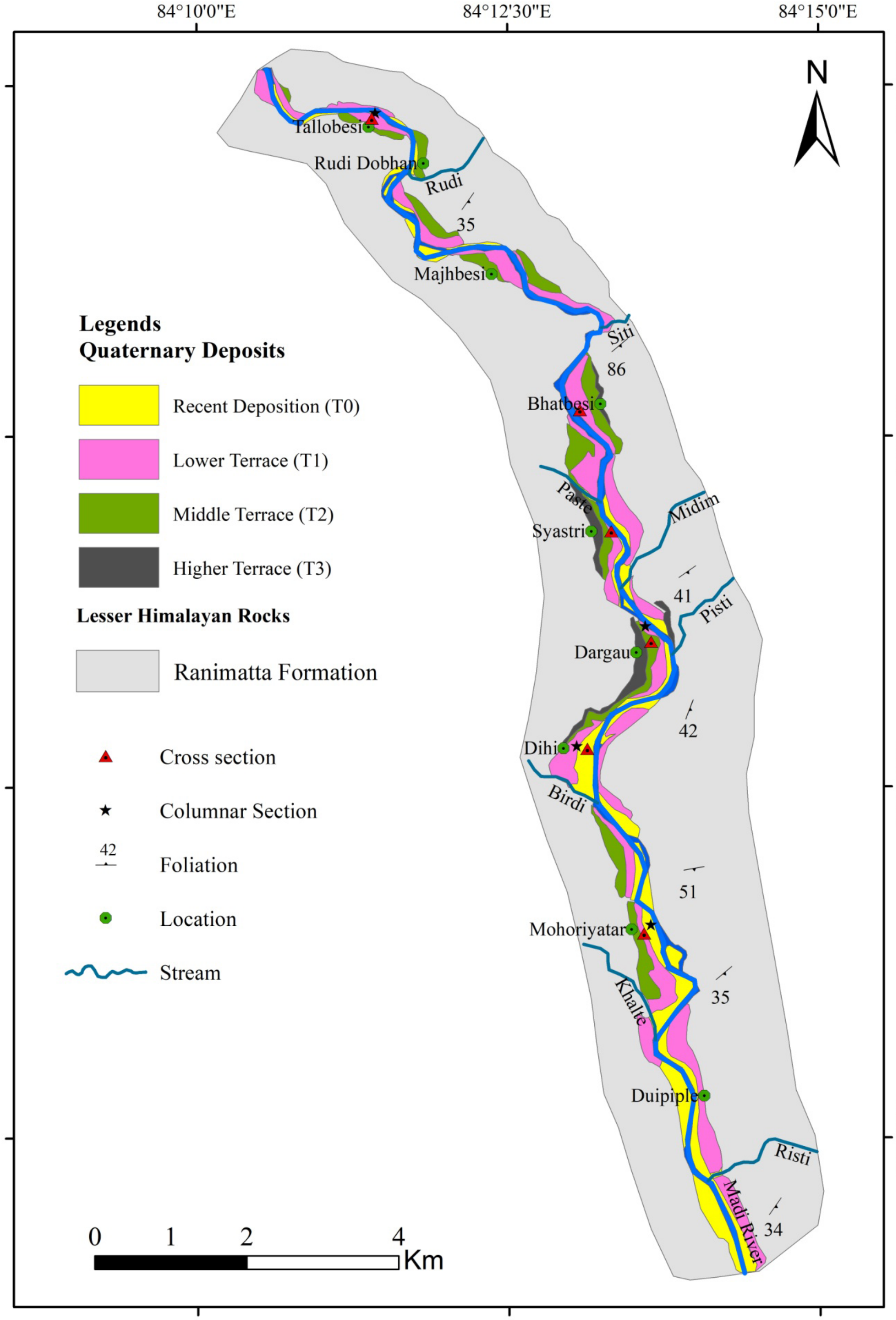

Fig. 4: Geological and terrace deposit map of the Middle Madi River section from the Duipiple to Rudi Doban

Table 1: Terrace of middle Madi River section and their characteristics

S. N.	Name of Terrace	GPS/ Elevation (Based on T_0)	T0	T1		T2		T3		Composition
				Height is measured from T0 in meter scale						
			W(m)	H	W	H	W	H	W	
1	Mohoriyatar	28° 06' 15" N/ 84° 13' 37" E (398m)	285	12	143	35	160			Middle Terrace consists of a matrix of weakly consolidated sub- angular boulder, cobble and pebble of gneiss, quartzite, schist and metasandstone. Lower Terrace consists of the matrix of unsorted, weakly consolidated, sub –rounded to rounded boulder, cobble and pebble, granules with sand, silt association of gneiss, quartzite, and granite.
2	Dihi	28° 07' 55" N/ 84° 13' 06" E (417m)	264	20	80	40	65	80	46	Large boulder of granite and gneiss in Higher Terrace, unsorted sediments in Middle Terrace and weakly consolidated, sub – rounded sediment in the Lower Terraces.
3	Dargau	28° 08' 40" N/ 84° 13' 30" E (434m)	106	12	72	40	81			Unconsolidated sediment in the Middle Terrace. Lower Terrace consists of alternation of sand and granules just above the Bed rocks.
4	Syastri	28° 09' 30" N/ 84° 13' 06" E (454m)	110	11	93	39	67			Poorly sorted, association of sub angular to sub – rounded sediment of granite, gneiss, quartzite, garnet schist, metasandstone and phyllite in both Lower and Middle Terrace.
5	Bhatbesi	28° 10' 16" N/ 84° 12' 50" E (470m)	88	18	104	39	98			Gentle slope consisting of boulder of gneiss, quartzite, and meta sandstone in T3, sub angular – rounded sediment of quartzite, schist and phyllite in T2 with sandy matrix sediment in T1.
6	Tallobesi	28° 12' 13" N/ 84° 11' 28" E (547m)	72	10	38	32	54			The lower part consists of a large boulder, middle part has matrix supported cobble, pebble and upper part has sandy soil of the Lower Terrace.

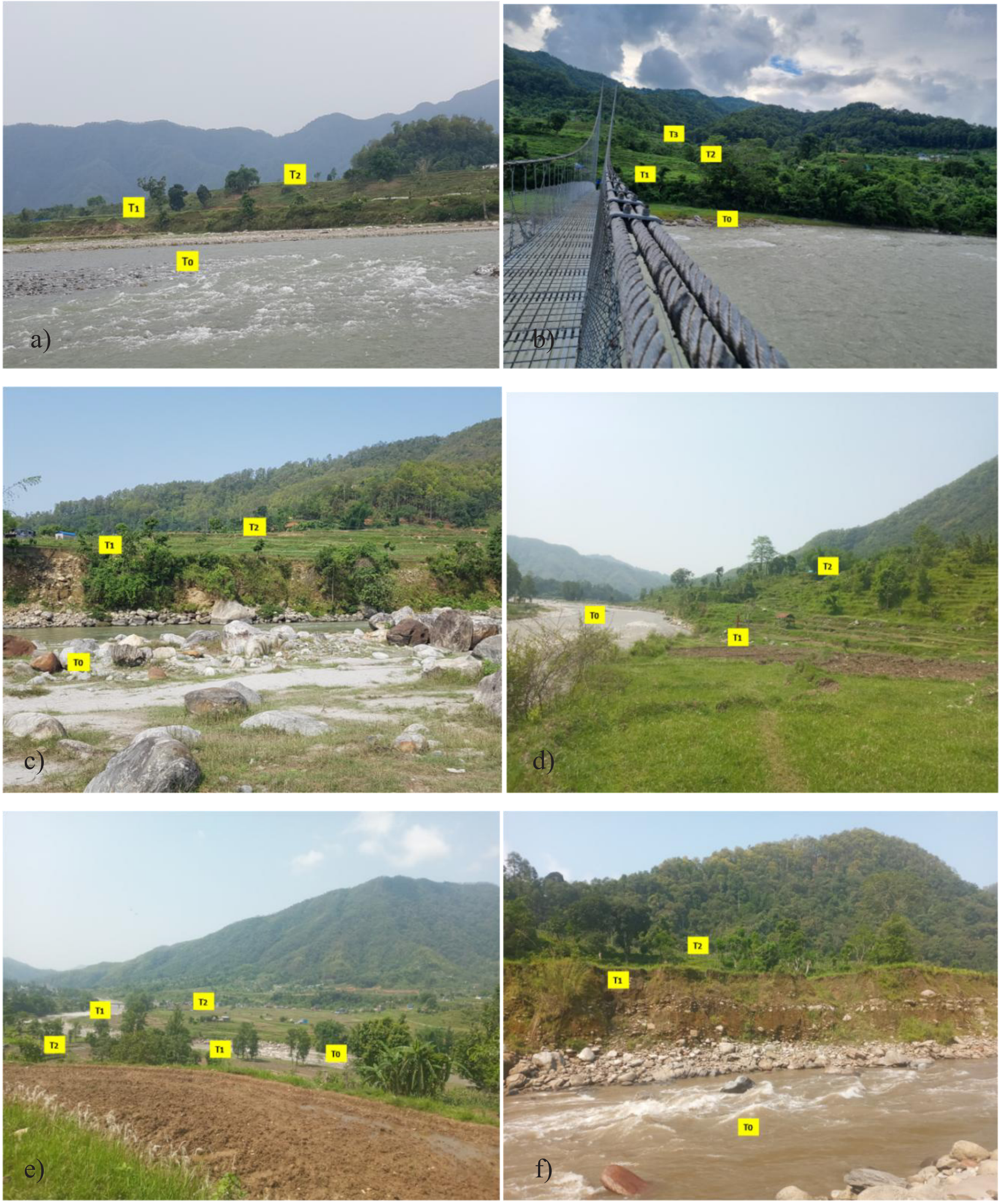

Fig. 5: Images of river Terraces in different part of the middle Madi River, (a) two level terrace with floodplain at Mohoriyatar, (b) three level terrace at Dihi, (c) two level terrace at Dargau, (d) lower and middle terrace at Syastri, (e) two level terrace in Bhatbesi – Thulabesi, (f) lower and middle terrace with flood plain at the right bank of Madi River at Tallobesi

Terrace Cross section

The illustrated cross-sections represent the stratigraphic and geomorphic arrangement of river terraces (T_0, T_1, T_2, and in one case T_3) along the middle section of the Madi River in the Lesser Himalaya (Fig. 6). Each profile demonstrates a distinct separation between the bedrock, composed of the Ranimatta Formation, and the overlying unconsolidated fluvial sediments. The bedrock is shown dipping predominantly towards the south or southeast and is overlain by terrace deposits of varying thicknesses. The lowest terrace (T_0) occurs adjacent to the modern river channel, composed primarily of coarse-grained fluvial sediments resting directly on the bedrock surface. Successively higher terraces (T_1, T_2, and T_3) are inset into the valley slopes, representing older depositional episodes, with the highest terraces occurring at elevations exceeding 500 m in some profiles. The stepped nature of these terraces reflects episodic river incision events, likely driven by tectonic uplift and climatic fluctuations.

A consistent pattern is observed in all cross-sections: the terrace sediments are sharply bound at their base by the bedrock surface, marking a pronounced erosional unconformity. The thickness of sedimentary cover varies laterally, with the highest terraces (T_2–T_3) containing thicker, well-preserved deposits compared to the more eroded lower terraces. The horizontal scale indicates that the valley width varies between 80 m and over 100 m in different sections, influencing terrace preservation. The stratigraphic architecture suggests multiple phases of river aggradation followed by incision, controlled by regional uplift of the Lesser Himalaya and episodic high-energy sediment supply from upstream catchments. This geomorphic and stratigraphic framework provides key evidence for reconstructing the Quaternary landscape evolution of the Madi River valley.

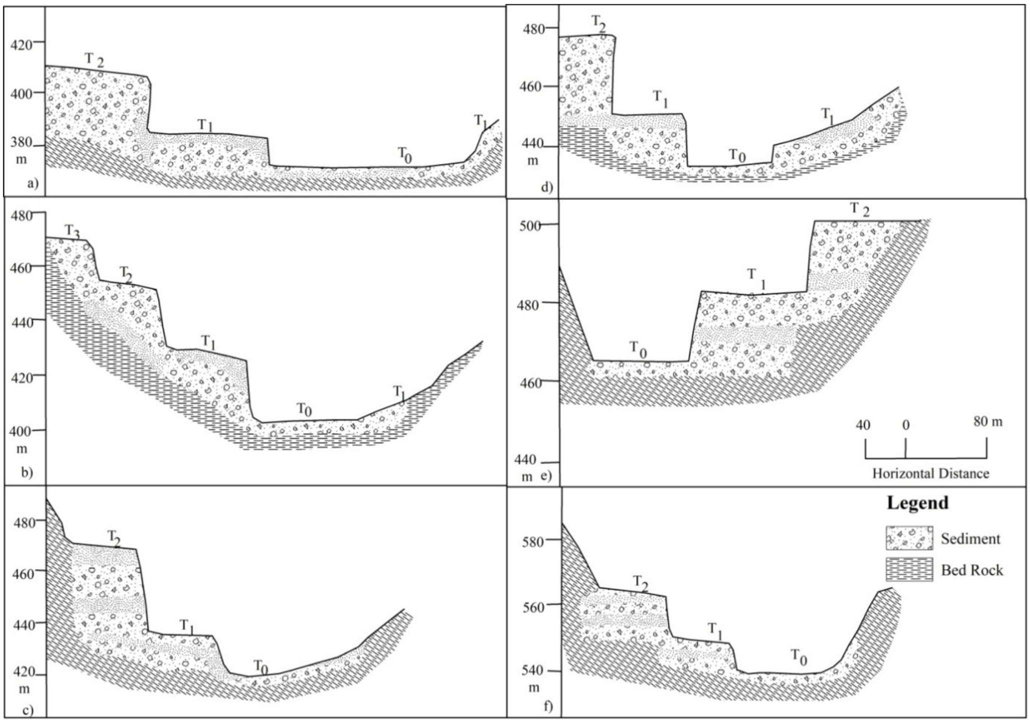

Fig. 6: Terrace cross sections of the middle Madi River, (a) two level terrace with floodplain at Mohoriyatar; (b) three level terrace at Dihi; (c) two level terrace at Dargau; (d) lower and middle terrace at Syastri; (e) two level terrace in Bhatbesi – Thulabesi; (f) lower and middle terrace with flood plain at the right bank of Madi River at Tallobesi

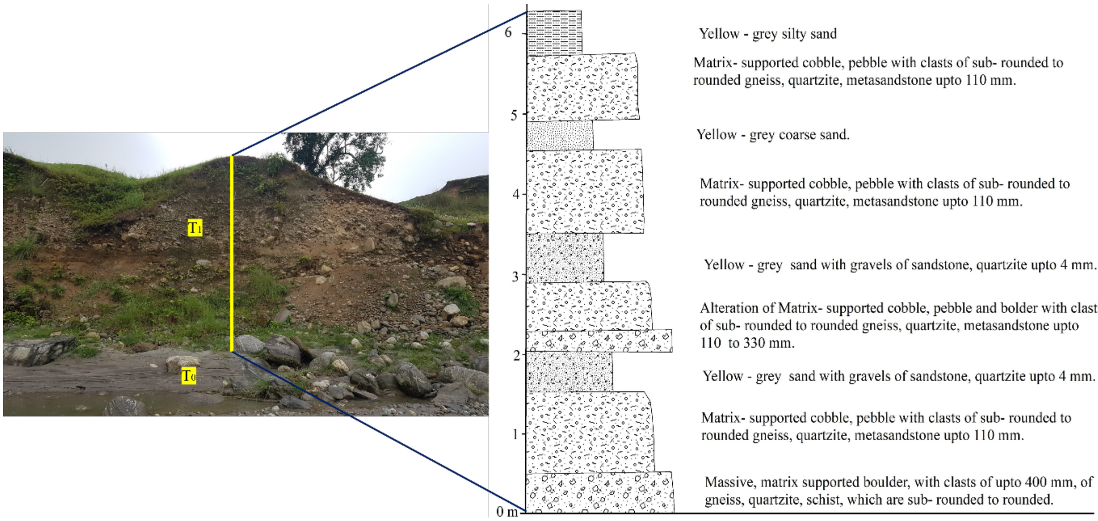

Fig. 7: Columnar section of Lower (T_1) of Mohoriyatar Terrace (Fig. 5a)

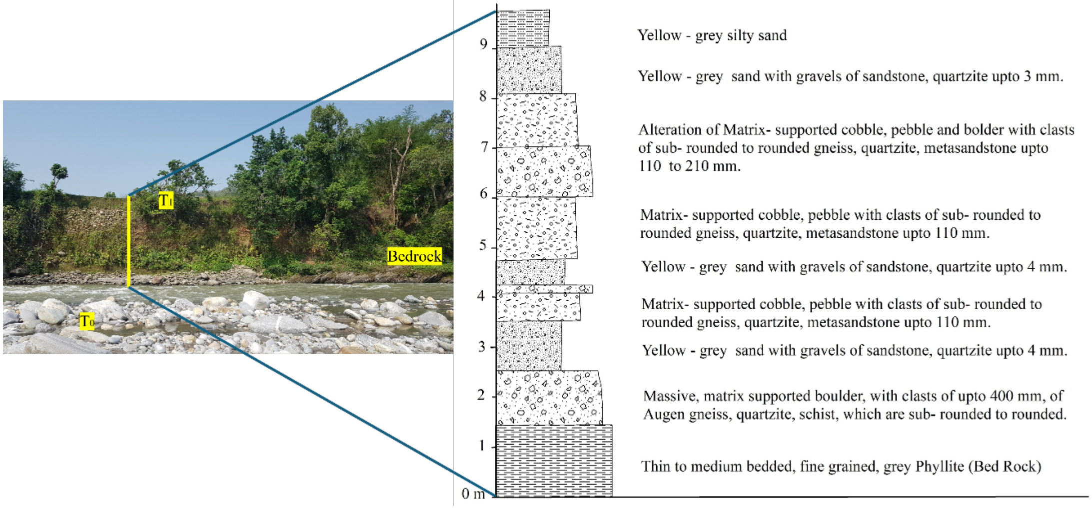

Fig. 8: Columnar section of Lower (T_1) of Dargau Terrace (Fig. 5c)

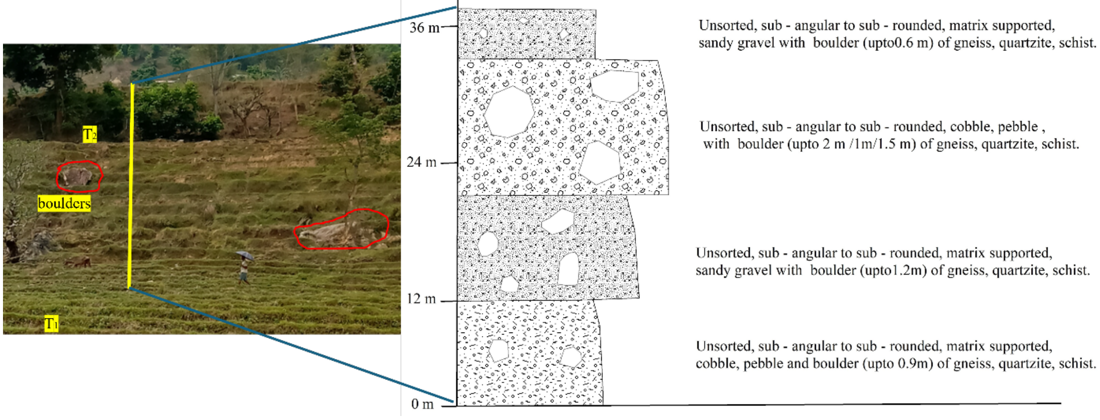

Fig. 9: Columnar section of Middle (T_2) of Dihi Terrace (Fig 5b)

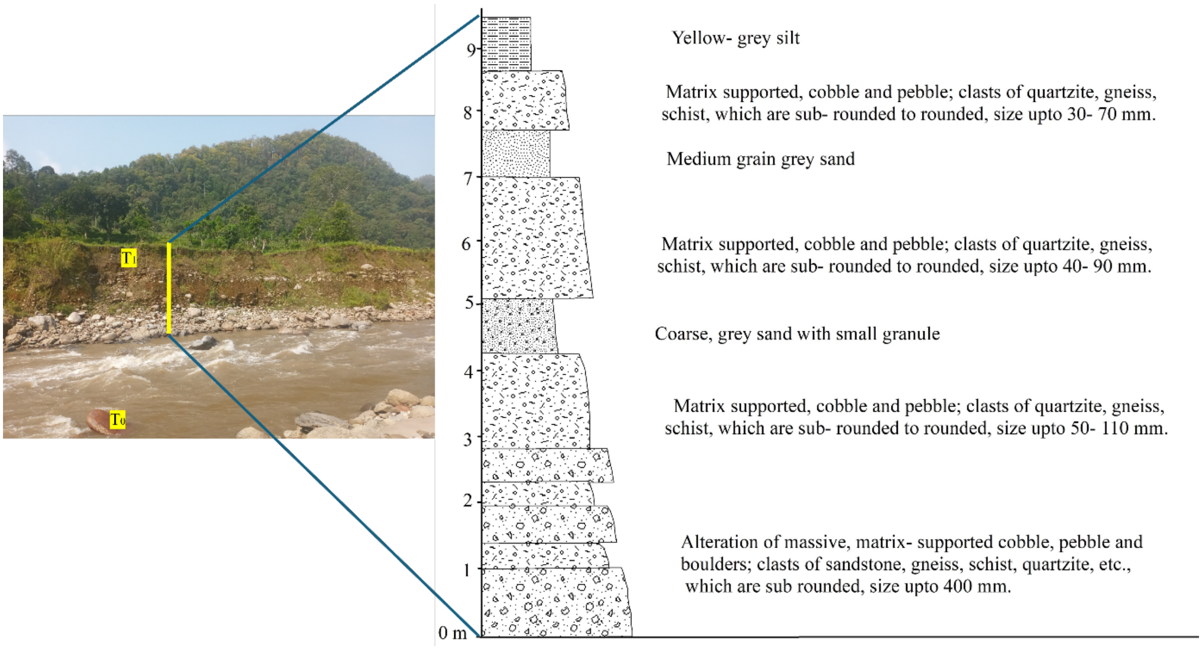

Fig. 10: Columnar section of Lower (T_1) of Tallobesi Terrace (Fig. 5f)

Sequences of Valley Development

Analysis of the river terrace cross-sections along the middle reach of the Madi River reveals three prominent regional terraces, which are interpreted to record three major phases of Himalayan uplift since the river's inception. During the initial phase, the Madi River occupied a broad floodplain, depositing extensive alluvial sediments under relatively stable tectonic conditions. Subsequent episodes of tectonic uplift and associated river incision produced the higher, middle, and lower terraces observed in the present landscape.

Well-developed terraces occur in the Dihi, Dargau, and Mohoriyatar sectors, representing distinct geomorphic levels formed during these incision phases. In addition, tributaries of the Madi River have contributed to the development of wide, laterally extensive terraces within the basin, suggesting a combination of regional uplift, climatic fluctuations, and local base-level adjustments as primary controls on valley evolution.

Terrace Genesis

Different factors are responsible for the genesis of terraces in different environments. The composition of sediment, their deposition pattern and geometry give the sediment origin and maturity. The Higher Terrace consist unsorted, sub – angular to sub – rounded large boulders in gentle slope; Middle Terrace consists consolidated, unsorted, sub- angular to sub – rounded, boulders, cobble, pebble with granules and the Lower Terrace is composed of fairly sorted, consolidated, sub – rounded to rounded small boulders, cobble and pebble, granules with sand and silt matrix. The sediment composition belongs to high grade metamorphic rock like granite, gneiss, schist, garnet schist, quartzite, metasandstone and phyllite. Lesser Himalaya and Higher Himalayan zone is the source of the sediment, which is composed of high-grade metamorphic rock. Recent flood channel consists of fine and coarse sediments which arrived from no of kilometers along with Madi River.

The deposition pattern is diverse in all terraces. The fine sediments (sand, silt) are deposited in alteration with coarser sediment (boulders, cobble, pebble, granules). Low current velocity river is favorable for the deposition of fine sediments. The coarse sediments are deposited by the high velocity current of Madi River. River channel's current velocity is low in winter season and high in summer season. So, finer sediments are deposited in winter season and coarser sediments are deposited in summer season.

Order of Terrace Development

The stratigraphic and geomorphic evidence indicates that the terraces along the middle Madi River were formed in three distinct phases of river incision and aggradation, corresponding to episodic tectonic uplift and changes in fluvial regime.

Higher Terrace (T3) – The Higher Terrace represents the earliest phase of terrace formation and is interpreted as a product of glaciofluvial deposition (Yamanaka and Iwata, 1982). This phase is associated with the initial regional uplift, during which the river established its first extensive floodplain. The T3 surface of the Dihi Terrace contains thick channel-fill deposits, dominated by large, poorly sorted sediments, indicative of high-energy flow conditions within a braided channel system.

Middle Terrace (T2) – The second uplift phase led to the incision of the Higher Terrace and the development of the Middle Terrace, both along the main Madi River and its tributaries. This terrace level is preserved throughout much of the study area and consists predominantly of fluvial deposits. These surfaces are more susceptible to erosion than the higher terraces, reflecting partial reworking of earlier deposits.

Lower Terrace (T1) – The Lower Terrace formed during the third uplift phase, marking the most recent major incision event. Compared with the older terraces, the T1 deposits are finer-grained, indicating reduced stream power and a transition toward more stable, meandering channel conditions.

Influence of Tributaries on Terrace Formation

The terrace morphology and sedimentology of the middle Madi River are significantly influenced by its major tributaries, including the Rudi Khola, Paste Khola, Midim Khola, Birdi Khola, and several smaller streams. Tributary junctions contribute additional sediment loads and influence local hydrodynamics, promoting terrace development. This influence is evidenced by the occurrence of angular to sub-angular phyllite and metasandstone clasts within the Middle and Lower Terraces, particularly well documented in the Dihi and Syastri terrace exposures. The confluence zones between the Madi River and its tributaries commonly host relatively wide terraces, reflecting enhanced sediment storage. These depositional surfaces result from alternating phases of aggradation and degradation, driven by tributary-supplied sediments and subsequent reworking during river incision.

CONCLUSION

River terrace mapping along the middle section of the Madi River reveals a well-preserved sequence of Higher (T3), Middle (T2), Lower (T1), and recent (T0) depositional surfaces, reflecting distinct phases of Himalayan uplift and fluvial response. The Higher Terraces, averaging 80 m in height and 46 m in width, are dominated by large boulder deposits formed under glacio-fluvial conditions during the earliest uplift phase. The Middle Terraces, with an average height of 40 m and width of 90 m, comprise a mixture of coarse and fine sediments, indicating fluvial deposition with significant tributary influence and partial reworking of earlier deposits. The Lower Terraces, averaging 20 m in height and 120 m in width, are composed predominantly of rounded, poorly sorted sediments deposited under lower-energy river conditions.

The spatial distribution, sediment composition, and geometry of these terraces demonstrate that terrace formation in the Madi River valley is the product of combined tectonic uplift, climatic fluctuations, and tributary sediment inputs. Wide terrace surfaces near tributary junctions reflect localized aggradation, while alternating phases of sediment accumulation and incision indicate a dynamic balance between uplift and river down-cutting. The multi-terrace system preserved in this region therefore serves as a geomorphic archive of Quaternary landscape evolution in the Lesser Himalaya, recording both the tectonic history and the changing hydrological regime of the Madi River and its tributaries.

Acknowledgement

We are grateful to the Central Department of Geology Tribhuvan University for the support on collection of literatures about terrace mapping. We would like to thank all the people who are staying around the study area for their cooperation and help.

Author Contributions

All the authors have made significant contributions to preparing these research articles. First Mr. Ashok Dhakal did the study of concept and design. Mr. Sunil Lamsal guided him in field study. Dr. Kabi Raj Paudyal analyzed the field data and provided the framework for the article. The first draft of the manuscript was written by Ashok Dhakal and all authors contributed to making the draft form of the manuscript into the final version. Finally, all the authors contributed to making corrections as per the suggestion of reviewers.

Conflict of Interest

The authors declare no conflict of interest.

Data Availability Statement

The data that supports the findings of this study are available from the corresponding author, upon reasonable request.

References

Bridgland, D.R., 2000. River terrace systems in north-west Europe: an archive of environmental change, uplift and early human occupation. Quat. Sci. Rev. 19 (13), 1293–1303. https://doi.org/10.1016/S0277-3791(99)00095-5.

Carney, J. and Napier, B., 2004. Floodplain Management: visualising floodplains through geological maps. In: Earthwise: Modern Geological Mapping. British Geological Survey, Keyworth, Issue 20, pp. 24–25.

Cunha, P.P., Martins, A.A., Huot, S., Murray, A. and Raposo, L., 2008. Dating the Tejo River lower terraces in the R´od˜ ao area (Portugal) to assess the role of tectonics and uplift. Geomorphology 102 (1), 43–54. https://doi.org/10.1016/j.geomorph.2007.05.019.

Department of Mines and Geology (DMG), 2020. Province map of Nepal, HMG/MOI/ DMG,

Hiroshima, M.,1972. Topography of Marsyandi River, Symposium; Nepal. 1. 45 -50 (In Japanese).

Iwata, S., Yamanaka, H. and Yoshida, M., 1982. Glacial landforms and river terraces in the Thakkhola region, Central Nepal. Journal of Nepal Geological Society, Vol. 2 Special Issue.

Iwata, S. and Yamanaka, H., 1982. River terraces along the middle Kaligandaki and Marsyandi Khola, Central Nepal. Journal of Nepal Geological Society, Vol. 2 Special Issue.

Meikle, C., Stokes, M. and Maddy, D., 2010. Field mapping and GIS visualisation of Quaternary River terrace landforms: an example from the Río Almanzora, SE Spain. J. Maps 6 (1), 531–542. https://doi.org/10.4113/jom.2010.1100.

Nandy. S., Taloor, A.K. and Kothyari, G.C., 2021. Mapping of major river terraces and assessment of their characteristics in Upper Pindar River Basin, Uttarakhand: A geospatial as approach.

Sharma, T., Upreti, B.N. and Vashi, N.M., 1980. Kali Gandaki gravel deposits of Central West Nepal- their neootectonic significance, Tectonophysics, 62, 127-139.

Smith, M.R. and Collis, L., 2001. Aggregates: Sand, Gravel and Crushed Rock Aggregates for Construction Purposes, vol. 17. The Geological Society, Engineering Geology Special Publications, London. https://doi.org/10.1144/GSL.ENG.2001.017.

Journal of Nepal Hydrogeological Association (JNHA), Vol (2), 16-29 (2025)
ISSN: 3059-9725 (Online)
https://doi.org/10.3126/jnha.v2i1.85372

RESEARCH ARTICLE

Long-term rainfall changes based on multiple observation stations in Eastern Nepal

***Damodar Bagale**
Central Department of Hydrology and Meteorology, Tribhuvan University, Kathmandu 44613, Nepal;
**Corresponding author: damu.bagale@gmail.com*

***(Submission Date**: 2 May, 2025;* ***Accepted Date:** 13 June, 2025)*

ABSTRACT

This study utilized 32 meteorological stations for rainfall analysis in Eastern Nepal over 42 years (1977–2018). It found significant fluctuations in seasonal to decadal rainfall. The study revealed that most rainfall occurs during the monsoon season. The northeastern region of Eastern Nepal has received heavier rainfall. The analysis revealed both excess and deficit monsoon rainfall events across various seasons. The year 1987 recorded the highest monsoon rainfall, while 1982 experienced the lowest. In total, eleven major deficit events and seven major excess rainfall events were identified throughout the study period. The deficit years primarily occurred between the late 1970s and mid-2010s, while the excess years were largely concentrated between the mid-1980s and early 2010s. The decadal analysis has indicated that monsoonal rainfall has decreased gradually in Eastern Nepal during the past four decades. The cause might be the changing climate indices. The Southern Oscillation Index (SOI) was strongly correlated with monsoon rainfall; this relationship was particularly pronounced in large deficit and excess events compared to the usual conditions.

Keywords: ***Deficit, Excess, Monsoon, SOI, Variability, Eastern Nepal***

INTRODUCTION

Variability in rainfall is influenced by climate phenomena such as the El Niño-Southern Oscillation (ENSO), which affects the intensity of the monsoon (Balme and Jadhav, 1984; Sein et al., 2015). The Indian Summer Monsoon Rainfall (ISMR) exhibits substantial inter-annual variability influenced by large-scale ocean-atmospheric phenomena such as the ENSO and the Indian Ocean Dipole (IOD) (Sabeerali et al., 2019; Webster et al., 1999). Research suggests that the warming of the Indian Ocean has contributed to increased extreme monsoon precipitation in the past couple of decades. The ongoing warming of the Indian Ocean and the Indian subcontinent plays a significant role in increasing extreme rainfall in the changing climate of South Asian regions (Jin and Wang, 2017). Due to the warming of the climate in South Asia, over the past couple of decades, it has been affected by droughts in India, Nepal, and

Bangladesh (Kumar et al., 2013; Bagale et al., 2021; Chaudhary, 2003). The increased flood and drought events make the livelihood of the poor people complex in this region (Revadekar et al., 2012). More research is essential to decrease the effects of extreme events in these regions. Previous studies have demonstrated a complex relationship between the IOD and ENSO, which influences rainfall patterns in South Asia (Ashok et al., 2003; Sein et al., 2015; Sigdel and Ikeda, 2012). Understanding these trends is critical for managing climate-induced risks and enhancing resilience. These climate drivers can lead to significant fluctuations in monsoon rainfall from year to year, impacting agricultural practices and water availability in South Asia as well as in Nepal (Bagale et al., 2021; Revadekar et al., 2012; Gentle and Marasini, 2012).

In Nepal, recent studies have indicated an increasing extreme precipitation events across various regions of the nation (Bagale et al., 2025; Bhattrai et al., 2025; Gaire et al., 2024; Bagale et al., 2024). Bagale et al. (2025) investigate the deficit and excess events in western Nepal using 28 met stations. The study reveals that the extreme drought years were identified in 1977 and 2004. Gaire et al. (2024) identified far western region received the heavier rainfall than the other parts. There has been a decrease in seasonal rainfall in the Kathmandu Valley in recent decades, which lies in central Nepal (Bhattrai et al., 2025). Bagale et al. (2024) identified the winter drought in Nepal. The results prefer that eastern Nepal was affected by drought than other regions in the past decades. Rainfall plays a crucial role in water availability, agriculture, and socio-economic conditions in Eastern Nepal, where it is influenced by ISMR from June to September, which accounts for most of the annual rainfall. Extreme rainfall events can lead to rapid runoff and soil erosion, exacerbating the risk of natural disasters. Studies indicate an increase in extreme rainfall events, which heighten the risk of drought, flooding, and climatic risk (Wang et al., 2020). In addition to examining historical data trends, this study will utilize statistical methods such as time series analysis and anomaly detection to quantify changes in rainfall patterns over time. This approach will facilitate a deeper understanding of how extreme precipitation events affect Eastern Nepal.

The analysis of rainfall in the present study across Eastern Nepal provides a valuable opportunity to comprehensively explore these dynamics. Examining monsoon anomalies and the relationship between monsoon rainfall and SOI records over four decades. This study aims to identify patterns of rainfall variability in Eastern Nepal.

MATERIALS AND METHODS

Study Area

Eastern Nepal lies from about 26.5º to 28º N latitude and about 85º to 88º E longitude. Elevations range from about 60 meters south to 8774 meters in the north (Fig.1). The Eastern region experiences four seasons: winter, pre-monsoon, monsoon, and post-monsoon. The 32 meteorological stations were used for the Eastern region of Nepal (Fig. 1).

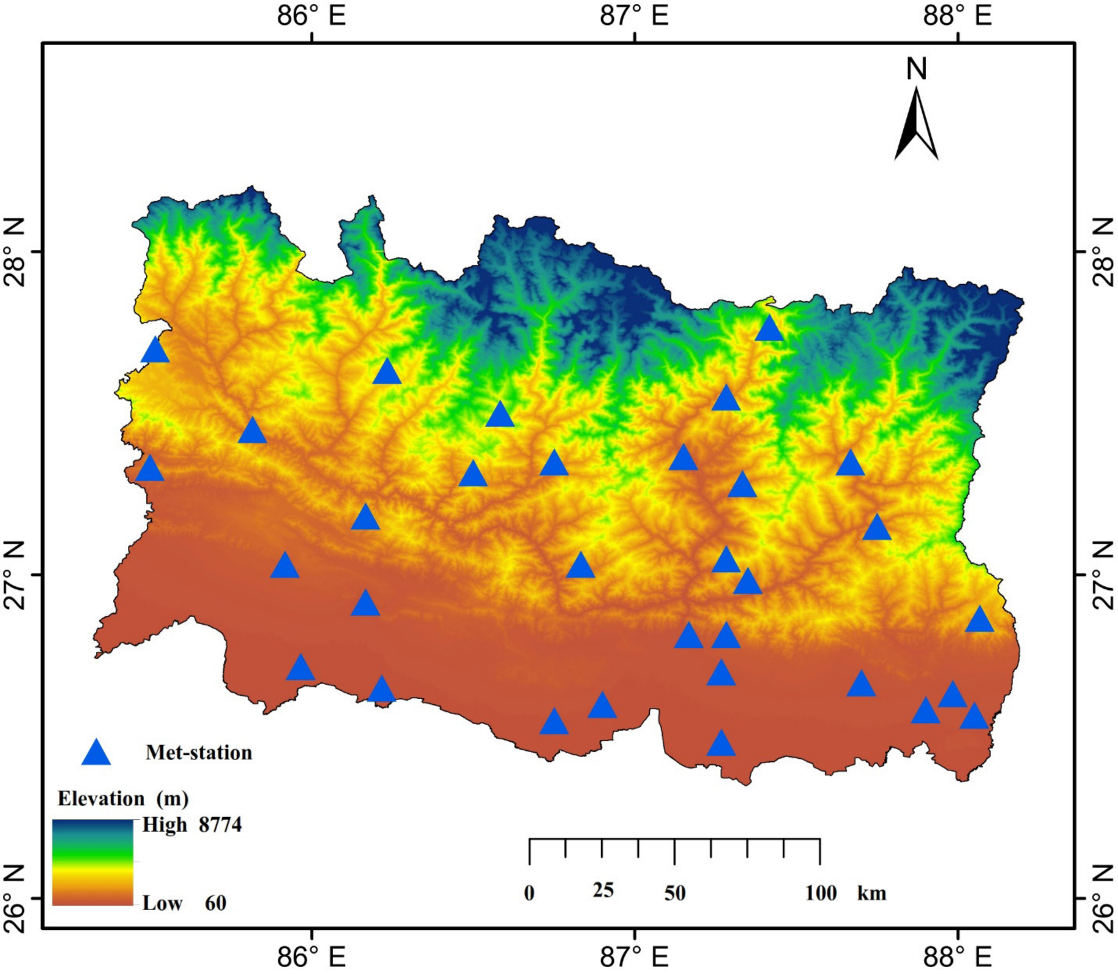

Fig. 1: Spatial distributions of meteorological stations in Eastern Nepal

DATA USED AND METHODOLOGY

The Department of Hydrology and Meteorology (DHM) of Nepal provided the daily rainfall data from 32 meteorological stations in Eastern Nepal between 1977 and 2018. The stations are chosen based on a uniform spatial distribution and data availability. The monthly total rainfall figures were calculated by adding the daily rainfall data. Similarly, the annual total rainfall figures were calculated by adding the monthly total rainfall data from January through December. Once the missing data were filled in, the annual rainfall at stations was determined. The arithmetic mean was used for the average monthly, seasonal, and yearly rainfall. This paper used the Normal Ratio method to estimate missing rainfall values and Student's t test to check statistically significant of rainfall (Bagale et al., 2023a; Bagale et al., 2023b). Spatial variability of rainfall was visualized by using inverse distance weighted method (Patel, et al., 2007). The monthly SOI data over the Nino 3.4 regions were acquired from https://origin.cpc.ncep.noaa.gov/products/precip/CWlink/MJO/enso.shtml.

RESULTS

Rainfall Statistics:

The average monthly rainfall from January to December in eastern Nepal is displayed in figure 2. With 495.54 mm on average, July has the most rainfall, followed by August with 397.37 mm. Rainfall from June to September is noticeably higher than during other months. With 9.97 mm on average, December has the least amount of rainfall. Rainfall gradually increases from March through July, then gradually decreases from August through December. Wet summers and dry winters are the hallmarks of the region's normal monsoon cycle, which is consistent with this trend.

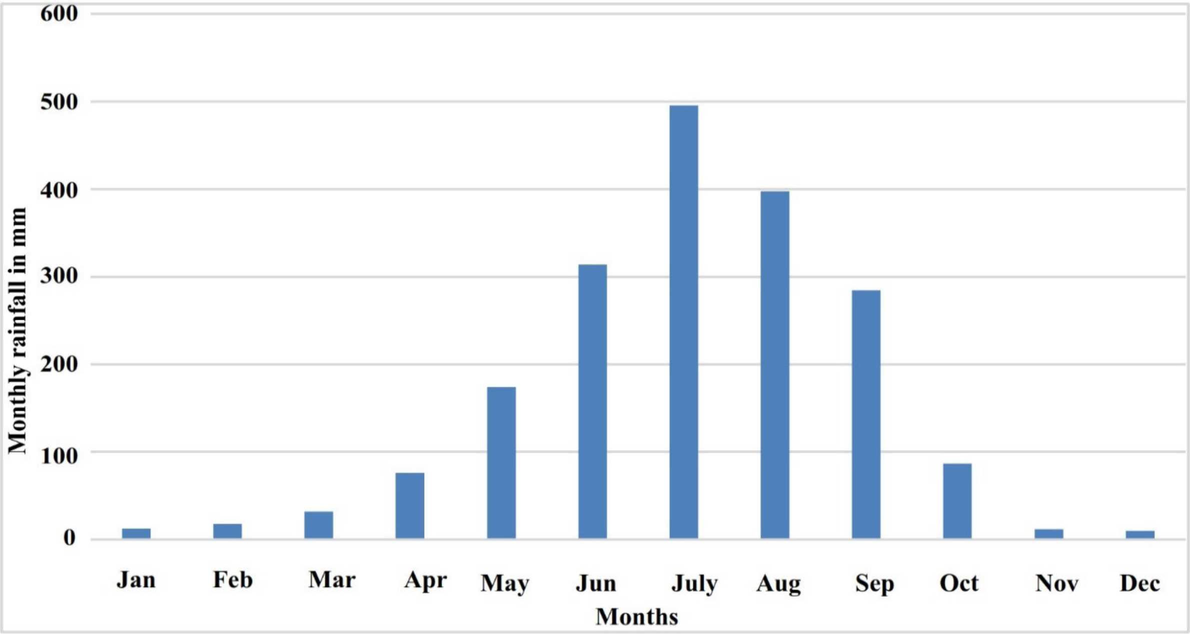

Fig. 2: Average monthly rainfall (mm) from 1977 to 2018

The monsoon season accounts for 78.01% (1491.19 mm) of Eastern Nepal's annual rainfall (1911.53 mm), followed by the pre-monsoon 14.75 %. Similarly, winter is 2.11 % across eastern Nepal, which is the lowest seasonal rainfall, whereas post-monsoon yields 5.13 %, (Table 1). The spatial variability of monsoon months is depicted in Fig. 3(a, b, c, and d).

Table 1: Average Season-wise Rainfall in Eastern Nepal from 1977-2018

Season	Winter	Pre-monsoon	Monsoon	Post-monsoon
Average rainfall (mm)	40.28	281.94	1491.19	98.12

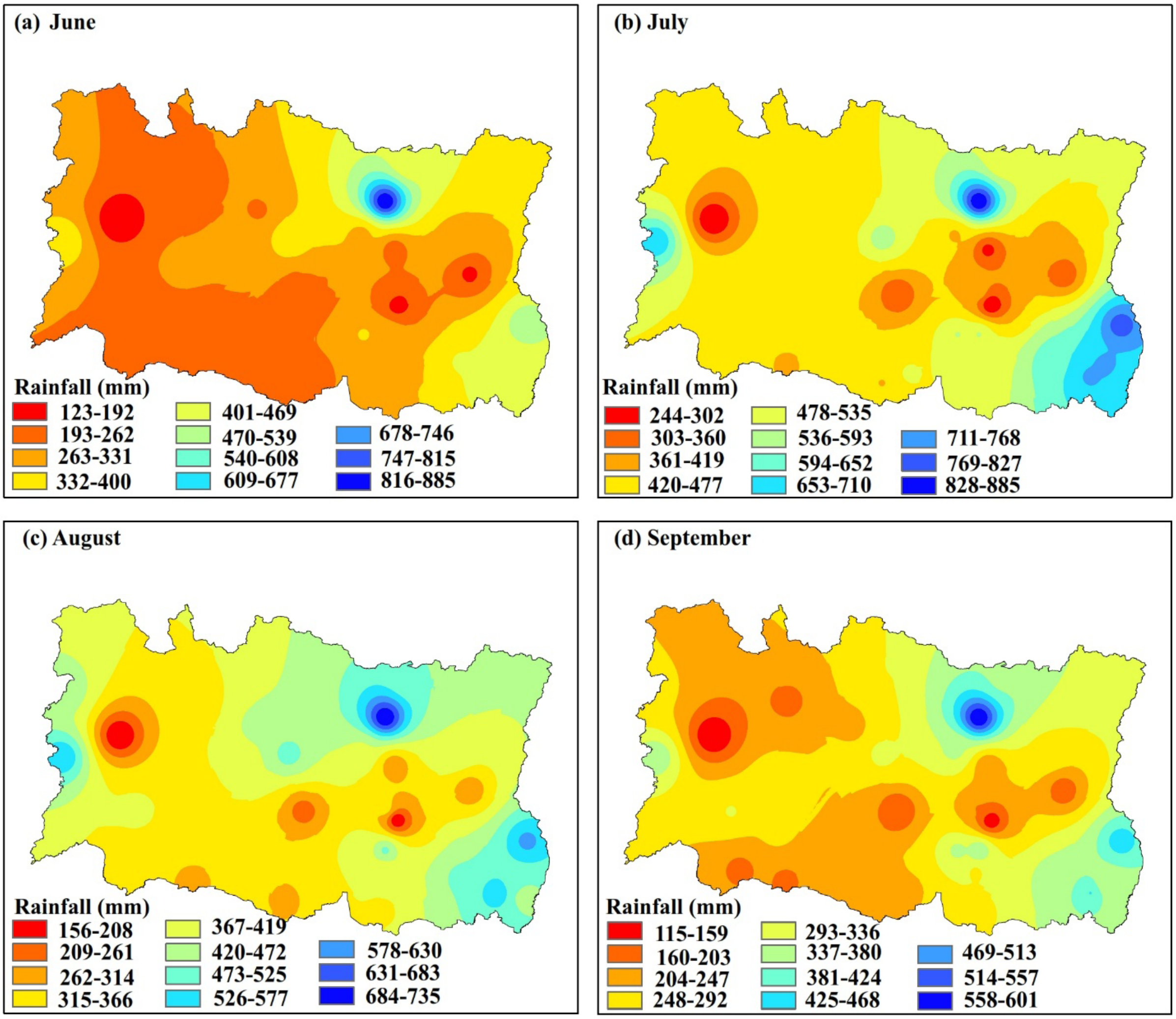

Fig. 3: Spatial variability of mean rainfall during (a) June, (b) July, (c) August, and (d) September from 1977 to 2018

The monthly rainfall variability for June to September is clearly shown in fig (3a, b, c, and d). In June, the northeastern highlands received more rainfall, with a large range of variability, from 73 mm to 318 mm. Similarly, the eastern region received more rainfall during July, decreasing towards the central parts. A similar rainfall pattern is shown (Fig. 3c, and d) in August and September, where the rainfall amounts are different.

Spatial Variability of Seasonal Rainfall

Winter rainfall ranged from 18 mm to 131 mm (Fig. 4a). The northeastern regions receive the most, while the eastern highlands also get relatively high amounts. In contrast, the southern lowlands receive the least. Pre-monsoon rainfall also shows wide variation, from less than 134 mm to more than 944 mm (Fig. 4b). The northern and central areas receive lower amounts during this season. Monsoon rainfall in Eastern Nepal varies greatly, ranging from 638 mm to over 3106 mm (Fig. 4c). The north-central part records the lowest rainfall, while areas known as "monsoon pockets" receive the highest (Fig. 4c). Post-monsoon rainfall ranges from under 39 mm to over 257 mm (Fig. 4d). The south and north eastern areas receive more rain during this period. The lower eastern region gets the highest rainfall, while the northeast receives the least.

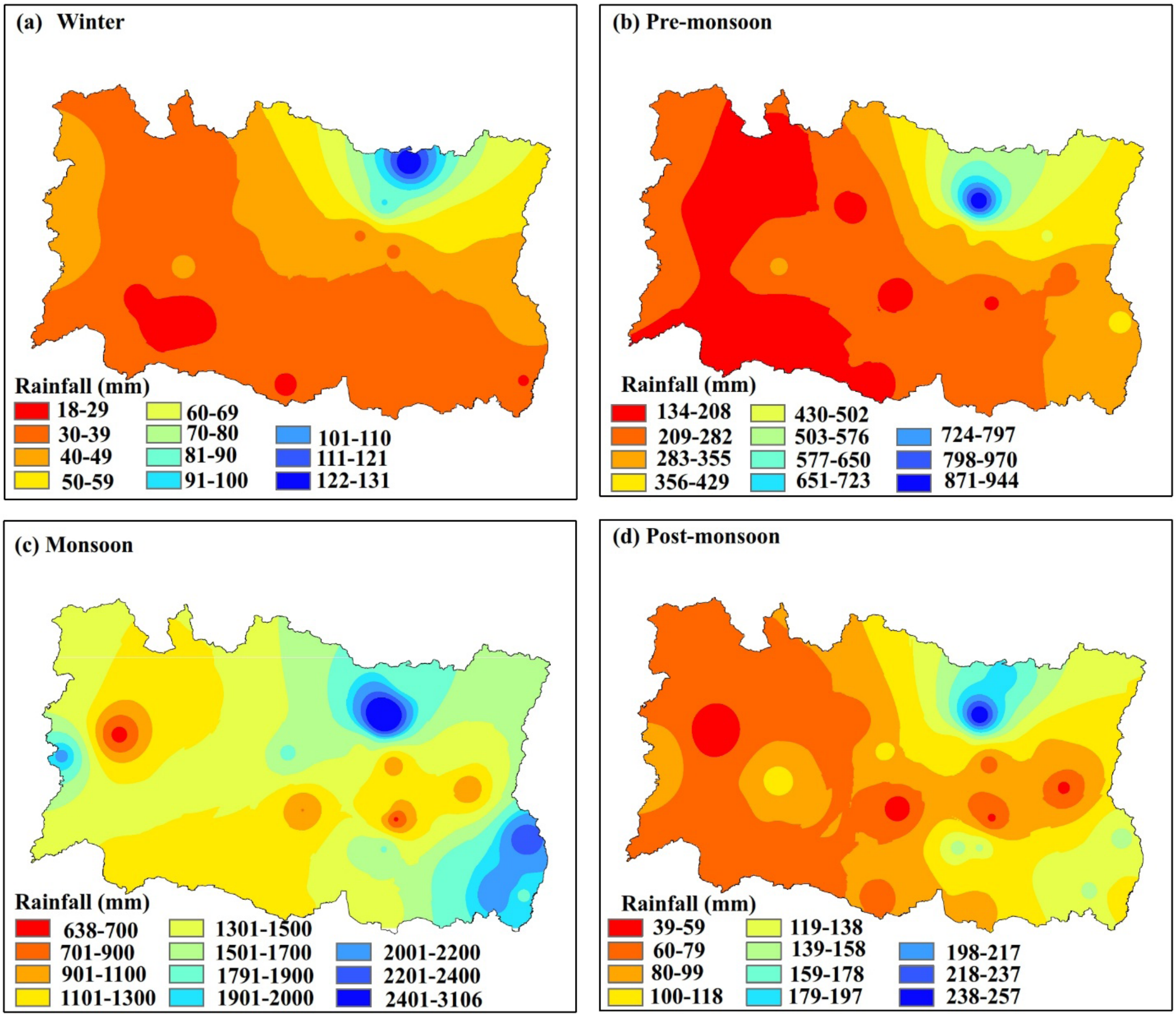

Fig. 4: Seasonal spatial variability of mean rainfall for (a) winter, (b) pre-monsoon, (c) monsoon, and (d) post-monsoon, from 1977 to 2018

Spatial Variability of Annual Rainfall

The high mountainous areas of eastern Nepal received high rainfall, particularly in the northeastern part has the highest rainfall, and the lower lowlands have the minimum. Figure 5 shows the variability of rainfall from 848 mm to more than 4400 mm in the northeast region.

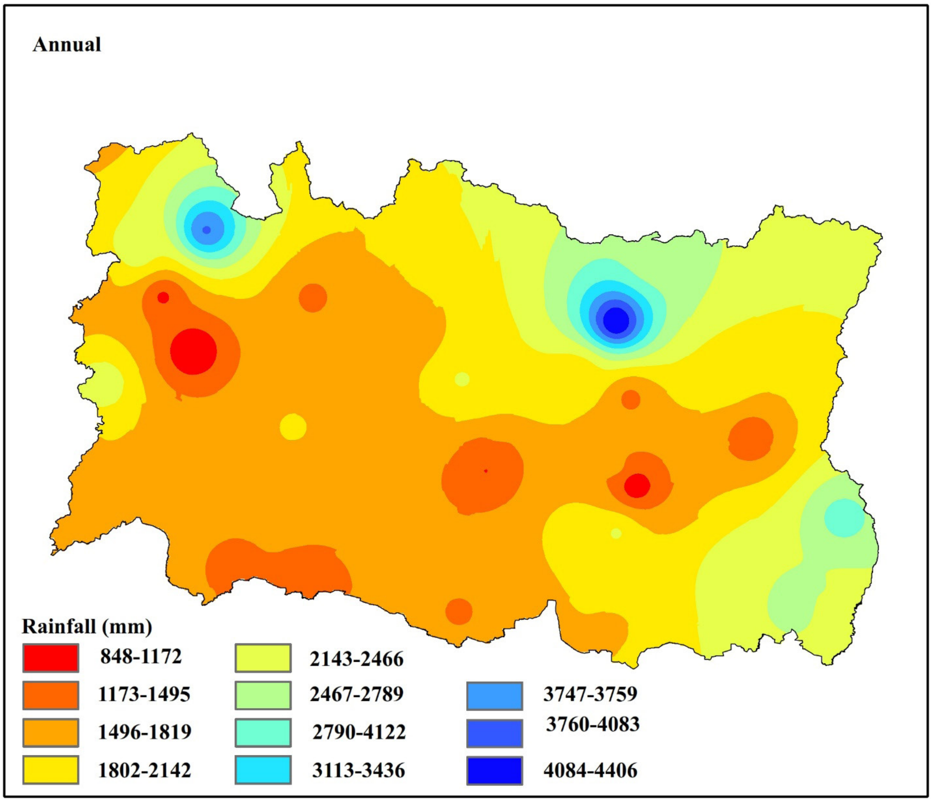

Fig. 5: The mean annual rainfall is spatially distributed in Eastern Nepal (1977-2020)

Temporal Variability of Rainfall

Eastern Nepal experiences significant annual variations in rainfall from 1977 to 2018. The average annual rainfall was 1911.53 mm. A notable deficit occurred in 1982 and an excess in 1987. The overall rainfall pattern is shown in figure 6.

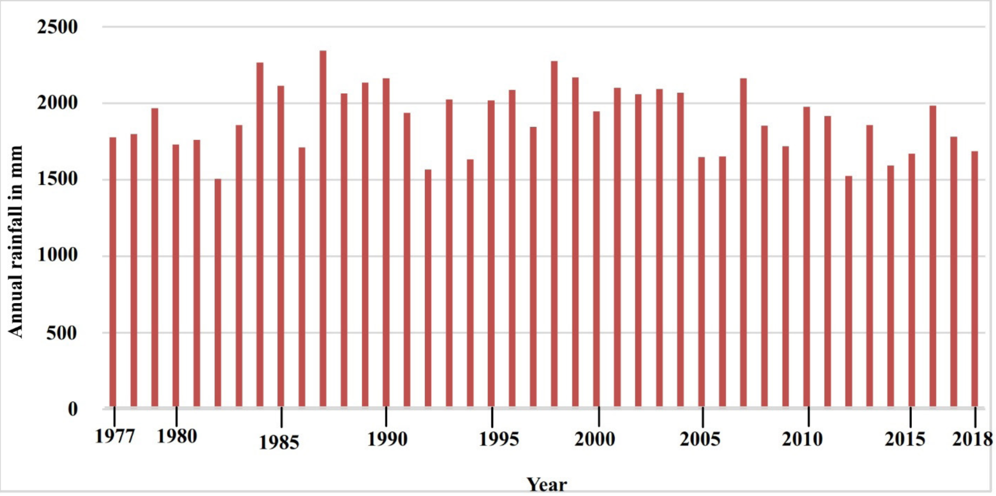

Fig. 6: Temporal variability of mean annual rainfall from 1977 to 2018

Monsoon Rainfall and Anomalies

Figure 7a shows large year-to-year changes in monsoon rainfall, with 1987 having the highest and 1982 the lowest. On average, eastern Nepal receives about 1491.19 mm of rainfall during the monsoon. Fig 7b displays monsoon rainfall anomalies in eastern Nepal. The largest negative anomalies (drier years) occurred in 1982 and 2012, while the highest positive anomalies (wetter years) were in 1984 and 1987. Positive values show above-average rainfall (wet years), while negative values indicate below-average rainfall (dry years). The graph highlights the strong annual variation in monsoon rainfall over the years.

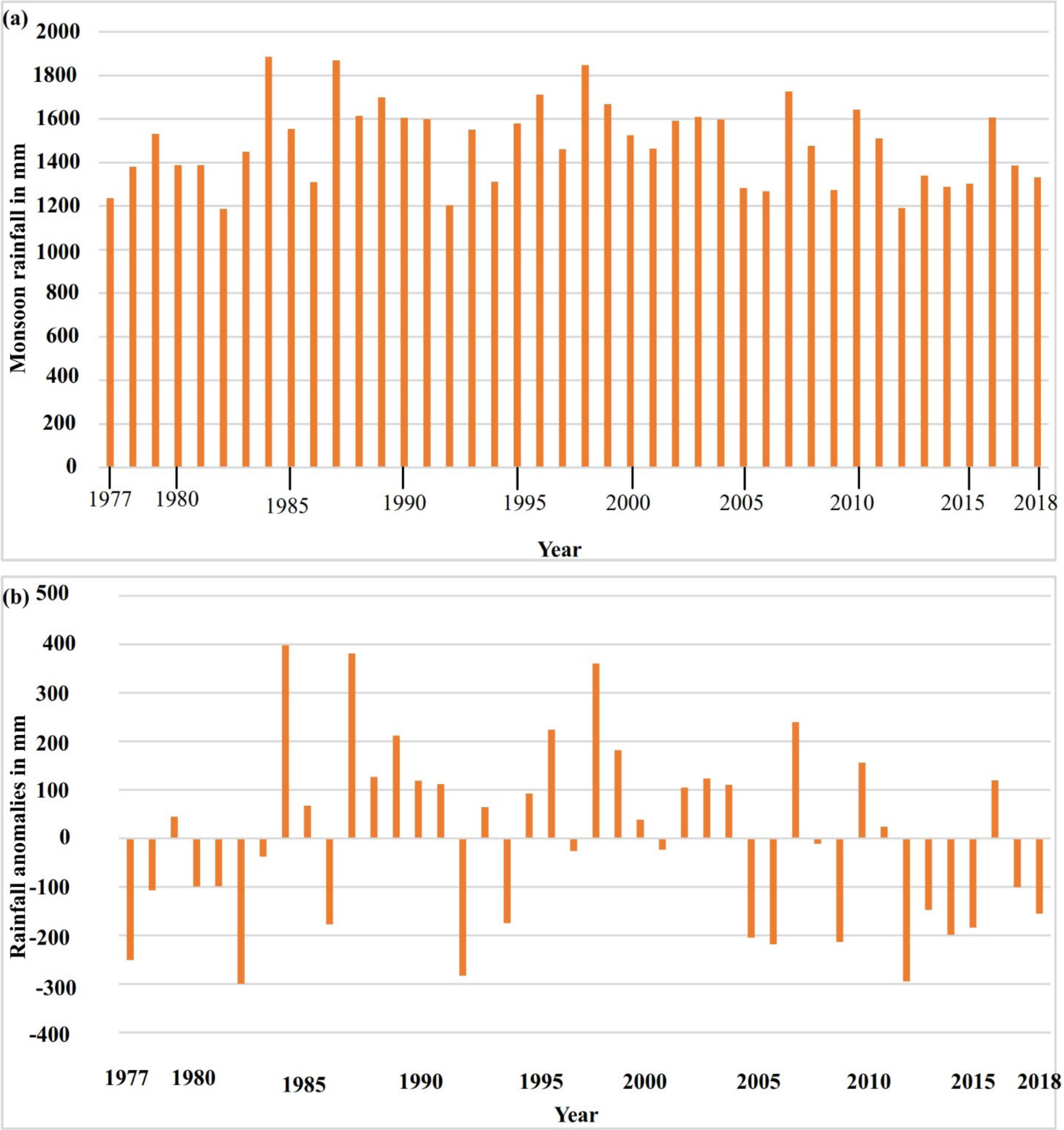

Fig. 7: Temporal variability of (a) mean monsoon rainfall and its anomalies (b) from 1977 to 2018

Decadal Rainfall of Monsoon

This study also examined the changes in decadal rainfall. Over the four multi-decadal periods (1981-1990, 1991-2000, 2001-2010, and 2011-2018), monsoon rainfall varied greatly across the region. The northwest consistently received less rainfall each monsoon season, while the northeast saw more than 3000 mm. Overall, the eastern region experienced higher monsoon rainfall compared to other areas. Figures 8a-d illustrate this significant decadal variation in rainfall across eastern Nepal.

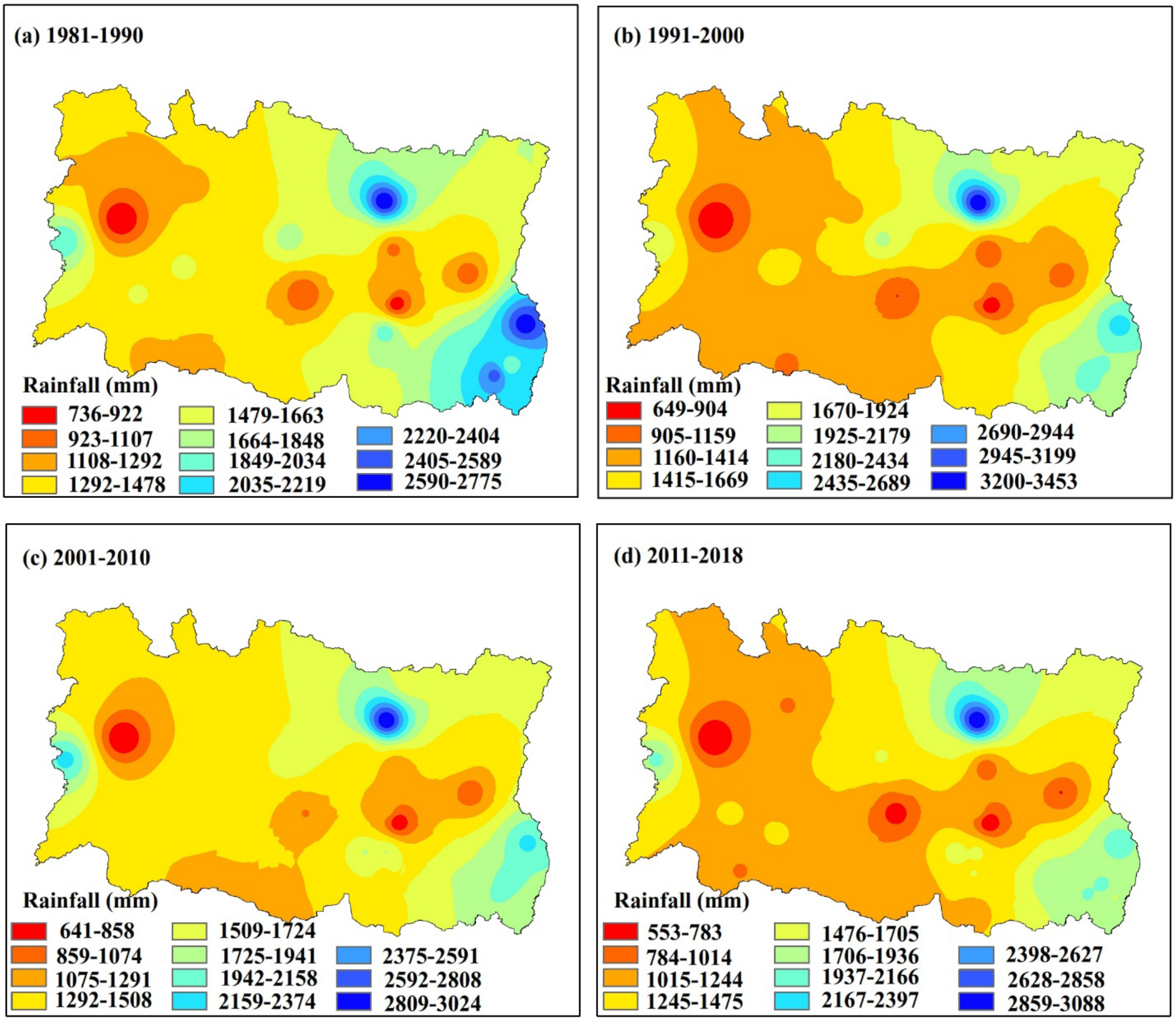

Fig. 8: Spatial rainfall distribution in multi-decadal windows (a) 1981-1990, (b) 1991-2000, (c) 2001-2010, and (d) 2011-2018 over Eastern Nepal

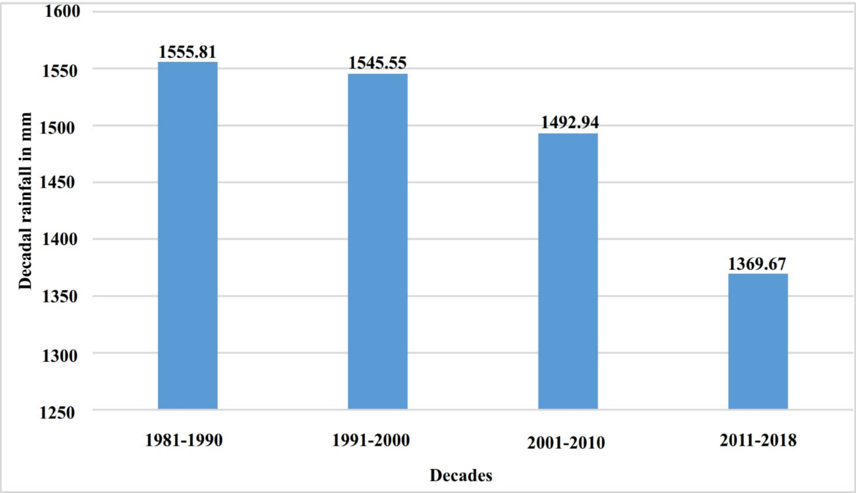

Fig. 9: Decreasing rainfall in the past four decades in Eastern Nepal

The mountainous areas of the eastern region showed consistently heavy rainfall patterns, as seen in Figures 8a-d. In contrast, the southern lowlands were much drier compared to other parts. Overall, the heaviest rainfall occurred in the mountain regions. However, there has been a gradual decline in average decadal rainfall across eastern Nepal over the past four decades (Figure 9).

Relationship between Monsoon Rainfall and SOI

The comparison between the standardized monsoon rainfall and the summer SOI series shows that the correlation coefficient between the standardized monsoon rainfall and summer SOI is 0.36 at a 95 percent confidence level. The standardized monsoon rainfall and the summer SOI series are moderately correlated in eastern regions. The correlation results supports by (Bagale et al., 2023), where description of relationship between monsoon rainfall and SOI are described trolley. The monsoon rainfall is influenced by the SOI in Eastern Nepal.

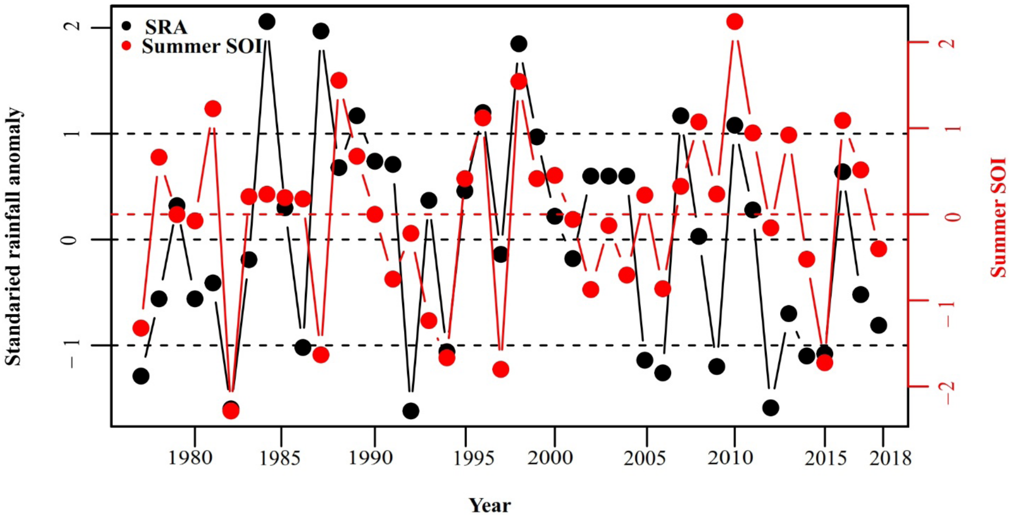

Fig. 10: Relationship between standardized summer rainfall anomaly and southern oscillation index

Based on standardized anomalies, this study has found a total of eleven large rainfall deficit episodes (1977, 1982, 1986, 1992, 1994, 2005, 2006, 2009, 2012, 2014, and 2015). Similarly, seven large excess rainfall episodes (1984, 1987, 1989, 1996, 1998, 2007, and 2010) occurred in different years throughout the study period. The temporal variability of monsoon large deficit and large excess years is shown in Figure 10 for the eastern region. The results have been supported by previous studies (Bagale et al., 2021; Bagale et al., 2023b).

Extreme Rainfall in Eastern Nepal

The large excess and deficit first and second events, spatial variability of rainfall, are depicted in figure 11 (a, b, c, and d). In the dry year of 1982, severe drought conditions were widespread across eastern Nepal (Fig.11a). During dry years, the lower regions still received the highest rainfall, with amounts ranging from 981 mm to about 3300 mm. The total rainfall during the 1982 monsoon was around 1187 mm. A similar pattern occurred in another dry year, 1987 (Fig.11b). In contrast, during the wetter years of 1987 and 2012, the eastern region saw concentrated pockets of heavy rainfall in the northeast and lower areas (Fig. 11c and d).

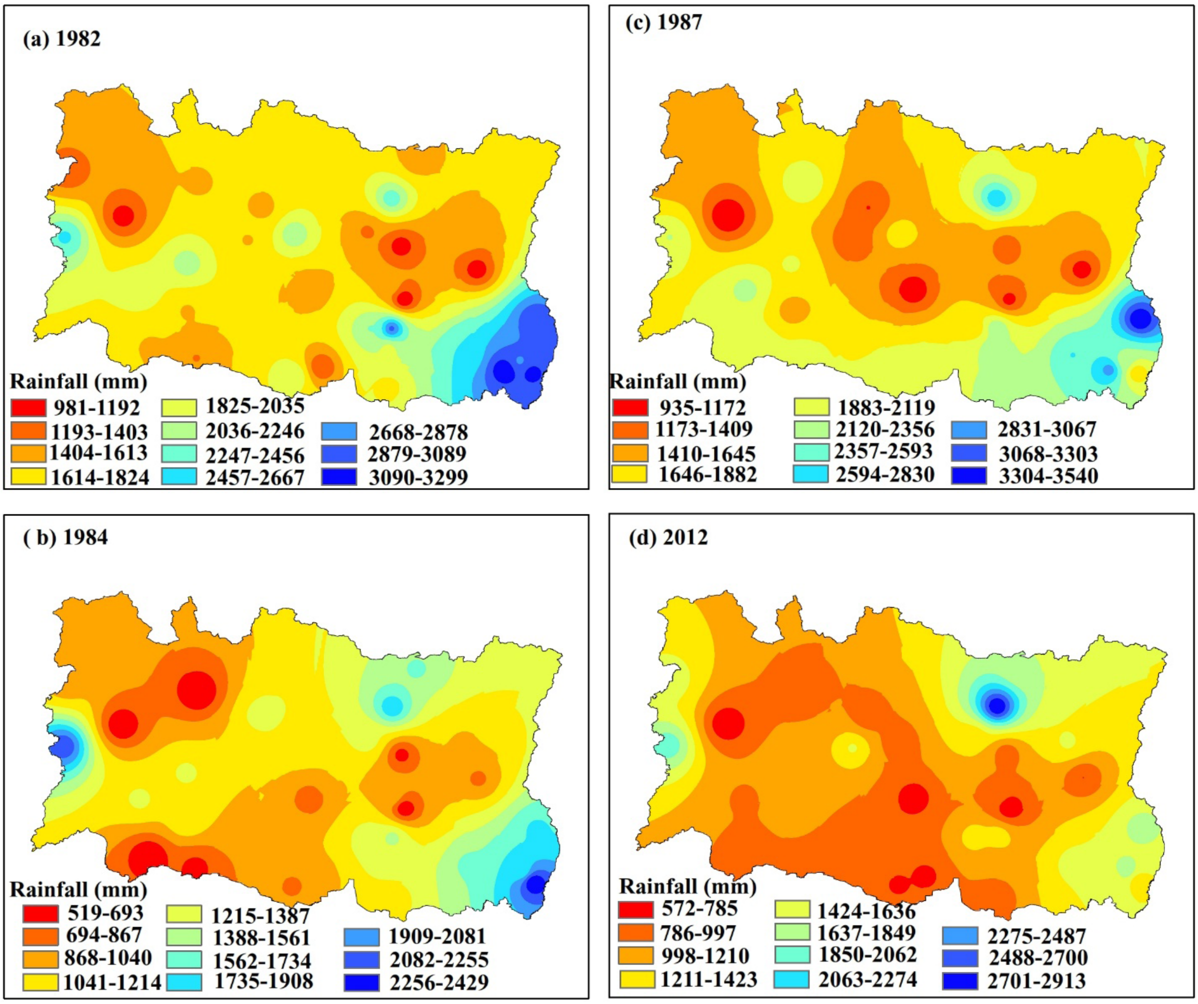

Fig. 11: Spatial variability of rainfall in extreme years (a) 1982, (b) 1987, (c) 1984, and (d) 2012

DISCUSSION

The study of rainfall (1977–2018) shows a significant increase from May, peaking in July due to the monsoon. Eastern Nepal receives 78.01% of its annual rainfall during this period, with high spatial variability, the northeast being the wettest. After 2000, consecutive dry years occurred were 2005 and 2006, and in recent years, 2014 and 2015. The findings of this study align with previous studies (Bagale et al., 2023).

North eastern region has received more monsoon rainfall because these parts faced the windward direction. The strong easterly winds support in monsoon and the westerlies in winter. The results support earlier studies (Sigdel and Ikeda, 2012; Ichiyanagi et al., 2007).

Previous studies in South Asia identified that in past decades, the dry monsoon years have been frequently observed in Myanmar and India (Sein et al., 2015; Kumar et al., 2013).These studies findings supports the decadal rainfall has decreased in eastern Nepal because the South Asian monsoon has been influenced by ENSO.

This study found that a total of eleven large deficit rainfall episodes and large excess rainfall episodes occurred in different years throughout the study period. Notable positive anomalies of around 21 % were observed in 1984. Conversely, approximately 25 % of strong negative anomalies were seen in 1982. The results are in line with (Sharma et al., 2020). The extreme events' similarity has been observed in India and Myanmar (Kumar et al., 2013; Sein et al., 2015).

A four-decade analysis of rainfall data from Eastern Nepal examines long-term rainfall variability, extreme events, and their links to climate drivers like ENSO. The results are similar to (Bagale et al., 2023; Shrestha et al., 2000). Similarly, in India, in line with (Ashok et al., 2003; Sabeerali et al., 2019). The analysis shows that Eastern Nepal has experienced a notable decrease in rainfall since 1990, possibly linked to the weakening southwest Indian monsoon. Similar trends in monsoon rainfall decline have been observed in other parts of South Asia, with potential links to frequent El Niño events. The reduction in rainfall patterns has been consistent across South Asia, with similar findings reported in Myanmar (Sein et al., 2015) and India (Varikoden et al., 2015). Additionally, the frequent occurrence of El Niño events may be contributing to these rainfall declines (Bagale et al., 2021; Varikoden et al., 2015). This study emphasizes the broader trend of diminishing monsoon rainfall in the region.

CONCLUSION

The present study showed significant spatial and temporal rainfall variability. Seasonal contributions to annual rainfall were dominated by the monsoon (78.01%), followed by pre-monsoon (14.75%), post-monsoon (5.13%), and winter (2.11%). Monsoon rainfall varied notably year-to-year, ranging from about 1187 mm to 1884 mm. The highest rainfall was recorded in 1984, while the lowest occurred in 1982. Eight large excess years and eleven large deficit years were identified, with extreme anomalies reaching +25% and -21%, respectively. Decadal trends suggest a decline in monsoon rainfall in recent decades. The SOI tracks El Niño and La Niña events, showing a general but inconsistent relationship with monsoon rainfall variation, with higher SOI values often linked to wetter conditions.

REFERENCES

Ashok, K., Gyan,Z. and Yamagata, T., 2003. Influence of the Indian Ocean Dipole on the Australian winter rainfall. Journal of Geophysical Research Oceans, VOL. 30, NO. 15, 1821, doi:10.1029/2003GL017926

Bagale, D., Sigdel, M. and Aryal, D., 2021. Drought Monitoring Over Nepal for the Last Four Decades and its Connection With Southern Oscillation Index. Water, 13: 3411. https://doi.org/10.3390/w13233411

Bagale, D., Devkota, L, Adhikari, T. and Aryal, D., 2023. Spatio-Temporal Variability of Rainfall over Kathmandu Valley of Nepal. Journal of Hydrology and Meteorology, 11(2): https://doi.org/10.3126/jhm.v11i1.59661

Bagale, D., Sigdel, M. and Aryal, D., 2023. Influence of Southern Oscillation Index on Rainfall Variability in Nepal During Large Deficient Monsoon Years. Journal of Institute of Science and Technology, 28(1): 11-24. https://doi.org/10.3126/jist.v28i1.43452

Bagale, D., Sigdel, M. and Aryal, D., 2024. Winter Drought Monitoring Using Standard Precipitation Index over Nepal. Natural Hazards, 2023:1-14. https://doi.org/10.1007/s11069-023-06242-0

Bagale, D., Dawadi, B. and Mahto, S.K., 2024. Drought Monitoring using Standarized Precipitation Index in Western Nepal. Journal Clean WAS, 9(1) (2025) 06-12. https://doi.org/10.26480/jcleanwas.01.2025.06.12

Bhalme, H. and Jadhav, S., 1984. The Southern Oscillation and its Relation to the Monsoon Rainfall. Journal of Climatology, 4: 509-520.

Bhattrai, S., Bagale, D. and Shrestha, S., 2023. Rainfall Variability in Kathmandu Valley, Nepal. Journal of Scientific World, 18(18): https://doi.org/10.3126/sw.v18i18.78437

Chowdhury, M. R., 2003. The el Niño-southern oscillation (ENSO) and Seasonal Flooding–Bangladesh. Theoretical and Applied Climatology, 76: 105-124. https://doi.org/10.1007/s00704-003-0001-z

Gaire, A., Bagale, D, Acharya, P. and Achraya, R., 2024. Spatial and Temporal Variability of Rainfall in the Western Region of Nepal. Journal of Hydrology and Meteorology, Vol. 12, No. 7: DOI: https://doi.org/10.3126/jhm.v12i1.72656

Gentle, P. and Maraseni, T. N., 2012. Climate change, poverty and livelihoods: Adaptation practices by rural mountain communities in Nepal. Environmental Science and Policy, 21(October 2017), 24–34. https://doi.org/10.1016/j.envsci.2012.03.007

Ichiyanagi, K., Yamanaka, M. D., Muraji, Y. and Vaidya, B. K., 2007. Precipitation in Nepal Between 1987 and 1996. Int. J. Climatol., 27: 1753-1762. doi:10 :1002/joc.1492

Jin, Q. and C. Wang, 2017: A revival of Indian summer monsoon rainfall since 2002. Nature Climate Change, 7: 587–594 (doi: 10.1038/nclimate3348)

Kumar, K. N., Rajeevan, M., Pai, D., Srivastava, A. and Preethi, B., 2013. On the Observed Variability of Monsoon Droughts Over India. Weather and Climate Extremes, 1: 42-50. https://doi.org/10.1016/j.wace.2013.07.006

Patel, N., Chopra, P. and Dadhwal, V., 2007. Analyzing Spatial Patterns of Meteorological Drought Using Standardized Precipitation Index. Meteorological Applications: A journal of Forecasting, Practical Applications, Training Techniques and Modelling, 14: 329-336. https://doi.org/10.1002/met.33

Revadekar, J. V. and Preethi, B., 2012. Statistical analysis of the relationship between summer monsoon precipitation extremes and food grain yield over India. International Journal of Climatology, 32(3), 419–429. https://doi.org/10.1002/joc.2282

Sabeerali, C. T., Ajayamohan, R. S., Bangalath, H. K. and Chen, N., 2019. Atlantic Zonal Mode: An emerging source of Indian summer monsoon variability in a warming world. Geophysical Research Letters, 46: 4460–4467. https://doi.org/10.1029/ 2019GL082379

Sharma, S., Hamal, K., Khadka, N. and Joshi, B. B., 2020. Dominant pattern of year-to-year variability of summer precipitation in Nepal during 1987–2015. Theoretical and Applied Climatology, 142(3–4), 1071–1084. https://doi.org/10.1007/s00704-020-03359-1

Sein, Z. M. M., Ogwang, B., Ongoma, V., Ogou, F. K. and Batebana, K., 2015. Inter-Annual Variability of May-October Rainfall Over Myanmar in Relation to IOD and ENSO. Journal of Environmental and Agricultural Sciences, 4: 28-36

Shrestha, A. B., Wake, C. P., Dibb, J. E. and Mayewski, P. A., 2000. Precipitation Fluctuations in the Nepal Himalaya and its Vicinity and Relationship with some Large Scale, 327: 317–327.

Sigdel, M. and Ikeda, M., 2012. Summer Monsoon Rainfall Over Nepal Related With Large-Scale Atmospheric Circulations. J Earth Sci Clim Change, 3: 112. https://doi.org/10.4172/2157-7617.1000112

Varikoden, H., Revadekar, J., Choudhary, Y. and Preethi, B., 2015. Droughts of Indian Summer Monsoon Associated with El Niño and Non-El Niño years. International Journal of Climatology, 35: 1916-1925. https://doi.org/10.1002/joc.4097

Webster, P. J., Magana, V. O., Palmer, T., Shukla, J., Tomas, R., Yanai, M. and Yasunari, T., 1998. Monsoons: Processes, Predictability, and the Prospects for Prediction.: Journal of Geophysical Research Oceans, 103: 14451-14510. https://doi.org/10.1029/97jc02719

Journal of Nepal Hydrogeological Association (JNHA), Vol (2), 30-44 (2025)
ISSN: 3059-9725 (Online)
https://doi.org/10.3126/jnha.v2i1.85376
RESEARCH ARTICLE

The ground based geological assessment of an active landslide: A case study of Jharlang Landslide in Dhading district, Lesser Himalaya, Central Nepal

***Jharendra K.C.[1], Depak Gautam[2], Purushottam Neupane[3], Shraddha Dhakal[4] and Kabi Raj Paudyal[5]**
[1]Rastriya Prasaran Grid Company Limited, Buddhanagar, Kathmandu, Nepal
[2]NEA Engineering Company Limited, Kathmandu, Nepal
[3]Energy & Infrastructure Maven (EIM) Pvt. Ltd., Kathmandu, Nepal
[4]Nepal Electricity Authority, Kathmandu, Nepal
[5]Central Department of Geology, Tribhuvan University, Kathmandu, Nepal
**Corresponding author: jharendrakc03@gmail.com*

***(Submission Date**: 30 May, 2025; **Accepted Date:** 3 July, 2025)*

ABSTRACT

Jharlang Landslide, also known as "Jharlang Pairo," is a large-scale, ongoing landslide that is situated in the northwest of the Dhading District. This article provides a detailed geological assessment and evaluates the causes, consequences and general mitigation plan of the landslide. The overall study of the landslide was carried out by desk study and field investigation. Field work was carried out to gather pertinent data and information about slope failures. The primary methods of evaluation are knowledge-driven approaches, kinematic analysis, visual inspection, satellite image interpretation, and topographic maps interpretation. The study facilitates comparative analysis through previous studies, satellite images and field observation. The study area is located in the Lesser Himalayan region in Central Nepal. The dominant lithological units in this area are Meta-sandstone, Ulleri Augen Gneiss and phyllite. The constant risk of the landslide to the local people and damage of farmed land and infrastructures is increasing. The area has been impacted by the "2015 Gorkha Earthquake," which has caused new tension cracks to emerge, slope failures to increase, and landslides to spread toward neighboring settlements. Slope failures in different dimensions are caused by the area's brittle, high density soil masses that lay on top of the weathered Ulleri Augen Gneiss, phyllite, and meta-sandstone.

The Jharlang Landslide is a composite of debris flows, debris slides, and rotational slides. The potential and weak section are mostly located in NE and SW direction of the study area. The tension cracks are noticeable that extend towards the villages. The result of the study exhibits weak geological condition, lithological composition, tectonic activity, oversaturation of soil mass, high precipitation and anthropogenic factors are the major causes of the landslide. According to the field assessment and the type of slope failures, the landslide is unstable, particularly during the rainy season. General recommendation incorporates structural and non-structural techniques to minimize the risk and mitigate the landslide hazard.

Keywords: ***Lesser Himalaya, Slope failures, Rotational slide, Debris flows, Ulleri augen gneiss***

INTRODUCTION

Nepal Himalaya lies at the center of Himalayan Mountain range of 2400 km. The region is geodynamically active which witness frequent and widespread landslides every year during rainy seasons. Slope instabilities are common problem in hilly and mountainous regions. Physiography of slopes, poor geological condition and triggering factors such as excessive monsoon rainfall, cloudburst and earthquakes etc. contribute to the frequency of landslides in Nepal (Paudyal et al., 2021). Landslides are one of the major land degradation processes that occur frequently in the Himalaya (Nepal et al., 2019). According to the Ministry of Home Affairs, Nepal (MoHA), approximately 230, 315 and 340 major landslides occurred in 2021, 2022 and 2023 respectively with the significant loss of lives and casualties. Landslides continue to be a terrible occurrence that obliterate human life, property, and the natural world's beauty (KC et al., 2018). Accurate evaluation and identification of high-risk locations are necessary for landslide research and mitigation initiatives (Budha et al., 2016; KC et al., 2018; Timalsina and Paudyal, 2018). Neupane et al. (2023) identified rivers for generating landslides in terrain with soft lithology like Siwalik.

Jharlang Landslide is commonly called 'Jharlang Pairo' (Fig. 1), located in Dhading District in Central Nepal. The landslide is active since 1954 AD and has been threatening to human lives. It is reported that the households near the landslide area have been resettled in the Western part of Nepal. The present study is a field-based geological assessment of the active landslide through visual inspection and observation. In this study, the landslide has been evaluated through geology of the area, lithological composition, hydrogeological interactions, rock and soil conditions and observation of slope failures. By the geological field investigation, this paper presents and discusses the associated causes and consequences of the landslide.

Numerous studies have been conducted to understand landslides from geological and geotechnical perspectives in Dhading and the surrounding districts. Ghimire et al. (2007) investigated the Ramche landslide, while Pant (2010) carried out structural analysis and geological mapping along the Trishuli Valley in Central Nepal. Thapa et al. (2007) employed a geographical information system (GIS) to perform quantitative landslide hazard prediction modelling on natural hill slopes in the study area. Dahal et al. (2006) discussed slope failures along road corridors during episodes of intense rainfall, which included parts of the current study region.

In addition, several recent studies have addressed landslide hazards across the Nepal Himalaya, geographically similar train of the present area (Paudyal et al., 2024; Acharya et al., 2023; Neupane et al., 2023; Paudyal and Maharjan, 2023; Paudyal and Maharjan, 2022; Shahi et al., 2022; Paudyal et al., 2021; Budha et al., 2016 and 2020; KC et al., 2018). Among these, Paudyal and Maharjan (2023) mapped landslide susceptibility in the Main Boundary Thrust zone in Arghakhanchi and Palpa districts, emphasizing the influence of geological structures on slope stability. Similarly, Acharya et al., (2023) identified active faults—such as the Badi Gad Fault—as a significant triggering factor for landslides.

Fig. 1: Satellite image of Jharlang Landslide and proximity of landslide to nearby villages (Source: Google Earth Pro 2024)

MATERIALS AND METHODS

Study Area

Jharlang Landslide is located in Dhading district which is approximately 250 km North West from Kathmandu Valley (Fig. 2). The study area has latitude 28˚07'30"N and longitude of 85˚02'30"E. The elevation of the study area is approximately 2500 m from mean sea level whereas slope varies from 20˚ to 55˚. The study area has been drained by several streams flowing from northeast to southwest direction. Ankhu Khola is the major stream whereas other small tributaries form the drainage system of this area. Geo-morphologically, the area is rugged, slightly steep to gentle hill slopes. The crown section of the landslide is covered by trees and cultivated land and characterized by unconsolidated sediments and highly weathered rocks.

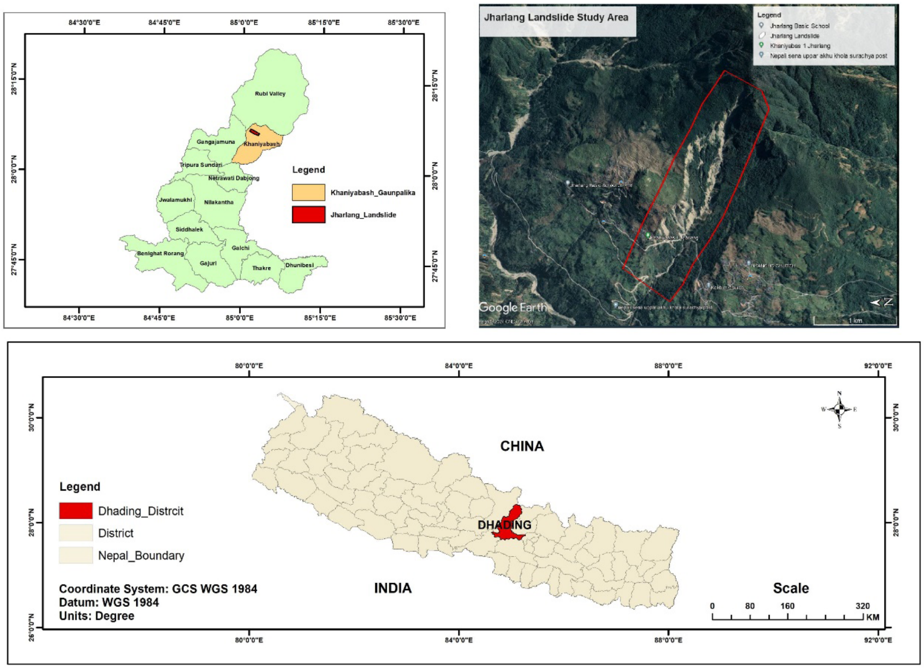

Fig. 2: Geological map showing the study area

According to Stöcklin and Bhattarai (1977), the research area is located in the Kuncha Formation, which is the oldest unit in the Lesser Himalaya. The Formation is composed with metasandstone, metaconglomerate, phyllite (psammatic and pellitic) and lesser proportion of quartzite (Fig. 3). One of the major lithological compositions in the study area is Ulleri Augen Gneiss. Highly crushed and deformed rocks and shear band of black clay (approximately 3-5 m width) were observed at the middle and toe sections of the landslide (Fig. 4 a). It indicates the area is affected by the seismic activities. Furthermore, alternating bedding sequences of metasandstone, phyllite and schist prevail slope failures in the study area (Fig. 4 b).

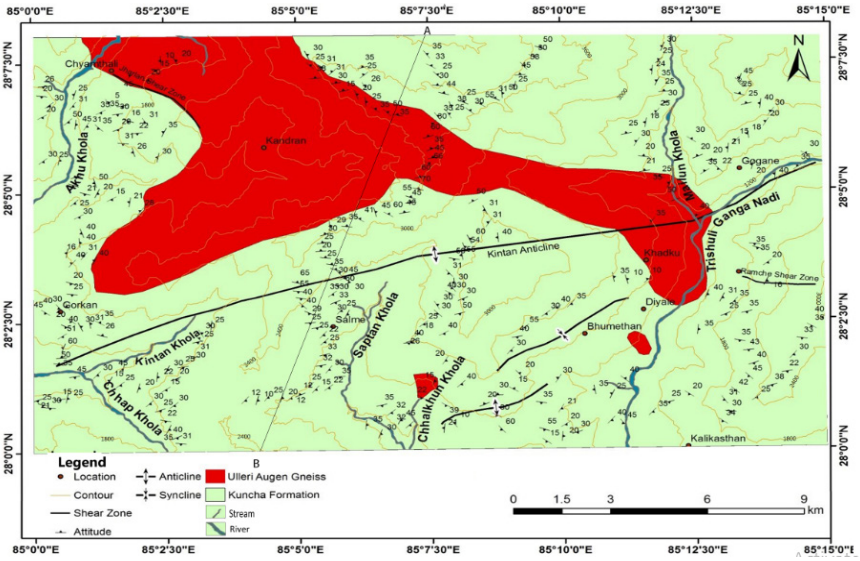

Fig. 3: Geological map of the study area and the landslide area is shown by the yellow enclosed boundary (KC et al., 2019)

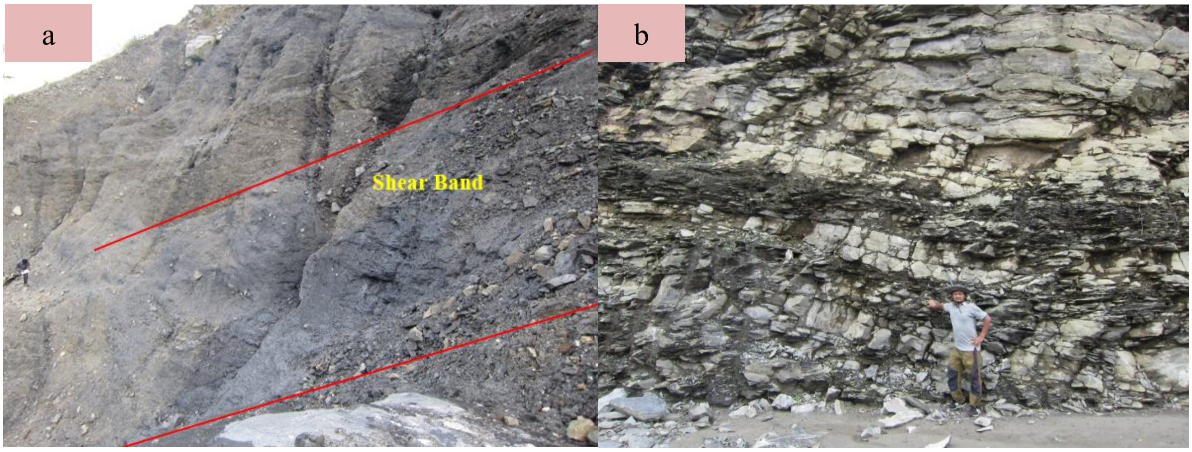

Fig. 4: Outcrop view of (a) Shear band interlayered with highly weathered rocks at the middle of the landslide and (b) metasandstone alternately bedded with schist and phyllite near the study area

Methods

Present study of the Jharlang Landslide focuses on geological implications, dimension and current status of the landslide, slope failure condition, propagating trend and the consequences that local people are facing. Two phases of the study were conducted: a desk study and a field inquiry.

Desk Study

During desk study, the landslide, erosional features, tectonic structures, land use pattern and lithological units were reviewed through aerial photographs, topo maps (issued by Survey Department) and google maps etc. Along with aerial photos, a 1: 25,000 scale topographical map served as the foundation map for gathering field data. Reports and maps pertaining to geology were also examined.

Field Investigation

Several traverses and walkover surveys were carried out in several landslide sections as part of the field study to assess the slope instability and its geological relationship. During the field investigation, along with the geological study, morphology of the landslide was examined. Additionally, hydrogeological phenomena, landslide dimension, newly formed cracks and subsidence, condition of rock and soil etc. were also determined. Similarly, the nature of the slide was classified based on the nature of flow, types and properties of materials present in the study area. To understand more about the landslide's nature, anthropogenic causes and its consequences interviews were conducted with the local people. The field investigation was concentrated mainly in three sections of the landslide i.e. crown, body and the toe. To evaluate the rock slope stability condition, kinematic analysis was performed by the discontinuity data from the rock outcrop positioned at the body of the landslide.

Moreover, field studies facilitate the actual scenarios of the area. It helps to identify the different attributes of landslide origination, its current status and activeness, propagating trend etc. Similarly, various consequences and damages that is incurred by the landslide were noted and tried to identify the mitigation measures and adaptation system for the local inhabitants. Field study was one of the crucial periods to collect different data and information of slopes, discontinuities, orientation of beds, slope gradient, types of failures, and structural relationship with the slope failures. It also supports to verify the collected data, reviewed materials with the actual condition of the landslide.

Fig. 5: Wide view of multiple scarps of the Jharlang Landslide

JHARLANG LANDSLIDE

Jharlang Landslide is one of the large and active landslides which is situated in the upper region of the Dhading District in Nepal. The landslide affected area is about 4 sq. km. It is regularly propagating in NE-SW direction. It is one of the renowned landslides in south Asia and has long history of its origination. The mostly affected villages are Chhyamthali, Kalmarn and Jharlang Gaon. Human settlements of these areas are at high risk of the landslide. More than 100 houses in the periphery of this landslide are at high risk. It is being propagating sharply towards the Chhyamthali Village. Most of the slope failures occurred due to intense precipitation and ground water flow during monsoon season, weak rock–mass and lack of bed rock support (Fig. 5). The average annual precipitation around the study area in 2023 published by Department of Hydrology and Meteorology is ranges from 1500-2000 mm (Fig. 6). Main features of the landslide are presented in Table 1.

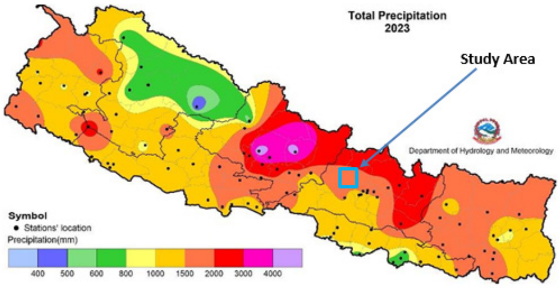

Fig. 6: Total annual precipitation (published by the Department of Hydrology and Meteorology in 2023)

Table 1: Main features of Jharlang Landslide

length	2.0 Km (approximate)
Width	1.5 Km (approximate)
Area	4.0 Sq. Km (approximate)
Slope angle	30°-50°
Type of failures	Rotational slide, debris slide and debris flow
Depth of failure	0.2-2.5 m
Mechanism of failure	Shear failure
Activity	Active
Rock Type	Ullleri Augen Gneiss, meta-sandstone and phyllite
Soil Type	Colluvial soil
land cover/use	Bare rocks, cobbles, pebbles, sand, cultivated land and sparse vegetation

Triggering causes	High precipitation and high degree of loose unconsolidated sediments.
Impact	Damage of settlements, declination of cultivated lands, destruction of foot trails and vegetation
Direction of propagation	North east and north west
Geometry of slope	Concave and nail scratching type

Consequences of Jharlang Landslide

On the basis of field study, the overall consequences of the landslide were drawn which are continuous weakening of the landmass, washing out the fertile and residential areas, damage of houses, water sources, vegetation, roads and foot trails. Unconsolidated materials and over saturation enhance the slope failures.

Symptoms of the landslide propagation

Landslide propagation towards residential areas is one of the main concern depicted by this study. Several prominent tension cracks, sliding and subsidence at crown and middle of the landslide were reported during field observation (Fig. 7). Additionally, tilting of trees, sliding and detachment of soil mass due to percolation of rainwater indicate active movement of the landslide.

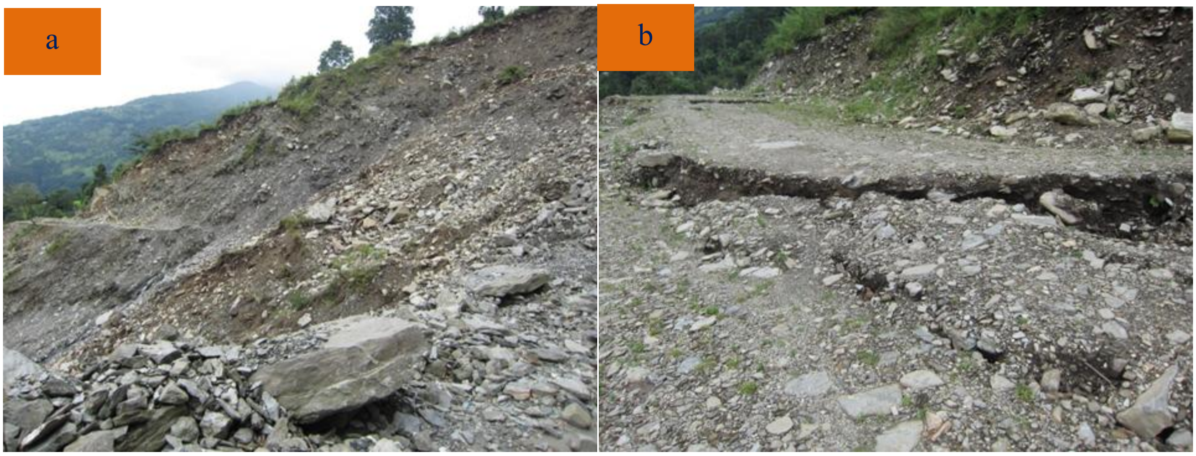

Fig. 7: (a) Slope failures blocking the foot-trail and (b) land subsidence (approximately 20 cm) near the landslide area

GEOLOGICAL INVESTIGATION AND SLOPE STABILITY RISK EVALUATION

Geologically, the Jharlang Landslide is located in the soft soil over the Ulleri Augen Gneiss, meta-sandstone and Phyllite (K C et al., 2018). Ulleri Augen Gneiss and phyllite are highly weathered whereas meta-sandstone is comparatively intact in the area. The landslide characterizes with rupture curved concavely upward indicates rotational slide (Fig. 8a) as defined by Varnes classification (1978). Field observation clearly shows that the landslide has unsorted and unconsolidated soil materials with limited bedrock support at the lower section of the landslide triggering for the debris flow during oversaturation. Debris deposit consist of unsorted materials of clay, silt, pebbles, cobbles and boulders of which cobbles and boulders are made up of the Augen Gneiss and meta-sandstone with rock fragments. Sliding soil mass with multiple newly generated tension cracks is profoundly distributed. Some boulders are up to 5-10 m in diameter.

During intensive monsoon rainfall in combination with surface runoff and water drain through cracks of slopes oversaturate the soil mass leads to slope failures. It has several slope failures occurred along with sliding blocks of soil mass and accumulation of boulders came at the toe from the upper portion of the landslide. Bedrock exposure is limited in the area. Highly deformed and weathered bed rock of phyllite, metasandstone and Ulleri Augen Gneiss are exposing at the body (center) of the landslide (Fig. 8b). Initially, the slope failures triggered in the uppermost part then seepage, tectonic movements, unplanned cultivation and deforestation give rise to debris flow and slide of the whole soil mass around the area.

Fig. 8: (a) Typical morphology of the landslide illustrating origination of new landslide, reactivation of old landslide and new cracks around the area and (b) Rock exposure at middle section of the landslide.

RESULTS AND DISCUSSION

Jharlang Landslide is a large and well distributed in the region. The trend of its propagation, regularly developed tension cracks and slope failures register great threats to the villages like Chhyamthali Village, Jharlang Gaon and Kalmarn Village. Based on the study and site investigation, it is clear that the landslide is supposed to be one of the great threats to the local inhabitants. Basically, the study was made based on various facts and information collected by various means such as documents, geological maps, news articles, satellite images and field investigation. Field study was major part of this study where geological assessment was conducted to find out the causes and consequences of the active landslide.

Causes of landslide

The geology of the area has remarkable cause of the landslide. Geological assessment deals with the study of the lithology, structural features, rock and soil mass condition, orientation of beds, weathering pattern etc. According to According to Dahal (2012) analysis, fine-grained soil mass, low internal friction angle, abundance of clay minerals, and bedrock hydrogeology are the prominent geological causes of the landslide. Geologically, the landslide area lies in the Kunchha Formation where phyllite, meta-sandstone and Ulleri Augen Gneiss are the major rock types (Fig. 9). Highly deformed and weathered Ulleri Augen Gneiss and phyllite prevails greater susceptibility for the slope failures (Fig. 10). Additionally, the unconsolidated soil materials with limited rock exposure around the area also aid to the slope failures.

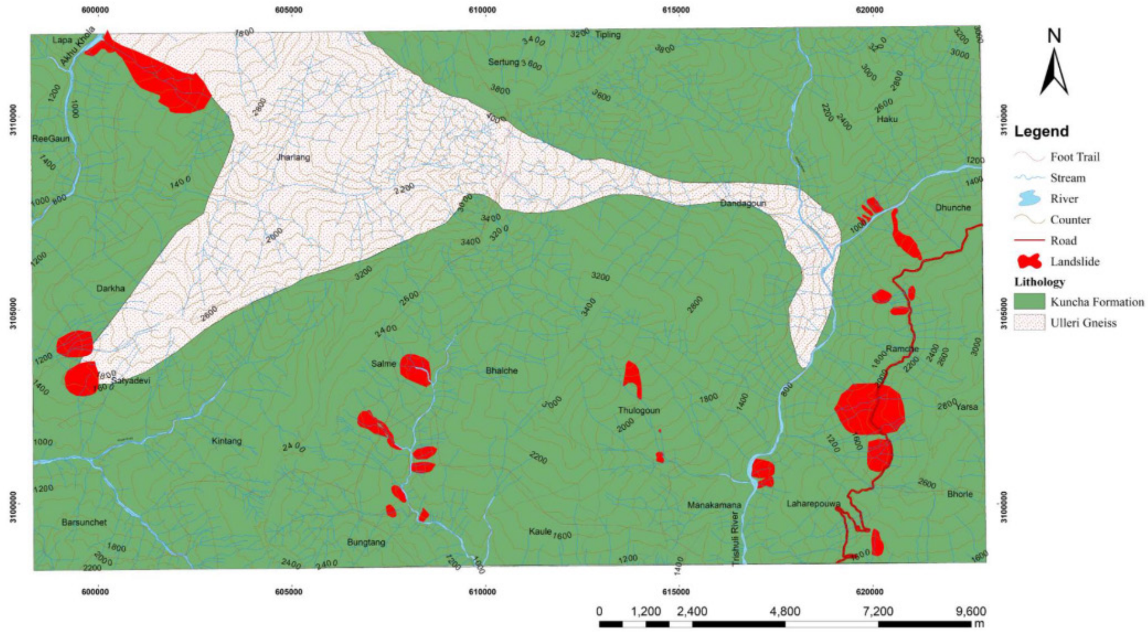

Fig. 9: Landslide inventory map of Ramche-Jharlang area indicating the Jharlang landslide by yellow boundary (KC et al., 2018)

Fig. 10: Outcrop view of weathered Ulleri Augen Gneiss and phyllite near the landslide area

Kinematic analysis was executed for identifying the mode of slope failures and slope stability analysis. Representative orientation of bedding and discontinuities were measured from the proximity of the landslide and were plotted in stereographic projection (Fig. 11). In the stereographic projection, three joint sets are formed including foliation plane i.e. F/J1, J2 and J3. There are two critical wedges are formed by the intersection of J1 and J2 and J1 and J3 which are in day light condition. From the kinematic analysis, it can be analyzed that the landslide area is prone to wedge failures.

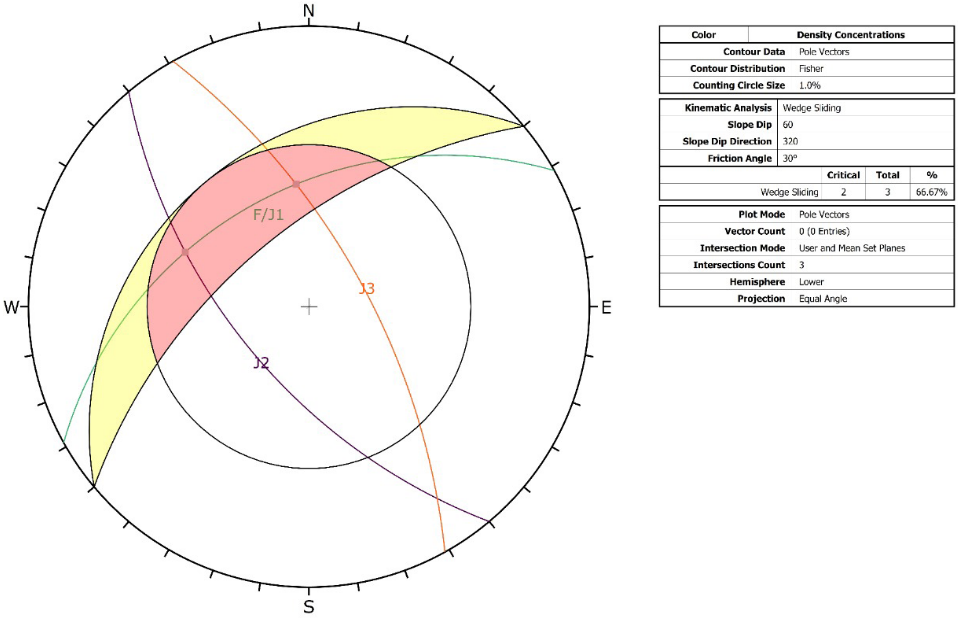

Color	Density Concentrations
Contour Data	Pole Vectors
Contour Distribution	Fisher
Counting Circle Size	1.0%

Kinematic Analysis	Wedge Sliding
Slope Dip	60
Slope Dip Direction	320
Friction Angle	30°

	Critical	Total	%
Wedge Sliding	2	3	66.67%

Plot Mode	Pole Vectors
Vector Count	0 (0 Entries)
Intersection Mode	User and Mean Set Planes
Intersections Count	3
Hemisphere	Lower
Projection	Equal Angle

Fig. 11: Representative stereographic projection of discontinuities in rock-mass exposed at the main body of the landslide

In the landslide area, slope failures are concentrated at NE and SW directions. Core information of the landslide based on field observation are tabulated in Table 2.

Table 2: Core information of the landslide based on the field observation

Observation	**North-East**	**South-West**
Number of slopes failures	10	15
Distance to proximity of villages	100 m	200 m
Type of slope failures	Debris Slide and Debris flows	Rotational slide with debris flow
Length of tension cracks	1-10 m	1-15 m
Depth of tension cracks	3-15 cm	5-30 cm
Displacement of cracks	1-2 m	1-3 m
Water content	damp to wet	damp to wet
Landslide susceptibility rating	moderate to high	moderate to high

Overall study shows that Jharlang Landslide is a combination of rotational slide, debris slide and debris flow and shows perceptible movement during rainy season. Debris flows are considered to occur more commonly in coarse-grained soil and on steeper slopes while the debris slides are more likely to occur in medium textured soil with a mixture of sand and mud in steep to gentle slopes. Slope failures have been exacerbated by human action, such as haphazard settlement, haphazard farming practices, deforestation etc. Comparative study of the landslide can be observed from 2011 to 2015 (Fig. 12). It shows gradual rise of the slope failures with the development of new tension cracks in northern portion and gaining natural stability in southern portion.

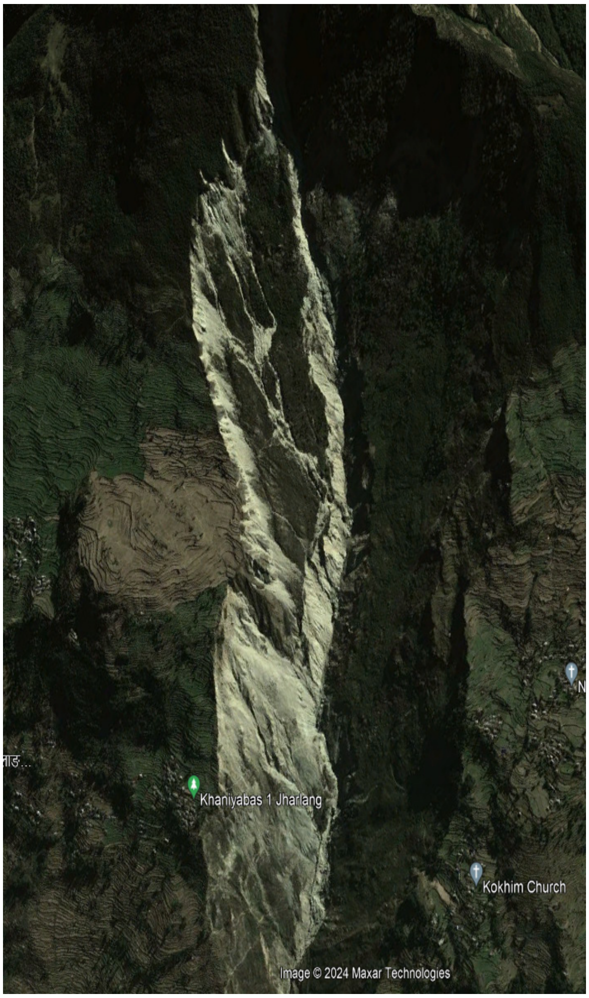

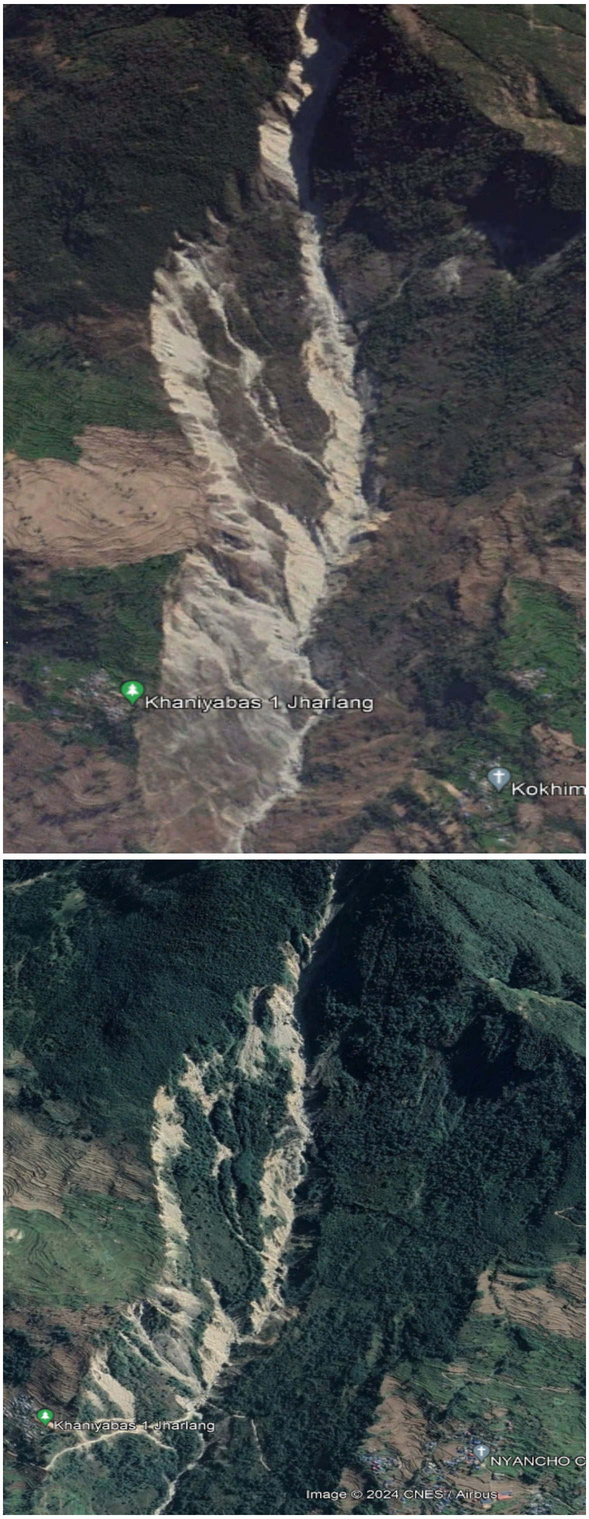

Fig. 12: Illustration of changing of the landslide from 2011 to 2024 (Source: Google Earth)

GENERAL RECOMMENDATION OF THE LANDSLIDE MITIGATION

A thorough understanding of the unique physical traits and mechanisms causing landslides in each location is essential to assessing the risk of landslides (Paudyal et al., 2024). Considering the slope failures and ruptures, generation of tension cracks and propagating trend, damages etc. landslide prevention and controlling works should be implemented. In other words, with the vulnerabilities and risk of the landslide there need to be mitigation measures should be formulated to save lives and properties. Based on the detailed geological studies and relevant findings of Jharlang Landslide, various reliable mitigation measures can be adopted.

In order to reduce future risk of the landslides, both structural and non-structural measures are recommended. Shallow and deep drainage wells would be the most effective measures to control surface and sub-surface flow of water. Surface runoff is captured by shallow drainage, which guides it away from potentially unstable locations. Bio-engineering could be done at upper and middle parts of the landslide. It will help to stabilize the agricultural lands. Similarly, to protect the cultivated lands, terrace farming is suggested. Other geotechnical in-situ testing, drilling and laboratory investigation of rocks and soil is important for in depth remedy for slope instability. In addition to structural mitigation measures, it is equally important to educate people regarding landslide, conducting public awareness and disseminating experiences to the communities. These are some of the non-structural counter measures to fight against the challenges of the hazard.

CONCLUSION

Landslide is one of the common natural disasters that Nepal is facing each year with loss of lives, properties and natural beauty. Jharlang is one of the active, large scale and catastrophic landslide in the Lesser Himalaya. Geological field assessment, knowledge based approach, kinematic analysis, visual observation, satellite image and topographic maps analysis are the primary methods of evaluation. It has been studied that the landslide occurred due to weak geological condition, high topographical relief, unconsolidated sediments, active hydrogeology, unscientific cultivation and anthropogenic causes. Kinematic analysis at the middle section of the landslide exhibit critical wedge failures that also contribute for the landslide. The area possesses thin to medium foliated, highly deformed, moderate to highly weathered phyllite, metasandstone and Augen Gneiss. Additionally, the evidences of shear bands encountered at the bottom of the landslide prevails the area has been affected by the historical seismic activities. Overall study shows the landslide is combination of rotational slide, debris flow and debris slide.

The activeness of the landslide can be observed by the newly formed tension cracks and land subsidence around the study area. The landslide propagation towards the adjacent villages registered great threats among the locals. To stabilize and control the mass movement, various prevention and general mitigation measures are suggested. Drainage ditches, drainage wells and support structures seems necessary. Likewise bioengineering technique can be adopted to stabilize the landslide and cultivated lands lying nearby. Geotechnical in-situ testing, drilling, laboratory investigation and continuous monitoring are essential attributes for long term slope stability. Similarly, public awareness and more detail study are some of the non-structural countermeasures to mitigate the hazard in future.

Present study is focused on the causes, consequences and general mitigation measures of the landslide. We wish this study will be helpful to understand the root cause of the landslide and to formulate effective management plan to mitigate the landslide at present and in future.

ACKNOWLEDGEMENT

We are grateful to Prof. Dr. Ram Bahadur Sah, Dr. Prem Bahadur Thapa, Dr. Krishna Devkota for their valuable suggestions throughout the study period. We are immensely thankful to Krishna Raj Khanal, Amit Neupane, Harish Dangi and Gunanidhi Pokhrel for their valuable help and suggestions in geological interpretation and GIS analysis. Sincere thanks are extended to Ashis K.C., Kamal Kafle, Balram Bhandari, Lokmani Oli, Sanjeew Bhujel Sudarshon Sapkota and Bhupendra K.C. for their support and advice throughout the research period.

AUTHORS CONTRIBUTION

All the authors have made remarkable contribution to preparing this research article. JKC has prepared the study concepts and design of the research. JKC, DG, PN, SD have the role for field observation, data acquisition and data analysis. Dr. Kabi Raj Paudyal contributed in the verification of data and review of the article. The first draft of the manuscript was written by Mr. Jharendra K.C. and all the authors supported to making the draft form of the manuscript into the final version.

CONFLICT OF INTEREST

The authors declare no competing interests.

DATA AVAILABILITY STATEMENT

The data that support the findings of this study are available from the corresponding author upon a reasonable request.

REFERENCES

Acharya, M., Dhakal, R. P. and Paudyal, K. R., 2023. Application of frequency ratio method for landslide susceptibility mapping at the Thulo Lumpek area, Gulmi, Nepal; Journal of Development Innovations, © 2022 Karma Quest International, Canada. Link: www.karmaquest.org/journal (ISSN: 2371-9540), 7 (2), 56-76.

Budha, P. B., Paudyal, K. and Ghimire, M., 2016. Landslide susceptibility mapping in the eastern hills of Rara Lake, western Nepal. Journal of Nepal Geological Society, 50 (1) 125-131.

Budha, P. B., Paudyal, K. and Ghimire, M., 2020. Indicator-based vulnerability assessment of Chhayanath-Rara Municipality, Western Nepal. Environment and Natural Resources Journal;18(3):224-233. DOI: 10.32526/ennrj.18.3.2020.21.

Crozier, M.J. and Glade, T., 2005. Landslide Hazard and Risk: Issues, Concepts and Approach. In: Landslide hazard and risk, Glade. T., Anderson. M., and Crozier, M., Chichester, Wiley, 1-40.

Dahal, R. K., Hasegawa, S., Masuda, T. and Yamanaka, M., 2006. Roadside slope failures in the Nepal during torrential rainfall and their mitigation. Journal disaster mitigation of debris flow, slope failure and landslides (Interpreted 2007), Universal, 2, 503–514.

Deoja, B.B., Dhital, M.R., Thapa, B. and Wagner, A., 1991. Mountain Risk Engineering Handbook. Kathmandu: ICIMOD.

Dwivedi, S.K., Dwivedi, S. and Joshi, G.R., 2007. Slope stability of the Pawati Landslide, Dolakha district, Central Nepal. Conference:UNSAT-ASIA, Beijing, China.

Ghimire, T., Poudel, L. and Pant, B., 2007. The devastating Ramche Landslide (Rasuwa) and the future of Polchet residents. Journal of Nepal Geological society (Spec. Issue), 36, 27.

Humagain, I.R., 2000. Engineering Geological Studies in Central Nepal with emphasis on

Stress Regime and Stability of Slopes and Tunnels. Mittilungen zur Ingenieurgeologie und Hydrogeologie (University of Engineering Geology and Hydrogeology), Aachen, Germany.

K.C, J., Gautam, D., Neupane, P. and Paudyal, K. R., 2018. Landslide inventory mapping and assessment along the Ramche-Jharlang area in Dhading, Rasuwa and Nuwakot districts, Lesser Himalaya Central Nepal. Journal of Nepal Geological Society, 55(1), 103–108. https://doi.org/10.3126/jngs.v55i1.22798

K.C, J. and Paudyal, K. R., 2019. Characteristics and field relation of Ulleri Augen Gneiss to country rocks in the Lesser Himalaya: A case study from Syaprubesi-Chhyamthali area, central Nepal. Journal of Nepal Geological Society, 58, 89–96. https://doi.org/10.3126/jngs.v58i0.24577

Nepal, N., Chen, J., Chen, H., Wang, X. a. and Pangali Sharma, T. P., 2019. Assessment of landslide susceptibility along the Araniko Highway in Poiqu/Bhote Koshi/Sun Koshi Watershed, Nepal Himalaya. Progress in Disaster Science, 3. doi: 10.1016/j.pdisas.2019.100037

Neupane, A., Paudyal, K. R., Devkota, K. C. and Dhungana, P., 2023. Landslide susceptibility analysis using frequency ratio and weight of evidence approaches along the Lakhandehi Khola watershed in the Sarlahi District, southern Nepal. Geographical Journal of Nepal, 16(01), 73–96. doi: https://doi.org/10.3126/gjn.v 16i01.53486.

Pant, B. R., 2010. Lithostratigraphy and Structural Analysis of the Lesser and Higher Himalaya, between Betrawati and Rasuwagadi, Central Nepal, unpublished M. Sc. Thesis, Geology. Tribhuvan University, p. 54.

Paudyal, K. R., Devkota, K. C., Parajuli, B. P., Shakya, P. and Baskota, P., 2021. Landslide Susceptibility Assessment using open-source data in the far western Nepal Himalaya: A case study from selected local level units. Journal of Institute of Science and Technology, 26(2), 31-42 (2021). ISSN: 2467-9062 (print), e-ISSN: 2467-9240 https://doi.org/10.3126/jist.v26i2.41327.

Paudyal K. R. and Maharjan R., 2022. Landslide susceptibility mapping of the Main Boundary Thrust (MBT) region in Tinau-Mathagadhi Section of Palpa District, Lumbini Province, Journal of Nepal Geological Society, vol. 63, pp. 99–108. https://doi.org/10.3126/jngs.v63i01.50845.

Paudyal, K. R. and Maharjan, R., 2023. Landslide susceptibility mapping of the Main Boundary Thrust region in Mandre-Khursanibari section of Arghakhanchi and Palpa districts, Lumbini province of Nepal. Nepalese Journal of Environmental Science, 11 (2), 35-53; https://doi.org/10.3126/njes.v11i2.58152.

Paudyal, K. R., Maharjan, R. and Shrestha, B., 2024. Landslide susceptibility mapping of the main boundary thrust region in Thungsingdanda-Bandipur section of Nawalparasi and Palpa Districts, Gandaki and Lumbini Provinces, Nepal. The Geographical Journal of Nepal, 17, 23-52, doi: https://doi.org/10.3126/gjn.v17i01.63934.

Paudyal, K. R., Maharjan, R., Shrestha, B. and Maharjan, N., 2024. A Comparative of Frequency Ratio Method, Weight of Evidence, and Analytical Hierarchy Process for Landslide Susceptibility Assessment in the Main Boundary Thrust (MBT) Region in Ranitar-Belarang Section of Udayapur District, Koshi Province, Nepal. Earth Sciences Research Journal, 28(3), 325-348 https://doi.org/10.15446/esrj.v28n3.112740.

Shahi, Y. B., Kadel, S., Dangi, H., Adhikari, G., KC, D. and Paudyal, K. R., 2022. Geological Exploration, Landslide Characterization and Susceptibility Mapping at the Boundary between Two Crystalline Bodies in Jajarkot, Nepal. Geotechnics, v. 2(4), pp. 1059-1083.

Shrestha, O.M., 1994. Landslide Inventory and Slope Stability Mapping in Seven Districts of Central and Western Nepal. Department of Mines and Geology, HMG.

Stöcklin, J. and Bhattarai, K.D., 1977. Geology of the Kathmandu area and central Mahabharat range, Nepal Himalaya. Report of Department of Mines and Geology/ United Nations Development Program (unpublished), p. 86.

Timalsina, K. and Paudyal, K. R., 2018. Fault-controlled geomorphic features in the Ridi-Shantipur area of Gulmi District and their implications for active tectonics. Journal of Nepal Geological Society, 55(1), 157-165.

Uperti, B.N. and Dhital, M.R., 1996. Landslides Studies and Management in Nepal. International Centre for Integrated Mountain Development (ICIMOD), Kathmandu, Nepal.

Varnes, D.J., 1978. Slope movement types and processes. In: Schuster, R.L, Krizek, R.J. (eds.) Landslides, analysis and control, special report 176: Transportation research board, National Academy of Sciences, Washington, D.C., 11-33.

Weidinger, J.T. and Schramm, J.M., 1995. A Short Note on the Tsergo Ri Landslide Langtang Himal, Nepal. Journal of Nepal Geological Society, 11, 43-53.

Journal of Nepal Hydrogeological Association (JNHA), Vol (2), 45-65 (2025)
ISSN: 3059-9725 (Online)
https://doi.org/10.3126/jnha.v2i1.85379

RESEARCH ARTICLE

Deformation and support analysis of headrace tunnels in three tectonic zones of Nepal: An empirical and numerical approach

Ijan Shrestha, Balkrishna Jha, Aashika Koju, Aanand Kumar Mishra, *Nirmal Kafle
Department of Civil Engineering, Khwopa College of Engineering,
Tribhuvan University, Nepal
**Corresponding author: nirmalkafle1917@gmail.com*

***(Submission Date**: 26 May, 2025; **Accepted Date:** 9 July, 2025)*

ABSTRACT

Tunneling in the Himalayan region presents significant engineering challenges due to complex geological formations, high seismicity, and variable rock mass conditions. This study focuses on the comparative analysis of headrace tunnels (HRTs) in three distinct geological regions of Nepal: the Siwaliks, the Lesser Himalayas, and the Higher Himalayas. The primary objective of this study is to evaluate stresses due to tunnel excavation, required support systems, and displacement in these distinct geological settings. The methodology used in this study includes empirical, and numerical approaches to assess tunnel performance in the selected regions. Finite Element Analysis (FEA) was performed to assess tunnel stability, in-situ stresses, and effectiveness of support systems. The findings show significant variations in stress generated, displacement, and required support systems across the three geological regions. The comparative analysis indicates that tunnels in weaker rock formations, like those in the Siwaliks, require substantial support systems, whereas tunnels in the Higher Himalayas experience higher in-situ stresses. This study highlights the behavior of rock masses, the consequent stresses and displacements and the required support systems in the three geological settings when constructing tunnels of the same shape and size.

Keywords: ***Displacement, FEA, Himalayas, Rock mass classification, Support systems***

INTRODUCTION

Background and Significance

The Himalayan range was formed as a consequence of the ongoing convergence and collision between the Indian and Eurasian plates, a process that began around 40 to 50 million years ago and continues today, thereby making the region seismically active (Yin and Harrison, 2000). The dynamic plate movement, combined with complex topography, contributes to frequent geological hazards such as earthquakes, landslides, and slope failures. The Nepal Himalayas is divided into several tectonic zones separated by major thrust faults, significantly influencing underground construction challenges (Paudyal and Panthi, 2010).

Complex topography and geological diversity of Nepal pose substantial challenges to underground excavation works (Panthi, 2004). Major problems encountered during tunneling in fault zones are excessive spalling, displacements, creep, and excessive water inflows. Fragile geological conditions and tectonic stresses have contributed to the rock mass of Nepal Himalayas to be highly deformed, weathered, folded and faulted (Upreti, 1999). Proper support system must be installed during underground construction. Under estimation of support system leads to failure of the structure while over estimation leads to unnecessary increasing cost of the project.

A comparative analysis is carried out in this study for headrace tunnels (HRTs) located in three distinct geological regions of Nepal: The Siwaliks, the Lesser Himalayas and the Higher Himalayas. HRTs from the three proposed hydropower projects were analyzed and designed for the study. For each tunnel, the optimum diameter was deter- mined based on tunnel hydraulics and estimated construction costs. The average of the three optimized diameters, which was 4.4 meters, was then taken as the representative value for further evaluation. Each tunnel, with an inverted D-shaped profile, serves as a case for examining how geological variations influence tunnel behavior.

Research Gap

Although tunnel construction in the Himalayas is increasing, few studies have conducted a systematic comparison of tunnel deformation and support systems across different geological zones using both empirical and numerical methods (Abbas et al., 2024; Azad et al., 2023; Thapaliya et al., 2025). Most existing works are project-specific and lack an integrated framework that accounts for variations in rock mass behavior, stress redistribution, and support optimization.

This study addresses this gap by applying consistent empirical and finite element modeling approaches to analyze tunnel behavior in the Siwaliks, Lesser Himalayas, and Higher Himalayas. It aims to provide comparative insights that support effective and geology-specific tunnel design strategies.

Research Questions

The central research questions are:

1. How do rock mass properties and overburden depth affect tunnel-induced stresses and displacements across different Himalayan tectonic zones?
2. What are the support system variations required for tunnels in the Siwaliks, Lesser Himalayas, and Higher Himalayas?
3. How effective is the integration of empirical classification systems with numerical models for predicting tunnel deformation and optimizing support design?

By addressing these questions, the study enhances the understanding of tectonic zone-specific tunnel behavior and offers practical guidance for safe and cost-effective tunnel engineering in the Himalayan region.

STUDY AREA

The study focuses on three headrace tunnels (HRTs): Super Lower Bagmati Hydropower Project (SLBHP) in the Siwaliks, Ranma Khola Hydropower Project (RKHP) in the Lesser Himalayas, and Humla Karnali Hydropower Project (HKHP) in the Higher Himalayas as shown in Fig 1.

The SLBHP lies in the Siwaliks region, which is a young sedimentary zone comprising mudstone and sand- stone. RKHP is situated in the Lesser Himalayas, where the rock mass mainly consists of moderately weathered quartzite and phyllite. HKHP is located in the Higher Himalayas characterized by high-grade metamorphic rocks like augen gneiss.

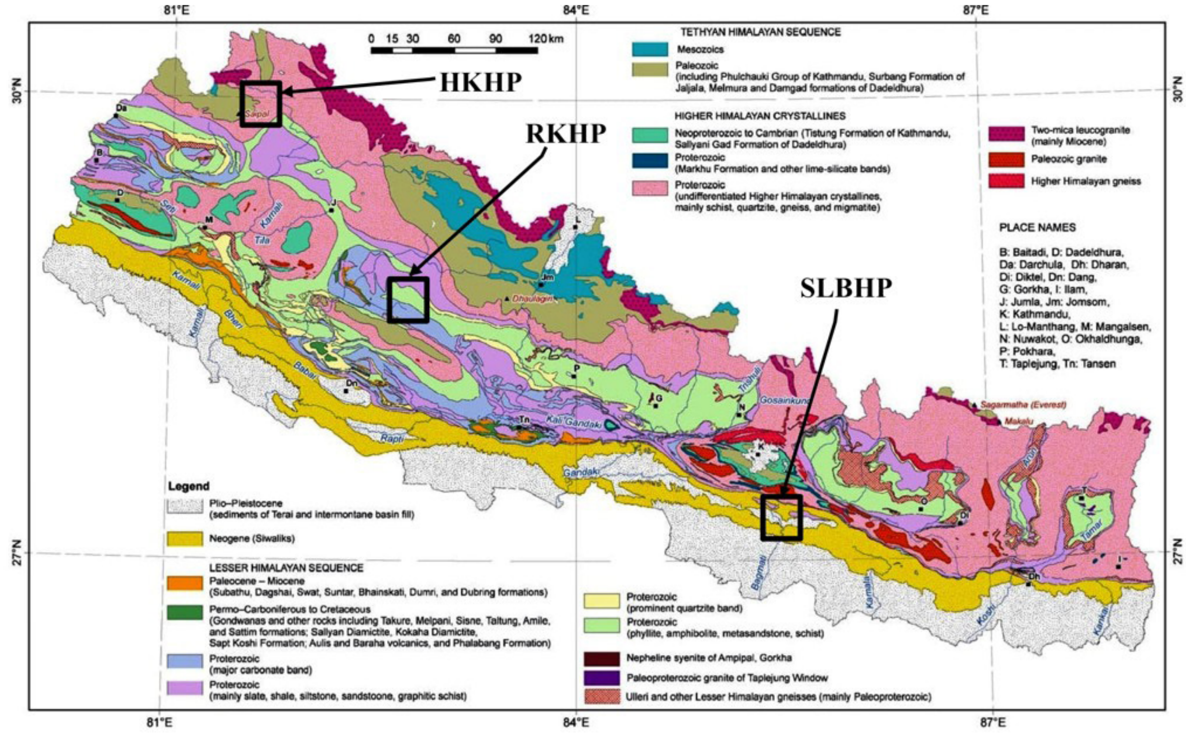

Fig. 1: Geological map of Nepal showing the study sreas *(Dhital, 2015)*

MATERIALS AND METHODS

Empirical methods and FEA were used to conduct the comparative analysis of HRTs in three distinct geological regions of Nepal.

SITE SELECTION AND DATA COLLECTION

The site selection for this study was based on three representative hydropower tunnel projects situated across Nepal's primary geological zones: the Siwaliks, the Lesser Himalayas, and the Higher Himalayas. The selected projects are either proposed or under construction and offer a diverse range of geological conditions suitable for comparative analysis.

Data collection was conducted exclusively using secondary sources, including design documents and geological investigation reports from consulting firms. These documents provided details on lithology, rock mass classification parameters (RMR, Q-values), overburden depth, deformation modulus, and proposed support systems. Geological Strength Index (GSI) values, intact rock properties (σ_{ci}, m_i), and stress ratio parameters were derived using empirical correlations from established literature. These secondary data were cross-referenced and validated using geological maps provided by the (Dhital, 2015) Though no direct field investigation or instrumentation data was collected, the reliability of the secondary data was ensured by selecting well-documented projects and comparing results across multiple literature sources.

ROCK MASS CLASSIFICATION

The rock mass at the tunnel sites was classified using the Rock Mass Rating (RMR) system, as proposed by Bieniawski (1989), which remains one of the most widely adopted empirical classification systems in underground excavation design. Although the Q-system was not directly applied for classification in this study, it was utilized indirectly through empirical correlations with RMR to derive essential input parameters for numerical modeling. Among the various empirical relationships proposed to interrelate RMR and Q, the correlation developed by Rutledge and Preston, as cited by Marinos et al. (2007) was identified as having the highest relevance and applicability for Himalayan rock masses. This relationship is given by:

$$RMR = 5.9 lnQ + 43 \text{ .... (1)}$$

This equation was used to estimate Q-values from RMR values, facilitating the derivation of additional rock mass properties required for deformation modulus estimation and input to the generalized Hoek–Brown failure criterion.

ESTIMATION OF IN-SITU DEFORMATION MODULUS

The in-situ deformation modulus (E_m) of rock mass is an essential parameter for numerical modeling and stability analysis. It was estimated empirically using correlations between RMR and Q values as follows:

$$E_m = 2 \times RMR - 100 \text{ ....(2)}$$

For moderately poor rock quality (RMR between 30 and 55), the expression developed by (Serafim and Pereira, 1983) was applied:

$$E_m = 10^{\frac{RMR-10}{40}} \text{ .... (3)}$$

For rock masses where Q values were greater than 1, the empirical formula from (Grimstad and Barton, 1993) was used:

$$E_m = 25 log_{10} Q \text{ .... (4)}$$

Table 1: Average in-situ deformation modulus obtained along the HRTs

	Chainage	Rock Type	RMR	Q	Overburden (m)	E_m (GPa)
Siwaliks	0+000 - 1+600	Sandstone	45	1.12	416.160	4.353
	1+600 - 3+700	Sandstone	40	0.64	496.957	2.812
	3+700 - 5+600	Mudstone	31	0.21	479.730	1.581
	5+600 - 6+888	Sandstone	32	0.26	165.499	1.774

Chainage	Rock Type	RMR	Q	Overburden (m)	E_m (GPa)

Lesser Himalaya	0+000 - 0+550	Quartzite	62	2.23	521	16.34
	0+550 - 1+500	Quartzite	66	2.91	749	21.79
	1+500 - 3+250	Sandstone	63	2.38	770	17.70
	3+250 - 4+000	Sandstone	64	2.54	702	19.07
	4+000 - 4+900	Sandstone	56	1.49	495	8.17
	4+900 - 6+000	Sandstone	61	2.08	736	14.98
	6+000 - 7+690	Sandstone	54	1.31	593	7.74

	Chainage	Rock Type	RMR	Q	Overburden (m)	E_m (GPa)
Higher Himalaya	0+000 - 1+150	Augen Gneiss	74	4.63	515	31.32
	1+150 - 3+300	Augen Gneiss	63	2.38	306	17.70
	3+300 - 4+300	Augen Gneiss	68	3.32	305	24.51
	4+300 - 6+880	Augen Gneiss	65	2.91	435	21.79

Determination of Parameters for Generalized Hoek–Brown Failure Criterion

In order to simulate the behavior of the rockmass, the generalized Hoek–Brown failure criterion was adopted to define the strength envelope in numerical modeling. The generalized Hoek–Brown criterion is expressed as follows (Hoek and Brown, 2018):

$$\sigma_1 = \sigma_3 + \sigma_{ci}\left(m_b \frac{\sigma_3}{\sigma_{ci}} + s\right)^a \text{ .... } (5)$$

where:

- σ_1 = major principal stress at failure
- σ_3 = minor principal stress

The following empirical relationships were used to derive the Hoek–Brown parameters:

$$m_b = m_i e^{\frac{GSI-100}{28}} \text{ .... } (7)$$

$$s = e^{\frac{GSI-100}{9}} \text{ .... } (8)$$

$$a = \frac{1}{2} + \frac{1}{6}\left(e^{-\frac{GSI}{15}} - e^{-\frac{20}{3}}\right) \text{ .... } (9)$$

Where m_i is the intact rock constant, determined from laboratory uniaxial compression tests or adopted from standard literature values for the encountered rock types.

The horizontal-to-vertical stress ratio (k) was computed based on the empirical equation proposed by (Sheorey, 1994):

- σ_{ci} = uniaxial compressive strength of intact rock
- m_b = reduced material constant for the rockmass
- s and a = constants that account for rock mass quality.

The parameters m_b, s and a were calculated based on the Geological Strength Index (GSI) and the intact rock constant m_i. Relation between Geological Strength Index (GSI) and RMR as per (Hoek and Diederichs, 2006) was used to calculate GSI which is given as:

$$GSI = RMR - 5 \quad \ldots\ldots\ldots\ldots\ldots\ldots (6)$$

$$k = 0.25 + 7 \times E_m(0.001 + \frac{1}{z}) \ldots\ldots\ldots\ldots (10)$$

- E_m = in-situ deformation modulus (GPa),
- z = overburden (m)

The Disturbance Factor (D) is a parameter that accounts for the extent of disturbance or relaxation in the rockmass due to excavation and blasting activities.

In addition to strength parameters, Poisson's ratio of the rockmass was calculated using the relation suggested by (Aydan, 2019), that can be stated as:

$$\upsilon_{rm} = 0.5 - 0.2 \times \frac{RMR}{RMR + 0.2 \times (100 - RMR)} \ldots\ldots\ldots\ldots (11)$$

Table 2: Parameters used for Generalized Hoek–Brown failure criterion along the HRTs

	Chainage	k	D	GSI	υ_{rm}	m_i	m_b	s	a	σ_{ci} (MPa)
Siwaliks	0+000 - 1+600	0.35	0.7	40	0.35	8	0.31	0.0002	0.51	114.4
	1+600 - 3+700	0.31	0.7	35	0.35	19	0.48	0.0001	0.52	114.4
	3+700 - 5+600	0.28	0.7	25	0.38	9	0.07	0.0007	0.53	63.0
	5+600 - 6+888	0.34	0.7	27	0.37	9	0.11	0.0005	0.53	114.4
	Chainage	k	D	GSI	υ_{rm}	m_i	m_b	s	a	σ_{ci} (MPa)
Lesser Himalaya	0+000 - 0+550	0.58	0.6	57	0.32	24	3.65	0.0043	0.5	214.9
	0+550 - 1+500	0.61	0.6	61	0.32	24	4.35	0.0071	0.5	214.9
	1+500 - 3+250	0.53	0.6	58	0.32	19	3.02	0.0049	0.5	150.0
	3+250 - 4+000	0.57	0.6	59	0.32	19	2.21	0.0018	0.51	150.0
	4+000 - 4+900	0.42	0.6	51	0.33	19	2.07	0.0018	0.51	150.0
	4+900 - 6+000	0.5	0.6	66	0.32	19	2.76	0.0038	0.50	150.0
	6+000 - 7+690	0.4	0.6	49	0.33	19	3.07	0.0035	0.51	150.0

	Chainage	k	D	GSI	υ_{rm}	m_i	m_b	s	a	σ_{ci} (MPa)
Higher Himalaya	0+000 - 1+150	0.59	0.5	68	0.32	25	6.10	0.0171	0.51	233.5
	1+150 - 3+300	0.90	0.5	58	0.33	25	4.82	0.0560	0.5	233.5
	3+300 - 4+300	0.78	0.5	63	0.32	25	5.30	0.0106	0.5	233.5
	4+300 - 6+880	0.69	0.5	61	0.32	25	4.86	0.0081	0.5	233.5

Finite Element Analysis

The HRTs were modeled numerically to simulate the stress distribution and deformation around tunnel excavations. The input parameters for the simulations such as rock mass properties, in-situ stress conditions, boundary conditions, and support configurations were derived from empirical classification systems (RMR and Q-system) and field investigations. The modeling process involved:

- Simulating tunnel behavior before and after support installation
- Analyzing principal stresses and displacement patterns
- Optimizing Support Systems as suggested by RMR

Tunnel excavation was simulated in 15 stages at random intervals to reflect real-world variability in geological and operational conditions. A graded mesh of 3-noded triangular elements (gradation factor 0.1) was used to increase density near tunnel boundaries which is critical for stress and deformation. This approach improved accuracy in capturing stress redistribution while optimizing computation. The mesh generated contained 150 nodes, which provided a compromise between model detail and processing time.

Tunnel Support Design and Optimization

Tunnel support design was initially done as suggested by RMR, providing baseline configurations for fiber-reinforced shotcrete (FRS), rock bolts, and steel sets. The properties of the FRS used in the modeling was based on the studies of (Shah and Rangan, 1971). The principles used for rock bolt design were guided by the work of (Li, 2017). The supports were then optimized to ensure effective load transfer and to maintain a factor of safety of 1.5.

DATA ANALYSIS

The data obtained from field investigations was used for numerical modeling and support system design. The in-situ deformation modulus of the rock mass was calculated for different chainages along the HRT alignment based on the RMR and Q values. The calculated average values of deformation modulus at various chainages are presented in Table 1. Likewise, the parameters used for the Hoek–Brown Failure Criterion is presented in Table 2 .

Table 3 Empirical support systems of each tectonic zone along the HRTs

	Chainage	Rock Type	RMR	Q	Support System According to RMR	Support System According to Q
Siwaliks	0+000 - 1+600	Sandstone	45	1.12	Systematic bolts 4 m long, spaced 1.5 m to 2 m in crown and wall with wire mesh in crown, 50 mm to 100 mm shotcrete in crown and 30 mm in walls.	Rockbolts of length 3.5 m long, spaced 2 m, 100 mm thick shotcrete
	1+600 - 3+700	Sandstone	40	0.64	Systematic bolts 4 m to 5m long, spaced 1 m to 1.5 m in crown and wall with wire mesh, 100 mm to 150 mm shotcrete in crown and 100 mm in walls, light to medium ribs spaces 1.5 m where required.	Rockbolts of length 3.5 m long, spaced 2 m, 110 mm thick shotcrete
	3+700 - 5+600	Mudstone	31	0.21	Systematic bolts 4 m to 5m long, spaced 1 m to 1.5 m in crown and wall with wire mesh, 100 mm to 150 mm shotcrete in crown and 100 mm in walls, light to medium ribs spaces 1.5 m where required.	Rockbolts of length 3.5 m long, spaced 2 m, 110 mm thick shotcrete
	5+600 - 6+888	Sandstone	32	0.26	Systematic bolts 4 m to 5m long, spaced 1 m to 1.5 m in crown and wall with wire mesh, 100 mm to 150 mm shotcrete in crown and 100 mm in walls, light to medium ribs spaces 1.5 m where required.	Rockbolts of length 3.5 m long, spaced 2 m, 110 mm thick shotcrete

	Chainage	Rock Type	RMR	Q	Support System According to RMR	Support System According to Q
Lesser Himalaya	0+000 - 0+550	Quartzite	62	2.23	Locally bolts in crown 3 m long, spaced 2.5 m with occasional wire mesh, 50 mm shotcrete in crown where required.	Rockbolts of length 3 m long, spaced 2 m, 80 mm thick shotcrete
	0+550 - 1+500	Quartzite	66	2.91	Locally bolts in crown 3 m long, spaced 2.5 m with occasional wire mesh, 50 mm shotcrete in crown where required.	Rockbolts of length 3 m long, spaced 2 m, 60 mm thick shotcrete
	1+500 - 3+250	Sandstone	63	2.38	Locally bolts in crown 3 m long, spaced 2.5 m with occasional wire mesh, 50 mm shotcrete in crown where required.	Rockbolts of length 3 m long, spaced 2 m, 65 mm thick shotcrete
	3+250 - 4+000	Sandstone	64	2.54	Locally bolts in crown 3 m long, spaced 2.5 m with occasional wire mesh, 50 mm shotcrete in crown where required.	Rockbolts of length 3 m long, spaced 2 m, 65 mm thick shotcrete
	4+000 - 4+900	Sandstone	56	1.49	Systematic bolts 4 m long, spaced 1.5 m to 2 m in crown and wall with wire mesh in crown, 50 mm to 100 mm shotcrete in crown and 30 mm in walls.	Rockbolts of length 3 m long, spaced 2 m, 85 mm thick shotcrete
	4+900 - 6+000	Sandstone	61	2.08	Locally bolts in crown 3 m long, spaced 2.5 m with occasional wire mesh, 50 mm shotcrete in crown where required.	Rockbolts of length 3 m long, spaced 2 m, 80 mm thick shotcrete
	6+000 - 7+690	Sandstone	54	1.31	Systematic bolts 4 m long, spaced 1.5 m to 2 m in crown and wall with wire mesh in crown, 50 mm to 100 mm shotcrete in crown and 30 mm in walls.	Rockbolts of length 3 m long, spaced 2 m, 85 mm thick shotcrete

	Chainage	Rock Type	RMR	Q	Support System According to RMR	Support System According to Q
Higher Himalaya	0+000 - 1+150	Augen Gneiss	74	4.63	Locally bolts in crown 3 m long, spaced 2.5 m with occasional wire mesh, 50 mm shotcrete in crown where required.	Rockbolts of length 2.6 m long, spaced 2.2 m, 60 mm thick shotcrete
	1+150 - 3+300	Augen Gneiss	63	2.38	Locally bolts in crown 3 m long, spaced 2.5 m with occasional wire mesh, 50 mm shotcrete in crown where required.	Rockbolts of length 2.6 m long, spaced 2.2 m, 65 mm thick shotcrete
	3+300 - 4+300	Augen Gneiss	68	3.32	Locally bolts in crown 3 m long, spaced 2.5 m with occasional wire mesh, 50 mm shotcrete in crown where required.	Rockbolts of length 2.6 m long, spaced 2.2 m, 60 mm thick shotcrete
	4+300 - 6+880	Augen Gneiss	65	2.91	Locally bolts in crown 3 m long, spaced 2.5 m with occasional wire mesh, 50 mm shotcrete in crown where required.	Rockbolts of length 2.6 m long, spaced 2.2 m, 60 mm thick shotcrete

RESULTS

Parameters such as total displacement, stress distribution, and the effectiveness of installed support systems were analyzed and compared across the three geological regions. By integrating the field data, empirical classification, and finite element simulations the design assumptions and support strategies were validated. Support systems recommended by empirical relations, viz, RMR and Q-system is presented in Table 3. Detailed numerical simulation results for various tunnel chainages that includes σ_1 and σ_3, total displacements before and after support installation and support systems are presented in Table 3 for Siwaliks, Table 5 and Table 6 for Lesser Himalayas and Table 7 for Higher Himalayas respectively.

FEA Results

Finite Element Modeling included analysis of total displacement, stress distribution, and the effect of installed support systems. The numerical simulations for selected sections are shown in Fig 2 for the Siwaliks, Fig 3 for the Lesser Himalayas and Fig 4 for the Higher Himalayas. FEA shows the initial stress redistribution and deformation patterns before support installation. The results showed that total displacement varied significantly across the three geological regions. The Siwaliks region exhibited the highest displacements, which can be attributed to weak mudstone and sandstone formations, with post-support displacements exceeding 0.10 m in some sections. In contrast, lower displacement was seen in the Lesser Himalayas and Higher Himalayas, generally ranging between 0.036 m and 0.056 m, suggesting the higher strength and stiffness of quartzite and gneiss.

The displacement was correlated with the overburden and the E_m of the rock mass. Areas with lower E_m values and higher overburden demonstrated increased deformation, requiring stronger support systems. The stress concentration around the tunnel boundaries also followed predictable trends:

Maximum principal stresses (σ_1) were observed near the crowns and walls of the tunnel, particularly in zones with low RMR values. The installation of support systems significantly reduced deformation and redistributed stresses more evenly.

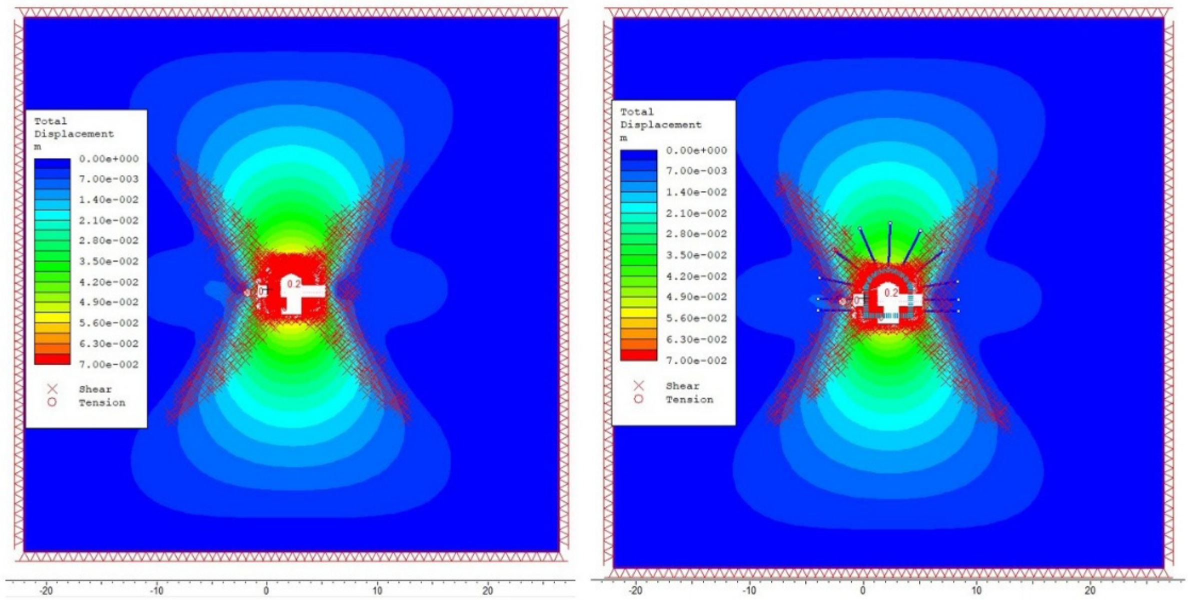

Fig. 2: Representative numerical simulation of HRT in Siwaliks before support installation and after support

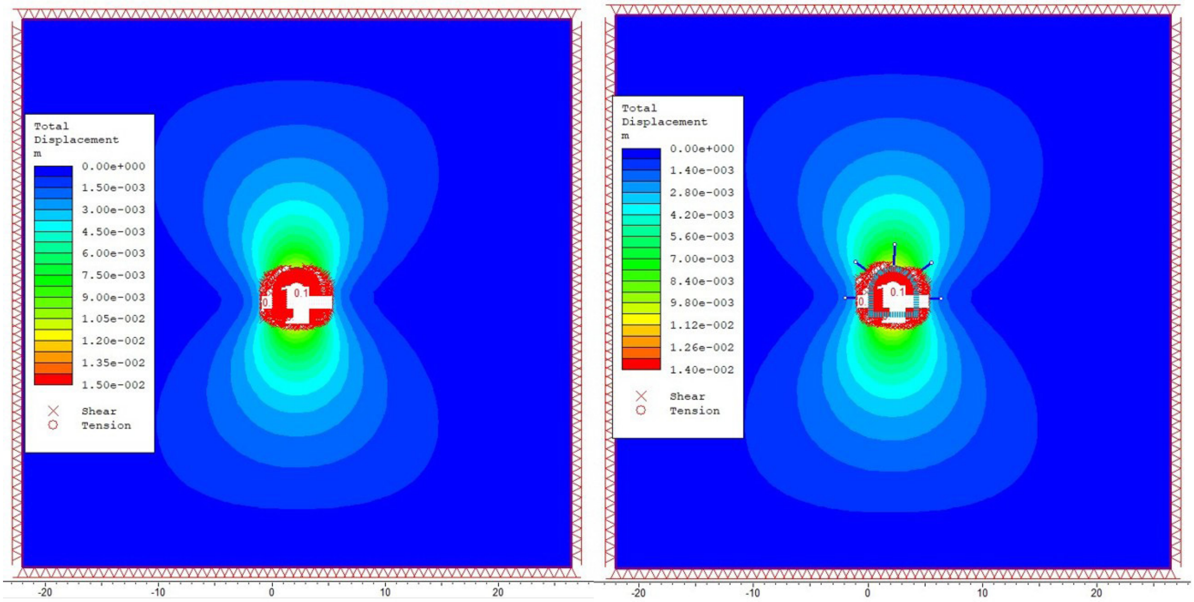

Fig. 3: Representative numerical simulation of HRT in Lesser Himalayas before support installation and after support installation

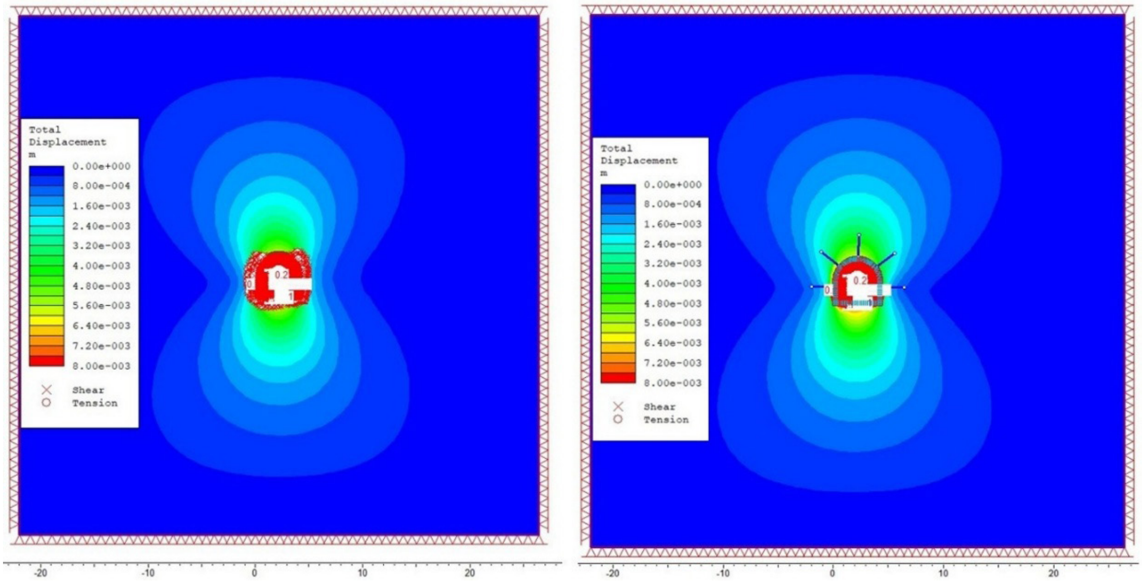

Fig. 4: Representative numerical simulation of HRT in Higher Himalayas before support installation and after support installation

Table 4: In-situ parameters for different chainages of Siwaliks

S.N.	Parameters	0+000 to 0+600	0+600 to 1+700	1+700 to 5+600	5+600 to 6+888
1	Rock Type	Sandstone	Sandstone	Mudstone	Sandstone
2	σ_1 (MPa) (Before Support)	9.81	10.22	15.82	5.27
3	σ_1 (MPa) (After Support)	12.62	13.20	18.72	6.15
4	σ_3 (MPa) (Before Support)	2.75	3.08	4.65	1.46
5	σ_3 (MPa) (After Support)	4.39	4.35	5.90	2.05
6	Total Displacement (m) (Before Support)	0.0646	0.0643	0.0820	0.0370
7	Total Displacement (m) (After Support)	0.0605	0.0606	0.0605	0.0325
8	Support Systems	FRS of thickness 8 mm at walls and crown with I beam W 360×196 at 2.5 m interval. Rockbolt of length 3.5 m at 1 m interval.	FRS of thickness 10 mm at walls and crown with I beam W 360×592 at 2 m interval. Rockbolt of length 3.5 m at 1 m interval.	FRS of thickness 10 mm at walls and crown with I beam W 360*1086 at 2 m interval. Rockbolt of length 3.5 m at 1 m interval.	FRS of thickness 8 mm at walls and crown with I beam W 360×196 at 2.5 m interval. Rockbolt of length 3.5 m at 1 m interval.

Table 5: In-situ parameters for different chainages of Lesser Himalayas

S.N.	Parameters	0+000 to 0+550	0+550 to 1+500	1+500 to 3+250	3+250 to 4+000
1	Rock Type	Quartzite	Quartzite	Sandstone	Sandstone
2	σ_1 (MPa) (Before Support)	17.42	18.05	61.90	19.34
3	σ_1 (MPa) (After Support)	15.30	19.77	54.90	20.51
4	σ_3 (MPa) (Before Support)	2.67	4.48	22.59	4.01
5	σ_3 (MPa) (After Support)	2.90	5.76	21.31	8.27
6	Total Displacement (m) (Before Support)	0.0140	0.0171	0.0118	0.0165
7	Total Displacement (m) (After Support)	0.0127	0.0155	0.0111	0.0155
8	Support Systems	FRS of thickness 5 mm at walls and crown.	FRS of thickness 5 mm at walls and crown with I beam W 360×634 at 3 m interval. Rockbolt of length 2.5 m at 2.5 m interval.	FRS of thickness 10 mm at walls and crown with I beam W 360×634 at 2 m interval. Rockbolt of length 2.5 m at 2.5 m interval.	FRS of thickness 8 mm at walls and crown with I beam W 360×463 at 3 m interval. Rockbolt of length 2.5 m at 2.5 m interval.

Table 6: In-situ parameters for different chainages of Lesser Himalayas

S.N.	Parameters	4+000 to 4+900	4+900 to 6+000	6+000 to 7+690
1	Rock Type	Sandstone	Sandstone	Sandstone
2	σ_1 (MPa) (Before Support)	15.50	20.44	11.61
3	σ_1 (MPa) (After Support)	15.64	25.12	13.22
4	σ_3 (MPa) (Before Support Installation)	3.05	5.68	2.59
5	σ_3 (MPa) (After Support)	3.80	7.77	4.62

6	Total Displacement (m) (Before Support)	0.0216	0.0146	0.0391
7	Total Displacement (m) (After Support)	0.0207	0.0121	0.0376
8	Support Systems	FRS of thickness 5 mm at walls and crown with I beam W 360*463 at 4 m interval. Rockbolt of length 2.5 m at 2.5 m interval.	FRS of thickness 10 mm at walls and crown with I beam W 360*463 at 3 m interval. Rockbolt of length 2.5 m at 2.5 m interval.	FRS of thickness 5 mm at walls and crown. Rockbolt of length 2.5 m at 2.5 m interval.

Table 7: In-situ parameters for different chainages of Higher Himalayas

S.N.	Parameters	0+000 to 1+150	1+150 to 3+300	3+300 to 4+300	4+300 to 6+880
1	Rock Type	Augen Gneiss	Augen Gneiss	Augen Gneiss	Augen Gneiss
2	σ_1 (MPa) (Before Support)	14.49	20.32	16.01	31.14
3	σ_1 (MPa) (After Support)	21.01	20.92	15.43	30.60
4	σ_3 (MPa) (Before Support)	3.32	3.90	1.92	13.54
5	σ_3 (MPa) (After Support)	4.14	4.34	2.09	14.28
6	Total Displacement (m) (Before Support)	0.00760	0.00595	0.00719	0.00382
7	Total Displacement (m) (After Support)	0.0094	0.0062	0.0059	0.0038
8	Support Systems	FRS of thickness 9 mm at walls and crown. Rockbolt of length 2.5 m at 2.5 m interval.	FRS of thickness 5 mm at walls and crown. Rockbolt of length 2.5 m at 2.5 m interval.	FRS of thickness 5 mm at walls and crown. Rockbolt of length 2.5 m at 2.5 m interval.	FRS of thickness 5 mm at walls and crown. Rockbolt of length 2.5 m at 2.5 m interval.

SUPPORT SYSTEM OPTIMIZATION

Support systems were initially proposed based on empirical RMR recommendations. It included a combination of FRS, rock bolts, and in some cases, steel sets. The initial support design was later validated and optimized by numerical modeling to make sure FoS was more than 1.5 in all sections. In Siwaliks, where displacement was largest, a thicker FRS (40 mm) and longer bolts (up to 4 m) were required. Compared to that, the Lesser Himalayas and Higher Himalayas required thin shotcrete layers (25–30 mm) and short bolts (2.5–3 m) because the quality of the rock mass was higher. The modeling results confirmed that after support installation, displacements were reduced by 20–40%, and stress concentrations were mitigated. This showed the effectiveness of the support systems used and allowed for optimization to avoid over-design while maintaining stability. The final installed support system for each tunnel segment was selected to balance between safety and cost effectiveness, suitable for the geological conditions of the area.

Stress Redistribution Relative to Overburden

There is redistribution of stress before the support installation due to release of confining pressure, leading to stress concentration at undesirable points along the tunnel path. The HRT of Higher Himalayas produced the highest average stress-to-overburden ratio, followed by the HRT of Lesser Himalayas, whereas the HRT of the Siwaliks produced the lowest stress levels. This is because of the solid geological condition in the Higher Himalayan Region.

It is also noted that the tunnel in the Lesser Himalayas develops the highest average stress. This can be attributed to the fact that the project area in the Lesser Himalayas has the highest overburden values compared to the other regions (ranging up to 770 m). This shows that the overburden pressure also plays a significant role in stress generation.

Subsequent to installation of the support system, the ratio of stress to overburden is increased slightly, mostly due to the load-sharing phenomenon of the installed support systems. The support systems do not, however, decrease the maximum principal stress significantly, but stabilize the tunnel by redistributing loads and avoiding excessive deformations. The stress ratio variation in the three regions follows the lithological and rock mass differences, strengthening the argument for site-specific reinforcement measures.

In the case of the Lesser Himalayas, the stress-to overburden ratio remained nearly constant before and after support installation. This can be attributed to the moderately stiff and relatively homogeneous rock mass which predominantly consists of quartzite and compact sandstone combined with high overburden, which provides substantial confinement. As a result, the HRT in this region maintained a relatively stable stress regime even during excavation, and the role of support was primarily preventive. Unlike in the Siwaliks or the Higher Himalayas, where stress redistribution is more noticeable, the stable geology and confinement resulted in limited variation in stress ratio post-support. A comparative graph of showing ratio of average stress (σ_1) to overburden before and after support installation is shown in Fig 5.

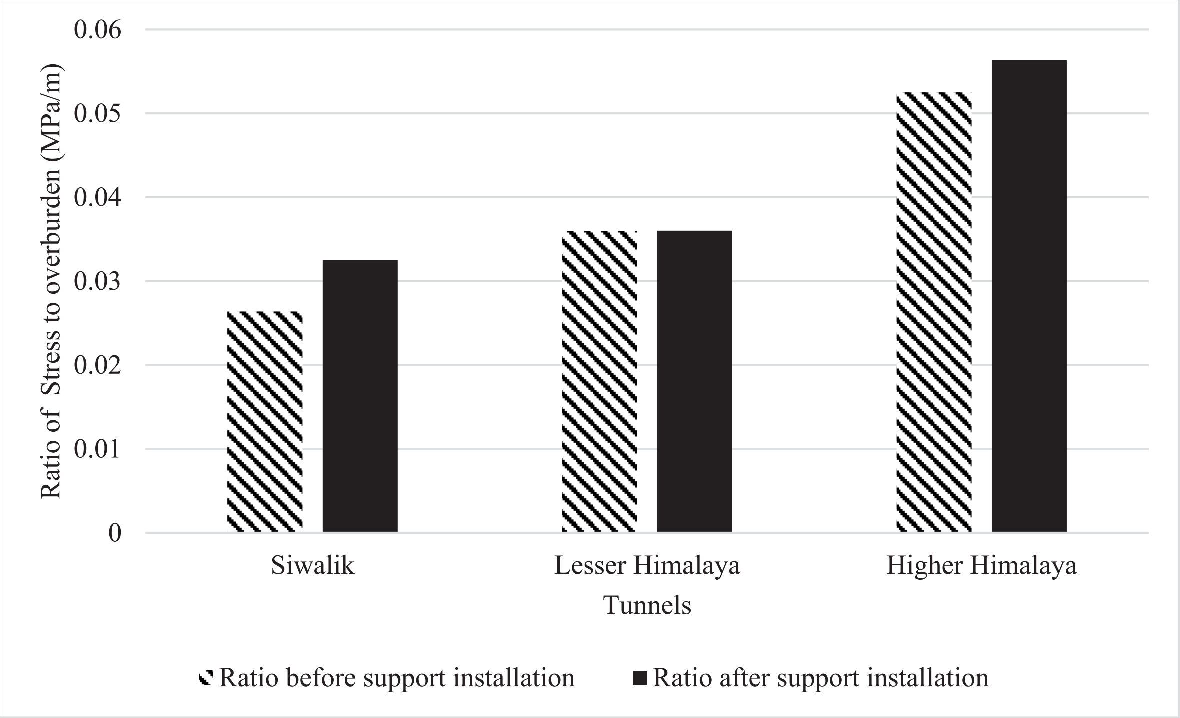

Fig. 5: Bar chart showing ratio of average stress (σ_1) to overburden before and after support installation

DISPLACEMENT-TO-DEFORMATION MODULUS RATIO ANALYSIS

The average displacement shows the deformation behavior of the rock mass under varying stress conditions. The ratio of average total displacement to deformation modulus provides a measure of the relative deformability of the rock mass before and after the installation of support. A higher ratio indicates a more deformable rock mass, whereas a lower ratio suggests greater stiffness and resistance to movement.

Before the installation of support, the displacement-to deformation modulus ratio is highest in the Siwaliks region, followed by the Lesser Himalayas and the Higher Himalayas. This corresponds to the geological properties of these regions, with the Siwaliks being composed of weaker, highly fractured rock masses, having low modulus of deformation resulting in greater displacements for the same applied stresses.

After the installation of support, the displacement-to deformation modulus ratio is reduced across all regions, demonstrating the effectiveness of reinforcement in limiting tunnel deformations. The reduction is most significant in the HRT of Siwaliks region, where intensive support systems (e.g., thicker fiber-reinforced shotcrete and closer steel sets and rock bolt spacing) were required to enhance tunnel stability.

Conversely, the HRT of Higher Himalayas showed minimal reduction in deformation, as the rock mass shows high stiffness and lower deformation tendencies. The ratio of average total displacement to deformation modulus before and after support installation showed little to no change. This further indicates that despite experiencing high stress levels, the strong and stiff rock mass in this region, enhanced by effective early confinement, limited the deformation. In this case, the support system primarily served to ensure long term stability, rather than significantly altering the mechanical response, which was already inherently strong due to favorable lithological conditions. A bar chart showing ratio of average total displacement to deformation modulus before and after support installation is shown in Fig 6.

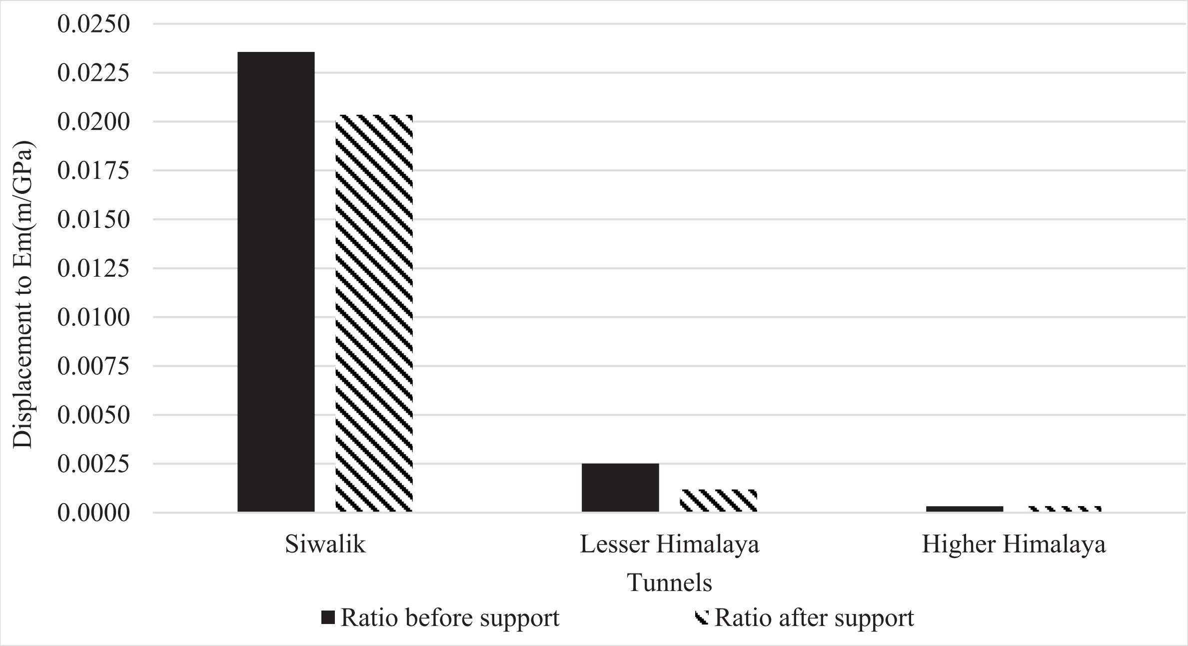

Fig. 6: Bar chart showing ratio of average total displacement to deformation modulus before & after support installation

Stress (σ_1) Before Support Installation Along the Tunnel

The stress distribution along the tunnel chainage before the application of support systems shows the stress concentration at various points along the tunnel alignment. The stress distribution trend for Siwaliks, Lesser Himalayas, and Higher Himalayas follows a varying pattern, with some sections experiencing significantly higher stress than others.

These variations can be due to changes in rock mass properties, lithological variations, overburden, and geological structures along the tunnel alignment. In sections where stress concentrations are high, additional reinforcement measures such as systematic bolting, reinforced shotcrete, or steel sets may be required to prevent excessive deformation and potential failure. A graph showing stress before installation of support along the tunnel alignment is shown in Fig 7.

Total Displacement Before Support Installation Along the Tunnel

The displacement profile along the tunnel chainage shows how the deformation behavior changes along different sections of the tunnel. Similar to the stress distribution, displacement varies with chainage, with some sections experiencing more movement due to weaker rock formations or increased overburden pressures. A graph showing the total displacement before installation of support along the tunnel alignments is shown in Fig 8.

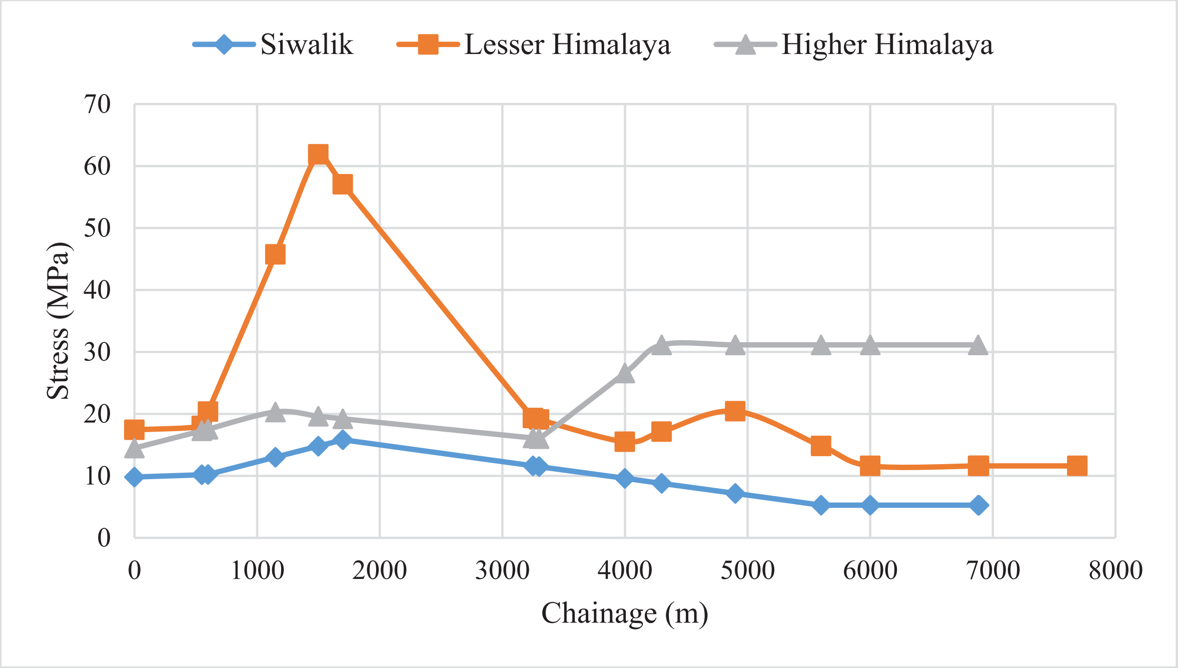

Fig. 7: Graph showing stress before support installation along the tnnel alignment

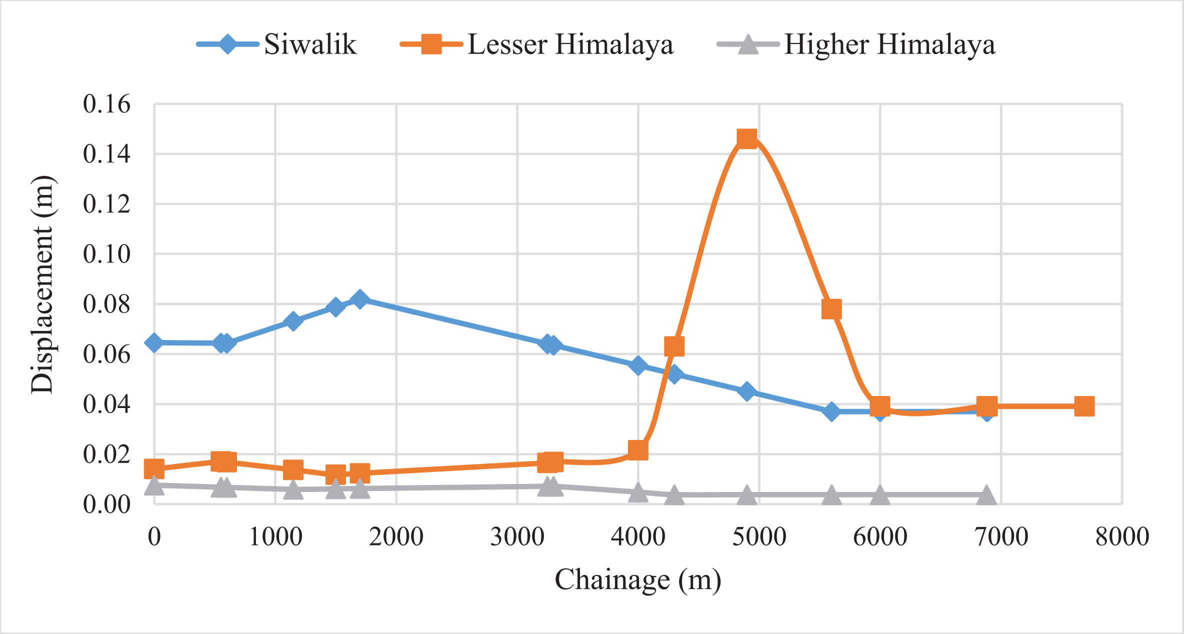

Fig. 8: Graph showing total displacement before support installation along the tunnel alignment

DISCUSSIONS

The comparative evaluation reveals clear lithological and mechanical contrasts between the three regions. The deformability and stiffness analysis reveals Siwaliks are highly deformable due to low deformation modulus and weak rock fabric. Higher Himalayas show stiffness from metamorphic rock masses. High overburden in Lesser Himalaya and Higher Himalaya significantly affects major principal stress values despite decent rock quality, emphasizing the compounded role of lithology and depth. The Siwaliks region consists of generally lower over- burden compared to the Lesser Himalayas and Higher Himalayas. In Siwaliks, intensive support like thicker FRS, closer I-beams and bolts was necessary. In contrast, Lesser and Higher Himalayas required simpler, cost-effective systems due to inherent geological stability Redistribution of stress patterns correlated well with RMR and GSI values, confirming the predictive power of empirical classification systems.

Although hydrogeological modeling was not directly included in this study, the engineering geological reports indicate variable groundwater conditions. The Siwaliks region, which has young sedimentary rocks such as mudstone and sandstone, is prone to higher groundwater inflows due to its porous and fractured nature. This may result in greater deformation and require strong drainage and support measures. In contrast, the Lesser Himalayas and Higher Himalayas, which have more compact quartzite and gneiss formations, showed relatively limited groundwater access and more stable drainage conditions. These differences in drainage and groundwater behavior partially explain the higher support requirements observed in the Siwaliks and should be considered during construction planning and long-term maintenance.

LIMITATIONS

This study presents certain limitations that highlight directions for future studies:

1. The analysis relies solely on empirical and numerical methods without validation from in-situ instrumentation or monitoring during construction. Integrating field monitoring data would help validate the models.
2. Two-dimensional numerical modelling was employed in this study, which may not fully capture the real word complexities. Performing three-dimensional numerical modelling can provide more accurate and comprehensive simulation results.

CONCLUSION

This study highlights the critical role of geological setting in tunnel deformation behavior and support requirements. Based on numerical and empirical analyses of three contrasting Himalayan regions.

1. Displacements in the Lesser and Higher Himalayas were 38.64% and 90.09% lower than in the Siwaliks, respectively.
2. The ratio of major stress to overburden was 36.33% higher in the Lesser Himalayas and 98.98% higher in the Higher Himalayas compared to the Siwaliks.
3. The Higher Himalayas showed the highest deformation modulus, indicating stiffer, more stable rock, whereas the Siwaliks had more fractured, deformable formations.

Consequently, the tunnels in the Siwaliks require the strong support systems to ensure stability, including thicker shotcrete layers, closer spacing of steel sets, and longer rock bolts. The Lesser Himalayas displayed moderate mechanical behavior, necessitating balanced and site-specific support designs influenced by both lithology and high overburden. In contrast, the Higher Himalayas presented the most favorable conditions for tunneling, with minimal deformation and reduced support demands despite undergoing higher stress levels, owing to competent rock formations.

Support systems significantly improve tunnel performance but cannot substitute for poor geological conditions. Hence, geology specific tunnel support strategies must be adopted rather than relying on uniform design standards.

While the reliance on secondary data is a limitation, it allows a realistic and resource-efficient approach in early project phases. Future studies should integrate in-situ monitoring and 3D modeling to validate and refine these findings.

This study showed that geological conditions have a significant influence on the deformation and support behavior of HRTs. The results highlight the necessity of geology- specific tunnel support strategies, as rock mass properties and overburden stress play a more critical role to tunnel performance and stability than the support systems.

ACKNOWLEDGEMENT

The authors are very grateful to Sujan Maka and Subeg Man Bijukchhen from Khwopa Engineering College, Prayag Maharjan from Hydro-Consult Engineering Ltd. and Bibek Thapa and Raju Miyan from Khwopa College of Engineering for their valuable insights and suggestions during various phases of the study. We would also like to express our sincere gratitude Khwopa College of Engineering for providing the platform to carry out this study successfully.

AUTHOR CONTRIBUTIONS

The study was conceptualized by Nirmal Kafle and Aanand Kumar Mishra, both of whom also provided overall academic supervision. Aashika Koju carried out the literature review, rock mass classification and analysis of stress-displacement behavior. Balkrishna Jha was responsible for the final result analysis, discussion, visualization including charts and figures and preparation of comparative tables. Ijan Shrestha did the analysis part and drafted the reports. All the authors contributed equally to the project and reviewed and approved the final version of the manuscript.

CONFLICT OF INTEREST

The authors declare that the paper has not previously published in another journal/bulletin.

REFERENCES

Abbas, N., Li, K., Fissha, Y., Lei, W., Emad, M. Z., Chandrahas, N. S., Pradhan, B., Chelani, A., Aydin, A. and Cheepurupalli, N. R., 2024. Stress-deformation and stability challenges in Himalayan tunnels: impact of geological discontinuities. Discover Materials, 4(1). https://doi.org/10.1007/s43939-024-00144-z.

Aydan, Ö., 2019. Rock Mechanics and Rock Engineering. London: CRC Press.https://doi.org/10.1201/9780367822293.

Azad, M. A., Naithani, A. K., Shekhar, S., Ahmad, S. and Singh, S. K., 2023. Tunnel Support Validation Using Numerical Modelling: A Case Study from NW HImalaya. Indian Geotechnical Journal, 4335-4349. doi:10.1007/s10706-023-02506-5.

Bieniawski, Z., 1978. Determining Rock Mass Deformability: Experience from Case Histories. International Journal of Rock Mechanics and Mining Sciences, 237-247. https://doi.org/10.1016/0148-9062(78)90956-7.

Bieniawski, Z., 1989. Engineering Rock Mass Classifications: A Complete Manual for Engineers and Geologists in Mining, Civil and Petroleum .

Dhital, M. R., 2015. Geology of the Nepal Himalaya: Regional Perspective of the Classic Collided Orogen. Berlin: Springer.DOI 10.1007/978-3-319-02496-7.

Hoek, E. and Brown, E.T., 2018. The Hoek–Brown failure criterion and GSI – 2018 edition. Journal of Rock Mechanics and Geotechnical Engineering, 445-463. https://doi.org/10.1016/j.jrmge.2018.08.001.

Grimstad, E. and Barton, N., 1993. Updating the Q-system for NMT. Proceedings of the International Symposium on Sprayed Concrete, (pp. 46-66).

Hoek, E. and Diederichs, M.S., 2006. Empirical Estimation of Rock Mass Modulus. International Journal of Rock Mechanics and Mining Sciences. , 43(2), 203-215. https://doi.org/10.1016/j.ijrmms.2005.06.005.

Li, C. C., 2017. Principles of rockbolting design. Journal of Rock Mechanics and Geotechnical Engineering, 396--414. https://doi.org/10.1016/j.jrmge.2017.04.002.

Palmström A. and Stille H., 2014. Rock Engineering. Emerald Publishing Limited.

Panthi, K. K., 2004. Tunnelling challenges in Nepal. BERGMEKANIKK/GEOTEKNIKK. 2004.

Panthi, K. K., 2008. Underground Space for Infrastructure Development and Engineering Geological Challenges in Tunneling in the Himalayas. Hydro Nepal: Journal of Water, Energy and Environment, 1, 43-49. https://doi.org/10.3126/hn.v1i0.890.

Paudyal H. and Panthi A., 2010. Seismic vulnerability in the Himalayan region. Himalayan Physics, 14-17. https://doi.org/10.3126/hj.v1i0.5165.

Serafim, J.L. and Pereira, J.P., 1983. Considerations on the Geomechanical Classification of Bieniawski. Proceedings of International Symposium on Engineering Geology and Underground Openings , (pp. 1133-1144).

Shah S.P., and Rangan B.V., 1971. Fiber reinforced concrete properties.

Sheorey, P., 1994. A theory for In Situ stresses in isotropic and transverseley isotropic rock. International Journal of Rock Mechanics and Mining Sciences, 23-34.

Thapaliya, B., Shrestha, N., Acharya, M. S., Yadav, S. K. and Thapa, P. B., 2025. Computational optimization of tunnel support systems under static and dynamic loads in the Himalayan region. Geotechnical and Geological Engineering, 43(6), 302.https://ui.adsabs.harvard.edu/link_gateway/2025GGEng..43..302T/doi:10.1007/s10706-025-03273-1.

Upreti, B., 1999. An overview of the stratigraphy and tectonics of the Nepal Himalaya. Journal of Asian Earth Sciences, 577--606.

Upreti, B., 2001. The Physiography and Geological Division of Nepal and Their Bearing on the Landlside Problem.

Yin A. and Harrison T. M., 2000. Geologic evolution of the Himalayan-Tibetan orogen. Annual Review of Earth and Planetary Sciences, 211--280.

Journal of Nepal Hydrogeological Association (JNHA), Vol (2), 66-74 (2025)
ISSN: 3059-9725 (Online)
https://doi.org/10.3126/jnha.v2i1.85380

RESEARCH ARTICLE

Hydrometeorology, sediment dynamics, and peak flow analysis of the Manohara Watershed, Kathmandu, Nepal

Prativa Pokhrel, Sanjeeb Pandey, *Kabi Raj Paudyal and Dinesh Pathak
Central Department of Geology, Tribhuvan University, Kirtipur, Kathmandu, Nepal
Corresponding Email: paudyalkabi1976@gmail.com

***(Submission Date**: 22 June, 2025; **Accepted Date:** 24 July, 2025)*

ABSTRACT

The Manohara River, a fifth order river, is located in the north-east part of the Kathmandu Valley. Manohara River is the main source of groundwater for Madhyapur Thimi, Changunarayan, Sali Nadi, Tribhuvan International Airport and other places located around this river. The research work mainly focusses on the Hydrometrological impacts, sediments distribution and peak flow estimation of the Manohara River covering the area of the Kathmandu and Bhaktapur districts within its watershed. Desk and field study were carried out to collect primary and secondary data: and was used to interpret the sediment distribution and the peak flow of different return period of the Manohara Watershed. Data from Department of Hydrology and Meteorology were collected to study the variation in the rainfall pattern within the study area. The Manohara watershed experiences highest rainfall during the monsoon season, with less precipitation in post-monsoon. Rainfall is highest in the northeast while decreases along the southwest, influencing sediment transport from boulders upstream to finer materials downstream. The Manohara Watershed experienced significant variations in annual average precipitation, with a maximum of 7.4 mm in 2016 in the Sankhu section and a minimum of 1.97 mm in 1991 in the Airport section, while the Bhaktapur section recorded a yearly maximum of 195 mm in 2002. Estimating peak flow rates using the updated DHM method yielded maximum discharges of 455 m^3/s and 92 m^3/s for 100-year and 2-year return periods, respectively, while the Dickens method provided estimates of 325 m^3/s and 110 m^3/s for the same periods.

Keywords: ***Manohara River, Artificial recharge, Sediment dynamic, Peak flow estimate***

INTRODUCTION

The Manohara watershed, located on the southern slope of the Nepal Himalaya within the Kathmandu basin, spans approximately 73 km². It is primarily filled with Quaternary fluvio-lacustrine sediments (Yoshida and Igarashi, 1984) and underlain by older geological units such as the Precambrian Bhimphedi Group and the Lower Paleozoic Phulchauki Group (Stöcklin and Bhattarai, 1977). The Manohara River, a major tributary of the Bagmati River, flows from northeast of the Kathmandu Valley and is fed by several tributaries including the Sali Nadi, Ghatte Khola, Mahadev Khola, and Satghatte Khola.

Water from the Manohara River is essential for groundwater recharge. However, high population density, agriculture, and industrial practices have led to water crises and declining groundwater levels. The primary sources of groundwater recharge include monsoonal and non-monsoonal rainfall, seepage from wet farming practices, and seepage from water bodies. Significant surface runoff exacerbates groundwater depletion, necessitating artificial recharge. Flooding and river channel shifts, driven by bank erosion, down-cutting, and land use changes, pose significant threats to life, property, and local heritage sites such as Changunarayan and Sali Nadi Temple. Understanding the hydrometeorology, sediment dynamics, and peak flow characteristics of the Manohara watershed is crucial for mitigating these hazards and promoting sustainable water management practices.

Dongol (1985) describes the fluvio-lacustrine sediments of the Kathmandu Valley as predominantly consisting of fine and coarse sand, sandy loam, sandy silty clay, and gravelly conglomerate, covering around 200 square kilometers of Cambrian-Precambrian rocks. In the central portion of the valley, these sediments are nearly horizontal, but they are tilted in the southern section. JICA (1990) grouped the valley's sediment composition into two geological successions: Quaternary deposits overlying the central part's basement rock and Precambrian to Devonian basement rocks surrounding the valley. The depth from the surface to the basement rock ranges from tens of meters to 500 meters. Quaternary deposits consist of lacustrine and fluvial sediments, classified as arenaceous, argillaceous, and intermediate types. JICA also proposed three groundwater districts in the Kathmandu Valley based on water accessibility and lithological variation.

Jnawali and Busch (2000) prepared an environmental geological map of the Kathmandu Valley to highlight geological hazards. They identified the Manohara, Bansbari, Dhobi Khola, and Gokarna well fields in the north, which extract water from sandy layers of the Gokarna and Tokha Formations, and the Pharping well field in the south, which draws from the Lukundol and Kobgaon Formations. They also noted that surrounding mountain ranges are potential areas for groundwater recharge. Tamrakar and Bajracharya (2009) conducted geomorphological, hydrological, and sedimentological analyses of the Manohara River, revealing significant instability, including an 8% increase in the meander belt area and a 32% expansion in the river's average width since 1995. They recommended minimizing anthropogenic disturbances, implementing bank protection measures, and regulating riverbed mining. Pandey et al. (2010) used DPSIR analysis to assess groundwater in the Kathmandu Valley, finding that population growth, urbanization, and tourism have reduced surface water availability, decreased aquifer recharge, and increased groundwater extraction, leading to a groundwater level drop of 13-33 meters from 1980-2000 and 1.38-7.5 meters from 2000-2008, raising subsidence risks in areas with compressible clay and silt layers.

With this background, this study will explore the interplay of hydrometeorology, sediment dynamics, and peak flow in the Manohara Watershed. It aims to understand the region’s precipitation and runoff patterns, how sediment transport affects stability and water quality, and how peak flow insights can inform flood risk management. As a result, it is expected to enhance the understanding of the watershed in order to support effective strategies for its sustainable development.

STUDY AREA

The Manohara River watershed (Fig. 1), located in the northeast of Kathmandu Valley, covers an area of 73 sq.km. Originating in the Shivapuri hills, the river has about 28 km length spanning between latitudes 27°40'00" N to 27°47'00" N and longitudes 85°20'07" E to 85°31'07" E. The study area includes parts of northeastern Kathmandu and certain regions of Bhaktapur districts. The river features a straightened upstream section and a meandering, broad downstream section. Its tributaries are the Sali Nadi, Satghatte Khola, Mahadev Khola, and Ghatte Khola. Well-connected by motor roads, including the Mulpani-Sankhu black-topped road and the Jadibuti-Mulpani road, the area is easily accessible.

DATA AND METHODS

For this study, a range of equipment and software was used. Fieldwork involved a GPS for location coordinates, a digital camera for photographs, a geological hammer for lithology, a measuring tape for sediment depth, and sample bags for collecting samples. Data processing and analysis utilized Google Earth, Microsoft Excel, Adobe Illustrator, and ArcGIS 10.4. Secondary data included topographic maps, published reports, and past rainfall records from the Department of Hydrology and Meteorology (DHM). High-resolution satellite images from Google Earth and a digital elevation model (DEM) from ALOS PLUE were used for recent land cover and geomorphological analysis.

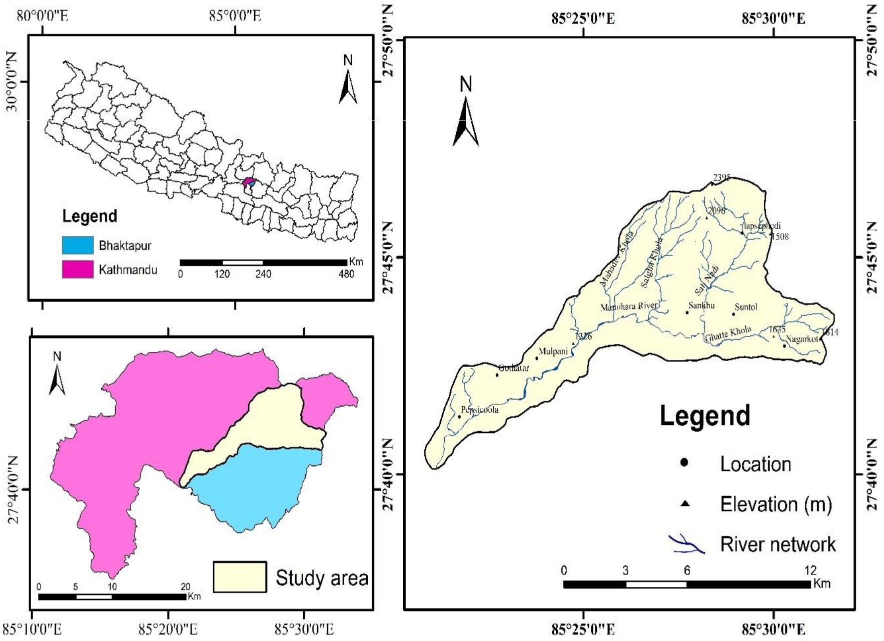

Fig. 1: Location map of the study area (a) Map of Nepal Showing Kathmandu and Bhaktapur districts (b) Present study area (c) Drainage pattern of the Manohara River watershed

Field work was carried out over 7 days to examine sediment distribution in the river deposits. This included documenting sediment dynamics, variations from upstream to downstream, and estimating the Manning's 'n' coefficient based on land use/land cover (LULC). Observations were made on river channel meandering, bank erosion, and sediment deposits. Land use/land cover and channel shifting were verified. Soil samples were collected from various locations for soil characterization and property analysis with preparation of the suitable columnar section of the different stretch of the Manohara watershed.

Estimation of peak flows of different return period

WECS/DHM method

The water and Energy Commission Secretariat (WECS) and Department of Hydrology and Meteorology (DHM) created empirical relationships based on data collected from many stations for use in the context of Nepal. The following equation form the basic approach.

$$Q_2=1.8767(A_{2000})0.8783$$

$$Q_{100}=14.639(A_{2000})0.7342$$

Where, Q_2 and Q_{100} are the 2-year and 100-year extreme flows respectively and A_{2000} is the Basin area (Km2) below 2000m elevation (higher elevation where monsoon rains have a stronger influences). The following Equation is used to determine discharge for other return period.

$$Qr= \exp (\ln Q2+ S\ \sigma)$$

Where Qr is the flood of T year return period (m3/s) S is the standard normal variate and σ is a parameter that is obtained from the following equation.

$$\sigma =\ln (Q_{100} /Q_2) /2.326$$

Modified Diken's Method

Modified Dikens method is also widely used method in Nepal (Rijal, 2014) to estimate the extreme discharge. The formula used is

$$Q = C \times A2/3$$

Where Q is discharge in m3/ s, A is drainage basin area in Km2 and C is coefficient ranging from 10 to 35 and is calculated by using the following formula.

$$C = 2.342 \log (0.6 \times T) \times \log(1185/p) +4$$

Where, T= return period in year, P= 100(a+6)/(a+A), A is total drainage basin area in Km^2 and "a "is perpetual snow area in Km^2.

RESULTS

Hydrometrological study

The hydro-meteorological conditions of the Manohara Watershed were assessed by using 22 years of rainfall data from Kathmandu Airport, Changunarayan, Bhaktapur, and Sankhu stations, sourced from the DHM. The study indicates that while precipitation influences river discharge, specific discharge data is unavailable as the river is ungauged. Rainfall data from Kathmandu Airport, Changunarayan, Bhaktapur, and Sankhu stations were used to calculate annual precipitation. The variation in annual average precipitation across these stations since 1990 is illustrated in fig 2.

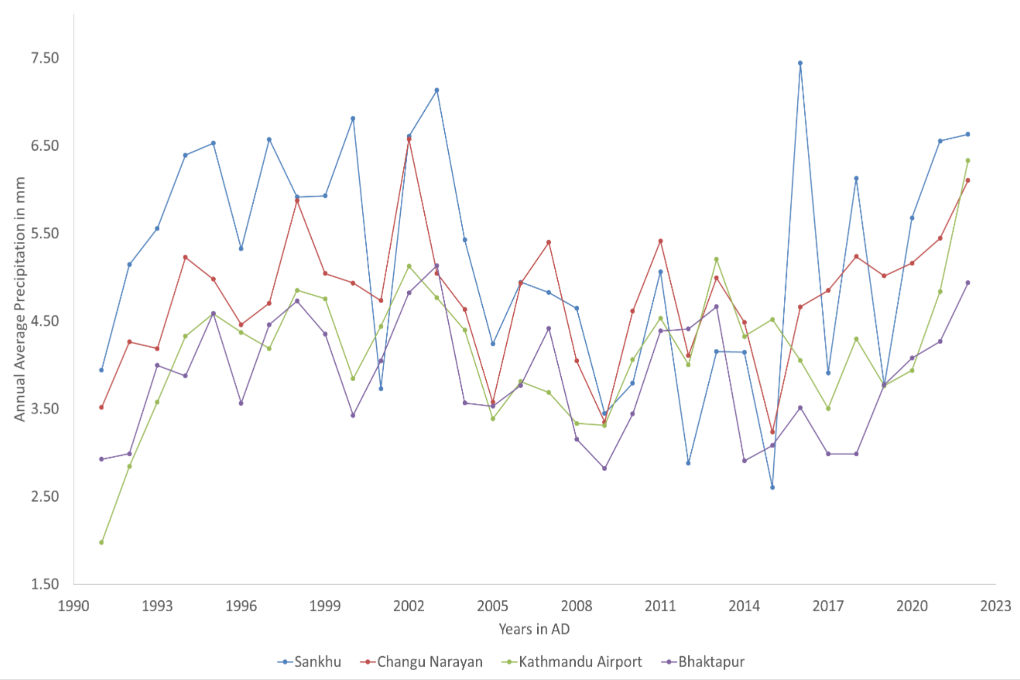

Fig. 2: Annual average precipitation of the Manohara watershed from 1991AD to 2022 AD of the different stations

The yearly maximum precipitation recorded at Changunarayan Station was 165 mm in 2002, with high levels during the monsoon (June-September) and lower amounts in the post-monsoon (October-January). The precipitation has fluctuated from 165 mm in 2002 to 86.5 mm in 2022, showing a decreasing trend over the years. For Sankhu Station, the maximum precipitation was also 165 mm in 2002, but it fluctuated between 179.5 mm and 41.6 mm over the years, with a similar decreasing trend. Kathmandu Airport Station recorded a maximum of 177 mm in 2002, with high precipitation in the monsoon and less in the post-monsoon period. The precipitation here ranged from 177 mm in 2002 to 75 mm in 2022, showing a decreasing trend as well. The maximum precipitation in different station of Manohara watershed yearly has been presented in fig 3.

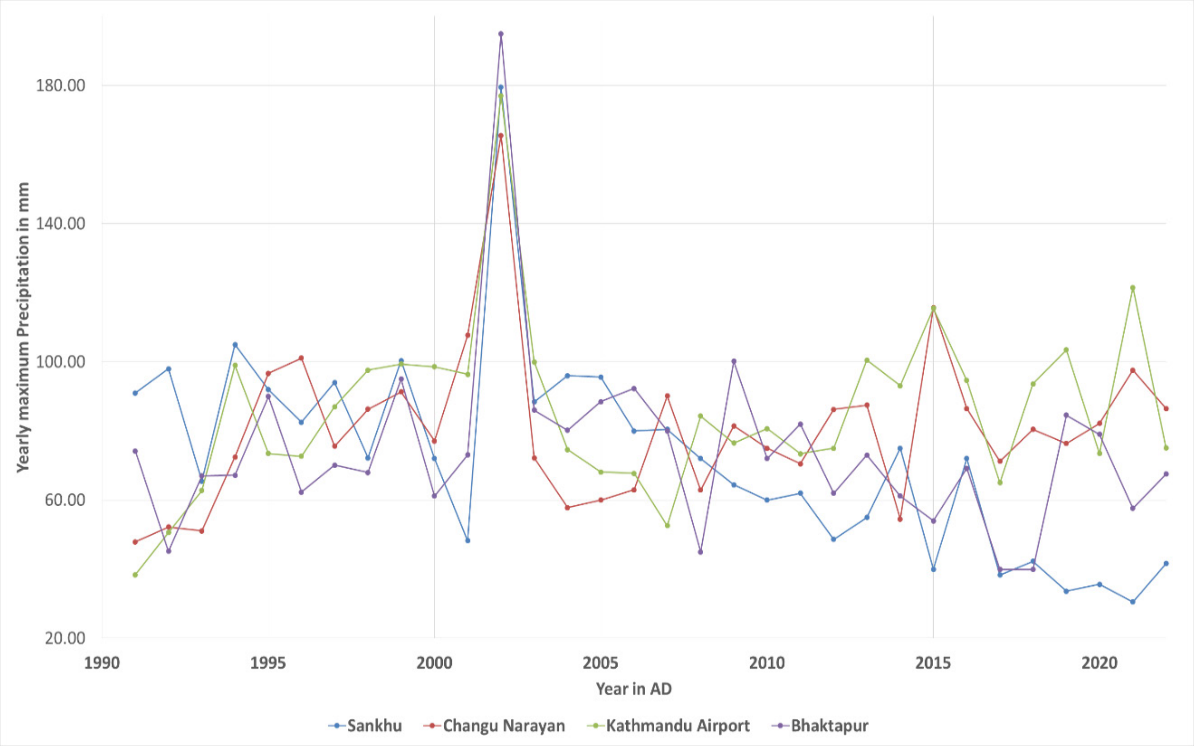

Fig. 3: Yearly maximum precipitation of the Manohara watershed from 1991AD to 2022 AD of the different stations

Sediment Dynamics

The origin of the Manohara River is at Shivapuri Hill and flows through flat plains of the Kathmandu Valley, depositing coarse sediments nearby its foothills section with sparse vegetation. The river deposits boulders, cobbles, pebbles, and sand, with larger gravel sizes up to 162 cm (dia) in the Danda Kateri and Sankhu segments. The middle section (Kurthali) is mostly sandy with some cobbles, pebbles, and clay, while the lower section (Mulpani to Sanothimi) has increasing sand deposits and decreasing pebble and cobble sizes, lacking boulders. Sediment composition (Fig. 4) varies, with upstream areas having sandy gravel and gravelly sand, and downstream areas having sandy silt and silty sand. Gravels in different sections are composed of various rock types, including granite, gneiss, and sandstone. During dry periods, abundant materials on the riverbanks are often extracted for construction.

Fig. 4: Sediment Distribution in the (a) Middle Section (Kurthali Section), (b) Middle Lower Section (near Nepal Engineering College), (c) Lower Stretch (near Har-Har Mahadev), and (d) Near the Confluence with the Hanumante River of the Manohara River

The columnar sections of the upper, the middle and the lower stretch of the Manohara River are presented in fig 5.

Peak flow estimation

The estimation of peak flow for the Manohara River across various return periods, calculated using three different methods, is detailed in Table 1, with a graphical comparison presented in Figure 6. The methods used to estimate peak flow include the WECS/DHM method and the Modified Dickens method. Among these, the modified WECS/DHM method consistently shows higher discharge values for longer return periods, indicating a greater expected peak flow during significant flood events. This comparison highlights the variability and potential impacts of using different methodologies for hydrological predictions.

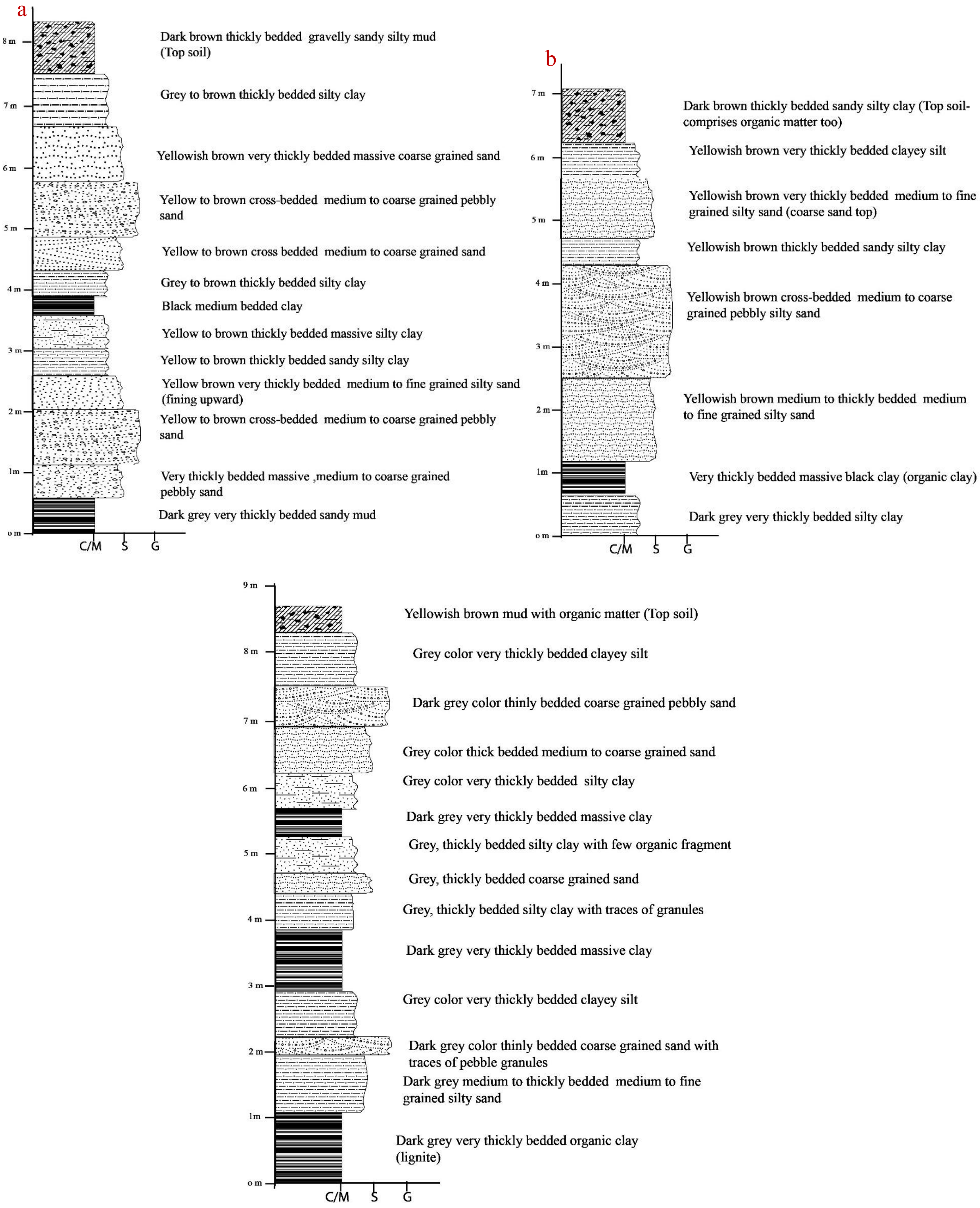

Fig. 5: Columnar section of (a) the upper stretch (Dadakateri Area), (b) the middle stretch (Kurthali area) and (c) the lower stretch (Jadbuti) of the Manohara River

Table 1: Estimated peak flow of Manohara River for different return periods

Return Period (Years)	Discharge (m³/s)		
	Modified Dicken's Method	(WECS/DHM method)	Updated (WECS/ DHM method)
2	110	82	92
5	160	138	164
10	198	181	222
50	287	292	377
100	325	345	455

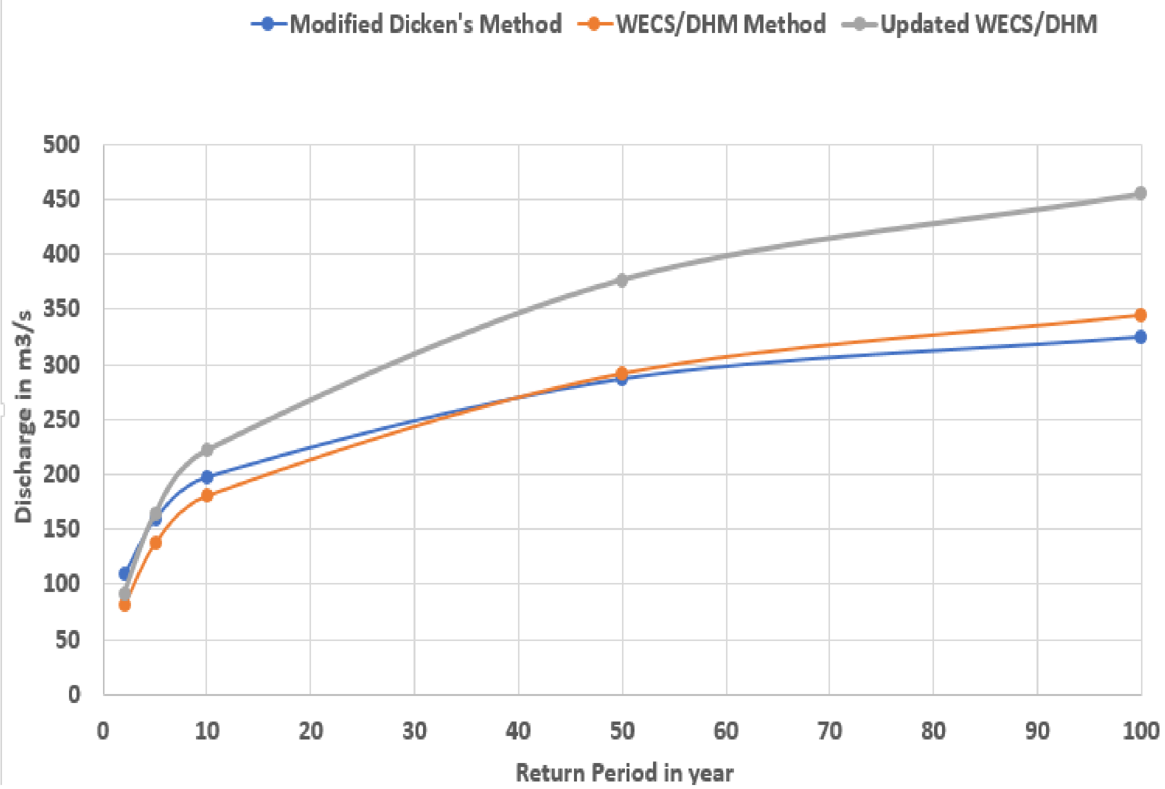

Fig. 6: Peak flow of the Manohara River estimated by different method for different return period

Analyzing the discharge for various return periods reveals that the Modified Dickens method estimates up to 325 m³/s for a 100-year return period, whereas the WECS/DHM method estimates a higher discharge of up to 455 m³/s. For a 2-year return period, the Modified Dickens method shows a higher discharge of about 110 m³/s, while the WECS/DHM method indicates a lower discharge of approximately 92 m³/s.

DISCUSSION

Similar to other regions globally, Nepal has experienced changes in rainfall patterns, with a noticeable increase in high-intensity rainfall events. This trend is largely attributed to ongoing climate change (Government of Nepal, 2011). As a result, the Manohara River is likely to face more frequent and severe floods, which could lead to greater inundation risks. By estimating peak flow rates, flood inundation maps can be created for various return periods. These maps are crucial for identifying potential hazard zones early, allowing for proactive measures to mitigate the impacts of flooding before disasters occur.

CONCLUSIONS

According to precipitation data from the DHM, the highest rainfall in the Manohara watershed occurs during the monsoon season (June to September), while the post-monsoon period receives significantly less precipitation. Long-term data indicate that average annual rainfall is highest in the northeastern part of the study area and it decreases toward the southwest. The Manohara Watershed experienced a maximum annual average precipitation of approximately 7.4 mm in 2016 in the Sankhu section, and a minimum of about 1.97 mm in 1991 in the Airport section. The watershed also recorded a yearly maximum precipitation of around 195 mm in 2002 in the Bhaktapur section.

The Manohara watershed, covering an area of 73 square kilometers, originates at Shivapuri Hill and flows through flat plains. Its major tributaries include the Ghatte Khola, Sali Nadi, Mahadev Khola, and Satghatte Khola. In the upper reaches, the river carries sediments ranging from boulders to gravel, while in the lower reaches, the sediment size decreases, with sand, silt, clay, and pebbles becoming more dominant.

Estimating peak flow rates enables the creation of flood inundation maps for various return periods. Using the updated DHM method, the maximum discharge was found to be approximately 455 m^3/s for a 100-year return period and 92 m^3/s for a 2-year return period. In contrast, the Dickens method estimates the maximum discharge to be 325 m^3/s and 110 m^3/s for the 100-year and 2-year return periods, respectively. These estimates are essential for identifying potential hazard zones early and implementing proactive measures to mitigate the impacts of flooding before disasters strike.

ACKNOWLEDGEMENTS

We express our gratitude to the Department of Hydrology and Meteorology, Government of Nepal, for generously providing historical hydrological and meteorological data. We also extend our sincere thanks to everyone who offered direct and indirect assistance throughout the course of this study.

REFERENCES

Dangol, G. M. S., 1985. Geology of the Kathmandu fluviatile lacustrine sediments in the light of new vertebrate fossil occurrences. Journal of Nepal Geological Society, 3. https://doi.org/10.3126/jngs.v3i0.32662

JICA., 1990. Groundwater management project in the Kathmandu Valley- Final Report, Supporting Report Kathmandu, pp. 114-117.

Jnawali, B. M. and Busch, K., 2000. Environmental geological map of the Kathmandu Valley, Nepal. Journal of Nepal Geological Society, 22. https://doi.org/10.3126/jngs.v22i0.32346

Pandey, V. P., Chapagain, S. K. and Kazama, F., 2009. Evaluation of groundwater environment of Kathmandu Valley. Environmental Earth Sciences, 60(6), 1329–1342. https://doi.org/10.1007/s12665-009-0263-6

Stöcklin, J. and Bhattarai, K. D., 1977. Geology of Kathmandu area and Central Mahabharat range: Nepal Himalaya. http://ci.nii.ac.jp/ncid/BA89416090

Tamrakar, N. K. and Bajracharya, R., 2009. Fluvial environment and existing stability condition of the Manahara River, central Nepal Himalaya. Journal of Nepal Geological Society, 39, 45–58. https://doi.org/10.3126/jngs.v39i0.31487

Yoshida,M. and Igarashi, Y., 1984. Neogene to Quaternary Lacustrine sediments in the Kathmandu Valley, Nepal. Journal of Nepal Geological Society, v. 43, pp. 73-100.

Journal of Nepal Hydrogeological Association (JNHA), Vol (2), 75-90 (2025)
ISSN: 3059-9725 (Online)
https://doi.org/10.3126/jnha.v2i1.85381

RESEARCH ARTICLE

Comparative study of aquifer characteristics and ground water potential of Dun Valley and Terai Area: Case study from Dang Valley and Kapilvastu area

Dharma Raj Pandey[1], ***Suman Panthee**[2] **and Prativa Ghimire**[1]
[1]*Groundwater Resources and Development Division, Siraha*
[2]*Central department of Geology, Tribhuvan University*
**Corresponding author: sumanpanthee@gmail.com*

(Submission Date**: 14 July, 2025;* ***Accepted Date: *13 August, 2025)*

ABSTRACT

This study compares aquifer characteristics in the Dang Valley and Kapilvastu area using litholog and pumping test data. It analyzed 20 lithologs and pumping tests from Dang and 27 from Kapilvastu. Subsurface formations were interpreted from lithologs, and key aquifer parameters were calculated using the Jacob method. The study found that Dang Valley and Kapilvastu share different subsurface formations, with groundwater typically occurring below the third or fourth layer. Pumping test analysis provided key aquifer parameters, including transmissivity, hydraulic conductivity, and specific capacity. The results show that the average transmissivity in Dang Valley is 2689.84 m^2/day, while in the Kapilvastu area it is 2296.58 m^2/day, indicating that the most of the aquifer in Dang Valley has a consistent capacity to transmit groundwater as compare to Kapilvastu areas, but highest transmissibility obtained in Valwad Kapilvastu (7120 m^2/day). Similarly, the average hydraulic conductivity is higher in Kapilvastu (246.87 m/day) compared to Dang Valley (123.32 m/day), suggesting that the aquifer materials in Kapilvastu allow water to move more freely. The specific capacity, is greater in Kapilvastu (229.71 m^3/day) than in Dang valley (194.72 m^3/day). The Dun Valley experienced a greater decrease in water levels compared to the Terai, with an average drawdown of 18.43 meters and a maximum drawdown of 37 meters.

Overall, these comparisons show that the central part of the Dang Valley including Dharna, Guruwagaun, Goltakuri, and Gairtilawari as well as in the northeastern part of Kapilvastu such as Bhaluwad, Mormi, Banganga, Nibuwa, and Gorusinge, the aquifer characteristics were found to be similar, indicating areas with good groundwater potential. In contrast, the peripheral areas of the Dang Valley and the southeastern part of Kapilvastu including Fattepur, Purnihawa, and Semari as well as the western areas such as Jawabhari, Birpur, and Turuntapur, have aquifers that showed relatively poor groundwater potential, which is likely due to differences in the depositional environment and the nature of the sediments.

Keywords: ***Hydraulic conductivity, Transmissibility, Specific capacity, Drawdown***

INTRODUCTION

Aquifer characterization specifies the determination of its hydraulic properties and its distribution pattern (Todd, 2001; Pandey at al., 2021). The aquifers develops in different geological phenomena and the environment of the aquifer formation time and later on stages plays significant role in aquifer development (Todd, 2001). The sedimentation and stratification of aquifer systems in inner mountain valley and Terai reason are different (Sharma, 1974; Shrestha et al., 2018). The mode of aquifer formation significantly controls the groundwater potential of the area. Inter-fingering modes are generally develops in Dun valley area. Pathak (2018) and Pathak and Rao (1998) study shown that linear stratification are seen in Bhabar and Terai area with different size of sediment depositions. In this study groundwater potential and aquifer characteristics of two similar ground but having different geological setting is comparing and attempt to show differentiating groundwater potential with respect to aquifer characteristics (Pandey at al., 2021). The understanding of aquifer system with their characteristics will not only help to know the groundwater potential but also planning for groundwater management and aquifer preventing from contamination. Urbanization in the Terai is rapid and has risk of aquifer pollution because of increasing landfill sites and other influents (Panthee, 2008).

The climate of both study area is tropical to subtropical. The mean annual rainfall of Dang valley ranges from 5 mm to 140 mm in month of April and June respectively and The rainfall of the Kapilvastu district is maximum about 500 mm-600 mm in June to August and minimum 0-5 mm in March and the temperature reached maximum about 40-45^{o}C in May and fall down 10-15^{o} C in the months of March.

The Babai River is one of the major rivers in the Dang valley, flowing east to west and passing through the southern end of the valley. Other perennial streams, such as the Sisne Gwar, Baulaha and the Katwa, originate in the lesser Himalaya and join the Babai River on the south, creating alluvial fan plains, sand and gravel bars, depositional basins and other depositional landforms. The subsurface is underlain by fluvio-lacustrine sediments that form aquifer systems ranging from unconfined near the recharge areas to semi-confined or confined (Rao and Piya, 1996) at depth, a pattern observed in Dun Valley (Dang) and in the Terai plains (Kapilvastu), where tubewell investigations and regional hydrogeological surveys document layered sand–silt–clay sequences controlling confinement and yield. The erosional activity of the rivers has indented the river terrace of the valley by 8 to 15 m and has created badland topography in the northern part. The Banganga is the main river of Kapilvastu flowing from north to south and middle part of Kapilvastu area and beside the Banganga River there are other small rivers in the Kapilvastu area.

Study area

The study area lies in Dang valley and Kapilvastu district of Lumbini Providence of Nepal. Dang valley lies between longitudes 82^{o} to 82^{o} 45' E and latitude 28^{o} to 28^{o} 10' N and Kapilvastu area is bounded between longitude 27^{o} to 27^{o} 65' 41" E and latitude 82^{o} to 82^{o} 99' 31" N (Fig. 1). The total study area at Kapilvastu and Dang valley are about 1738 km^{2} and 2400 Km^{2}. The Valley elevations range from 600 meters along the Babai with alluvial slopes gradually rising northward to 700 meters along the base of the Mahabharat Range. The Kapilvastu area is situated at a height of 93 to 1,491 meters. Both of the study area are easily accessible from motor road i.e. Mahendra (East –West) Highway. The Dang valley is about 25 km north from Lamahi and the study area of the Kapilvastu district is near Chandrauta surrounding which is easily accessible by motor road from east-west Highway.

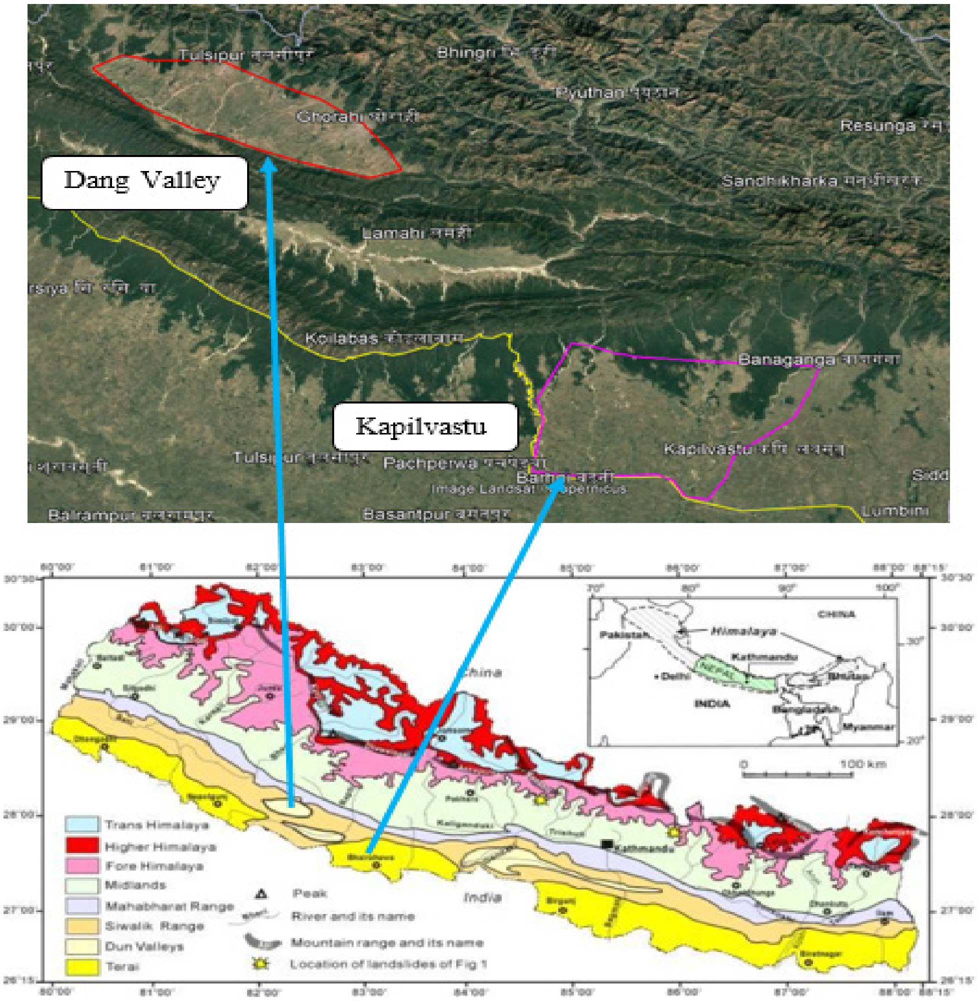

Fig. 1: Study area location map

Hydro-geological setting of the study area

Hagen (1969) classified Nepal into ten geomorphic regions, including the Dun Valley, with Dang Dun Valley being a tectonic Dun Valley within the Siwalik range. Dang Valley stretches 55 km WNW-ESE and is up to 18 km wide, surrounded by Siwalik formations on three sides and Lesser Himalaya to the north. The Siwalik rocks mainly consist of Neogene conglomerates, sandstones, and clays. The valley is a tectonic depression filled with fluvio-lacustrine deposits, alluvial fans, and river terraces formed by tributaries of the Babai River (Rao and Piya, 1996). These sediments include angular to sub-angular pebbles and cobbles derived from the Main Boundary Thrust area, with terraces located along local rivers and their tributaries. Groundwater occurs predominantly below the third and fourth sedimentary formations in the valley, stored within the porous and permeable alluvial deposits. The aquifer system is thus controlled by the depositional environment, sediment type, and tectonic activity, making Dang Valley an important groundwater reservoir in the region.

Similarly, Kapilvastu district, located in Nepal's Terai region south of the Siwalik range and bordered by the Main Frontal Thrust (MFT), consists of thick sediment deposits formed by mountainous outwash from the softer geological ranges. Morphologically, it has two alluvial plains: the northern Bhabar Zone and the southern Gangetic plain. The Bhabar Zone contains alluvial materials beneath it, while the Gangetic plain lies directly to the south. These sediments form the main aquifer for groundwater in the area. The northern part has coarse and uniform alluvial sediments, while the Gangetic alluvium consists of mixed layers of silt, clay, sand, pebbles, and gravel, with higher silt and clay content near the Churia foothills.

Methodology

A field survey was undertaken to determine the hydrogeological conditions in the study area, and the preliminary data was collected at the Groundwater Irrigation Development Division (GWIDD) Lamai, Dang. Deep tubewells selected for present study were located in a location map (Fig.1). The study was conducted during the monsoon. Geological information regarding the deep tubewell section of the fluvial terrace was correlated with the nearest Fence diagram band these data was obtained from boreholelogs. Transmissivity is very useful and important parameter for the estimation of aquifer potential and calculated using Jacob's curve method of pump test data for analysis of aquifer characteristics is expressed as:

$T=2.303Q/4\pi\Delta S$ ……………………..........…… (I)

Where,

Q is discharge measured in m^3/day;

ΔS is the change in drawdown in meters.

and hydraulic conductivity from geophysical methods is determined using the following formula:

$T = Kb$……………………………………….. (II)

$K=T/b$……………………...………………. (III)

Where T is transmissivity measured in m^2 /day,

b is the aquifer thickness measured in meters and

K is hydraulic conductivity measured in m/day.

Specific capacity is a quantity that which a water well can produce per unit of drawdown. It is normally obtained from a step drawdown test. Specific capacity is expressed as:

$Sc =Q/h_0\text{-}h$…………………………… (IV)

Where;

Sc is the specific capacity; m^2/day or USgal/day/ft)

Q is the pumping rate; m^3/day or USgal/day),

and h_0-h is the drawdown; m or ft)

The above parameter showed the potential of groundwater in the both areas and the possibility of future extraction for irrigation and other human needed purpose.

Result

The observation well data from both study area were analyzed. The detailed bore log study and pumping test data analysis on the both study area were summarized in the following subsections.

SUBSURFACE GEOLOGY

Dang Valley is an intermountain basin filled with fluvio-lacustrine deposits, including alluvial fans and river terraces mainly formed by tributaries of the Babai River. These sediments, observed around areas like Jaspur village and northwest of Ghorahi, consist largely of angular to sub-angular pebbles, cobbles, sand, gravel, and boulders transported from surrounding mountains. The sediment distribution is relatively uniform and dominated by coarse materials such as sand, gravel, and boulders, especially on the valley's periphery. The northern part of the valley has more boulders and hard rock formations, while clay and silt are more common in the southern parts along the Babai River. Overall, the subsurface lithology is composed of mixed layers of sand, gravel, silt, clay, and Quaternary detritus, showing little variation across the valley shown in (Fig. 2).

The Kapilvastu area, located in the Terai region, is characterized by thick alluvial deposits, primarily formed from sediments from mountainous regions south of the Siwalik range. The geology is divided into two main units: the Bhabar Zone and the southern Gangetic plain, with silt and clay being the primary aquifer system shown in (Fig. 3).

The comparative study of these wells shows that the peripheral part of the Dang valley and north eastern part of the Kapilvastu area has coarse sand and gravel. Towards the south and especially along the Babai River and southern part of Kapilvastu area are dominant by clay and silt. Intermixing of gravel and fines is dominant in the middle part of the both studied area. The subsurface lithology is composed of boulder, cobble, pebble, gravel, and sand with intercalation of clays as well as detritus of quaternary age.

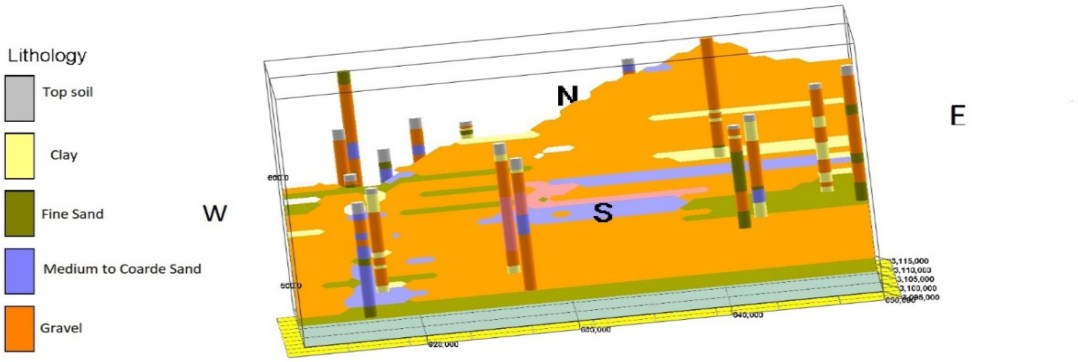

Fig. 2: Fence diagram showing the different layers of aquifer at Dang Valley

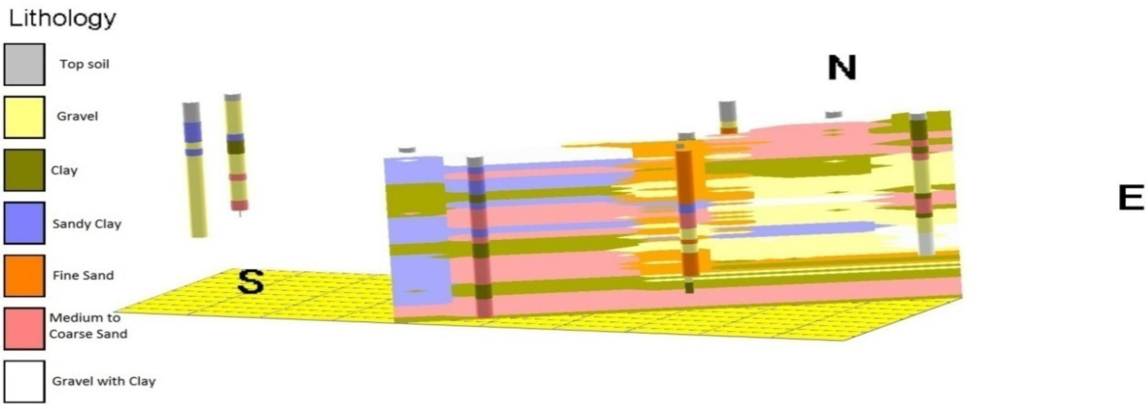

Fig. 3: Fence diagram showing the different layers of aquifer at Kapilvastu area

AQUIFER CHARACTERISTICS

The characteristics of an aquifer depend on the amount of groundwater it can discharge. The different types of aquifers in both areas were studied, and their characteristics are explained in the following sections. Specific Capacity (Sc), Hydraulic conductivity (K) and transmissivity (T) were calculated using available pumping test data. These data were analyzed using Jacob's type curve method for confined aquifers, and three empirical formulas were also used. The results are presented in Tables 1 and 2.

TRANSMISSIVITY

Transmissivity values in Kapilvastu range from 302 to 7120 m²/day, with higher values in the north eastern regions, indicating productive aquifers. In Dang Valley, transmissivity varies more widely, from 95.4 to 4605.12 m²/day, with the highest values in the central and western parts. Although both areas show spatial variation, Dang valley generally has higher and more consistent transmissivity, suggesting more extensive and conductive aquifer zones compared to Kapilvastu. But north eastern part of kapilvastu (7120 m²/day) shows more transmissible than Dang valley shown in (Fig. 4 and 5).

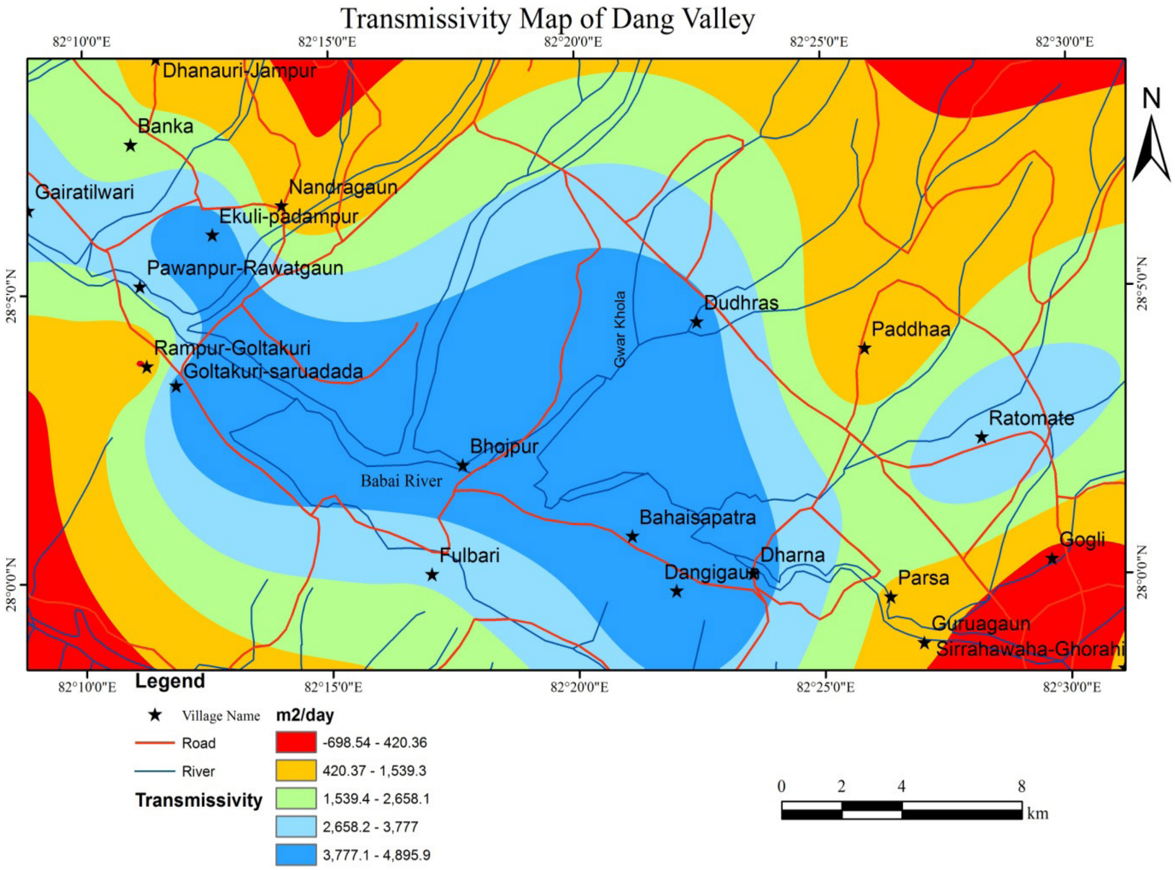

Fig. 4: Transmissivity map of Dang valley

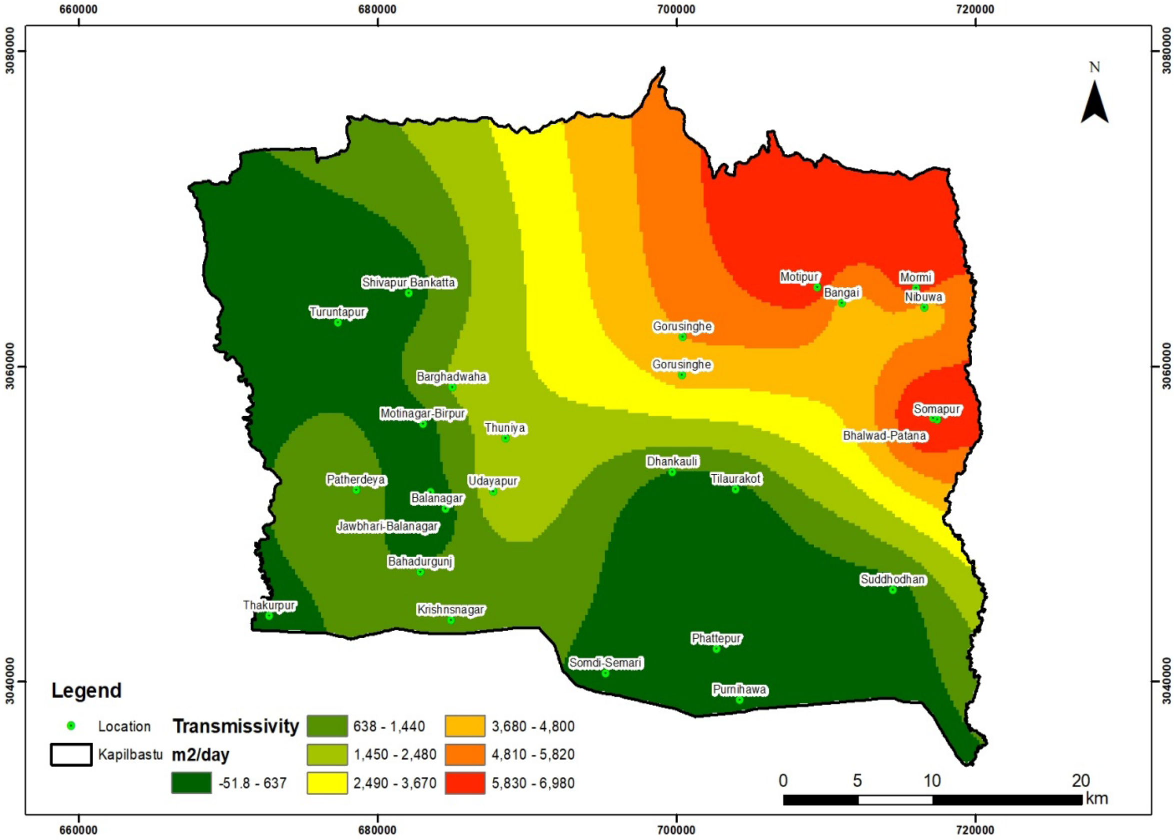

Fig.5: Transmissivity map of Kapulvastu.

HYDRAULIC CONDUCTIVITY

The average hydraulic conductivity of Dang Valley is 124.70 m/day, while that of Kapilvastu is 216.01 m/day. However, the highest value in Kapilvastu is 326.56 m/day, and in Dang Valley, it is 219.29 m/day. From this, it can be concluded that the aquifer in the Terai areas discharges water better than that in the valley. Furthermore, the north eastern part of Kapilvastu and the central part of Dang valley have the beter hydraulic conductivity than other parts of the both studied areas as shown in (Fig. 6 and 7).

SPECIFIC CAPACITY

Specific capacity in Kapilvastu ranges from 37.73 to 388.80 m^3/day, with higher values in the northern and north eastern regions and lower ones in the southern and western. In contrast, Dang Valley shows a much wider range, from 7.0 to 240 m^3/day, with the highest capacities in the central and western areas. Lower values are found in the periphery of the valley, while the south-central region also shows higher well efficiency. These spatial differences reflect variations in aquifer properties and groundwater potential between the two areas shown in (Fig. 8 and 9).

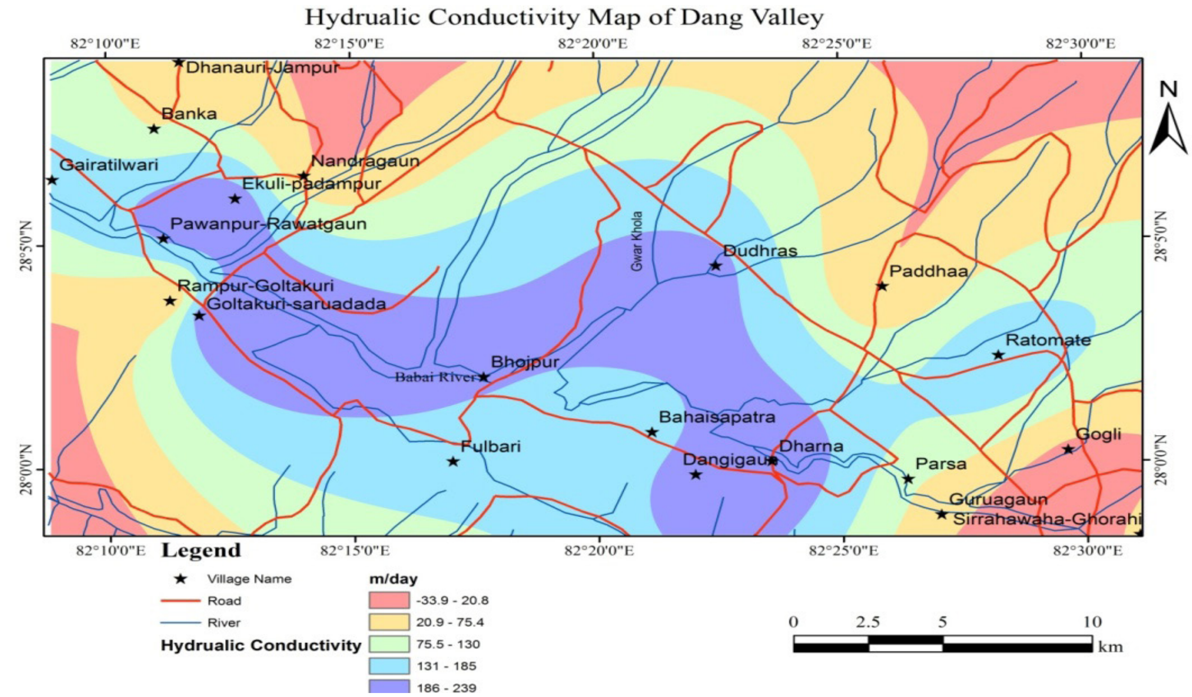

Fig. 6: Hydraulic conductivity map of Dang valley

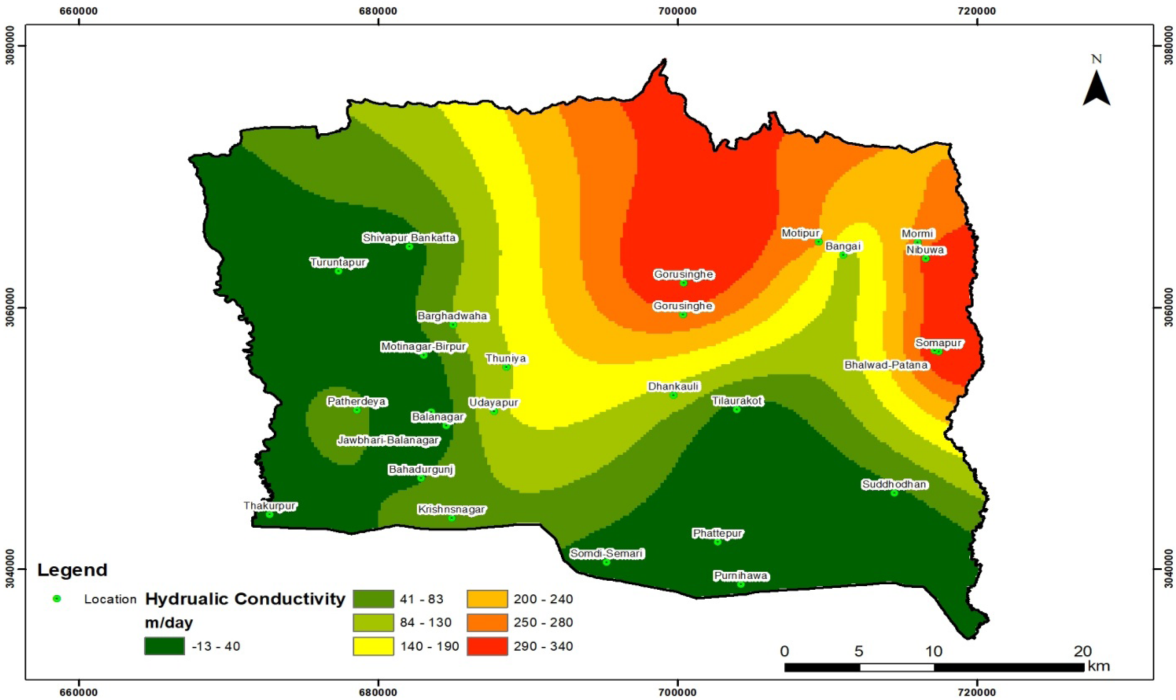

Fig. 7: Hydraulic conductivity map of Kapilvastu

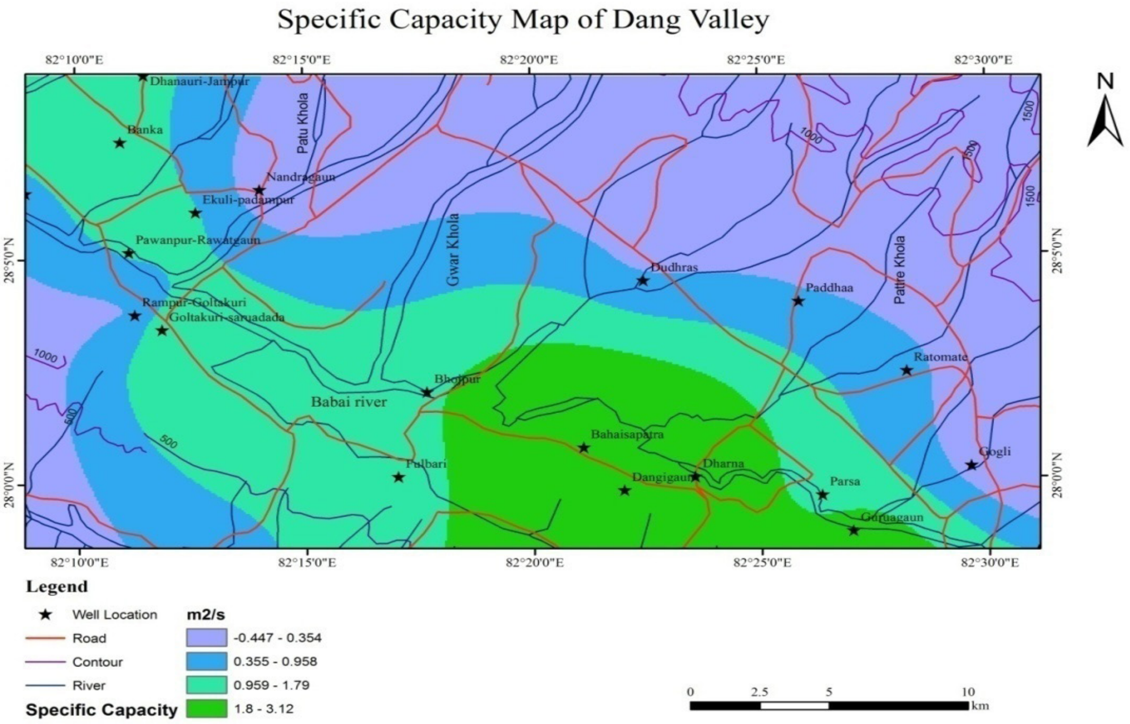

Fig. 8: Specific Capacity map of Dang valley

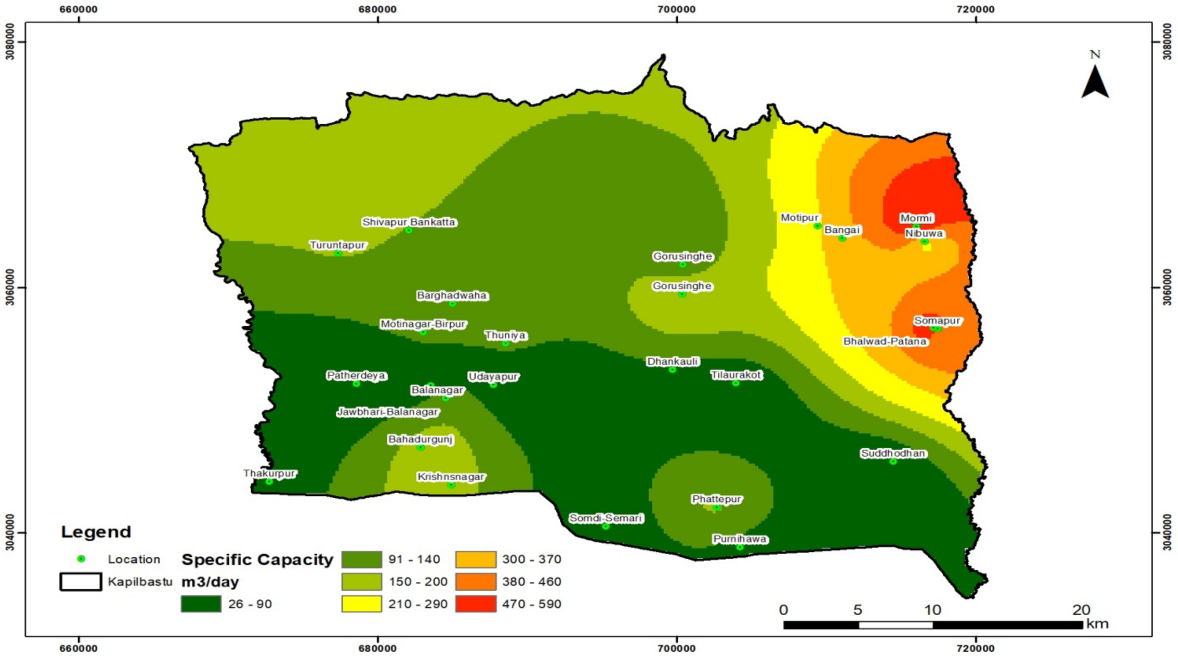

Fig. 9: Specific Capacity map of Kapilvastu

Table 1: Aquifer characteristics of Kapilvastu study area

Well no.	Location	Elevation (m) asl	Northing	Easting	Total depth (m)	Aquifer thickness (m)	Yield lps	Specific capacity (m3/ day)	Draw down (m)	Hydraulic conductivity (m/day)	Transmissivity (m2/day)
KV1	Bahadurgunj	100	3046957.4	682837.5	135	18	24.5	162.83	13.0	38.14	686.5
KV2	Barghadwaha	127	3058641.6	685008.1	125	18	25.5	122.40	18.0	84.42	1519.5
KV3	Gorusinghe	115	3061867.25	700402.37	112	15	15	108.00	12.0	317.55	4763.2
KV4	Dhankauli	114	3053293.22	699744.32	122	18	22	77.58	24.5	115.92	2086.5
KV5	Krishnsnagar	97	3043860.7	684914.7	113	18	25	163.86	11.2	61.91	1114.3
KV6	Patherdeya	106	3052125.63	678571.59	155	21	11	43.20	22.0	47.08	988.6
KV7	Phattepur	99	3042049.79	702693.51	145	21	27	145.80	16.0	18.94	397.8
KV8	Gorusinghe	119	3059432.69	700359.65	125	15	23	198.72	10.0	273.71	4105.6
KV9	Nibuwa	108	3063715.25	716617.53	120	15	26.5	286.20	8.0	292.38	4385.7
KV10	Somapur	125	3056589.8	717483.43	128	18	18	388.80	4.0	326.57	5878.2
KV11	Udayapur	124	3052028.54	687745.28	124	14	13	59.51	18.0	132.14	1850
KV12	Thuniya	138	3055396.95	688543.63	153	16	16	172.80	31.0	125.26	2380
KV13	Jawabhari	133	3051984.73	683520.08	171	22	10	41.14	21.0	13.73	302
KV14	Balanagar	124	3050963.94	684524.38	155	9	14	67.20	18.0	37.89	341
KV15	Tilaurakot	126	3052165.8	703956.47	122	18	13	59.12	19.0	23.39	421
KV16	Motipur	144	3065006.31	709465.84	123	25	24	172.80	12.0	250.64	6266
KV17	Bangai	148	3063979.6	711077.17	88	18	23	198.72	10.0	116.00	2088
KV18	Shivapur Bankatta	163	3064626.6	682070.52	79.5	13	14	57.60	21.0	27.23	354
KV19	Bhalwad-Patana	143	3056701.9	717216.31	124	23	27	333.26	7.0	309.57	7120
KV20	Mormi	165	3064958.4	716067.2	88	25	25	270.00	8.0	253.12	6328
KV21	Turuntapur	166	3062771	677329.55	61	11	10	48.00	18.0	29.91	329
KV22	Motinagar-Birpur	140	3056329.1	683044.75	127	19	9	37.03	21.0	20.84	396
KV23	Jawbhari-Balanagar	130	3050963.9	684524.38	142	20	11	41.32	23.0	18.85	377
KV24	Suddhodhan	119	3045805.6	714488.67	126	12	14	46.52	26.0	29.58	355
KV25	Purnihawa	116	3038815.9	704225.68	99	18	18	74.06	21.0	18.94	341
KV26	Somdi-Semari	112	3040522.9	695267.38	110	18	14	50.40	24.0	20.94	377
KV27	Thakurpur	124	3044175.7	672741.73	127	21	16	47.67	29.0	19.48	409

Table 2: Aquifer characteristics of Dang valley study area

Well No.	Well Location	Elevatin (m)	Easting	Northing	Well Depth (m)	Aquifer thickness (m)	Discharge (lps)	Specific capacity (m3/ day)	Drawdown (m)	Hydrulic conductivity (m/day)	Transmissivity (m2/day)
DH1	Guruagaun	611	642665	3096805	95	15	22	211.2	9	46.65	699.84
DH2	Nandragaun	615	621242	3110789	110	24	3	7	37	3.975	95.4
DH3	Gogli	661	646911	3099502	100	15	4.5	12.15	32	8.78	131.76
DH4	Parsa	602	641542	3098271	95	15	16	115.2	12	88.70	1330.56
DH5	Pawanpur-Rawatgaun	571	616532	3010819	102	15	18	88.86	17.5	189.79	2846.88
DH6	Rampur-Goltakuri	551	616757	3010563	106	21	10	29.79	29	19.97	419.4
DH7	Paddhaa	673	640667	3106235	116	24	12	38.4	27	23.4	561.6
DH8	Fulbari	603	626264	3098988	120	18	10	108	8	157.68	2838.24
DH9	Sirrahawaha-Ghorahi	646	649341	3095992	125	18	18	77.76	20	38.39	691.1
DH10	Goltakuri-saruadada	565	617737	3105019	96	21	15	129.6	10	217.33	4564.08
DH11	Ratomate	661	644568	3103389	110	21	14	46.52	26	175.68	3689.28
DH12	Gairatilwari	558	612797	3110622	110	21	21	181.44	0	156.75	3291.84
DH13	Dudhras	624	635076	3107075	121	21	10	39.27	22	199.54	4190.4
DH14	Dhanauri-Jampur	655	617051	3111548	125	21	20	101.64	17	63.36	1330.56
DH15	Bhojpur	582	627289	3102583	122	24	13	140.4	8	190.26	4566.24
DH16	Banka	607	616217	3112735	117	24	13	70.2	16	77.76	1866.24
DH17	Ekuli-padampur	590	618937	3109850	100	21	18	129.6	18	219.29	4605.12
DH18	Dharna	556	636963	3099008	80	18	25	240	9	237.6	4276.8
DH19	Dangigaun	561	634414	3098453	92	21	24	172.8	12	216	4536
DH20	Bahaisapatra	570	632938	3100208	100	27	22	271.54	7	163.2	4406.4

GROUNDWATER CONDITION

The Dang Dun valley aquifers are primarily filled with highly porous and permeable unconsolidated to poorly consolidated pediment alluvium or fan deposits, known as Dun Fan Gravels. These deposits from the main aquifer system appear homogeneous in tubewell logs and hydraulic properties. There are two types of aquifer systems: confined and unconfined. Confined aquifers are common in the valley, with thicknesses ranging from 15m to 27m. Unconfined aquifers are found in granular zones like gravel and sand in western part of the valley.

In contrast, the Kapilvastu area, in the Terai plain, has porous and permeable pediment deposits and a multilayer aquifer system. The porous and permeable pediment deposits from the main large aquifer system in this area. The aquifer system is multilayer in nature, as commonly found in alluvial deposits. Groundwater is under unconfined or water table types in shallow aquifers and under semi-confined or leaky confined conditions in deeper aquifers. Perched water table conditions also present in some places. The deeper aquifers are productive and have been tapped through hundreds of tube wells. Well inventory of deep wells are presented in Table 1 and 2 of Kapilvastu area and Dang valley respectively.

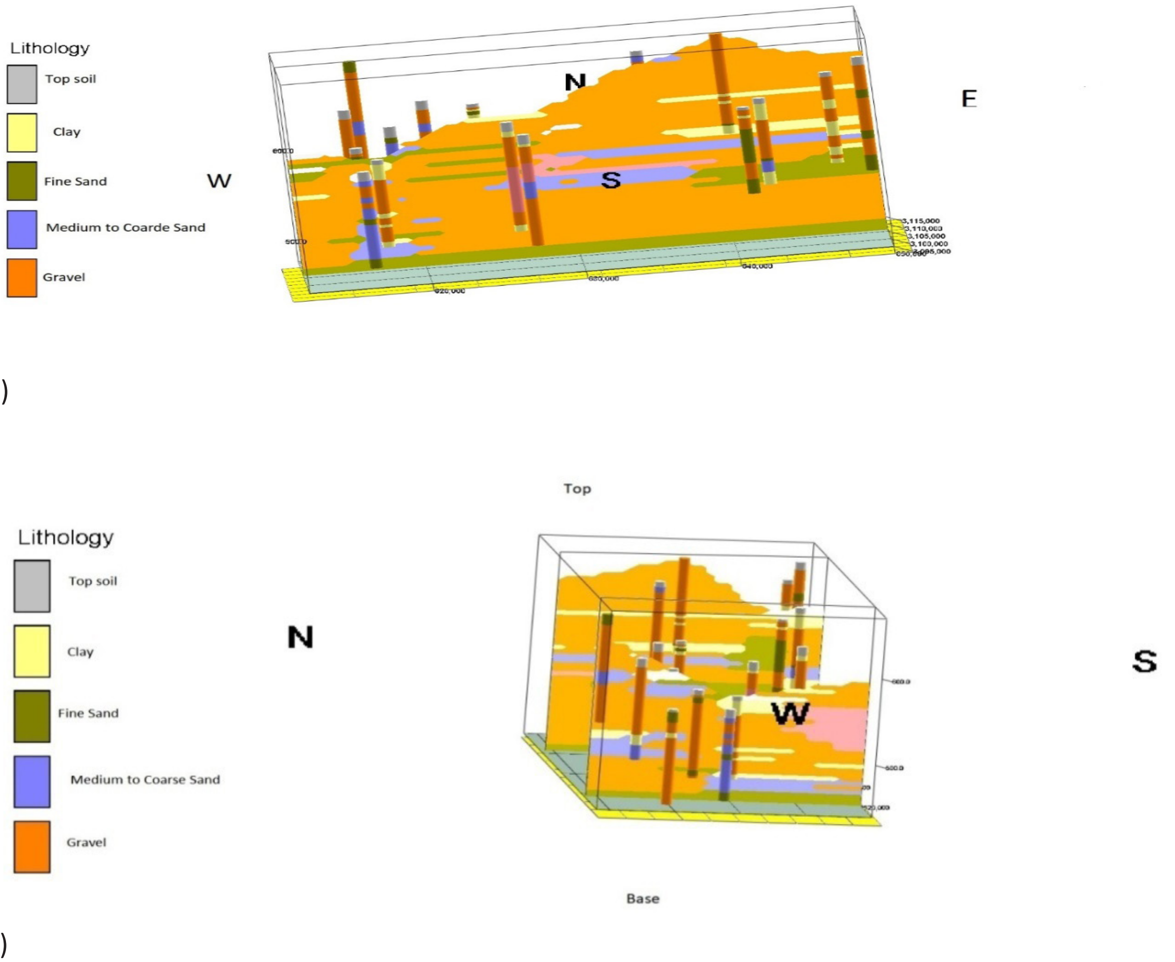

Fig.10: Fence diagram (A) E-W view of different aquifer layers and (B) N-S view of different aquifers layers

Dang Valley shows significant variation in groundwater levels, ranging from 0 to 25 m below ground level (bgl), with deeper levels in the north and shallower ones near southern rivers, due to the lack of impermeable layers. In contrast, Kapilvastu has more stable water levels, mostly between 0 and 7 m bgl during April–May. The greater fluctuation in Dang is likely due to low porosity or high transmissivity, leading to rapid recharge in the north and fast discharge to the south. Groundwater flow is fastest in central Dang, with the highest discharge at Gairatilwari (25 l/s) and the lowest at Nandragaun (3 l/s). In Kapilvastu, the highest discharges are at Valwad (27 l/s) Nibuwa (26.5 l/s), Bargadawaha (25.5 l/s), and Krishnanagar (24.5 l/s), with the lowest at Birpur (9 l/s).

GROUNDWATER RECHARGE

In the study area, the aquifers are mainly recharged through rainwater infiltration. Additionally, parallel streams flowing across the valley contribute to the recharge of the Dang Valley. Since the northern fringes of both the Dang Valley and Kapilvastu district consist of coarse materials such as gravels and boulders, major recharge occurs in these zones. In the Kapilvastu area, rivers flowing from the foothills of the mountain front, along with the Banganga River, serve as important sources of groundwater recharge.

SAFE YIELD

The storage co-efficient is much lower in confined aquifers because they are not drained during pumping. Any water released from storage is obtained primarily by compression of the aquifer and expansion of the water when pumped. Thus, assuming the higher value for the aquifer in the study area, which is 10^{-4} (Driscoll 1987) and on the basis of the data average safe yield of the area were estimated as given in the table 3.

Safe yield = area of aquifer × storage coefficient × mean piezometric surface fluctuation.

Table 3: Average safe yield of the study area

SN	Study area	Mean piezometric surface fluctuation(m)	Average safe yield (m^3/ year)
1	Dang area	13.2	$3.16*10^7$
2	Kapilvastu	6	$1.05*10^6$

Discussion

The aquifer properties in Dang Valley and Kapilvastu differ due to their unique depositional environments, though both are shaped by fluvial processes. Dang Valley has a complex basin-fill with interlayered textures, while Kapilvastu's aquifers develop from north-to-south flowing rivers. In the Terai, aquifers mainly form from alluvial fan and meandering river deposits. Overall, the depositional environment controls aquifer distribution, characteristics, and groundwater recharge in both areas. The aquifer properties of the two different physiographic areas were analyzed. The depositional characteristics of the both area are different. The Dang area has basing fill depositional environment and the different textural layers are positioned in almost inter-fingering condition (Yamanaka and Yagi 1984, Sapkota, 2003 and Shrestha and Neupane, 2009). Similarly, the Kapilvastu area is also deposited fluvial process rivers running from north to south. The aquifer developed in the Terai area are dominantly by fluvial processes, at mountain front alluvial fan type of deposits are dominant and at southern part it is dominated by meandering type of river deposits (Sharma, 1974; Hagen, 1969; Rao and Pathak,1996; Pathak, 2016; Shrestha at el., 2014). The aquifer distributions in the deposits are fully controlled by the depositional environment of the area. The depositional positions in the both area are highly influencing the aquifer characteristics and ground water recharge.

In Kapilvastu, high recharge occurs in the Bhabar zone, while in Dang, it is concentrated in the peripheral parts of the valley. The texture of aquifer materials significantly affects hydraulic conductivity and transmissibility. In Kapilvastu, coarser aquifers are found in the north eastern part and Bhabar zones, with texture and aquifer quality gradually decreasing southward, leading to a decline in specific capacity. In contrast, the Dang Valley shows a different pattern, generally exhibits higher and more consistent transmissivity, indicating larger and more conductive aquifer zones than those found in the Kapilvastu area. Where, the aquifer quality diminishes toward the valley center as well as south and western part of Kapilvastu.

The central part of the Dang Valley and north eastern part of Kapilvastu has higher transmissivity, hydraulic conductivity and specific capacity, meaning water can move more easily through the ground there. But peripheral part of Dang valley and in the southeastern part of Kapilvastu — such as Fattepur, Purnihawa, Semari — as well as in the western areas like Jawabhari, Birpur, and Turuntapur, the aquifers have not shown very good potential for groundwater. These differences are mainly due to the varying nature of the underground layers, or aquifer properties, in each area.

Conclusions

The comparison of the aquifer properties in both area were carried out in different aspects and following conclusions were given based on the observations.

a. The grain size of the alluvium gradually decreased from north to south. The aquifers are multi layered interconnected lenses of sand, gravel and pebble alternating with silt and clay. Aquifer materials for unconfined and semi-confined aquifers are generally sand, gravel, pebble and even cobble and boulder.

b. Deep aquifers are recharged by inflow of the Babai River and shallow aquifers may be recharged in the lower reaches of the Dang valley. It may not be possible to recharge the terraces of study area because present bed level of the Babai River is 570 m a.m.s.l., whereas these terraces are in higher elevation, i.e., 700 m a.m.s.l.. At Kapilvastu district's aquifer may recharge by rain water infiltration and by Banganga River.

c. The Dun Valley's aquifers are made up of coarser materials like sand, gravel, and boulders, allowing water to flow more easily. This results in thicker layers with higher and nearly similar transmissivity, while the Terai region has finer sediments like silt, sand and clay mixed gravel slowing groundwater flow. But the northeastern portion of Kaplvastu shows the better potential aquifer than Dang valley.

d. The aquifer characteristics of Dang Valley are almost similar across all areas except peripheral parts, whereas the aquifer characteristics of Kapilvastu were found to be quite different compared to Dang. For example, the aquifers in the northeastern part of Kapilvastu like Bhalwad, Mormi, Banganga, Nibuwa, Gorusinge area showed behavior similar to those in Dang, while the aquifers in the southeastern part of Kapilvastu — including Fattepur, Purnihawa, Semari and the western localities such as Jawabhari, Birpur, and Turuntapur exhibit limited groundwater potential.

e. Groundwater potential at both areas are satisfactory and groundwater draft is in safe level. Present water demand of both area are fulfilled by the groundwater resources. In case of Dang valley, it is at saturation level in dry season but in Kapilvastu area it is not so serious.

References

Aryal, P., Pandey, V.P. and Thapa, B.R., 2023. Assessment of groundwater availability in western Terai of Nepal: A study in Kailali District. *Proceedings of the 14th IOE Graduate Conference*, 14, 500–505.

Dhital, M.R., 2015. Geology of Nepal Himalaya: Regional perspective of the classical collided orogen. Springer International Publishing, Switzerland. p. 498.

Driscoll, F.G., 1987. Groundwater and wells, 2nd ed. St. Paul (Minnesota): Johnson Filtration System Inc. 1089 p.

Groundwater Resources Development Board (GWRDB), 2020. Publications – Hydrogeological studies. GWRDB.

Hagen, T., 1969. Report on the geological survey of Nepal. Denkschr. Schweiz. Naturf. Ges., *81*, 185.

Pandey, V.P., Ray, A., Khadka, M., Urfels, A., McDonald, A. and Krupnik, T.J.,2021. *Towards conjunctive use of surface water and groundwater resources as a response to water access challenges in the western plains of Nepal.* Cereal Systems Initiative for South Asia (CSISA).

Pathak, D., 2018. Status of groundwater exploitation and investigation in Terai and Inner Teri region of Nepal. Bulletin of Nepal Hydrogeological Association. v. 3, pp. 77-83

Pathak, D., 2018. Status of groundwater exploitation and investigation in Terai and Inner Terai region of Nepal. Bulletin of Nepal Hydrogeological Association, 3, pp. 77–83.

Pathak, D., 2018. Status of groundwater exploitation and investigation in Terai and Inner Teri region of Nepal. Bulletin of Nepal Hydrogeological Association. v. 3, pp. 77-83

Pathak, D., 2018. Status of groundwater exploitation and investigation in Terai and Inner Teri region of Nepal. Bulletin of Nepal Hydrogeological Association. v. 3, pp. 77-83

Pathak, D. and Rao, G.K., 1998. Groundwater recharge to the confined aquifer system in the Terai plain of Nawalparasi District, western Nepal: a hydro chemical approach. Journal of Nepal Geological Society, 17, pp. 37–41.

Panthee, S., 2008. Possible methods of preventing groundwater contamination at landfill sites; case studies from Nepal. Bulletin of the Department of Geology, 11, 51–60. https://doi.org/10.3126/bdg.v11i0.1542

Pathak, D., 2018. Status of groundwater exploitation and investigation in Terai and Inner Teri region of Nepal. Bulletin of Nepal Hydrogeological Association. v. 3, pp. 77-83

Pathak, D., 2018. Status of groundwater exploitation and investigation in Terai and Inner Teri region of Nepal. Bulletin of Nepal Hydrogeological Association. v. 3, pp. 77-83

Pathak, D., 2016. Water availability and hydrogeological condition in the Siwalik foothill of eastern Nepal. Nepal Journal of Science and Technology, v. 17(1), pp. 31-38.

Rao, G.K. and Pathak, D., 1996. Hydrogeological conditions in the Terai plain of Nawalparasi District, Lumbini Zone, Nepal with special reference to groundwater recharges. Journal of Applied Hydrology, 9, pp. 69–75.

Rao, G.K. and Piya, B., 1996. Hydrogeological conditions in Dun valley of Dang, western Nepal: a case study. Journal of Nepal Geological Society, 14, pp. 93–98.

Sapkota, B., 2003. Hydrogeological conditions in the southern part of Dang valley, mid-western Nepal. Himalayan Journal of Sciences, v. 1, Issue 2, pp. 119-122. *DOI*: 10.3126/hjs.v1i2.210

Sharma, C.K., 1974. Groundwater Resources of Nepal. Navana Printing Works Pvt. Ltd., Calcutta. pp. 140–142

Shrestha, S.D. and Neupane, R., 2009. Hydrogeological Assessment and groundwater reserve evaluation in northwestern parts of Dun Valley aquifers of Chitwan, inner Terai. Bulletin of the Department of Geology, Tribhuvan University, Kathmandu, Nepal, 12, pp. 43–54.

Shrestha, S.R., Shrestha, S. and Shah, S., 2014. Status of Shallow Tubewells Irrigation and Shallow Aquifer in Rupandehi. Groundwater Resource

Development Board (GWRDB), Babarmahal, Kathmandu. 151 p.

Shrestha, S.R., Tripathi, G.N. and Laudari, D., 2018. Groundwater Resources of Nepal: An Overview. In: Mukherjee, A. (ed.) Groundwater of South Asia. Springer Hydrogeology. Springer, Singapore. pp. 169–193.

Todd, D.K., 2001. Groundwater hydrology, 2nd edition. John Wiley and Sons Inc., Singapore.

Yamanaka, H. and Yagi, H., 1984. Geomorphological development of the Dang dun. Journal of Nepal Geological Society, 4, pp. 151–159.

Journal of Nepal Hydrogeological Association (JNHA), Vol (2), 91-111 (2025)
ISSN: 3059-9725 (Online)
https://doi.org/10.3126/jnha.v2i1.85384

RESEARCH ARTICLE

Evaluating the Topographical Factors Contributing to Landslide Occurrences in the Thuligad Watershed of Far-Western Province, Nepal

***Bharat Prasad Bhandari[1,2] , Tekendra Bahadur Saud[2], Prakash Bahadur Ayer[2]**
[1]*Central Department of Environmental Science, Tribhuvan University, Nepal*
[2]*College of Applied Sciences, Tribhuvan University, Kathmandu, Nepal*
**Corresponding author: bbhandri@cdes.edu.np*

***(Submission Date**: 2 July, 2025; **Accepted Date:** 16 August, 2025)*

ABSTRACT

The Thuligad watershed in the Farwestern Province has been facing a substantial landslide challenge for a long time, especially during the monsoon season. The harsh topography, characterized by numerous steep slopes, is prevalent across the Thuligad watershed, resulting in a significant incidence of landslides across the area.This research aims to evaluate the impact of topographical factors to trigger landslide within the Thuligad watershed located in the Sudurpaschim province of Nepal. The work began with the use of satellite imagery and ArcGIS to develop a comprehensive spatial and temporal inventory map of landslides. The map illustrating the five topographical factors was generated utilizing a 12.5 m digital elevation model obtained from Alaska Satellite Fascility of United States Geological Survey. The dimensions of the pixel sizes pertaining to the subclasses of factors, as well as those associated with landslides within these subclasses, were ascertained. In a comparable manner, the quantity of landslides identified in relation to aspect, curvature, and slope was derived from both field observations and spatial analyst tool of ArcGIS. The dimensions of the landslide were determined through area measurement and subsequently correlated with the classification of the slope. A statistical index model was employed to ascertain the significant relationship between topographical factors and landslides. A notable positive correlation exists between slope and landslide density; however, the incidence and extent of landslides are greater within the slope range of 30 to 45 degrees. The density of landslides is markedly higher on slopes exceeding 60 degrees. The concave slope with a southern aspect exhibits a notably high incidence of landslides. The topographical wetness index exhibits an inverse correlation with landslide occurrences. The stream power index exhibits a positive correlation with the frequency of landslides. The interplay of slope, stream power index, aspect, and curvature has collectively contributed to the occurrence of landslides in the study area.

Keywords: ***Topographical control, landslide, Thuligad watershed, Farwestern province***

INTRODUCTION

Landslides are regarded as the most consequential and destructive phenomena occurring in mountainous areas worldwide. Mountainous regions exhibit a susceptibility to mass movements as a result of both conditioned and triggering variables (Zhang et al., 2016; Hasegawa et al., 2009). Precipitation, seismic activity, geological condition, topographical attributes and land use act as external catalysts for mass movement (Bhandari and Dhakal, 2018; Tsou et al., 2018; Gerrard 1994; Hasegawa et al., 2009; Zhang et al., 2016; Dahal et al.,2008;

Bhandari and Dhakal, 2019; Bhandari and Dhakal, 2021). Intense precipitation frequently correlates with the initiation of landslides, particularly during the peak monsoon season from June to September in Nepal (Bhandari and Dhakal, 2021; Timalsina and Bhandari, 2024). The interplay of geological conditions, rock weathering, soil erosion, soil moisture, and topographical variables plays a significant role in the dynamics of slope instability (Bhandari and Dhakal, 2018; Bhandari and Dhakal, 2021; Tsou et al., 2018). The impact of human activities, particularly the unrestrained expansion of road networks, and the explosive techniques employed in tunnel construction, and the lack of regulation in agricultural practices on sloped terrains, has been identified as significant factors leading to the recent occurrences of shallow landslides in the Nepal Himalaya (Dahal, 2014; Chamlagain and Dangol, 2022; Thapa et al., 2023; Sharma et al., 2025; McAdoo et al., 2018).

Landslides occur with greater frequency in mountainous regions, causing significant property damage and resulting in fatalities and injuries in many mountainous areas of the developing world, especially in Nepal (Froude and Petley, 2018). Numerous authors have meticulously documented the challenges posed by landslides in the Siwalik and Lesser Himalaya regions of Nepal. Rock avalanches and snow avalanches represent significant hazards in the Higher and Tethys Himalaya region of Nepal. Landslides are becoming more frequent and widespread in the Lesser Himalaya region of western Nepal (Manchado et al., 2021). The regions of Doti, Kailali, Baitadi, and Dadeldhura in Nepal exhibit numerous noteworthy and substantial landslides that have yet to receive comprehensive examination. Topographical data are employed by numerous researchers to assess landslide susceptibility; however, the examination of topographical studies and their correlation with landslides remains limited. The body of work concerning landslide research in Nepal reveals a notable lack of focus on bivariate susceptibility analysis (Regmi et al., 2014; Dahal et al., 2012; Pokharel and Bhandari, 2019; Thapa and Bhandari, 2019; Bhandari et al., 2024), in addition to quantitative assessment and the dynamics observed across various spatial and temporal scales (Bhandari and Dhakal, 2021; Manchado et al., 2022). Nonetheless, there exists a paucity of research exploring the implications and underlying factors, such as precipitation acting as a catalyst and the conditions of the soil (Mugagga et al., 2012; Knapen et al., 2006). The configuration of land surfaces is a fundamental attribute that plays a pivotal role in the likelihood of landslide events (Bhandari and Dhakal, 2019). Nugraha et al. (2015) suggested that the geomorphometric features of terrestrial surfaces are significantly linked to the distribution of landslides. Fernandes et al. (2004) and Broothaerts et al. (2012) have highlighted the significance of investigating the influence of topography on the landslide phenomenon. Giuseppe et al. (2016) contend that the stability of slopes is influenced by a reduction in soil suction across the watershed during precipitation events, in conjunction with increased water pressures that build up in concave areas, where water is directed through saturated subsurface flows as a result of topographical characteristics.

Hung et al. (2018) observed that landslides primarily occurred on steep slopes exceeding 35° within V-shaped inner gorges, as well as on geologically influenced steep slopes, including the scarp slopes of mountain ridges and terrace scarps. Their findings revealed that landslides occur on slopes shaped by topographic and litho-structural factors. The topographic characteristics of hill slope formation and the contributing area have a profound impact on the geographical distribution of landslides. The characteristics of the terrain, including hill slope, aspect, elevation, and curvature, play a significant role in the occurrence of landslides in the hilly regions of Nepal (Bhandari and Dhakal, 2019a). The primary factors influencing landslides encompass the topographical features, especially within the vulnerable and delicate area of the Siwalik Hills

(Bhandari and Dhakal, 2020). Shallow landslides are primarily influenced by topographical features, notably the slope gradient, which is a particularly sensitive factor, as well as lateral concavity (Hennrich and Crozier, 2004). The influence of topography on slope stability is profound; however, the majority of stability models predominantly consider only the slope angle as the relevant topographical variable (Talebi et al., 2008).

The challenging landscape significantly influences the progress of society in the western region of Nepal. In the Far-Western Region, a significant 45.6% of the population resides in poverty (ADB, 2017) and experiences restricted access to essential services (CBS, 2016). Traditional cultural frameworks, intricately associated with religious beliefs and customs, significantly hinder progress (UNFCO, 2012). The demographic patterns observed in the examined region have demonstrated one of the most significant relative surges in Nepal over the last two decades (Worldpop, 2020). This advancement has resulted in significant growth of agricultural areas on steep slopes and the enhancement of infrastructure. The expansion of the road network is particularly noteworthy, frequently linked to inadequate engineering practices (Sudmeier-Rieux et al., 2019). In this context, the configuration of the terrain plays a crucial role in the manifestation of landslides. This study investigates the influence of topographical parameters on landslide occurrences in the Thuligad watershed of Far-Western Province, Nepal

Study area

The study area is located within the Sudurpashchim Province, formerly known as the Far-Western Development Region of Nepal (Fig. 1). The area includes the Thuligad watershed within the Karnali sub-basin, spanning an area of 872.66 km². The elevation of the study area ranges from 252 to 2825 meters above sea level. The study area is situated within the Doti and Kailali Districts of Sudurpaschim Province, Nepal.

Geology and Geomorphology

The region is composed of two distinct geological sequences: the Sub-Himalayan (Siwalik) sequence and the Lesser Himalayan sequence (Fig.2). The geological map of the Thuligad watershed in the Siwalik region was developed in the field, although a comprehensive geological map of the Lesser Himalayan sequence is lacking. The southern, southwestern, and western regions of the study area are defined by the Siwaliks zone, which features extensive fragile sedimentary successions of mudstone and sandstone, characterized by upward coarsening sequences (Gansser, 1964). The main boundary thrust (MBT) delineates the separation between the Siwalik and Lesser Himalayan zone, running parallel to the Thuligad River. The region is profoundly shaped by tectonic movements and vigorous rock weathering mechanisms. The Siwalik group within the study area is categorized lithologically into two formations: Lower Siwalik and Middle Siwalik, arranged in ascending order according to their lithology (Fig. 2). The study area encompasses two primary thrusts: the Main Boundary Thrust (MBT) and the Thuligad Thrust (TT). A significant number of landslides have occurred on the steep slopes surrounding the thrust region. The Main Boundary Thrust region is highly susceptible to landslide in the Nepal Himalaya (Paudyal and Maharjan, 2022). Some of the representative landslides near the thrust zone are shown in the Figure 3. The Lower Siwalik is composed of fine-grained sandstone and mudstone, with thicknesses varying from ten centimeters to meters, occurring in nearly equal proportions (Dhital, 2015). The Middle Siwalik is characterized by substantial bedded, multistoried, pepper and salt sandstone, interspersed with notably thick gray mudstones. The majority of the sandstones exhibit a dark grey-green hue, characterized by a medium to fine grain size, and are interspersed with subtle gray to gray-green shale (Dhital, 2015). This study area comprises a significant quantity of dolomite and limestone at the upper boundary of the Middle Siwaliks. The Lesser Himalaya within the study area is composed of limestone and low-grade metamorphic rocks, including pink dolomite, grey slate, phyllite, and quartzite.

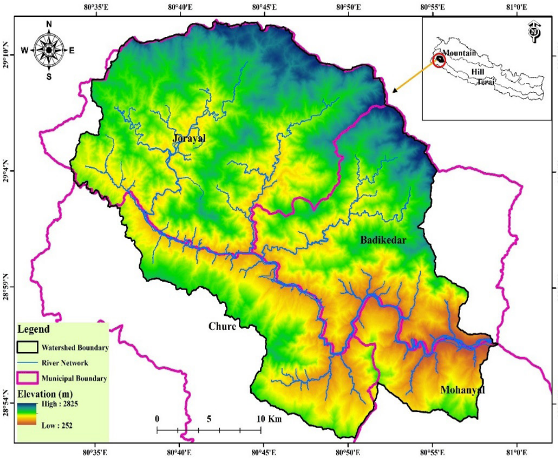

Fig.1: Location map of study area

The morphology of area is dynamically changing due to landslides, frequent flash floods and debris flows (Dhital, 2015). The north eastern part of the region is characterized by steep slope, which attains the highest elevations and exhibits the steepest topographies.

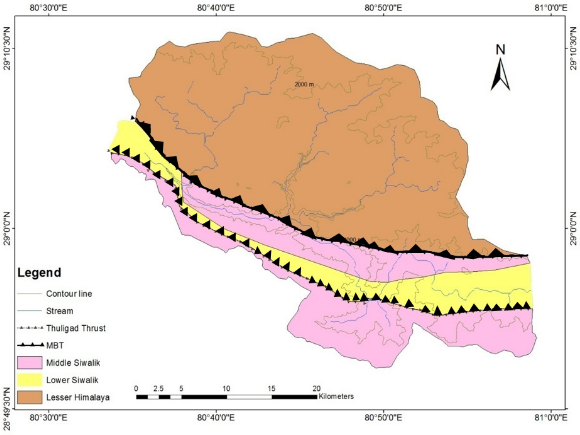

Fig. 2: General geological map showing the Siwalik and Lesser Himalayan sequences separated by Main Boundary Thrust (MBT)

CLIMATE

Temperature and precipitation fluctuate according to both seasonal changes and elevation. Data from meteorological and hydrological stations show that the average annual temperature in the Thuli Gad watershed is 23°C. The average maximum and minimum monthly temperatures vary from 5°C to 24°C during winter and from 21°C to 40°C in summer. The watershed exhibits a climatic gradient from subtropical conditions in the south to alpine characteristics in the north, with elevations ranging from 252 meters in the southern areas to 2825 meters in the northern regions. The study area commences in the Siwalik region and transitions through hilly terrain into mountainous regions. The watershed experiences a total annual rainfall of approximately 3017 mm, with an average of 2160 mm per year.

METHODS

Landslide inventory

The landslide inventory map of the study area was prepared by using utilizing satellite imagery sourced from Google Earth and Landsat having 30 m resolution, considering both spatial and temporal factors. The overlapping imagery was eliminated, characterized by significant cloud cover, blurring effects, or darkness, to enhance the interpretation of features related to landslides. The identified landslides were delineated by the polygon extending from the scar to the toe area. The generated traced map was acquired using GIS for spatial analysis, topological correction, and feature post-processing (Fig. 4). The area and summary statistics of the landslides were derived from the GIS analysis. Several field visits and onsite mapping were conducted to clarify the confusion sites.

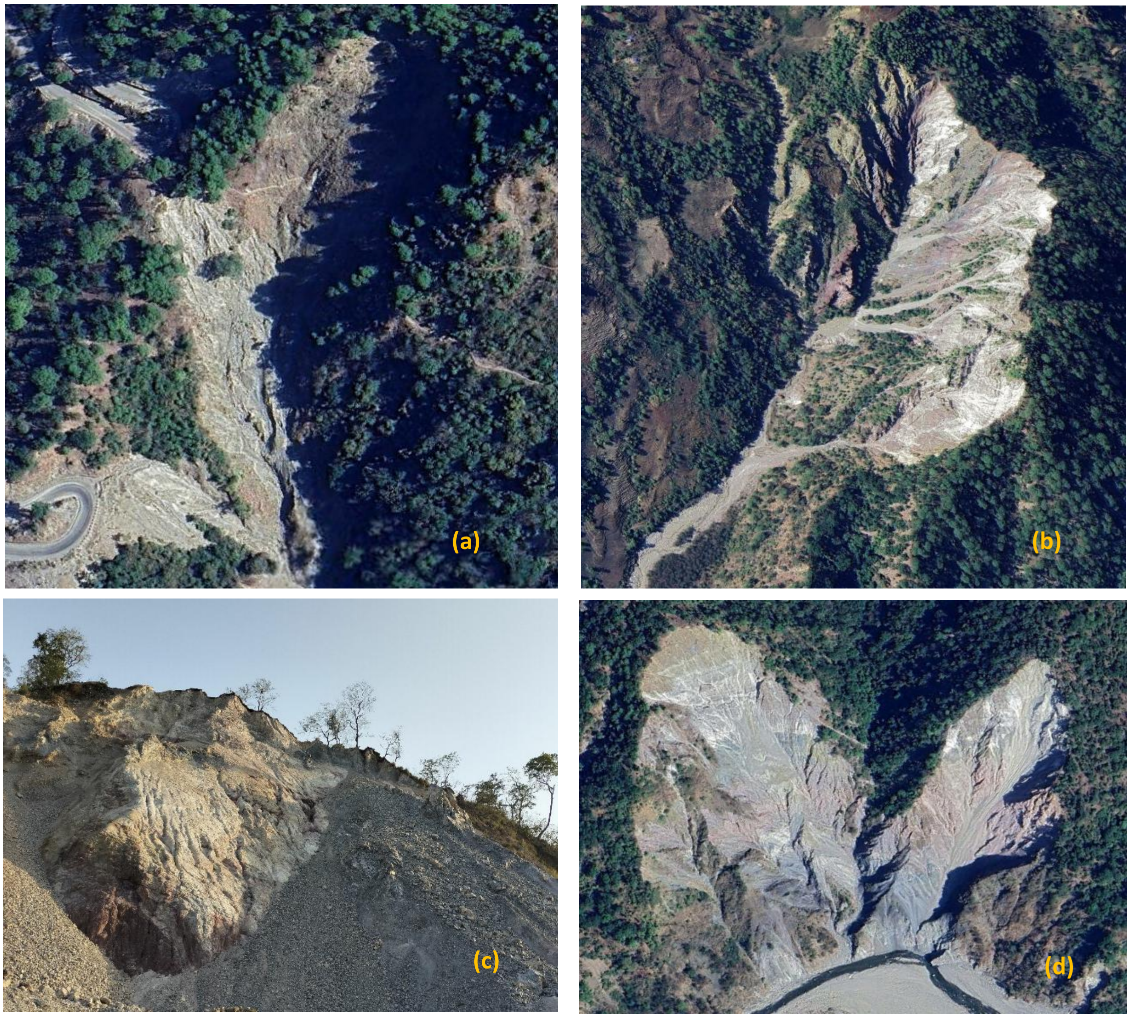

Fig.3: The four major active landslides occurred on the steep slope near the thrust zone

Field observation

A field survey was executed in the study area to validate the inventory map developed through satellite imagery analysis. A GPS (Garmin 60sx) was utilized to georeference and validate the landslide scars that were not discernible from the imagery. The locations of the landslides were represented through unique polygons and/or points that correspond to the scarps of the movements illustrated on the map. The observations conducted during fieldwork focused on slope gradient, position, curvature, and aspect, aiming to evaluate the role of topography as a significant factor in the incidence of landslides within the research area. The ancient scars presented a formidable challenge for classification, owing to the ambiguous shapes resulting from erosion and the encroachment of vegetation. A thorough analysis of the scars and depletion zones was undertaken to ensure accurate mapping. The interviews were conducted with certain key individuals to obtain additional insights concerning the date, scope, and nature of the movement.

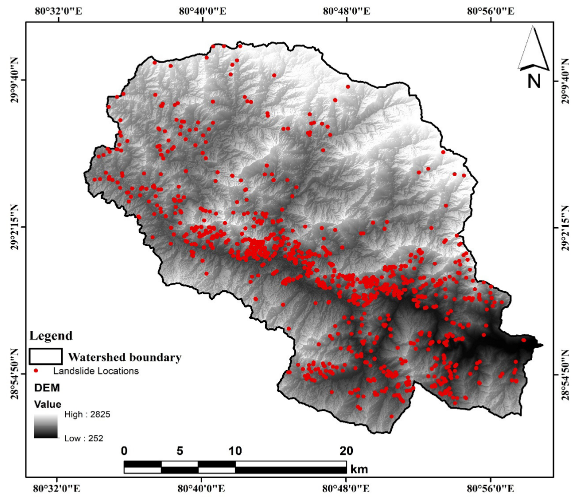

Fig. 4: Landslide inventory map of the Thuligad watershed

Topographical factors

A Digital Elevation Model (DEM) with a resolution of 12.5 m, obtained from the ALOSPALSAR website, was used to create an influencing factor map for landslides. The topographical factor maps such as slope, aspect, Topographic Wetness Index (TWI), curvature, and Stream Power Index (SPI) were obtained from the spatial analyst tool of ArcGIS.

Slope

The slope serves as a pivotal element, significantly influencing the occurrence of landslides. Slope failure generally arises from variations in shear stress along the slope, which are affected by gravitational forces. On any slope, there exist forces that facilitate movement downwards, alongside counteracting forces that impede such motion. Diverse forms of slope movements identified stem from conditions that compromise the stability of the slope, ultimately leading to displacement (Karimi et al., 2020). Mass wasting or sliding events occur with greater frequency on steep terrain in contrast to gentle slopes. The slope angle map was produced automatically in ArcGIS 10.8 utilizing a digital elevation model (DEM) with a grid cell size of 12.5 m. This map is categorized into five distinct ranges: 0-15, 15-30, 30-45, 45-60, and exceeding 60 degrees, reflecting the variations in terrain morphology (Bhandari et al., 2024) (Fig.5).

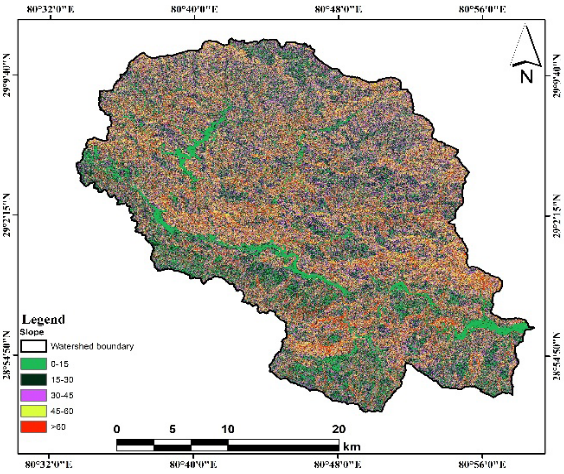

Fig. 5: Slope map of the Thuligad watershed, Far western province, Nepal

Aspect

Soil moisture patterns and regional physiographic trends are relevant to this feature. Its effects on weathering, plant life, and root growth are amplified by the way it changes the direction of evapotranspiration and frontal precipitation (Bhandari and Dhakal, 2020). Assessing geomorphologic stability is greatly influenced by slope aspect, which controls a variety of environmental variables including soil moisture, rainfall intensity, received radiation, and wind (dry and wet) (Huang, 2015). Based on the classification of natural breaks, the aspect map sorts aspects into nine groups: Flat, North, Northeast, East, Southeast, South, Southwest, West, and Northwest (Fig.6).

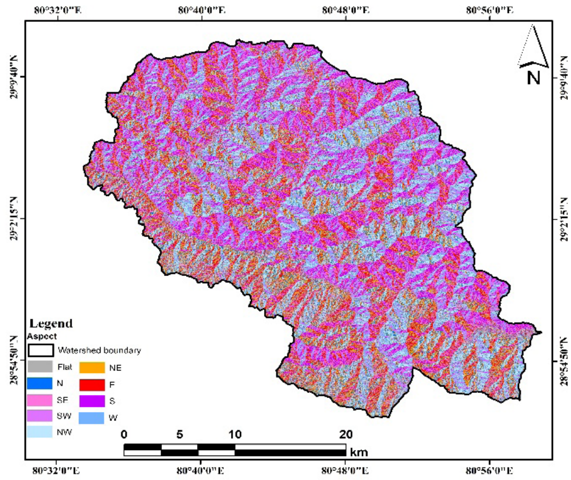

Fig. 6: Aspect map of the Thuligad watershed, Far western province, Nepal

Plane and Profile Curvature

The curvature is considered as the slope of the slope or second darivative of the slope. The Curvature tool available in the Spatial Analyst or 3D Analyst toolbox facilitates the creation of three distinct curvature: an output curvature, a profile curvature, and plan curvature. Profile curvature is aligned with the direction of the maximum slope. A negative value signifies that the surface exhibits upward convexity at that cell. A positive profile indicates that the surface is upwardly concave at that cell. A value of zero indicates that the surface is linear Profile curvature influences the acceleration or deceleration of flow over the surface. Both plane and profile Curvature values were classified into three classes (concave, flat (linear) and convex) based on the obtained raster class value (Fig.7 & 8). The area consists of more or less equal pixels of each curvature however, flat curvature seems dominant due to color contrast and uneven distribution of the curvature.

Topographic wetness index (TWI)

The TWI map was generated using GIS software and calculated with the formula TWI = ln (A / tanβ), utilizing a Digital Elevation Model (DEM) from ALOSPALSAR with a resolution of 12.5 meters. The thematic map displays the Topographic Wetness Index (TWI) values across a watershed, categorized into five ranges using the natural breaks classification method to indicate varying levels of soil moisture and potential for water accumulation. The TWI values are divided into the following ranges: -0.9 - 2.8, 2.8 - 4.8, 4.8 -7.5, 7.5-11.8, and 11.8- 26(Fig.9).

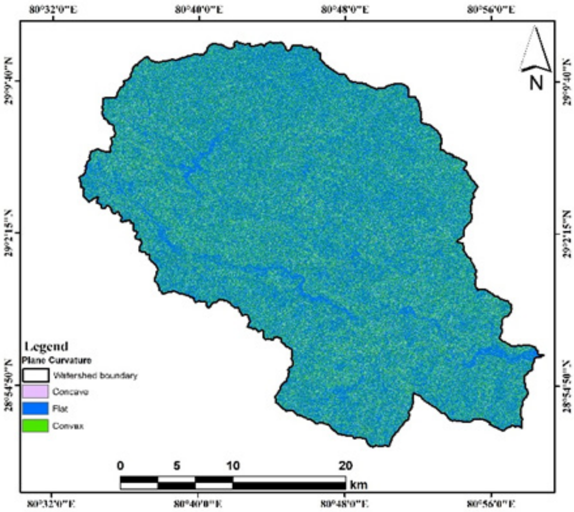

Fig. 7: Plan curvature map of the study area

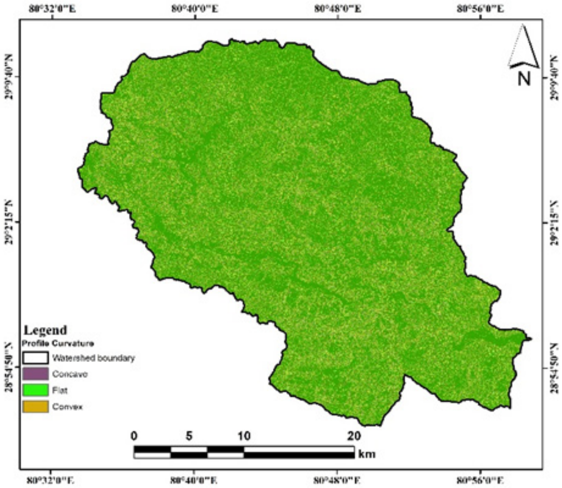

Fig. 8: Profile curvature map of the study area

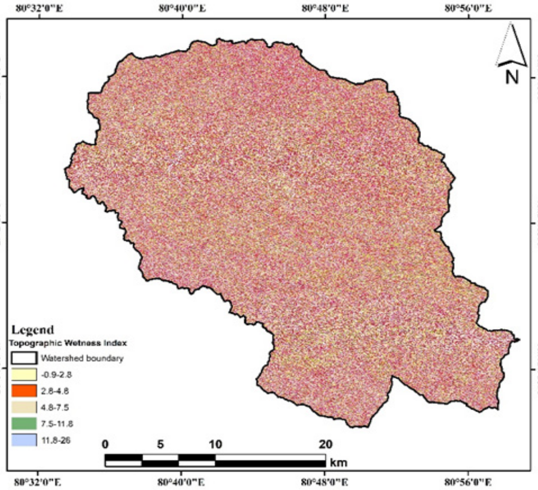

Fig. 9: Topographical wetness index map

Stream power index

The Stream Power Index (SPI) quantifies the erosive capacity of flowing water. The SPI is determined by the slope and the contributing area. SPI estimates potential locations for gully formation within the landscape. The thematic map displays the SPI values across a watershed, categorized into five ranges indicate varying levels of erosive power of flowing water. These colors help visualize areas within the watershed that experience different levels of erosion and sediment transport, with red indicating the lowest SPI and blue indicating the highest SPI (Fig. 10).

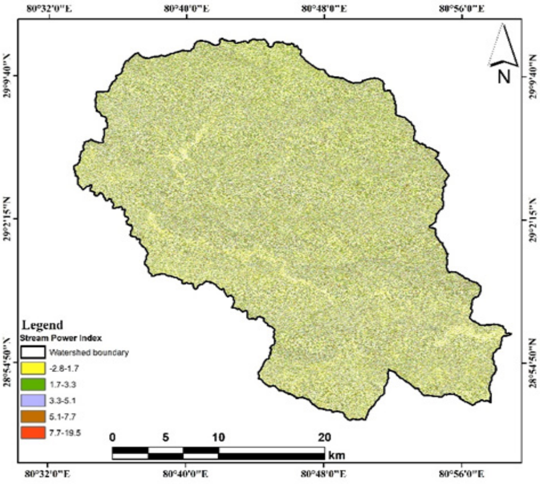

Fig. 10: Stream power index map of the study area

Landslide analysis

Various authors applied statistical index model for finding the correlation between landslides and causative factors (Cui et al., 2017; Firomsa et al., 2019, Cheng et al., 2022). The statistical index is a bivariate statistical method developed by van Westen (1997) for assessing landslide susceptibility (Pardeshi et al., 2013). This method defines a weighted value for a parameter class as the natural logarithm of the landslide density within the class divided by the landslide density throughout the entire map (Pradhan et al., 2012). Mezughi et al. (2011) demonstrate that the outcome generates a cross table, which is subsequently employed to calculate the density of landslides for each parameter class, with each causative or thematic map being separately overlaid and intersected with landslide inventory data. This study employs this method to establish the correlation between landslide occurrences and slope factors, thereby assessing the influence of topographical elements on landslide events. Pradhan et al. (2012) state that SIM is computed using the equation

$$Wij = \ln\left(\frac{fij}{f}\right) = \ln\left(\frac{\frac{Lij}{Aij}}{\frac{L*}{A*}}\right)$$

Where, Wij represents the weight value of category j of factor i, fij represents the landslide density in class j of factor i, f represents the landslide density in the entire study area, Lij represents the number of landslide units in class j of factor i, Aij represents the number of units contained in class j of factor i, L∗ represents the total number of landslide units in the study area, and A∗ represents the total number of units in the study area.

The Wij value signifies the correlation between the causal factors classification and landslide distribution.

So that this statistical index model is used in this study to identify the correlation between the classes of factors with the landslide density. A high weight value for a class implies a significant association between the causative elements and prior landslides, whereas a low weight value signifies a weak relationship. In the current investigation, Wij values of causal factors were computed. In the absence of landslide occurrences within a causative factor class, Wij is assigned a value of zero (van Westen, 1997). The causative factor maps were overlaid using landslide inventory data. The Wij values for the causative factor classes without relationships were not weighted (zero values were assigned).

RESULTS

The sub class of topographical factors and number of landslide as well as the area of landslides were obtained from the summary statistics of ArcGIS. The research investigates landslides in the Thuligad watershed through satellite imagery and field visits, identifying 1156 landslides in total.

Topographical distribution of landslide

We acquired the statistical index values and landslide density for each class of factors. Table 1 presents the SI value and landslide density for each slope class where the SI value rose with the steepening of the slope. Only 47% of the area has a slope over 30 degrees, although it covered roughly 73% of landslides area on it. Only 15% of landslides area lied on slopes between 15 and 30 degrees, while only 2% occur on slopes less than 15 degrees. The Figure 11 illustrates the percentage of area occupied by slope class and landslide. On slopes over 60^{o}, the density of landslides is highest however, the landslide percentage in total is highest between the slopes 30^{o} to 45^{o}. The landslide percentage on the slope greater than 60^{o} is lowest indicates that the landslide number decreased on the slope greater than 45^{o} however, the overall result signifies that the percentage of land having slope greater than 45^{o} is less in the study area. In case of landslide density, it is highest on the slope greater than 60^{o}. This result indicates that the landslides are mainly controlled by slope in the study area. Similarly, the statistical index values increased with increasing the slope. The landslide intensified as the slope increased. Steep slopes typically reduce the incidence or extent of landslides, as the steep region may be smaller than other classifications. However, density analysis can yield a more accurate assessment of slope stability in landslides. The area of the slope class is smaller than other classes, but the area of the landslide is larger when considering the landslide class area ratio. The percentage of landslide density has markedly risen with the elevation of the slope.

The four major landslides that are located in the same regions and have a similar rainfall pattern and geology but slope angle exceeded 30^{o} are shown in the figure 12. The mechanisms of landslide initiation are comparable on slopes that are similar.

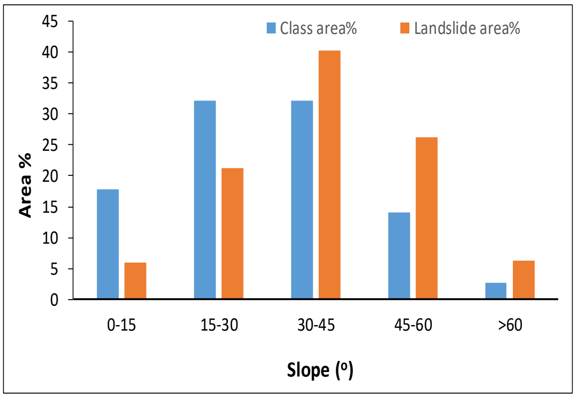

Fig. 11: The distribution of slope class percentage and landslide percentage on the particular classes

The topographical wetness index demonstrated an inverse relationship with landslides. The SI value and landslide density decreased with an increase in TWI value. Increased TWI levels correlate with a reduction in the frequency of landslides. In the lowest TWI class (-0.9 to 2.8), the SI value is 0.061; in contrast, in the highest TWI class (7.5 to 11.8), the SI value is -0.004.

The results indicate that the southern, southeastern, and southwestern aspects exhibit a higher susceptibility to landslides. The SI values for the southern, southeastern, and southwestern aspects surpass those of the other aspects. The north, northeast, and northwest aspects show significantly lower SI values, suggesting a decreased susceptibility to landslides in the studied area. Concave and convergent curvatures exhibit a greater susceptibility to landslides, attributed to their significantly elevated SI values in comparison to convex, divergent, and planar surfaces. The results of plan and profile curvature are similar. The SPI range of (-2.8-1.7) corresponds to a SI of -0.001; the range of (1.7-3.3) has a SI value of 0.537; the range of (3.3-5.1) shows a SI of 1.105; the range of (5.1-7.7) indicates a SI value of 1.212; and the range of (7.7-19.5) presents a SI value of 1.751. The SI value has increased in conjunction with the rising SPI.

Number based landslide distribution on the topography

The incidence of landslides escalated with the slope angle, peaked between 30° and 45°, and thereafter diminished beyond 45°(Fig.13). The landslide distribution curve is more likely to follow a normal distribution.

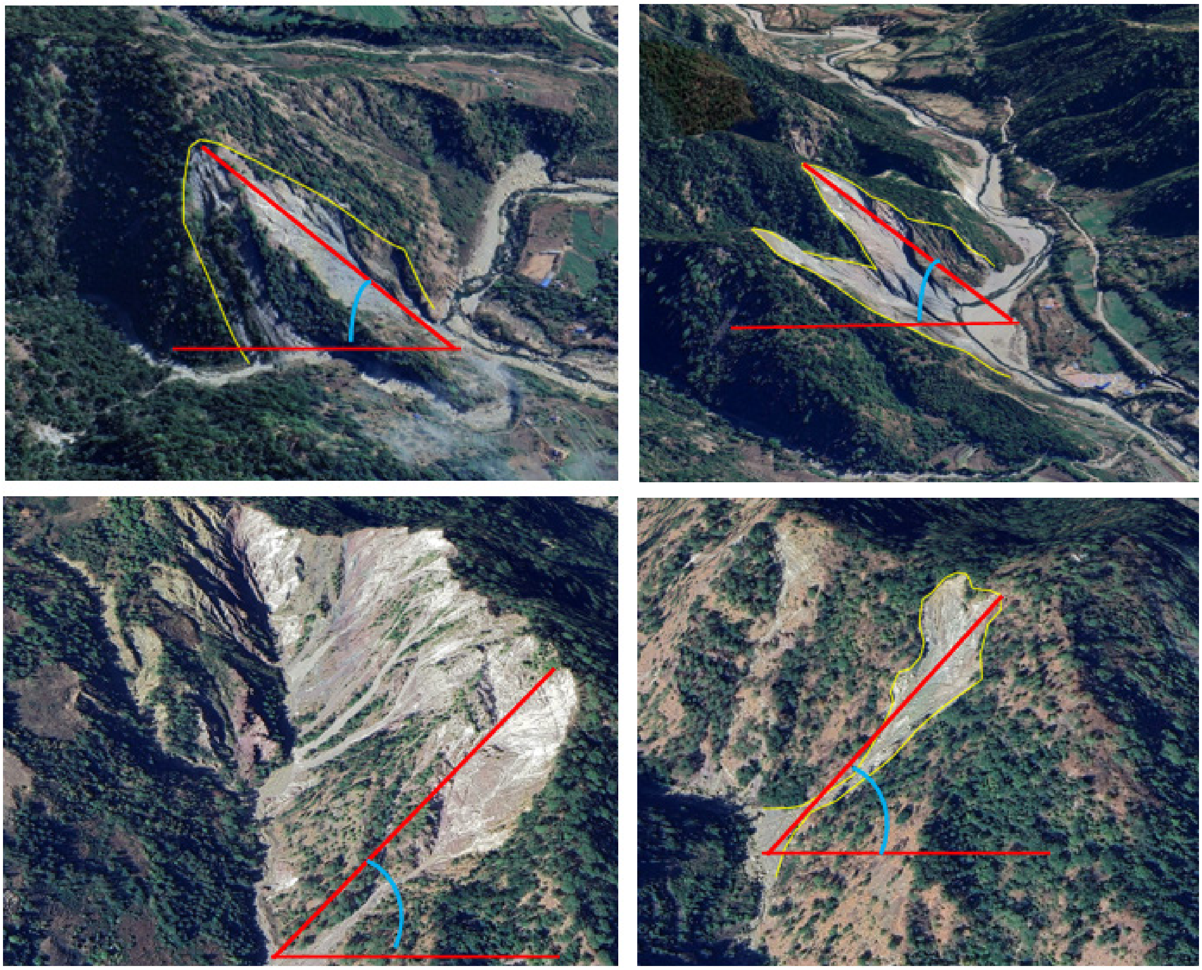

Fig.12: The slope control landslides form four different locations in the study area

Table 1: Landslide density and SI value in the different factors classes

Factors	Class	Class pixel	Landslide pixel	Landslide density	Statistical Index
Slope	0-15	8334816	6647	0.0081	-0.481
	15-30	15033101	23859	0.0163	-0.180
	30-45	14995626	45042	0.032	0.096
	45-60	7032186	29365	0.042	0.240
	>60	1268508	7095	0.056	0.367
	(-0.9-2.8)	18987256	52282	0.245	0.061
TWI	2.8-4.8	17039500	33452	0.195	-0.086
	4.8-7.5	7446831	19077	0.180	-0.029
	7.5-11.8	2698667	6424	0.145	-0.004
SPI	(-2.8-1.7)	25256789	43366	0.0017	-0.001
	1.7-3.3	9778201	23787	0.0024	-0.537
	3.3-5.1	5866302	19903	0.0033	1.105
	5.1-7.7	3845670	14267	0.0037	1.212
	7.7-19.5	1934567	10087	0.0052	1.751
Aspect	North	6576674	6274	0.0493	-0.397
	Northeast	6055454	5659	0.0483	-0.408
	East	5509576	12594	0.1183	-0.022
	Southeast	5864100	22028	0.1944	0.193
	South	5904078	26742	0.2344	0.276
	Southwest	5879987	18513	0.1629	0.117
	West	5368486	10655	0.1027	-0.080
	Northwest	5505882	9543	0.0897	-0.142
Profile curvature	(-531- -22)	3450803	11471	0.0033	0.141
	(-22-11)	34997953	75231	0.0021	-0.047
	11-686	8249477	15306	0.003	0.106
Plan curvature	(-841.8--21.7)	2101993	7958	0.0037	0.1981
	(-21.7-3.8)	28850891	64875	0.0022	-0.0281
	3.8-785.7	15745349	39175	0.0024	0.0158

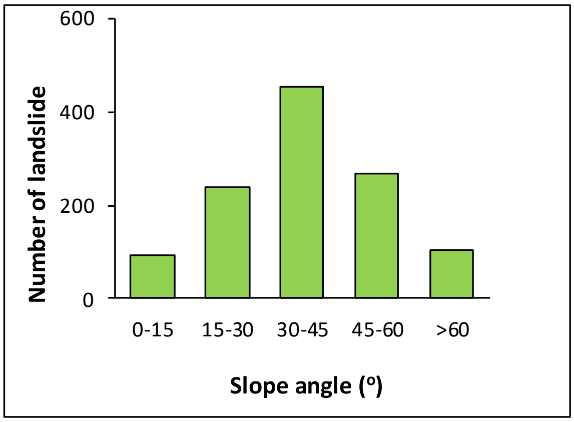

Fig.13: Distribution of landslide on the of slope classes

The incidence of landslides is significantly higher on concave slopes compared to convex and planar slopes (Fig.14).

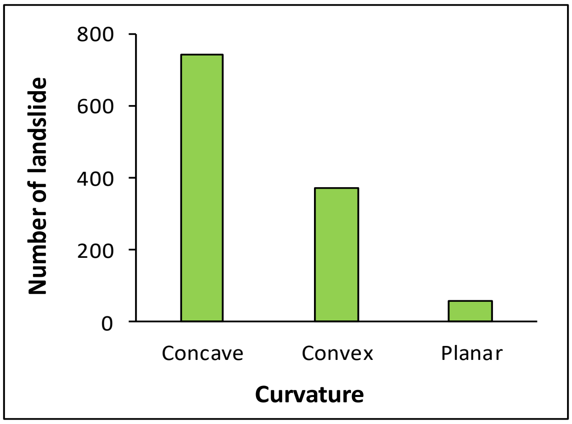

Fig.14: Distribution of landslide on the curvature

Likewise, the incidence of landslides on the southern side is markedly greater than that on other aspects.

Both the field observation and model-based results exhibited comparable outcomes. Likewise, the decadal temporal inventory map indicated that the frequency of landslides is greater on slopes ranging from 30° to 45°.

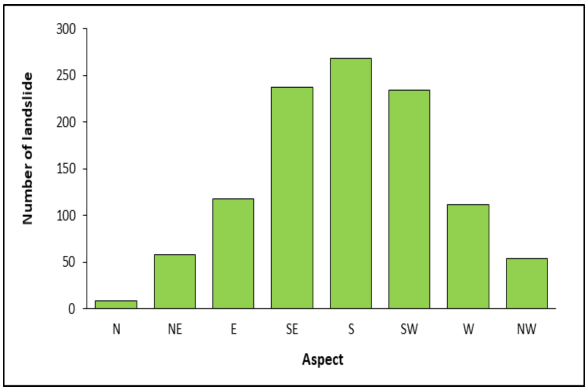

Fig. 15: Distribution of landslide on the aspect

Temporal slope distribution

The overall number of landslides from 2010 to 2024 was derived from the temporal landslide inventory mapping over three years. The temporal inventory maps were superimposed on the slope map in ArcGIS. The total number of landslides was quantified for the specific slope pixel, hence determining the landslide count for that slope. The temporal distribution of landslides on the slope revealed that the frequency of landslides is greater on slopes ranging from 30° to 45° across various years. Every three years, the incidence of landslides is markedly higher on slopes between 30° and 45°, and considerably lower on slopes below 15° and above 60°. Nonetheless, the results of landslide density indicated that it is increased on slopes greater than sixty degrees. The frequency of landslide events increased with the steepening of the slope. The surface area above the slope class 60° is smaller compared to other slope classes. The area of the slope class 30° to 45° is significantly greater in the study area so that the landslide distribution is also greater. The year wise distribution of landslide form 2010 to 2024 is shown in the figure 11.

Size based slope distribution

Landslide sizes were categorized into five classifications: very small, small, medium, large, and very large (Bhandari and Dhakal, 2019). The size of the landslides were determined based on the area.

Bhandari and Dhakal (2019) classify landslides as follows: less than 100 m² is very small, 100 to 1,000 m² is small, 1,000 to 10,000 m² is medium, 10,000 to 100,000 m² is large, and greater than 100,000 m² is very large. The total number of landslides across various slopes was evaluated, and the distribution of landslides according to their sizes within specific slope classes is illustrated in Figure 16.

The medium-sized landslide is prevalent on slopes greater than 15 degrees. Very small landslides are predominantly observed on the slopes less than 15 degrees. Distribution of both very large and very small landslides are limited on slopes between 30 and 45 degrees. A higher incidence of very large landslides was observed on slopes greater than 60°. A significant number of landslides occurred solely on slopes exceeding 30 degrees; however, the majority of large sized landslides are found on slopes greater than 60 degrees.

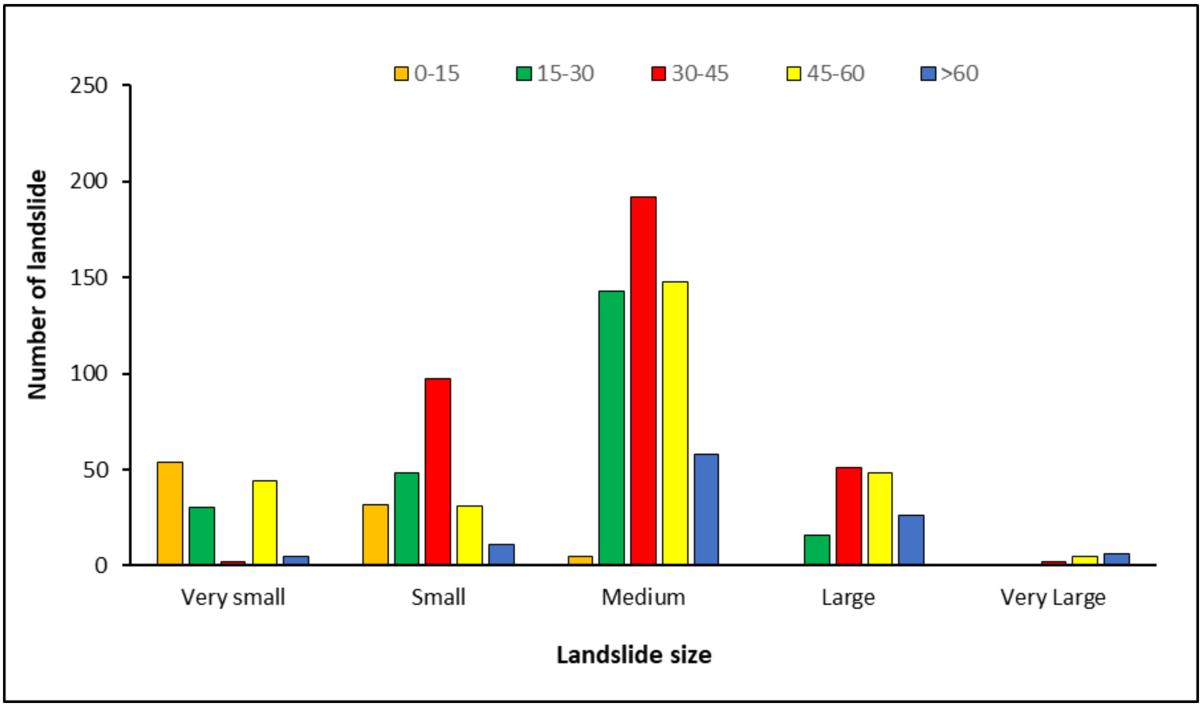

Fig.16: Size based landslide distribution on the slopes

A notably higher frequency of very small landslides was observed on slopes ranging from 30° to 45°, while the occurrence of large and very large landslides is more prevalent on slopes exceeding 45°. The findings indicated that the slope determines the extent of the landslide.

DISCUSSION

The presence of little streams on the slope, generated by rainwater drainage, indicates the number of dissections in the natural slope. The drainage pattern of these streamlets is dendritic. In the study region, haphazard road construction is a major issue that contributes to soil erosion and landslides. The Budar-BP Nagar highway is located in the Siwalik region and traverses the highly fractured dolomite and slate that mark the boundary between the Siwalik and the Lesser Himalaya. Forest fires are another major problem in the study region, so the deforestation issue is growing. Vegetation on slopes no longer serves its protective purpose due to deforestation and changes in land use caused by urban development. Deforestation and unmanaged agriculture on the steep slope are causing a huge amount of soil loss. Loss of soil-stabilizing root systems can make erosion worse and landslides more likely (Singh et al., 2021). Changes in land use within the research area may have significantly impacted slope stability. Unregulated development activities, particularly road construction and building settlement, accelerated this shift in land use.

The stability of slopes is greatly affected by their shape, gradient, and configuration, which are measured and analyzed in slope morphometry. Slopes in the Thuligad watershed generally face south and have an average angle of 27 degrees. Erosion and the formation of numerous rill and gullies are consequences of first and second-order streams cutting over the slopes during times of high discharge during the wet seasons. Between 250 and 1850 meters is the altitude of the areas. Gravitational forces acting on soil and rock are directly affected by the slope angle, according to studies. Saturated conditions, in particular, increase the risk of failure as the slope angle rises (Ghosh et al., 2020). Landslides tend to be more common on steeper slopes. A concave pattern is visible on the slope. Failures occur as a consequence of increased pore pressure caused by water collected on the concave slopes (Sharma et al., 2019). Similarly, the region's small hills, valleys, and overhangs can change the way silt accumulates and drains, which can affect the likelihood of landslides. Slope collapse and increased saturation can occur when water collects in nearby concave (Lee et al., 2022). Microclimates, shaped by the slope aspect, impact soil moisture levels and plant growth. While the majority of the area's slopes face northeast, southeast, and southwest, the number of landslides is highest in the southeast, southwest, and southwest directions. Furthermore, the presence of several springs, seepages, and puddles on the slope suggests that the water table is quite shallow in the area. The shear strength of the materials that constitute the slope was greatly diminished as the slope angle increased, which in turn affected the soil erosion and landslide. In a similar vein, increasing the slope angle affected surface runoff and weathering by increasing the shear stress of the slope materials. Additionally, landforms have been significantly damaged and landslides have increased due to the careless construction of roads on the geologically fragile slope. Because it alters natural drainage patterns and adds soil stress, road development on a slope can destabilize the slope. Landslides can occur when excavation techniques and heavy machinery are used on slope surfaces, as they can disturb the geological stability (Gupta et al., 2021). Soil surface conditions have been worsened by recent changes in vegetation cover, which have increased insufficient water pressure, undermined slope stability, and made rainwater interception more difficult.

Bhandari and Dhakal (2019b) conducted a study on the influence of topography on gully-type landslides within the Malai River catchment in Nepal, emphasizing the considerable impact of the topographical factor “T” on landslide occurrences. In that work, the authors further elucidated the synergistic influence of slope and geological factors on the initiation of landslides. Bhandari et al. (2024), Thapa and Bhandari (2019), Pokharel and Bhandari (2019), Ayer and Bhandari (2024), Paudyal et al. (2024) and Paudyal and Maharjan (2023) established a correlation between topographical factors and landslide pixels. Bhandari and Dhakal (2020) examined the correlation between landslides and topographical factors within the Babai River watershed in Nepal, highlighting the substantial influence of topography in the occurrence of landslides. Nakileza and Nedala (2022) studied topographical influences on the landslide characteristics of Mt. Elgon, Uganda and highlighted the outcome as the topography play significant role to control landslide mechanism. The authors further highlighted the relation between the slope and hydrological processes so that the development of the landslide becomes faster in the weak geological conditions. Knapen et al. (2006) highlighted that slope segments that are steep, plan concave, and oriented to the prevalent rainfall direction are the most sensitive to mass movement. The movement occurs at a particular distance from where the water divide. This was the case for slope segments that meet all of these criteria.

The distribution of landslides is significantly related to land surface and morphometric features, according to Nugraha et al. (2015). In the Tinalah watershed, for example, they found that landslides typically occur at an elevation greater than 400 m.a.s.l., on slopes that are 20 degrees, oriented east to west, and with a flat curvature. According to them, the topographical factors show the effects together and control the landslide mechanism. Dahle et al. (2011) studied the spatial distribution of debris-slides and noted that the spatial distribution of debris slides are determined by the aspect, slope angle, stream density, plan curvature, and altitude. According to research conducted by Nseka et al. (2019), a greater frequency of landslides occurred on slopes ranging from 25 degrees to 35 degrees in the western highlands of Uganda. According to Bizimana and Sonmez, (2015), the locations that are most susceptible to landslides are those that have slope angles that are greater than 14 degrees on convex slopes and greater than 41 degrees on concave slopes. In the Democratic Republic of the Congo, Depicker et al. (2018) found that the slope threshold was 24.8 degrees, however in South Africa, slopes ranging from 21 degrees to 30 degrees had the highest landslide frequency. On the other hand, Zhuang et al. (2015) discovered that the largest density of landslides, specifically 51.81 percent, was found in a higher slope range of 15–40 degrees. Shear forces that act on the hillside are controlled by the slope gradient (Silalahi et al., 2019), and as a result, slopes that are steeper are more likely to be affected by these forces. In the present study, the result shows that the landslides are mostly controlled by slope. Paudyal et al. (2021) noted that the southern aspect having slope greater than 20o is more susceptible to cause landslide in the terrains of Farwestern Nepal. Zhuang et al. (2015) reported that landslide occurrences are numerous at areas with convex and concave surfaces. According to Regmi et al. (2014) debris flows are more likely to take place in areas of topographic convergence that are covered by unconsolidated deposits. The majority of rock slides take place on slopes that are steep and convex to planar. Many researchers reported that the concave curvature is highly prone to landslide in the Himalaya. The flow type landslide is very common on the concave slope. The topographic wetness index (TWI) exposes the diversity and complexity of the topographic surface of landslides. It does this by identifying zones of preferential drainage within the landslide body as well as comparatively dry areas within its limits. Low TWI values are generally observed in the top regions of landslides, particularly steep head. For landslides that are created in slope hollows and are launched as shallow slides, the relationship between the depletion zone and low TWI is less obvious. Timalsina and Bhandari (2024), along with Bhandari et al. (2024) and Ayer and Bhandari (2024), have documented the inverse relationship between TWI class and landslide pixels. Their findings indicate that the landslides pixel diminishes as the TWI value rises.

The SPI measures the erosive capacity of flowing water by considering both the drainage area and the local slope. Moore et al. (1993) illustrated the efficacy of SPI in delineating areas of concentrated water flow and erosion potential, which has a direct impact on landslide hazard assessment. Tarolli et al. (2012) demonstrated a significant correlation between SPI and the initiation of channels as well as erosion hotspots in steep mountainous regions due to fast flowing water. Reichenbach et al. (2018) demonstrated through a comprehensive global review that SPI is often incorporated into data-driven models of landslide susceptibility. A multitude of researchers have underscored the affirmative relationship between the stream power index and landslides occurring on slopes. Timalsina and Bhandari (2024) elucidated the robust correlation between SPI and landslides at the catchment scale because stream power index is one of the major hydrological factor to cause landslide. This study reveals a significant correlation between the SPI and landslide occurrences within the examined region. Elevated SPI values manifest at the confluence of steep slopes and extensive contributing areas. The characteristics of these locations frequently exhibit elevated water discharge and velocity, thereby augmenting the potential for erosion. The erosion of slopes at their base, commonly referred to as toe erosion, caused by hydrological action of streams can significantly diminish slope stability, potentially leading to the occurrence of rotational or translational landslides. SPI delineates regions susceptible to gully formation, which may develop into more profound incised features. The presence of these gullies serves to concentrate runoff, thereby exacerbating local erosion and compromising the stability of the adjacent slope. In steep catchments, elevated SPI zones may align with the origins of debris flows, particularly following periods of intense precipitation or snowmelt. SPI serves as a valuable tool for modeling the trajectories of debris flow and assessing the potential for sediment yield.

CONCLUSION

This study revealed the impact of topographical factors on triggering landslides within the Thuligad watershed of Sudurpaschim Province, Nepal. The development of the topographical factors map, including slope, aspect, topographical wetness index, stream power index, and plan and profile curvature, was executed using ArcGIS. The results indicate that slope is crucial in landslide occurrence, with a significant increase in landslide density associated with an elevation in slope angle. The gradient between 30 and 45 degrees is most prone to landslides in the research area. The reduction in the statistical index value as TWI rises indicates an inverse correlation between TWI and landslides. The study area has multiple gullies and inclines over 15 degrees, leading to an increased stream power index. The incidence of landslides increased in response to the elevated stream power index. The concave slope demonstrates significant sensitivity in the research area, with a higher incidence of landslides recorded in this terrain relative to the convex slope. The southern aspect, marked by a slope angle more than 30 degrees and a concave contour, resulted in an increase in the SPI. The TWI increases as one nears the hill's base and persists while ascending until its peak. The comprehensive findings suggest that topographical elements together regulate landslide activities. This investigation may aid in comprehending the topography's influence on landslides in analogous places of Nepal. It offers both basic and specialized information regarding slope management for landslides, thus enabling local planners and designers to create roads in a scientific manner.

REFERENCES

ADB, 2017, Country poverty analysis (detailed) Nepal, Asia Development Bank. https://www.adb.org/sites/default/files/linked-documents/cps-nep-2013-2017-pa-detailed.pdf. Accessed 24 June 2020.

Ayer, P. B. and Bhandari, B. P., 2024. Landslide Susceptibility Mapping Using Frequency Ratio and Weight of Evidence Models in Purchaudi Municipality, Baitadi District, Nepal, *Nepal Journal of Environmental Science*, *12*(2), 59-72.

Bhandari, B. P. and Dhakal, S., 2018. Lithological control on landslide in the Babai Khola watershed, Siwaliks zone of Nepal, *American Journal of Earth Sciences*, *5*(3), 54-64.

Bhandari, B. P. and Dhakal, S., 2019a. Evolutional characteristics of debris flow in the Siwalik

Hills of Nepal, *International Journal of Geosciences*, *10*(12), 1049.

Bhandari, B. P. and Dhakal, S., 2019b. Topographical and geological factors on gully-type debris flow in Malai River catchment, Siwaliks, Nepal, *Journal of Nepal Geological Society*, *59*, 89-94.

Bhandari, B. P. and Dhakal, S., 2020. Spatio-temporal dynamics of landslides in the sedimentary terrain: a case of Siwalik zone of Babai watershed, Nepal, *SN Applied Sciences*, *2*, 1-17.

Bhandari, B. P. and Dhakal, S., 2021. A multidisciplinary approach of landslide characterization: A case of the Siwalik zone of Nepal Himalaya, *Journal of Asian Earth Sciences: X*, *5*, 100061.

Bhandari, B. P., Dhakal, S. and Tsou, C. Y. 2024. Assessing the prediction accuracy of frequency ratio, weight of evidence, Shannon entropy, and information value methods for landslide susceptibility in the Siwalik Hills of Nepal, *Sustainability*, *16*(5), 2092.

Bizimana, H. and Sönmez, O., 2015. Landslide occurrences in the hilly areas of Rwanda, their causes and protection measures, *Disaster Science and Engineering*, *1*(1), 1-7.

Broothaerts, N., Kissi, E., Poesen, J., Van Rompaey, A., Getahun, K., Van Ranst, E. and Diels, J., 2012. Spatial patterns, causes and consequences of landslides in the Gilgel Gibe catchment, SW Ethiopia, *Catena*, *97*, 127-136.

CBS, 2016. Annual household survey report 2014-15. Central Bureau of Statistics - National Planning Commission Secratariat, Government of Nepal, UNDP. Thapathali, Kathmandu, Nepal 120 pp

Chamlagain, D. and Dangol, V., 2002. Landslide hazard evaluation in and around the Ilam Hydropower Project, Eastern Nepal Himalaya, *Journal of Nepal Geological Society*, *27*, 131-143.

Cheng, C., Yang, Y., Zhong, F., Song, C. and Zhen, Y., 2022. An optimization of statistical index method based on Gaussian process regression and geodetector, for higher accurate landslide susceptibility modeling, *Applied Sciences*, *12*(20), 10196.

Cui, K., Lu, D. and Li, W., 2017. Comparison of landslide susceptibility mapping based on statistical index, certainty factors, weights of evidence and evidential belief function models, *Geocarto International*, *32*(9), 935-955.

Dahal, R. K., 2014. Regional-scale landslide activity and landslide susceptibility zonation in the Nepal Himalaya, *Environmental Earth Sciences*, *71*, 5145-5164.

Dahal, R. K., Hasegawa, S., Bhandary, N. P., Poudel, P. P., Nonomura, A. and Yatabe, R.,2012. A replication of landslide hazard mapping at catchment scale, *Geomatics, Natural Hazards and Risk*, *3*(2), 161–192. https://doi.org/10.1080/19475705.2011.629007

Dahal, R. K., Hasegawa, S., Nonomura, A., Yamanaka, M., Dhakal, S. and Paudyal, P., 2008. Predictive modelling of rainfall-induced landslide hazard in the Lesser Himalaya of Nepal based on weights-of-evidence, *Geomorphology*, *102*(3-4), 496-510.

Dahl M.P.J., Mortensen, L.E., Jensen, N.H. and Veihe, A., 2011. Magnitude–frequency characteristics and preparatory factors for spatial debris-slide distribution in the northern Faroe Islands, Geomorphology 188(2013):3–11

Depicker, A., Govers, G., Van Rompaey, A., Havenith, H.B., Mateso, J.C.M. and Demitte, O., 2018. Landslides in a changing tropical environment: North Tanganyika-Rift Kivu zones. https://www.researchgate.net/publication/325176935

Dhital, M. R., 2015. Geology of the Nepal Himalaya: Regional Perspective of the Classic Collided Orogen. Berlin: Springer. https://doi.org/10.1007/978-3-319-02496-7

Fernandes, N. F., Guimarães, R. F., Gomes, R. A., Vieira, B. C., Montgomery, D. R. and Greenberg, H., 2004. Topographic controls of landslides in Rio de Janeiro: field evidence and modeling, *Catena*, *55*(2), 163-181.

Firomsa, M. and Abay, A., 2019. Landslide assessment and susceptibility zonation in Ebantu district of Oromia region, western Ethiopia, *Bulletin of Engineering Geology and the Environment*, *78*, 4229-4239.

Froude, M. J. and Petley, D. N., 2018. Global fatal landslide occurrence from 2004 to 2016, Nat. Hazards Earth Syst. Sci., 18, 2161–2181, https://doi.org/10.5194/nhess-18-2161-2018.

Gansser, A., 1964. Geology of the Himalayas. Wiley Inter Science, New York, 289

Gerrard, J, 1994. The landslide hazard in the Himalayas: geological control and human action. In *Geomorphology and natural hazards* (pp. 221-230).

Ghosh, T., Bhowmik, S., Jaiswal, P., Ghosh, S. and Kumar, D.,2020. Generating substantially complete landslide inventory using multiple data sources: a case study in Northwest Himalayas, India, *Journal of the Geological Society of India*, *95*(1), 45-58.

Giuseppe, F., Simoni, S., Godt, J. W., Lu, N. and Rigon, R., 2016. Geomorphological control on variably saturated hillslope hydrology and slope instability, *Water Resources Research*, *52*(6), 4590-4607.

Gupta, V., Kumar, S., Kaur, R. and Tandon, R. S., 2022. Regional-scale landslide susceptibility assessment for the hilly state of Uttarakhand, NW Himalaya, India. *Journal of Earth System Science*, *131*(1), 2.

Hasegawa, S., Dahal, R. K., Yamanaka, M., Bhandary, N. P., Yatabe, R. and Inagaki, H., 2009. Causes of large-scale landslides in the Lesser Himalaya of central Nepal, *Environmental geology*, *57*, 1423-1434.

Hennrich, K. and Crozier, M. J., 2004. A hillslope hydrology approach for catchment-scale slope stability analysis, *Earth Surface Processes and Landforms: The Journal of the British Geomorphological Research Group*, *29*(5), 599-610.

Huang, R., 2015. Understanding the mechanism of large-scale landslides, In *Engineering Geology for Society and Territory-Volume 2: Landslide Processes* (pp. 13-32). Springer International Publishing.

Hung, C., Liu, C. H. and Chang, C. M., 2018. Numerical Investigation of Rainfall-Induced Landslide in Mudstone Using Coupled Finite and Discrete Element Analysis, *Geofluids*, *2018*(1), 9192019.

Karimi-Sangchini, E., Emami, S. N., Shariat-Jafari, M., Rezazadeh, F. and Raeisi, H., 2020. Landslide hazard zonation using multivariate statistical models in the Doab Samsami watershed, Chaharmahal Va Bakhtiari Province, Iran, *Jordan J Earth Environ Sci*, *11*, 174-182.

Knapen, A., Kitutu, M. G., Poesen, J., Breugelmans, W., Deckers, J. and Muwanga, A., 2006. Landslides in a densely populated county at the footslopes of Mount Elgon (Uganda): characteristics and causal factors, *Geomorphology*, *73*(1-2), 149-165.

Lee, J. U., Cho, Y. C., Kim, M., Jang, S. J., Lee, J. and Kim, S., 2022. The effects of different geological conditions on landslide-triggering rainfall conditions in South Korea. *Water*, *14*(13), 2051.

Manchado, A. M. T., Ballesteros-Cánovas, J. A., Allen, S. and Stoffel, M., 2022. Deforestation controls landslide susceptibility in Far-Western Nepal, *Catena*, *219*, 106627.

McAdoo, B. G., Quak, M., Gnyawali, K. R., Adhikari, B. R., Devkota, S., Rajbhandari, P. L. and Sudmeier-Rieux, K., 2018. Roads and landslides in Nepal: how development affects environmental risk, *Natural Hazards and Earth System Sciences*, *18*(12), 3203-3210.

Mezughi, T. H., Akhir, J. M., Rafek, A. G. and Abdullah, I., 2011. Landslide susceptibility assessment using frequency ratio model applied to an area along the EW highway (Gerik-Jeli), *American Journal of Environmental Sciences*, *7*(1), 43.

Moore, I. D., Gessler, P. E., Nielsen, G. A. E. and Peterson, G. A., 1993. Soil attribute prediction using terrain analysis, *Soil science society of america journal*, *57*(2), 443-452.

Mugagga, F., Kakembo, V. and Buyinza, M., 2012. A characterization of the physical properties of soil and the implications for landslide occurrence on the slopes of Mount Elgon, Eastern Uganda. *Natural hazards*, *60*, 1113-1131.

Muñoz-Torrero Manchado, A., Allen, S., Ballesteros-Cánovas, J.A., Dhakal, A., Dhital, M. R. and Stoffel, M., 2021. Three decades of landslide activity in western Nepal: new insights into trends and climate drivers. *Landslides* 18, 2001–2015 (2021). https://doi.org/10.1007/s10346-021-01632-6

Nakileza, B. R., Mugagga, F., Musali, P. and Nedala, S., 2022. Assessment of Landslide susceptibility and risk to road network in Mt Elgon, Uganda.

Nseka, D., Kakembo, V., Bamutaze, Y. and Mugagga, F., 2019. Analysis of topographic parameters underpinning landslide occurrence in Kigezi highlands of southwestern Uganda, *Natural Hazards*, *99*, 973-989.

Nugraha, H., Wacano, D., Dipayana, G. A., Cahyadi, A., Mutaqin, B. W. and Larasati, A., 2015. Geomorphometric characteristics of landslides in the Tinalah watershed, Menoreh Mountains, Yogyakarta, Indonesia, *Procedia Environmental Sciences*, *28*, 578-586.

Pardeshi, S. D., Autade, S. E. and Pardeshi, S. S., 2013. Landslide hazard assessment: recent trends and techniques, *SpringerPlus*, *2*, 1-11.

Paudyal, K. R., Maharjan, R. and Shrestha, B., 2024. Landslide susceiptibility mapping of the main boundary thrust region in Thungsingdanda-Bandipur section of Nawalparasi and Palpa Districts, Gandaki and Lumbini Provinces, Nepal, The Geographical Journal of Nepal. Vol. 17:23-52, 2024. DOI: https://doi.org/10.3126/gjn.v17i01.63934.

Paudyal, K.R. and Maharjan, R., 2023. Landslide susceptibility mapping of the Main Boundary Thrust region in Mandre-Khursanibari section of Arghakhanchi and Palpa districts, Lumbini province of Nepal, Nepalese Journal of Environmental Science, 11(2),35-53; https://doi.org/10.3126/njes.v11i2.58152

Paudyal, K. R., Devkota, K.C., Parajuli, B.P., Shakya, P. and Baskota, P., 2021. Landslide Susceptibility Assessment using open-source data in the far western Nepal Himalaya: A case study from selected local level units, *Journal of Institute of Science and Technology,* 26(2), 31-42 (2021) *ISSN: 2467-9062 (print),e-ISSN:2467-9240*. https://doi.org/10.3126/jist.v26i2.41327.

Paudyal K. R. and Maharjan R., 2022. Landslide susceptibility mapping of the Main Boundary Thrust (MBT) region in Tinau-Mathagadhi Section of Palpa District, Lumbini Province, Journal of Nepal Geological Society, vol. 63, pp. 99–108. *https://doi.org/10.3126/jngs.v63i01.50845*

Pokhrel, K. and Bhandari, B. P., 2019. Identification of Potential Landslide Susceptible Area in the Lesser Himalayan Terrain of Nepal, Journal of Geoscience and Environment Protection, 7, 24-38. https://doi.org/10.4236/gep.2019.711003

Pradhan, A. M. S., Dawadi, A. and Kim, Y. T.,2012. Use of different bivariate statistical landslide susceptibility methods: a case study of Khulekhani watershed, Nepal, *Journal of Nepal Geological Society*, *44*, 1-12.

Regmi, A.D., Yoshida, K., Pourghasemi, H.R., DhitaL, M. R. and Pradhan, B., 2014. Landslide susceptibility mapping along

Bhalubang — Shiwapur area of mid-Western Nepal using frequency ratio and conditional probability models, *J. Mt. Sci.* 11, 1266–1285 (2014). https://doi.org/10.1007/s11629-013-2847-6

Reichenbach, P., Rossi, M., Malamud, B. D., Mihir, M. and Guzzetti, F., 2018. A review of statistically-based landslide susceptibility models, *Earth-science reviews*, *180*, 60-91.

Sharma, K. K., Bhandary, N. P., Subedi, M. and Rajan, K. C., 2025. Integration of Landslide Susceptibility and Road Infrastructure Vulnerability for Risk Assessment and Mountain Road Resilience Enhancement, *Indian Geotechnical Journal*, 1-17.

Sharma, S. and Mahajan, A. K., 2019. A comparative assessment of information value, frequency ratio and analytical hierarchy process models for landslide susceptibility mapping of a Himalayan watershed, India, *Bulletin of Engineering Geology and the Environment*, *78*, 2431-2448.

Silalahi, F. E. S., Pamela, Arifianti, Y. and Hidayat, F., 2019. Landslide susceptibility assessment using frequency ratio model in Bogor, West Java, Indonesia, *Geoscience Letters*, *6*(1), 10.

Singh, A., Pal, S. and Kanungo, D. P., 2021. An integrated approach for landslide susceptibility–vulnerability–risk assessment of building infrastructures in hilly regions of India, *Environment, Development and Sustainability*, *23*(4), 5058-5095.

Sudmeier-Rieux, K., McAdoo, B., Devkota, S., Rajbhandari, P. C. L., Howell, J. and Sharma, S., 2019. Invited perspectives: mountain roads in Nepal at a new crossroads, Nat Hazards Earth Syst Sci 19:655–660

Talebi, A., Uijlenhoet, R. and Troch, P. A., 2008. Application of a probabilistic model of rainfall-induced shallow landslides to complex hollows, *Natural Hazards and Earth System Sciences*, *8*(4), 733-744.

Tarolli, P., Sofia, G. and Dalla Fontana, G., 2012. Geomorphic features extraction from high-resolution topography: landslide crowns and bank erosion, *Natural Hazards*, *61*, 65-83.

Thapa, D. and Bhandari, B., 2019. GIS-Based Frequency Ratio Method for Identification of Potential Landslide Susceptible Area in the Siwalik Zone of Chatara-Barahakshetra Section, Nepal, *Open Journal of Geology*, 9, 873-896. doi: 10.4236/ojg.2019.912096.

Thapa, D. and Bhandari, B. P., 2019. GIS-Based frequency ratio method for identification of potential landslide susceptible area in the Siwalik zone of Chatara-Barahakshetra section, Nepal, *Open Journal of Geology*, *9*(12), 873.

Thapa, P. B., Phuyal, B. and Shrestha, K. K., 2023. Spatial variability of slope movements in central and western Nepal Himalaya: Evaluating large-scale landslides to cut-slopes, *Journal of Nepal Geological Society*, *65*, 183-194.

Timalsina, A. and Bhandari, B. P., 2024. Hydrological influences of the landslide mechanisms: insight into the Aakhu Khola Watershed, Dhading District, Nepal, *Journal of Nepal Hydrogeological Association*, *1*, 67-78.

Tsou, C. Y., Chigira, M., Higaki, D., Sato, G., Yagi, H., Sato, H. P., Wakai, A., Dangol, V., Amatya, S.C. and Yatagai, A., 2018. Topographic and geologic controls on landslides induced by the 2015 Gorkha earthquake and its aftershocks: an example from the Trishuli Valley, central Nepal, *Landslides*, *15*, 953-965.

UNFCO, 2012. An overview of the Far Western Region of Nepal. United Nations Field Coordination Office (UNFCO) Dadeldhura, Nepal, Transition Support Strategy, RCHC Office, Nepal Worldpop (2020) WorldPop: population counts. In: Worldpop.org. https://www.worldpop.org/project/categories?id=3. Accessed 23 Sep 2020.

Van Westen, C. J., 1997. Statistical landslide hazard analysis. *Ilwis*, *2*, 73-84.

Zhang, J. Q., Liu, R. K., Deng, W., Khanal, N. R., Gurung, D. R., Murthy, M. S. R.and Wahid, S., 2016. Characteristics of landslide in Koshi River basin, central Himalaya, *Journal of Mountain Science*, *13*, 1711-1722.

Zhuang, J., Peng, J., Iqbal, J., Liu, T., Liu. N., Li, Y. and MA, P., 2015. Identification of landslide spatial distribution and susceptibility assessment in relation to topography in the Xi'an Region, Shaanxi Province, China, Front Earth Sci 9(3):449–462. https://doi.org/10.1007/S11707-014-0474-3

.

Journal of Nepal Hydrogeological Association (JNHA), Vol (2), 112-126 (2025)
ISSN: 3059-9725 (Online)
https://doi.org/10.3126/jnha.v2i1.85385

RESEARCH ARTICLE

Physicochemical characterization and aquaculture suitability of Taudaha Lake, Kathmandu, Nepal

Samichhya Poudel and *Indira Parajuli
Central Department of Environmental Science, Tribhuvan University, Kirtipur, Nepal
**Corresponding Author: indira.parajuli@cdes.tu.edu.np*

***(Submission Date**: 27 May, 2025; **Accepted Date:** 22 August, 2025)*

ABSTRACT

Taudaha Lake, the only natural lake in Kathmandu, Nepal, was studied to evaluate its potential for aquaculture following the Nepal Water Quality Guidelines for Aquaculture (NWQGA, 2015). The study aimed to characterize physicochemical parameters, determine hydrochemical processes, and assess suitability for fish farming. Ten water samples were collected during January 2024 from strategically selected sites around Taudaha Lake, including inflow and outflow points as well as accessible locations along the lake boundary. In-situ measurements included temperature, pH, dissolved oxygen (DO), electrical conductivity (EC), and total dissolved solids (TDS). Laboratory analyses measured total hardness, alkalinity, major cations (Ca^{2+}, Mg^{2+}, Na^+, K^+), anions (Cl^-, SO_4^{2-}, HCO_3^-), and nutrients (ammonia, phosphate) following APHA-AWWA-WEF (2017) standard methods. Results indicated that most parameters, including temperature (15.9–17.2 °C), pH (7.45–7.92), TDS (211–223 mg/L), phosphate (0.018–0.188 mg/L), and ammonia (0.030–0.097 mg/L), were within NWQGA limits, supporting cold and intermediate water fish species. However, DO levels (2.76–5.54 mg/L) were below recommended thresholds, and total hardness (98–150 mg/L) exceeded optimal limits potentially limiting fish growth and reproduction. Geochemical analyses using Piper, Gibbs, and mixing diagrams revealed a mixed Ca^{2+}–Mg^{2+}–Cl^-–SO_4^{2-} hydrochemical facies dominated by silicate and carbonate weathering with minimal anthropogenic influence. Overall, Taudaha Lake shows moderate aquaculture suitability. Long-term water quality monitoring, management of nutrient inputs, and maintenance of adequate oxygen levels are recommended to improve fish productivity while preserving the lake's ecological and cultural values.

Keywords: ***Taudaha lake, Water quality, Aquaculture, Physicochemical, Hydrochemistry***

INTRODUCTION

Wetlands and lakes are vital freshwater ecosystems that support biodiversity, provide essential ecosystem services such as water purification, flood regulation, and carbon sequestration, and sustain human livelihoods (Keddy, 2010; Zedler and Kercher, 2005). These ecosystems are also directly important for human activities such as aquaculture, where the physical, chemical, and biological characteristics of water critically influence ecological health and support the optimal growth, survival, and productivity of aquatic species (Boyd, 2017; Shaltami and Bustany, 2021).

Water quality in lakes and wetlands is influenced by natural processes including rainfall, rock weathering, and evaporation, as well as anthropogenic activities such as agricultural runoff and wastewater discharge (Pant et al., 2019; Paudyal et al., 2016). Monitoring these parameters provides critical insights into ecosystem functioning, trophic status, and the suitability of water for aquaculture, domestic use, and irrigation.

Taudaha Lake, the only natural lake in central Nepal, is situated at 1350 m above sea level (27°38.88' N, 85°17.05' E), approximately 10 km from Kathmandu city. Covering 4 hectares with a mean depth of 3 m, the lake has cultural, spiritual, and ecological significance, including providing habitat for birds, fish, and aquatic plants. It receives inflow from surrounding agricultural fields and discharges via a permanent outlet, with its water managed by the Karkotak Nagraja Nagrani Resident Restoration Society (KNNRRS) (Pradhananga et al., 2013). Despite its ecological and cultural importance, there is limited information on its water quality and suitability for aquaculture particularly under the pressures of urbanization and seasonal changes.

This study was conducted during January 2024 (winter season) to evaluate the physicochemical characteristics of Taudaha Lake and its suitability for aquaculture according to the Nepal Water Quality Guidelines for Aquaculture (NWQGA, 2015). Sampling in winter provides insight into water quality during a season of lower rainfall and reduced inflow, which may concentrate minerals and influence dissolved oxygen levels. Ten water samples were collected during January 2024 from strategically selected sites around Taudaha Lake, including key inflow and outflow points, as well as other accessible boundary locations, with replicate samples taken to ensure reliability. Hydrochemical analysis, including Gibbs, Piper, and mixing diagrams, were used to understand the natural and anthropogenic factors controlling water chemistry. The primary objectives of this study were to characterize the lake's water quality, assess its potential for aquaculture especially for cold and intermediate water fish species and identify geochemical processes influencing water chemistry. By linking water quality to aquaculture potential, this research aims to inform strategies for pollution control, nutrient management, and the sustainable use of Taudaha Lake while maintaining its ecological and cultural significance

MATERIALS AND METHODS

Study area

Taudaha Lake is located in Kirtipur Municipality-6 within the Kathmandu district of Nepal at an elevation of 1,291 meters above sea level (27º 38' 55.5" N, 85º 16' 54.8" E). The lake lies approximately 6 km southwest of central Kathmandu along the route to the Dakshinkali shrine. Although relatively small, covering an area of about 4 hectares, Taudaha Lake has an irregular shape with eight distinct corners and reaches a maximum depth of 6 meters. The lake has a single outflow and receives water mainly from two inlets, which are particularly active during the monsoon season. The surrounding catchment is a mix of agricultural fields, forest patches, and built-up areas reflecting a mosaic of land use and land cover typical of the suburban Kathmandu region. The geology of the area is predominantly composed of fluvio-lacustrine deposits, alluvium, and weathered bedrock, which influence the lake's hydrochemistry and sediment composition. The region experiences a subtropical climate with warm, wet summers and cool, dry winters, and receives most of its precipitation during the monsoon season (June to September).

Taudaha Lake provides essential habitat for a variety of flora and fauna, including numerous fish species, benthic macroinvertebrates, and approximately 118 bird species, many of which are migratory. Despite its ecological and cultural importance, the lake is under environmental stress from multiple sources. These include nutrient enrichment and eutrophication from agricultural runoff, sedimentation, encroachment from urban development, and limited management of wastewater and solid waste. Such pressures can alter the water quality affecting both biodiversity and the lake's potential for aquaculture. This study focuses on characterizing the physicochemical properties of Taudaha Lake and evaluating its suitability for aquaculture, taking into account the lake's hydrology, surrounding land use, and environmental stressors.

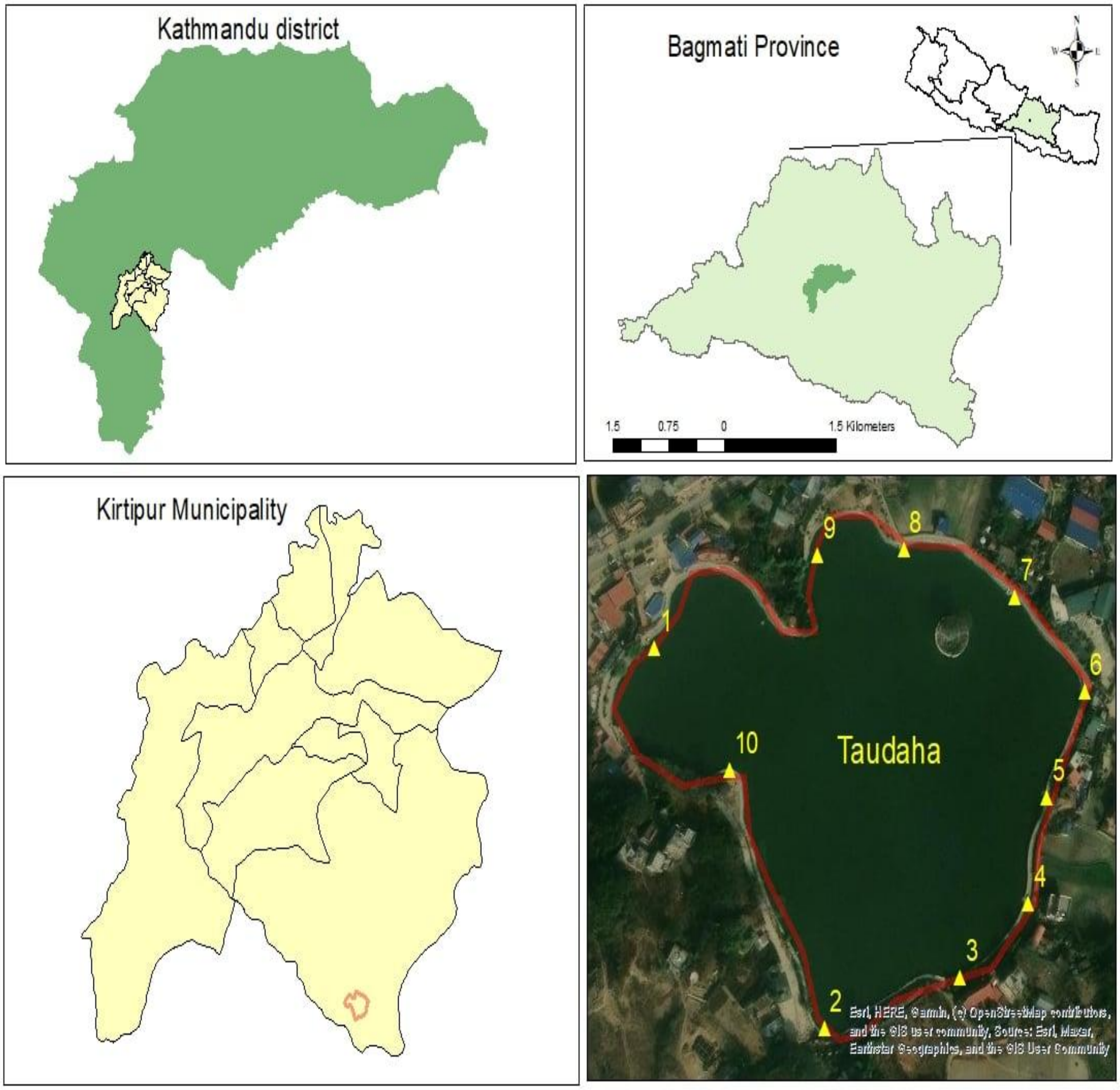

Esri, HERE, Garmin, (c) OpenStreetMap contributors, and the GIS user community, Source: Esri, Maxar, Earthstar Geographics, and the GIS User Community

Fig. 1: Map representing the study area with sampling stations

Research Methodology

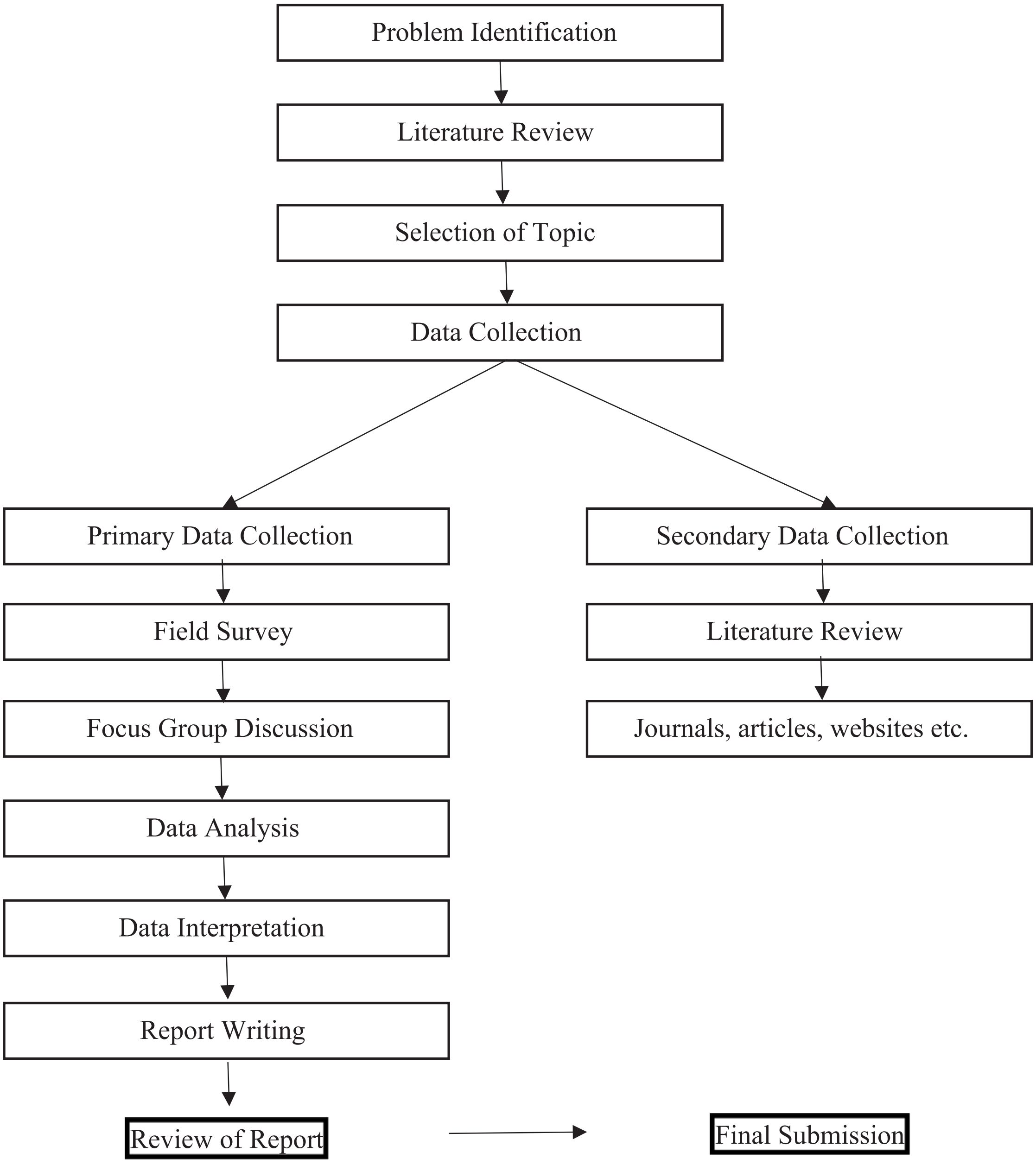

Fig. 2: Research methodology

Sampling and Physicochemical analysis

In January 2024, fieldwork and water sampling were conducted in Taudaha Lake which is located at an altitude of 1350 m. Following a purposive stratified sampling method, ten water samples were collected from strategically selected sites along the accessible paths and inflow/outflow points of the lake to capture spatial variability influenced by human activity and surrounding land use. Samples were collected from the surface layer (0.5 m depth) to ensure consistency and to target the zone most relevant to aquaculture species and water quality assessment. Each site was examined to ensure water samples were clear, uncontaminated, and free from debris, and sampling equipment was rinsed thoroughly with site water prior to collection to minimize contamination.

At each site, one-liter High-Density Polyethylene (HDPE) bottles were used for sample collection from the designated points along the lake's paths and shores. On-site measurements of water temperature (°C), pH, electrical conductivity (EC, µS/cm), and total dissolved solids (TDS, mg/L) were recorded immediately using a multiparameter probe. The instruments were calibrated according to manufacturer guidelines prior to field use with calibration checks performed every 24 hours and the relative error was maintained within ±2%.

Collected samples were transported in an ice bag to maintain a temperature close to 4°C and stored at 4°C in the laboratory until analysis. This precaution prevented changes in chemical characteristics prior to laboratory measurements. Laboratory analyses were carried out at the Central Department of Environmental Sciences, Tribhuvan University, Kirtipur, which was selected for its fully equipped facilities, trained personnel, and experience in freshwater quality analysis. In the laboratory, turbidity was measured using a turbidity meter. Major cations, sodium (Na^+) and potassium (K^+), were analyzed using a flame photometer (Wagtech Model 1382, UK). Dissolved oxygen (DO) was measured using a DO meter, and chemical oxygen demand (COD) was determined following standard APHA-AWWA-WEF (2017) methods. Other parameters, including chloride (Cl^-), total hardness (TH), alkalinity (HCO_3^-), and free CO_2, were evaluated using argentometric titration, EDTA titration, and acid-base titration with phenolphthalein indicator. Nutrients and trace elements, including ammonia (NH_4^+), nitrate (NO_3^-), sulphate (SO_4^{2-}), phosphate (PO_4^{3-}), and iron (Fe^{3+}), were measured using a UV-Visible spectrophotometer (SSI-UV2101, UK) following standard procedures (APHA-AWWA-WEF, 2017).

Quality assurance and control practices included duplicate sampling at select sites, calibration of instruments before and during analysis, procedural blanks, and the use of reagent-grade chemicals and uncontaminated bottles to prevent cross-contamination. These measures ensured the accuracy and reliability of the data, allowing for a comprehensive characterization of the physicochemical properties of Taudaha Lake and providing a robust basis for assessing its suitability for aquaculture and ecological management.

Table 1: Different parameters along with the methodology

S.N.	Parameters	Methods	Instruments
1	Temperature	Electrometric	Milwaukee pH55, Uk
2	Ph	Electrometric	Milwaukee pH55, Uk
3	EC	Electrometric	Milwaukee EC59, Europe
4	TDS	Electrometric	Milwaukee EC59, Europe
5	DO	Electrometric	Oxy 70 Vio Dissolved Oxygen Meter
6	Turbidity	Nephelometric	Wagtech(2100 AN Turbidity Meter)
7	Free-CO^2	Titrimetric (Sodium hydroxide method),	Conical flask, Measuring cylinder, Pipette, Burette and Burette stand
8	Chloride	Argentometric method	Conical flask, Measuring cylinder, Pipette, Burette and Burette stand
9	Total Alk	Titrimetric	Conical flask, Measuring cylinder, Pipette, Burette and Burette stand
10	Total Hardness	Titrimetric	Conical flask, Measuring cylinder, Pipette, Burette and Burette stand
11	Calcium Hardness	Titrimetric	Conical flask, Measuring cylinder, Pipette, Burette and Burette stand
12	Sodium	Microprocessor flame photometer	Flame Photometer(Model 1382)
13	Potassium	Microprocessor flame photometer	Flame Photometer(Model 1382)
14	Sulphate	Turbidimetric method	Spectrophotometer (SS1 UV 2101)
15	Phosphate	Ammonium Molybdate method	Spectrophotometer (SS1 UV 2101)
16	Ammonia	Nessler's Reagent Method	Spectrophotometer (SS1 UV 2101)
17	Iron	Phenonthroline method	Spectrophotometer (SS1 UV 2101)
18	BOD	Titrimetric	Conical flask, Measuring cylinder, Pipette, Burette and Burette stand
19	COD	Titrimetric	Conical flask, Measuring cylinder, Pipette, Burette and Burette stand

The laboratory analysis of physicochemical parameters were carried out as per APHA-AWWA-WEF (2017).

Data Analysis

Descriptive statistics including mean, standard deviation, minimum and maximum of all parameters using IBM SPSS 26. The results obtained from descriptive statistics analysis provides the overall hydrochemistry of the lake. Also, this analysis helps to compare spatial variation in water quality parameter as well as comparison with Nepal Water Quality Guidelines for Aquaculture (NWQGA).

Piper Diagram

A trilinear graphical tool for classifying the chemical properties of water is called a Piper diagram (Piper, 1944). Origin Pro22 software was used to construct this diagram, which has two distinct triangle plots, one for cations and the other for anions, and a diamond-shaped field in the middle that mixes the two. In water quality research, piper plots are frequently used to categorize water samples into six different hydrochemical groups according to their predominant ion composition. These types are as follows: 1) calcium-bicarbonate (Ca^{2+}-HCO_3^-), 2) sodium-chloride (Na^+-Cl^-), 3) mixed calcium-sodium-bicarbonate (Ca^{2+}-Na^+-HCO_3^-), 4) mixed calcium-magnesium-chloride (Ca^{2+}-Mg^{2+}-Cl^-), 5) calcium-chloride (Ca^{2+}-Cl^-), and 6) sodium-bicarbonate (Na^+-HCO_3^-) (Chalaune et al., 2020; Khadka and Ramanathan, 2021).

Gibbs Plot

Gibbs plots are used to evaluate the variables affecting the lake's water chemistry. The ratios of sodium to the sum of sodium and calcium [$Na^+/(Na^+ + Ca^{2+})$] and chloride to the sum of chloride and bicarbonate [$Cl^-/(Cl^- + HCO_3^-)$] are plotted against total dissolved solids (TDS) in this diagram. It helps in determining the main mechanisms governing the chemistry of water, including rock weathering, evaporation, and precipitation (Gibbs, 1970; Prasanna et al., 2011). Precipitation is the major controlling factor when samples show low TDS levels (about 300 mg/L) along with high ion ratios (0.5–1) (Pant et al., 2018).

Mixing Diagram

To better understand the hydrochemical changes, a mixing diagram was applied. This approach involved plotting molar ratios normalized to sodium (Na^+), such as calcium to bicarbonate (Ca^{2+}/HCO_3^-) and calcium to magnesium (Ca^{2+}/Mg^{2+}), to examine spatial variations in water chemistry. The study showed that the lake's water chemistry is mainly shaped by minerals coming from three sources: carbonates, silicates, and evaporites (Gaillardet et al., 1999)

RESULTS

Descriptive Statistics of Physiochemical parameters

Table 2 summarizes the minimum, maximum, mean, and standard deviation of water quality parameters in the winter season in Taudaha Lake. The total sample size is 10. It is also compared with the guideline's values for aquaculture.

Table 2: Descriptive statistics of hydrochemical variables

Parameters	Minimum	Maximum	Average	SD	Nepal Standard for Aquaculture (2015)
Temperature(°C)	15.9	17.2	16.68	0.4284	4-18 °C for cold water fish 16-32 °C for intermediate species. 4-30 °C for warm water fish.
pH	7.45	7.92	7.6	0.1331	6.5-9.0
DO(mg/l)	2.76	5.54	3.823	0.74121	6-9 mg/l for cold water species. 5-8 for intermediate water species 5-8 for warm water species
EC(µS)	344.5	374.6	360.64	9.23	
TDS(mg/l)	211.2	222.72	217.312	3.6357	<2000mg/l
Turbidity	85	236	153.3	47.36	<25NTU
Chloride(mg/l)	63.9	215.84	124.96	44.466	Value not recommended (fish can survive at <600 but the production is not optimum.
Alkalinity(mg/l)	170	225	199	16.093	
Ca-hardness(mg/l)	50	130	93	24.417	
Mg- hardness (mg/l)	20	74	36	16.97	<15mg/l
Total hardness(mg/l)	98	150	129	18.466	20-100mg/l
Free $C0_2$(mg/l)	17.6	33	26.62	3.990	
Sulphate (mg/l)	13.13	21.73	17.29	2.9117	
Phosphate(mg/l)	0.018	0.188	0.090	0.05037	
Ammonia(mg/l)	0.02981	0.0968	0.0612	0.01832	<30µg/l
Iron(mg/l)	0.243	0.26	0.2486	0.005589	<10µg/l
Sodium(meq/l)	19.7	24.9	22.06	1.3771	
Potassium(meq/l)	13.2	13.7	13.4	0.1612	
BOD(mg/l)	1.018	1.800	1.4628	0.247	
COD(mg/l)	60	256	141.6	65.292	<40mg/l

The physicochemical analysis of Taudaha Lake showed several important characteristics in relation to aquaculture suitability. Water temperature ranged from 15.9 to 17.2°C, with an average of 16.68°C which falls within the recommended range for cold-water fish species (4–18°C). The pH of the lake varied slightly between 7.45 and 7.92 (mean 7.6) indicating a neutral to slightly alkaline environment suitable for aquaculture (6.5–9.0). Dissolved oxygen (DO) levels ranged from 2.76 to 5.54 mg/L, averaging 3.82 mg/L, which is below the recommended 6–9 mg/L for cold-water fish and 5–8 mg/L for intermediate and warm-water species, suggesting potential oxygen limitation.

Electrical conductivity (EC) ranged from 344.5 to 374.6 µS/cm with a mean of 360.64 µS/cm, while total dissolved solids (TDS) averaged 217.31 mg/L (range 211.2–222.72 mg/L), both indicating low to moderate mineral content. Turbidity was high (85–236 NTU, mean 153.3 NTU), exceeding the recommended <25 NTU which may affect light penetration and aquatic productivity. Chloride concentrations varied from 63.9 to 215.84 mg/L (mean 124.96 mg/L), which is within tolerable limits for fish survival (<600 mg/L), though higher concentrations may reduce optimal production.

Alkalinity ranged from 170 to 225 mg/L (mean 199 mg/L), while calcium hardness (50–130 mg/L) and magnesium hardness (20–74 mg/L) were observed resulting in total hardness of 98–150 mg/L (mean 129 mg/L) exceeding the recommended range (20–100 mg/L) which could influence water buffering capacity and fish health. Free CO_2 levels averaged 26.62 mg/L (range 17.6–33 mg/L), and sulphate concentrations were low (13.13–21.73 mg/L, mean 17.29 mg/L). Nutrients such as phosphate (0.018–0.188 mg/L) and ammonia (0.0298–0.0968 mg/L) were generally within acceptable limits for aquaculture.

Trace elements, including iron (0.243–0.26 mg/L) and sodium (19.7–24.9 meq/L), as well as potassium (13.2–13.7 meq/L) were measured, with iron concentrations exceeding the recommended <10 µg/L for aquaculture indicating potential concern. Biological oxygen demand (BOD) ranged from 1.018 to 1.8 mg/L (mean 1.46 mg/L) suggesting low organic pollution while chemical oxygen demand (COD) was elevated (60–256 mg/L, mean 141.6 mg/L) exceeding the recommended <40 mg/L indicating the presence of oxidizable pollutants.

Overall, while Taudaha Lake's temperature, pH, and many nutrient levels are suitable for aquaculture, the low dissolved oxygen, high turbidity, elevated total hardness, and high COD highlight potential environmental limitations that would need to be managed to ensure sustainable fish farming.

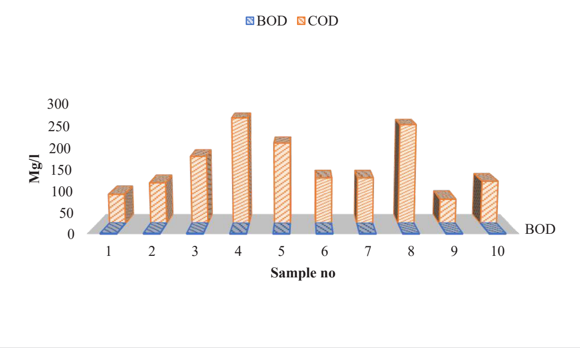

Fig. 3: Comparative representation of BOD and COD of water samples in Taudaha Lake

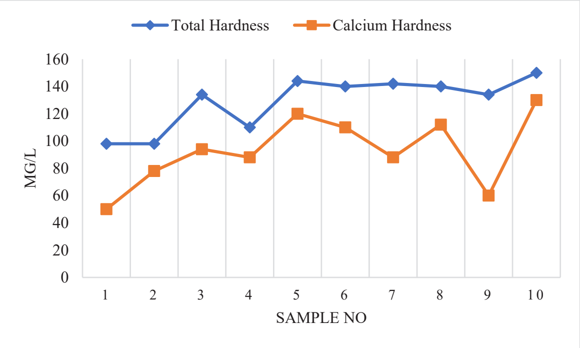

Fig. 4: Chart showing total hardness and calcium hardness of the water samples in Taudaha Lake

Hydrochemistry of Taudaha Lake

The Gibbs diagram is a valuable tool for unraveling the geochemical processes determining the chemistry of natural waters (Fig. 5). It can be used to identify whether it is precipitation, weathering of rocks, or evaporation controlling water chemistry. Two Gibbs plots are illustrated in the given figure: panel (a) is the plot of Total Dissolved Solids (TDS) against the ionic ratio $Na^+/(Na^+ + Ca^{2+})$, and panel (b) is the plot of TDS against $Cl^-/(Cl^- + HCO_3^-)$. These plots are utilized to classify the geochemical processes occurring in the water samples.

The blue dots in the two graphs represents the collected water samples. The majority of data points are within the rock dominance zone showing that the chemical characteristics of the water are mainly influenced by interactions with rocks. This indicates that minerals like carbonates and silicates especially are dissolving into the water from surrounding rocks, contributing to the ionic content. Because the samples do not group in the precipitation and evaporation areas, it is a sign that the two processes do not significantly affect water chemistry at this point. The moderate TDS values also support this as high evaporation would have resulted in elevated TDS concentrations. Therefore, the Gibbs diagram also confirms that mineral dissolution due to rock weathering is the governing factor controlling the composition of water

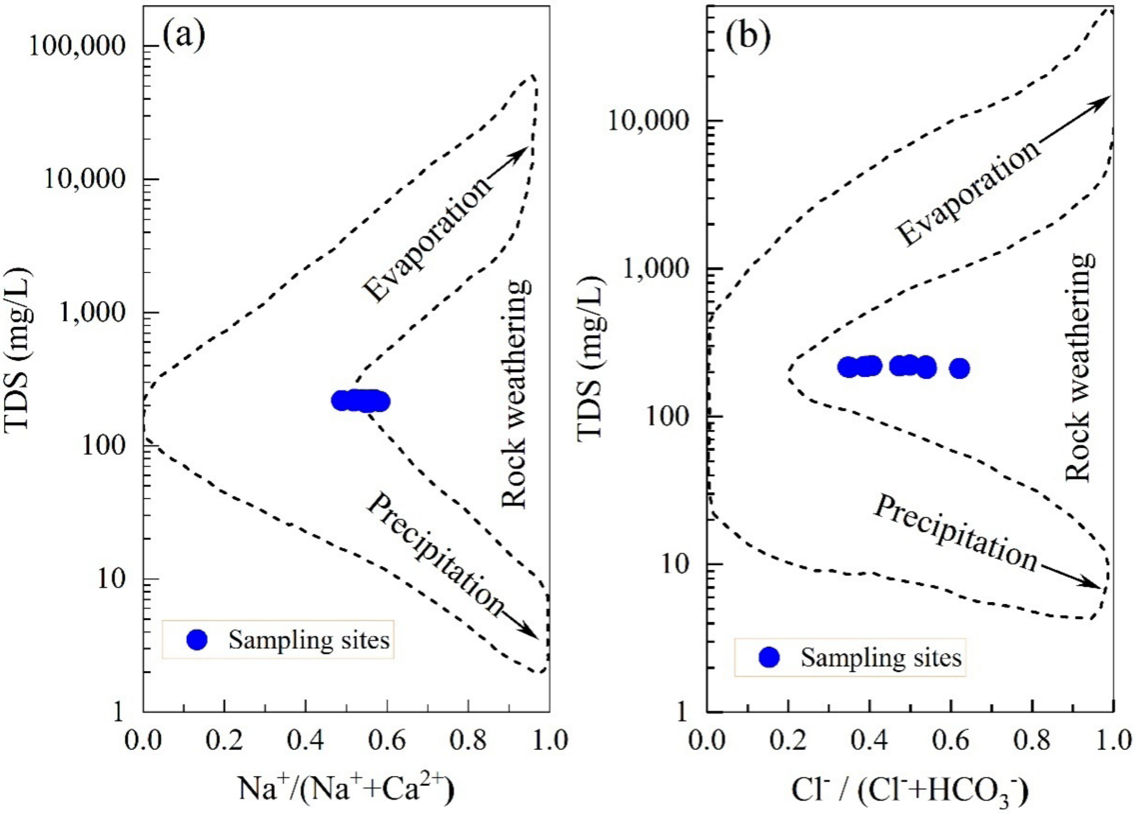

Fig. 5: Gibbs diagram showing (a) TDS vs. $Na^+/ (Na^+ + Ca^{2+})$ and (b) TDS vs. $Cl^-/(Cl^- + HCO^{3-})$ for Taudaha Lake, Nepal

Mixing diagram

Figure 6 shows the lithological controls on the water chemistry. The image displays two geochemical mixing diagrams. Panel (a) plots the bicarbonate to sodium ratio (HCO_3^-/Na^+) against calcium to sodium (Ca^{2+}/Na^+), and panel (b) plots the magnesium to sodium ratio (Mg^{2+}/Na^+) against Ca^{2+}/Na^+. These visual aids are useful for determining whether silicate, carbonate, or evaporite weathering is responsible for the predominant geochemical fingerprints in the water.

In both graphs, the plotted water samples (blue dots) are mostly clustered in the region representing silicate weathering. The presence of silicate weathering in which calcium and bicarbonate are produced during the decomposition of silicate minerals is suggested by panel (a)'s moderate HCO_3^-/Na^+ ratios (approximately ranging from 3 to 10) and Ca^{2+}/Na^+ values near 1. This interpretation is supported by Panel (b), which shows that silicate rock dissolution is the predominant source of dissolved ions due to the relatively low Mg^{2+}/Na^+ ratios and the intermediate Ca^{2+}/Na^+ values.

Additionally, areas showing carbonate or evaporite influence show little to no grouping, indicating that such lithologies have contributed very little. In conclusion, silicate weathering is the dominant geochemical activity influencing the water chemistry in the region as indicated by the arrangement of the data points in these diagrams which reflects the basin's lithological composition.

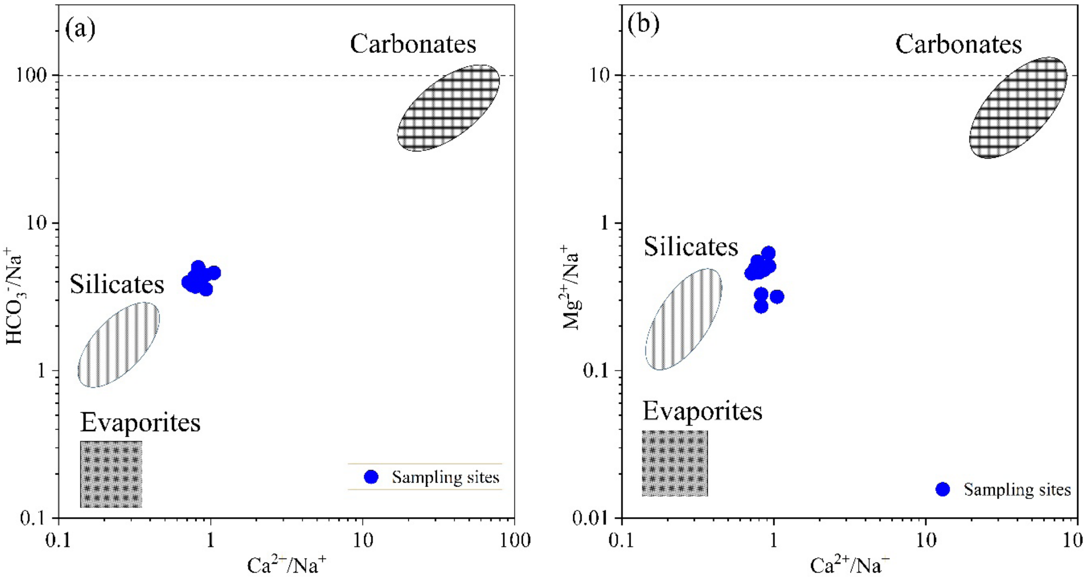

Fig. 6: Mixing diagram for Taudahaa Lake, showing Na+-normalized molar ratios of (a) Ca^{2+} vs. HCO^{3-} and (b) Ca^{2+} vs. $Mg^{2+.}$

Characterization of Geochemical Facies

Tracing the origin and geochemical evolution of both surface and groundwater requires the use of hydrochemical facies which are distinctive water types that reflect the geochemical processes affecting water composition. The Piper diagram integrates two triangular plots representing major cations and anions into a central diamond to indicate the overall water type making it a popular method for visualizing water facies (Fig.7).

The water samples are shown as blue dots in the Piper plot. The samples are primarily grouped toward the Ca^{2+} and Mg^{2+} corners according to the cation triangle indicating that they are the primary cations with calcium being somewhat more prevalent.

A larger concentration of Cl^- and SO_4^{2-} ions in comparison to bicarbonate is suggested by the anion triangle which also shows that the majority of samples trend toward these apexes. The distribution of points that results from projecting the cation and anion compositions onto the central diamond field is within the Ca^{2+}– Mg^{2+}– Cl^-– SO_4^{2-} hydrochemical facies. The results suggest that the water chemistry is mainly influenced by the dissolution of carbonate and sulfate minerals via natural rock weathering, while Cl^- and SO_4^{2-} levels may reflect anthropogenic inputs, including sewage and agricultural runoff.

When every factor is considered, the Piper diagram clearly shows that the predominant water type in the region at this time of year is a mixed Ca^{2+}– Mg^{2+}– Cl^-– SO_4^{2-} type influenced by both potential human activities and natural geological interactions.

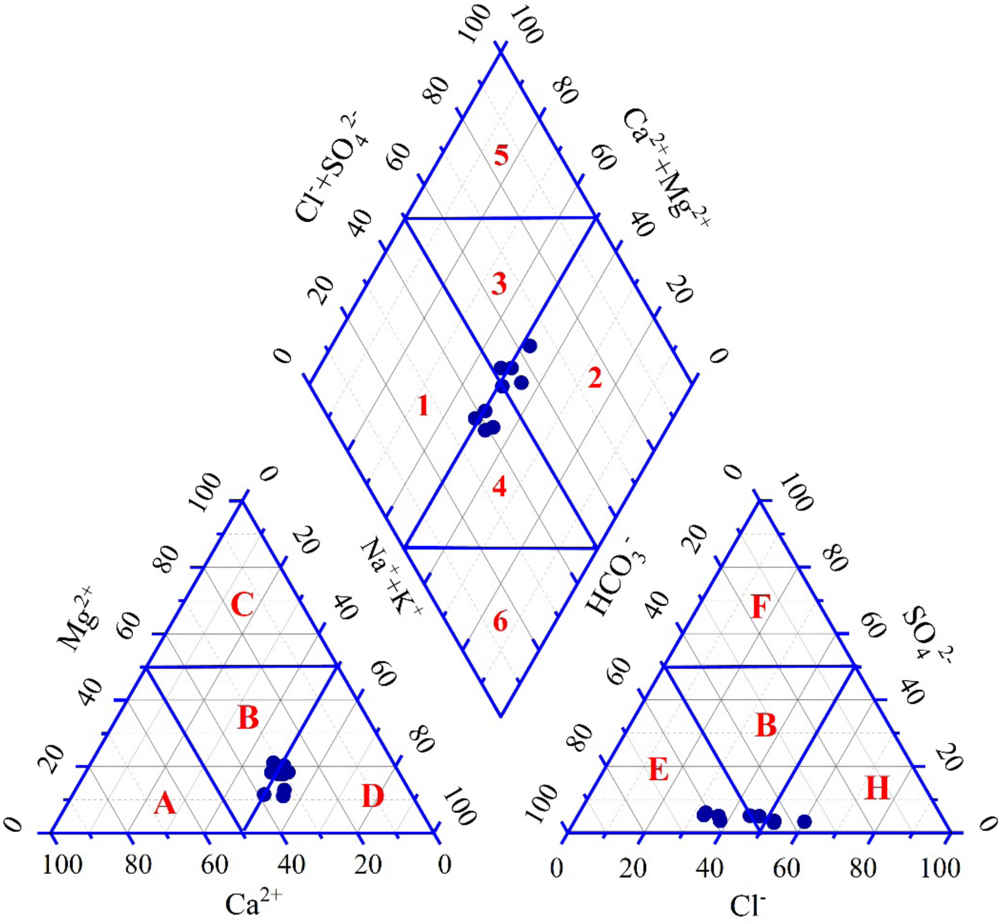

Fig.7: Piper diagram characterizing the hydrochemical facies for Taudaha Lake, Nepal

DISCUSSIONS

The physicochemical assessment of Taudaha Lake indicates that most water quality parameters generally comply with the Nepal Water Quality Guidelines for Aquaculture (NWQGA, 2015). The average water temperature of 16.68 °C falls within the range suitable for cold-water and intermediate aquaculture species, though it is below the optimal range for warm-water species. Dissolved oxygen (DO) concentrations averaged 3.82 mg/L which is below the recommended minimum of 5 mg/L suggesting that fish and other aquatic organisms may experience oxygen stress during the pre-monsoon season. This illustrates the potential need for interventions to improve oxygenation if aquaculture is to be promoted.

The water chemistry was stable with respect to pH which averaged 7.6 and remained within the acceptable range of 6.5–9.0. Total hardness (129 mg/L) classified the water as moderately hard, slightly above the ideal range (20–100 mg/L) likely due to reduced flow and evaporation during the dry season (Thakur et al., 2023). Chloride concentrations (average 125 mg/L) were well below levels considered harmful to fish (<600 mg/L) indicating minimal salinity stress. Alkalinity and total dissolved solids (TDS) were generally within acceptable limits with slight elevation in alkalinity potentially affecting buffering capacity. Nutrient concentrations including ammonia, phosphate, and BOD were within safe ranges indicating a low risk of nutrient-induced eutrophication and favorable conditions for aquatic life (Boyd and Tucker, 1998). Overall, while most parameters are suitable for aquaculture, low DO and slightly elevated hardness may limit optimal fish health and growth.

Hydrochemical facies analysis using the Piper diagram revealed that Ca^{2+} and Mg^{2+} were the dominant cations, with Ca^{2+} slightly exceeding Mg^{2+}, while Cl^- and SO_4^{2-} dominated the anions. The pre-monsoon water type is therefore classified as mixed Ca^{2+}– Mg^{2+}– Cl^-– SO_4^{2-} facies, reflecting contributions from both natural geological sources and anthropogenic inputs, such as agricultural and residential runoff (Pant et al., 2018). This composition indicates ongoing rock-weathering processes and human impacts shaping the water chemistry.

The Gibbs diagram further supports this interpretation with most data points falling in the rock-weathering dominance zone highlighting mineral dissolution and geologic interactions as the primary processes controlling the lake's hydrochemistry. TDS values ranged from 94 to 315 mg/L, while $Na^+/(Na^+ + Ca^{2+})$ and $Cl^-/(Cl^- + HCO_3^-)$ ratios confirmed the predominance of geochemical processes over precipitation or evaporation effects. These findings are similar with observations in other Nepalese river basins, such as the West Seti and Dudhkoshi, where rock-water interactions similarly dominate hydrochemistry (Shrestha et al., 2023; Ghimire et al., 2021).

Collectively, the results suggest that Taudaha Lake's water quality supports aquaculture for cold-water and intermediate species while also reflecting underlying geological and anthropogenic influences. The identified limitations particularly low DO point to the importance of regular monitoring and potential management interventions to maintain ecosystem health and ensure sustainable use of the lake for aquaculture and conservation purpose.

CONCLUSION

Based on the Nepal Water Quality Guidelines for Aquaculture (NWQGA), Taudaha Lake's physicochemical parameters indicate that the water quality is generally suitable for aquaculture, particularly for cold-water and temperate fish species. The average water temperature of 16.68°C and pH of 7.6 provide favorable conditions for fish metabolism and overall health. However, the average dissolved oxygen (DO) level of 3.82 mg/L falls below the recommended minimum of 5 mg/L which may induce physiological stress, reduce growth rates, and limit reproductive success in fish. This low DO represents a key limitation for aquaculture sustainability in the lake and indicates the potential need for aeration or periodic water exchange to maintain optimal oxygenation.

The lake's total hardness, averaging 129 mg/L classifies the water as moderately hard and slightly above NWQGA guidelines. Elevated hardness can influence osmoregulation in fish, affect nutrient availability, and potentially reduce feed efficiency. This condition is likely linked to seasonal factors including reduced water flow and evaporation which concentrate dissolved minerals. Other parameters including chloride, TDS, alkalinity, free CO_2, BOD, ammonia, and phosphate generally fall within permissible limits suggesting a balanced nutrient load and relatively low pollution levels that support aquaculture.

Hydrochemical analyses using Piper and Gibbs diagrams indicate that rock-water interactions particularly weathering of silicate and carbonate minerals dominate the lake's geochemistry. The water is characterized as mixed Ca^{2+}– Mg^{2+}– Cl^{-}– SO_4^{2-} facies reflecting both natural geological contributions and minor anthropogenic inputs such as agricultural runoff.

While most parameters are suitable for aquaculture, the identified limitations low DO and moderately high hardness underscore the need for adaptive management. Potential mitigation strategies include implementing aeration systems, promoting riparian vegetation to reduce organic load, regulating nutrient inflow from surrounding agriculture, and enhancing water circulation. Routine monitoring of DO, hardness, and nutrient levels should be prioritized, particularly before and during the dry season, to anticipate and prevent conditions that could impair fish health and productivity. Linking these interventions directly to the study's findings provides a practical framework for sustaining aquaculture protecting the lake's ecological integrity and maintaining its cultural and economic significance for the local community

REFERENCES

APHA—AWWA-WEF, 2017. WEF - Standard Methods for the Examination of Water and Wastewater (24th ed.). Washington, American Public Health Association, American Water Works Association and Water Environment Federation.

Boyd, C. E. and Tucker, C. S., 1998. Water quality and aquaculture: preliminary considerations. In *Pond aquaculture water quality management* (pp. 1-7). Boston, MA: Springer US.

Boyd, C. E., 2017. General relationship between water quality and aquaculture performance in ponds. In Fish diseases (pp. 147-166). Academic Press.

Chalaune, T. B., Dangol, A., Sharma, J. and Sharma, C. M., 2020. First results on physico-chemical status and bathymetry of lakes in Ramaroshan Wetland, Far West Nepal. Nepal Journal of Environmental Science, 8, 17–27. https://doi.org/10.3126/njes.v8i1.34464

Gaillardet, J. D. B. L., Dupré, B., Louvat, P. and Allegre, C. J., 1999. Global silicate weathering and CO2 consumption rates deduced from the chemistry of large rivers. Chemical geology, 159(1-4), 3-30.

Ghimire, N. P., Adhikari, N., Pant, R. R. and Thakuri, S., 2021. Characterizations of water quality in west-Seti and Tamor river basins, Nepal. Scientific world, 14(14), 106-114.

Gibbs, R. J., 1970. Mechanisms controlling world water chemistry. Science, 170 (3962), 1088-1090. https://dou.org/10.1007/s00244-007-9117-y.

Keddy, P. A., 2010. Wetland ecology: principles and conservation. Cambridge university press.

Khadka, U. R. and Ramanathan, A. L., 2021. Hydrogeochemical analysis of Phewa lake: A lesser Himalayan Lake in the pokhara valley, Nepal. Environment and Natural Resources Journal, 19(1), 68–83.

NWQGA, 2015. *Nepal Water Quality Guidelines for Aquaculture*. Department of Agriculture Development, Government of Nepal.

Pant R.R., Zhang F., Rehman F.U., Wang G., Ye M., Zeng C. and Tang H., 2018. Spatiotemporal variations of hydrogeochemistry and its controlling factors in the Gandaki River Basin, Central Himalaya, Nepal. Science of Total Environment, 622, 770-782.

Pant, R.R., Dhakal, T.M., Thapa, L.B., Baral, U., Dangol, A., Chalaune, T.B. and Pal, K.B., 2019. Water quality assessment of the Betkot Lake, Sudurpaschim Province, Nepal. North American Academic Research, 2 (12), 36–62.

Paudyal, R., Kang, S., Sharma, C. M., Tripathee, L. and Sillanpää, M., 2016. Variations of the physicochemical parameters and metal levels and their risk assessment in urbanized Bagmati River, Kathmandu, Nepal. Journal of Chemistry, 2016.

Piper, 1944. A Graphic Producer in the Geochemical Interpretation of Water Analysis. American Geophysical Union, 914-928.

Pradhananga, A. R., Shakya, R. K. and Shakya, P. R., 2013. Assessment of physico-chemical parameters of surface water quality of Taudaha lake of Kathmandu and their comparison with other global published values. Bibechana, 9, 141-150.

Prasanna, M. V., Chidambaram, S., Gireesh, T. V. and Jabir Ali, T. V., 2011. A study on hydrochemical characteristics of surface and sub-surface water in and around Perumal Lake, Cuddalore district, Tamil Nadu, South India. *Environmental Earth Sciences*, *63*(1), 31-47.

Shaltami, O. and Bustany, I., 2021. Water Quality- A review.

Shrestha, O. H., Thakuri, S., Bobori, D. and Bhusal, D. R., 2023. Fish Diversity and Water Quality Parameters of Dudhkoshi River, Nepal. Egyptian Journal of Aquatic Biology and Fisheries, 27(4).

Thakur, K., Sharma, D., Chauhan, D., Mahajan, D., Choudhary, K., Brar, B., Sharma, A.K., Sinha, R., Kumar, R., Kumar, S. and Kumar, R., 2023. A Systems Biology Approach in Fisheries Science. In Systems Biology, Bioinformatics and Livestock Science (Vol. 76). Bentham Science Publishers.

Zedler, J.B. and Kercher, S., 2005. WETLAND RESOURCES: Status, Trends, Ecosystem Services and Restorability. Annual Review of Environment and Resources, 30(1), 39-74.

Journal of Nepal Hydrogeological Association (JNHA), Vol (2), 127-143 (2025)
ISSN: 3059-9725 (Online)
https://doi.org/10.3126/jnha.v2i1.85392

RESEARCH ARTICLE

Mapping aquifer zones in the Terai region of Nepal using the natural electromagnetic field technique: A case study from Rajbiraj Municipality, Saptari

Nirab Pandey[1], *Birat Shrestha[2], Arun Shrestha[2], Sanjeeb Pandey[2], Nishant Pandey[3] and Gaurav Sharma[2]
[1]Lumbini Province Government, Ministry of Energy, Water Resources and Irrigation
[2]Central Department of Geology, Tribhuvan University, Kathmandu, Nepal
[3]Northern Kentucky University, Kentucky, USA
Corresponding Author: birat.stha@gmail.com

*(**Submission Date**: 20 July , 2025; **Accepted Date:** 25 August, 2025)*

ABSTRACT

This research paper demonstrates the application of the Natural Electromagnetic Field Frequency Selection System (specifically the PQWT-TC150 instrument) for mapping aquifer units in the Terai region of Nepal. The electromagnetic method, utilizing very low frequency (VLF) signals (0–30 kHz), was employed to delineate groundwater-bearing zones through resistivity contrasts in Quaternary alluvial sediments of Rajbiraj Municipality, Saptari District. Three survey profiles identified low-resistivity anomalies indicative of productive saturated formations below 15 m depth. This aquifer depth can be correlated with the nearby borehole and results from the existing literatures. Based on the lithological composition and hydrogeological characteristics, the present study area lies in the transition zone between the Bhabar Zone and Middle Terai. The Bhabar Zone characterized by coarse, permeable sediments has low (seasonal) drainage density, as it facilitates rapid groundwater recharge, whereas the Middle Terai has dense drainage network as the river gains water in this region, due to presence of fine-grained sediments, promoting higher storage capacity but slow flow rates. This quick non-invasive technique offers significant socio-economic benefits as it reduces costs and risks associated with drilling. It aids to prevent financial losses caused by unsuccessful drilling. This saves time and resources.

Keywords: ***Aquifer mapping, Groundwater exploration, Natural electromagnetic field, Terai region, Bhabar zone, Middle Terai zone, Aquifer mapping***

INTRODUCTION

The Terai region of Nepal, a northern extension of the Indo-Gangetic Plain, hosts vital aquifer systems that sustain agriculture, industry, and >50% of Nepal's population. In Nepal, like many developing countries, agriculture remains the backbone of the economy. Nearly 60% of the working population depends on farming for their livelihood, and the agriculture sector contributes 23.92% of the nation's Gross Domestic Product (GDP) (Yogi et al., 2025).

Among the arable land with irrigation facilities, 65.7 percent have surface irrigation infrastructures, while 34. 1 percent have groundwater irrigation infrastructures (Economic Survey 2023/24). For industrial, drinking, and agricultural uses, groundwater is the primary supply of water (Shrestha et al., 2018). But as extraction rates have increased, water tables have dropped and water quality has deteriorated due to contamination from industrial discharge and agricultural runoff.

A geological structure is considered permeable when there are interconnected empty spaces in the ground. More groundwater is stored and produced by an aquifer with higher porosity and permeability (Wright, 1992). In natural condition, gravity pulls groundwater downhill. However, the groundwater can flow from low elevation to higher elevation under artesian condition (Alley et al., 2002; Guru et al., 2017).

The present study area located in Rajbiraj Municipality, 09 lies on quaternary alluvial deposit. These Quaternary alluvial aquifers exhibit high heterogeneity, with productivity varying across the Bhabar, Marshy, and Southern Terai subzones (Pathak, 2016). There have been a few studies that look into how groundwater is being explored and used in such region. Traditional drilling methods for aquifer characterization are costly and spatially limited. Geophysical techniques like the Electromagnetic Field method offer rapid, non-invasive alternatives by measuring resistivity contrasts between saturated and unsaturated sediments (Reynolds, 2011).

This paper evaluates the Near Electromagnetic Fied technique using the PQWT-TC150 instrument to map aquifer units in Rajbiraj Municipality (Saptari District) in delineating aquifer depth, and lithological constraints. Geoelectric parameters (thicknesses and resistivities) of subsurface layers and aquifer zones were ascertained by conducting a thorough electromagnetic survey. The results thus obtained aids in identifying precise drilling location for the drilling companies by knowing the thickness and position of the aquifers. Using the PQWT-TC150 groundwater detector equipment and the Magnetotelluric method of passive electromagnetic techniques, which image the subsurface condition up to 300 m, the goal of this paper is to determine the aquifer zone for groundwater resources management in Rajbiraj Municipality by correlating with existing borehole logs.

Study Area

The study area is located near the Rajbiraj Industrial Area, Rajbiraj Municipality-09, Saptari District of Madhesh Province (Fig. 1). The geographical location of the study area is 26°34'24.78"N, 86°44'8.60"E.

Geologically, the study area is located within the Quaternary alluvial river deposits of Nepal’s Terai region, which forms part of the Ganga foreland basin. Composed of Pleistocene to Holocene sediments, the Terai Plain extends south of the Siwalik Hills. The region's elevation gradually decreases from 100–200 m (east to west), with a general southward slope.

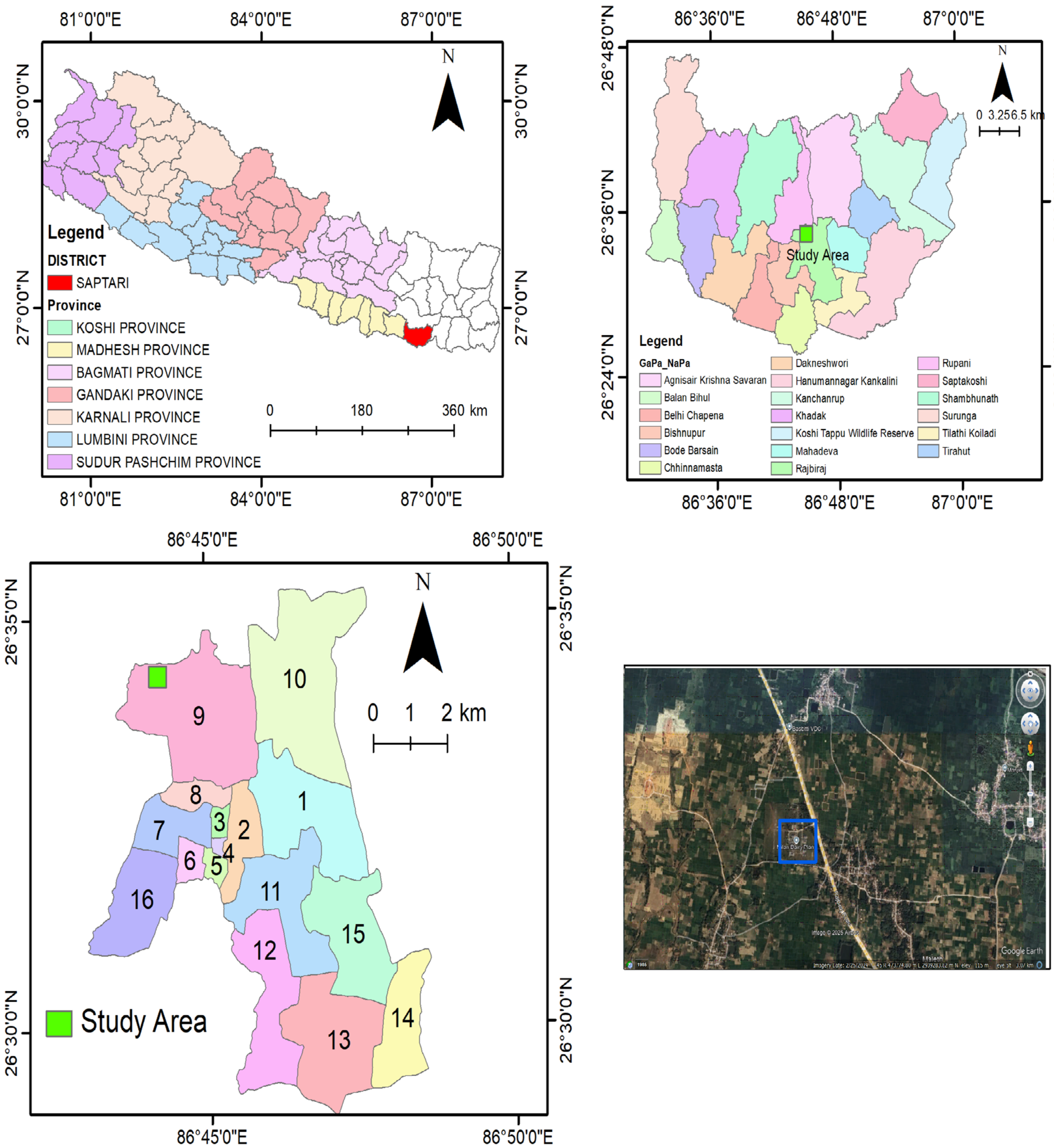

Fig. 1: Map of Nepal showing Saptari District (Study area)

Based on depositional characteristics, the Terai can be divided into three distinct zones (Fig. 2), from south to north as,

i. Bhabhar Zone – Proximal to the Siwaliks, characterized by coarse, permeable sediments (boulders, cobbles and pebbles).

ii. Middle Terai – Intermediate area with mixed sedimentology.

iii. Southern Terai – Distal fine-grained deposits (sand, silts and clay), representing typical Gangetic plain.

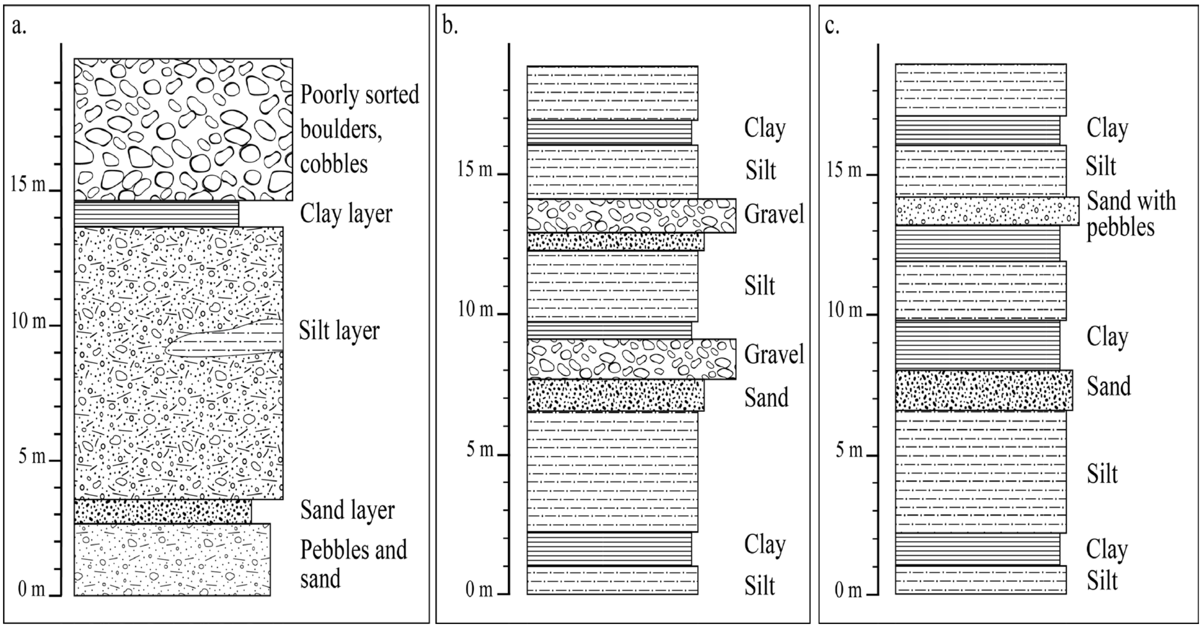

Fig. 2: Generalized lithologs of (a) Bhabar Zone, (b) Middle Terai, and (c) Southern Terai of Nepal (modified after Pathak, 2016)

Specifically, the study area lies on the boundary between the Bhabar Zone and the Middle Terai, comprising of Pleistocene–Holocene boulders, pebbles, cobbles, sand, silt and clay derived from the Siwalik Hills. The Bhabar zone acts as a primary recharge area for Terai aquifers but exhibits seasonal water table fluctuations (Upadhyay and Sah, 2012). The Middle Terai represented by the presence of gravels and sand, alternating with red, black and yellow clays is a marshy land where artesian condition prevails (Sah, 2015). Unconsolidated loose sediments of Terai and inner Terai, karstified and fractured carbonate rocks of midland and Tethys group has developed good potential source for groundwater. The Siwaliks and non-karstic but fractured carbonate rocks in Lesser Himalaya and Tethys Group acts as moderately productive aquifers. Unfractured high-grade rocks of Midland Group and crystalline rocks of higher Himalaya are considered to constitute poor aquifer quality formations (Shrestha et al., 2018).

The study area exhibits dense network of seasonal streams (hydrologically active during the monsoon period) with the Koshi river and Khado Khola being the perennial (Fig. 3). The drainage pattern initially follows a north-south direction before shifting to west-east, as seen in major rivers like the Koshi. Additionally, the study area features numerous lentic water bodies (ponds), likely formed by depression filling, and groundwater seepage.

Objectives

The main purpose of this study is to identify subsurface geological features associated with water-bearing zones (aquifers) to facilitate the extraction of a sufficient volume of water, as well as to determine suitable drilling locations and depths for effective groundwater resource exploitation

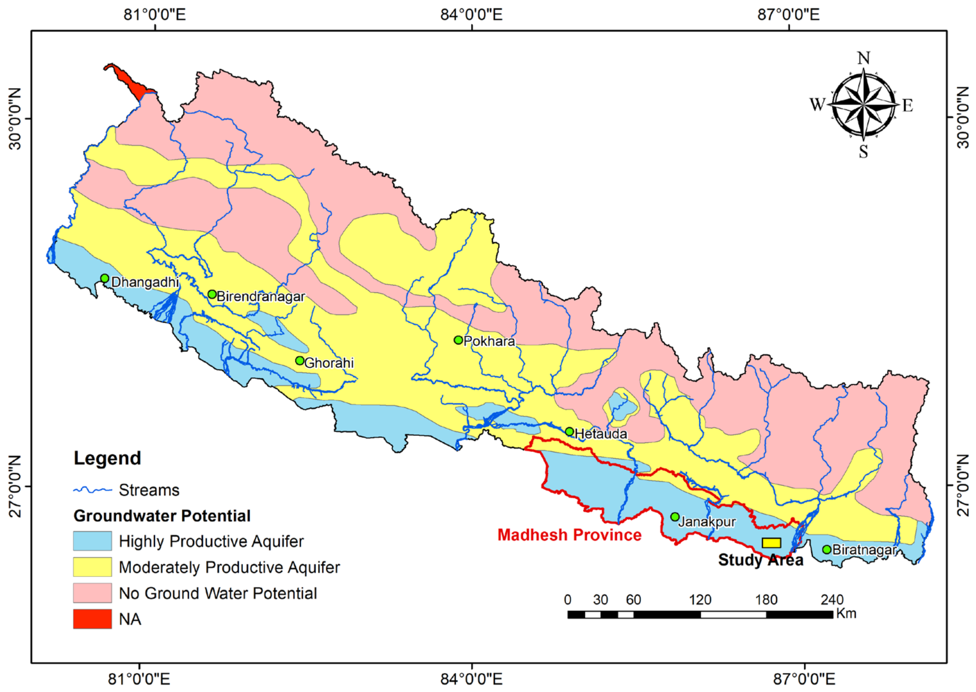

Fig. 3: Groundwater potential map of Nepal (modified after Shrestha et al., 2018)

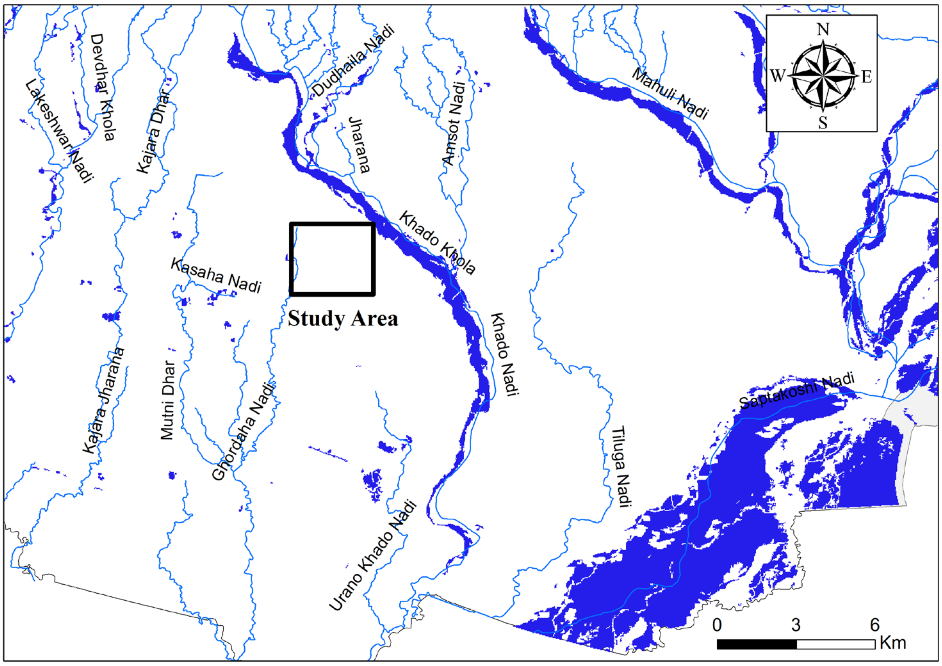

Fig. 4: Drainage map of the study area and adjacent regions

Material and Methods

Natural Electromagnetic Field Technique

The PQWT-TC150, a novel geophysical exploration instrument (Fig. 5), was used to assess the electromagnetic field in the study area. The instrument utilizes the theory of Electromagnetic Field (NEF) for geophysical exploration, primarily for detecting subsurface water resources. This method is based on the principle that variations in the Earth's natural electric and magnetic fields can reveal differences in the conductivity properties of underground geological structures.

The PQWT-TC150 uses the natural electromagnetic field variations (0–30 kHz) as its primary field source. This electric field is influenced by the Earth's steady magnetic field, which is primarily generated by the self-sustaining geodynamo action within the Earth's liquid outer core.

The PQWT technology integrates three key geophysical methods (Heilig et al., 2018):

1. **Nuclear Magnetic Resonance (NMR)**: This principle involves nuclei in a strong constant magnetic field being perturbed by a weak oscillating magnetic field. They then respond by producing an electromagnetic signal with a frequency characteristic of the magnetic field at the nucleus. The performance of NMR is dependent on the magnitude of the natural geomagnetic field, the electrical conductivity of rocks, and electromagnetic noise.

2. **Magnetotelluric (MT)**: This method measures the electrical differences of the natural Earth's magnetic field and their variations at different frequencies and depths. The PQWT-TC150 passively measures the electric (E) and magnetic (B) fields in an orthogonal direction at the ground surface using two non-polarizable potential electrodes. The geomagnetic field is considered a plane wave, perpendicular to the ground and distributed far from the source.

3. **Induced Polarization (IP)**: Induced polarization generally involves observing the voltage response in the ground after the cessation of an applied current, which can indicate the presence of certain minerals or fluid-filled pores.

Measurement and Interpretation

Data Acquisition: The precise location of each Electromagnetic survey profile station was determined and recorded using a Garmin 64 Global Positioning System (GPS) device. The core of the electromagnetic method employed is the measurement of the Earth's natural electric field. This technique, often referred to as the natural electric field method, involves selecting a specific frequency for measurement. The equipment, described as a "potential frequency of detecting instrument" or "natural selected frequency electric field instrument," is designed for geological exploration. A significant advantage of this instrument is its reliance on the Earth's natural electromagnetic field as a source, eliminating the need for an artificial power supply system. This design choice contributes to a simpler and lighter instrument, enhancing its portability and ease of use in the field. The PQWT-TC150 (Hunan Puqi Geologic Exploration Equipment Institute, China) measures the electric field component of thirty-six different frequencies in the geomagnetic field in millivolts (mV). This is achieved by placing two potential electrodes (N and M) 10 meters apart on the ground to take initial readings, and then moving them progressively along a traverse line (Fig. 6).

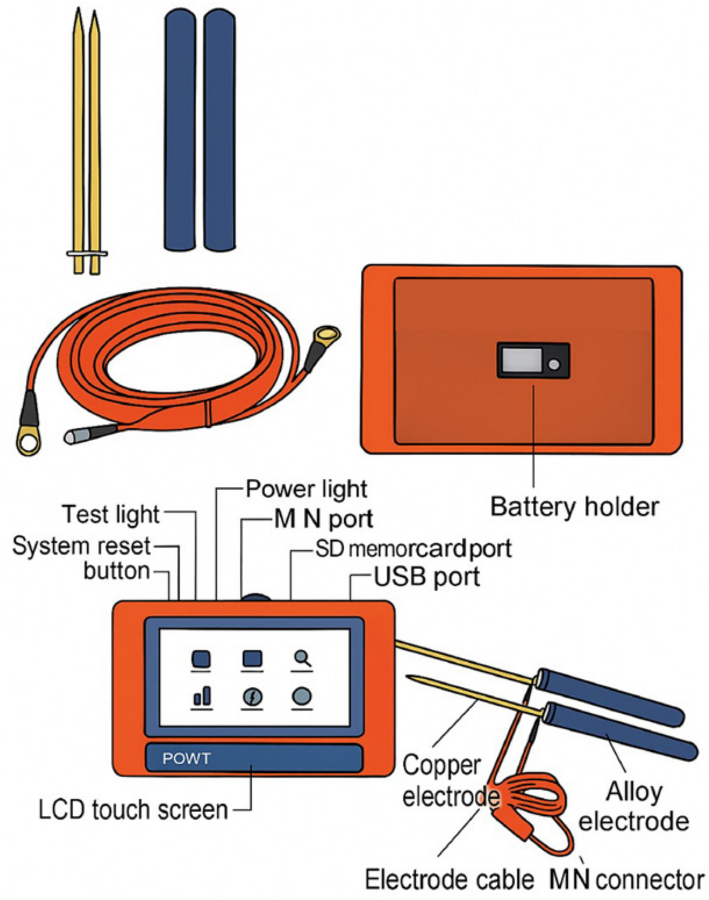

Fig. 5: Equipment (PQWT-TCP150) used for VLF survey

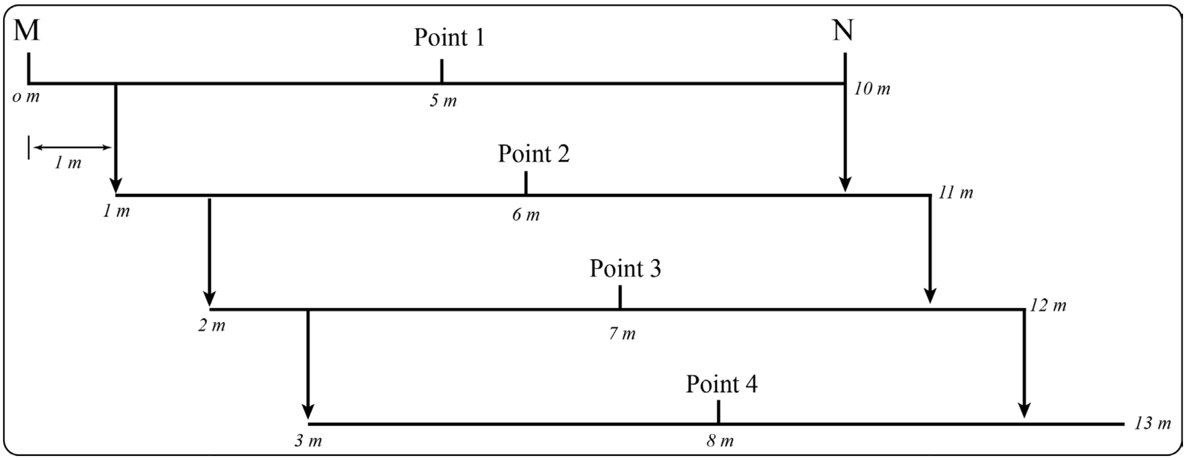

Fig. 6: Field setup and measurements

Resistivity Calculation: The instrument calculates the resistivity structure of the Earth based on the ratio of the horizontal electric field (Ex) and the magnitudes of the magnetic field (Hy). This relationship is derived from Cagniard's scalar resistivity formulae, given by (Cagniard, 1953; Waff, 2000):

$$r_m = \frac{1}{5f} * \left(\frac{E_x}{H_y}\right)^2$$

Where:

r_m is the resistivity of the medium under interaction,

f is the operating frequency, and

Ex and Hy are the electric and magnetic field components, respectively.

Depth of Penetration: The penetrating depth (d) of plane electromagnetic waves is directly proportional to the resistivity of the media at a constant frequency, as described by:

$$d = 503.3\sqrt{\frac{r_m}{f}}$$

Where:

d is the depth of penetration,

r_m is the resistivity of the medium,

f is the frequency,

This equation allows for a one-dimensional depth inversion, assuming a homogeneous, isotropic, and horizontally layered ground.

The study area displays inherent heterogeneity due to lateral and vertical variations in grain size of deposited alluvial sediments along with varying depositional patterns. Though, the equation provides a theoretical approximation, we acknowledge that anisotropy and heterogeneity exist in the study area.

Profile Mapping: The PQWT-TC150 generates a frequency curve and a profile map.

Frequency Curve: This plots the frequency responses of the Earth's electromagnetic field (in mV) against the lateral sampling distance. A straight line indicates a homogenous subsurface, while curvy or angular lines suggest variations in rock properties.

Profile Map: This pictorial interpretation uses a resistance bar (red at the top for highly resistive zones, transitioning to blue at the base for low resistive zones). Regions with concentrated blue color indicates high tendency for groundwater, while concentrated contour lines at the bottom layer suggest high resistive rock formation/coarse sediments.

Results

Three surveys were carried out in the study area. The cable layout alignment is shown in Fig. 7. The V-shape curve of the measured electromagnetic values (distance vs potential difference) for each profile were plotted with several color bands showing different frequency levels. The peak anomaly indicates the higher resistivity, presumed to be the geological structures of unsaturated features in the area. The sink V-shape curve indicate an anomaly with groundwater features, presenting low resistivity values pointing down. This sinking zone is termed the water bearing formation that will be viable for groundwater potential (Fig. 9, Fig. 12 and Fig. 15). The lithological description is based on field observation and nearby borehole logs (Fig. 8).

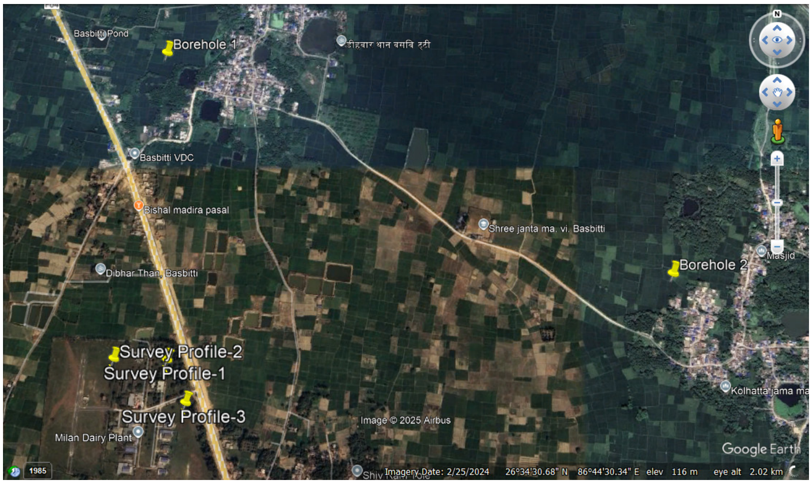

Fig. 7: Survey profiles on Google Earth Image along with nearby borehole locations

Survey Profile-1

The iso-resistivity profile map shows electric potential values (in millivolt) up to the depth of 150 m. Three subsurface layers can be delineated: saturated, partially saturated and unsaturated geological formations (Fig. 10 and Fig. 11). Clay/silty clay to dry sand and gravel is expected at the top layer. The second layer with low resistivity zone at 40-50 m depth indicates saturated sand with few gravels. The saturated layer is followed by mixture of gravel-sand-silt, sandy gravel and cobbles boulders up to 150 m depth.

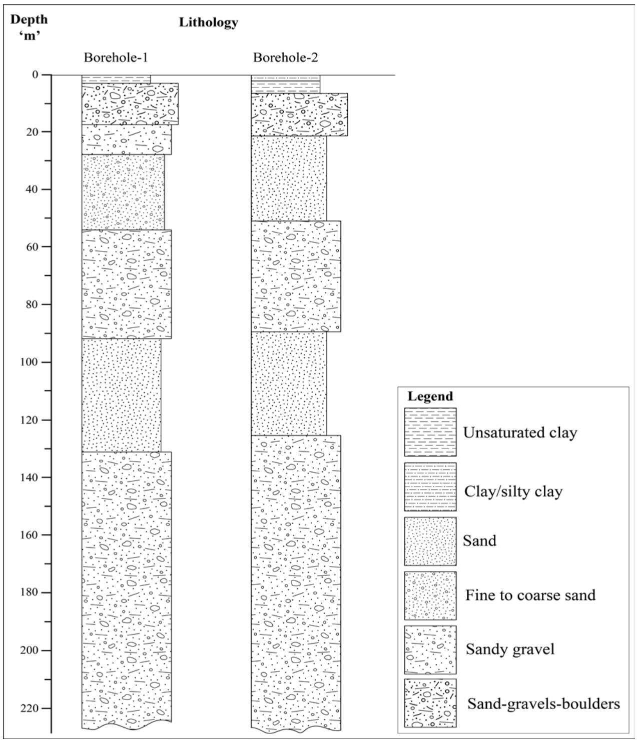

Fig. 8: Borehole logs around the study area

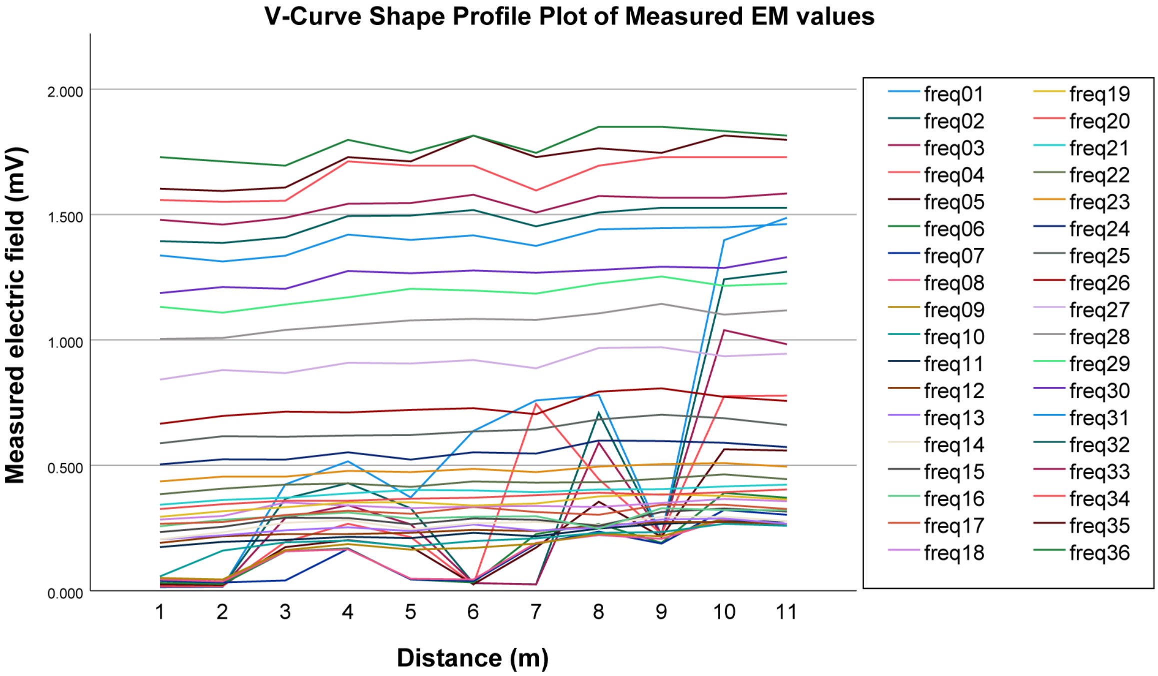

Fig. 9: Measured electric potential values with distance (Profile-1)

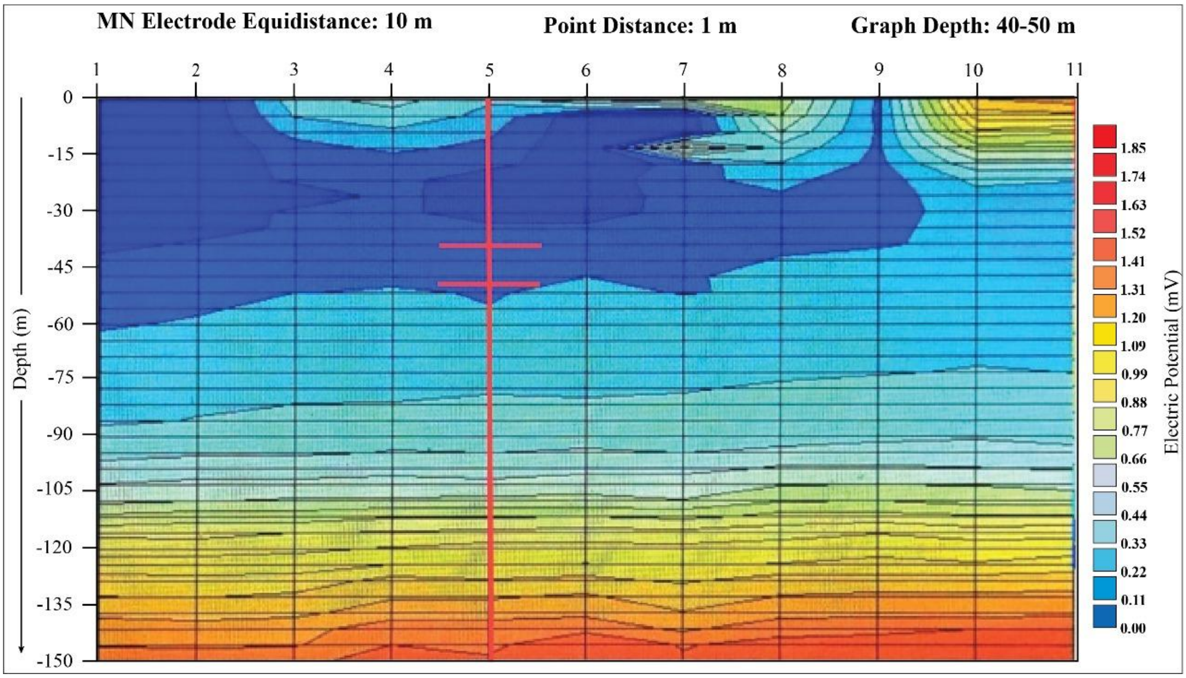

Fig. 10: Iso-Resistivity Profile Map (Profile-1)

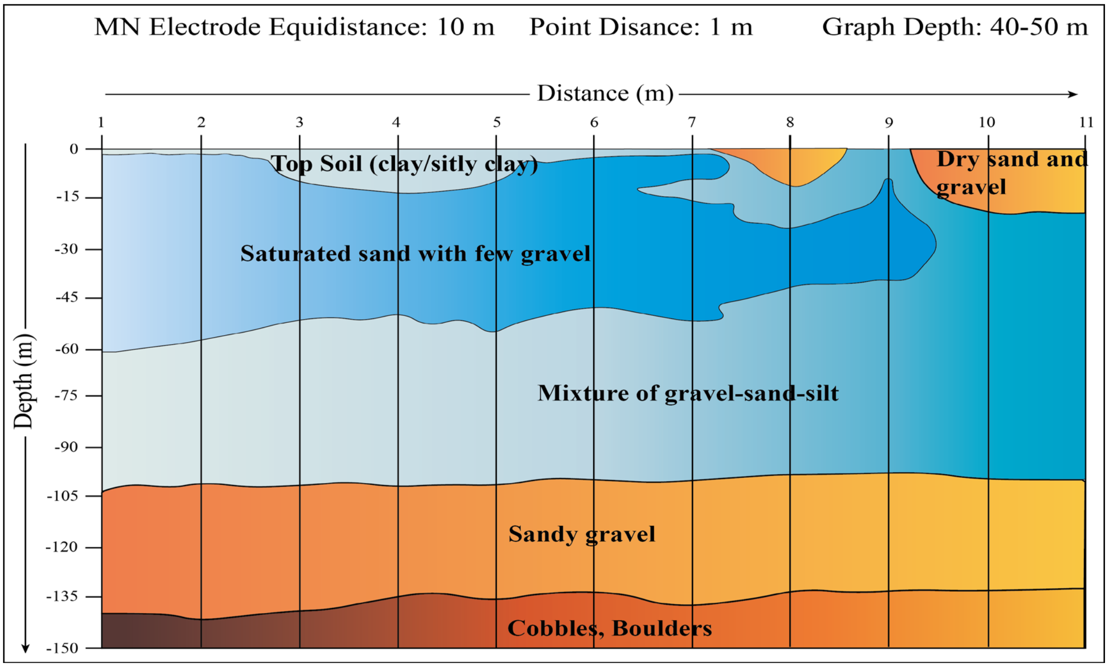

Fig. 11: Lithological Description (Profile-1)

Survey Profile-2

From iso-resistivity profile map, 3 subsurface layers can be delineated: saturated, partially saturated and unsaturated geological formations (Fig. 13 and Fig. 14). Clay/silty clay is present as the top layer up to about 15 m depth. At the second layer, mixture of gravel-sand-silt is expected. From 70 m to 100 m depth, saturated sand with few gravel is expected. From 100 m to about 135 m depth, saturated sandy gravel is expected. From 135 m to 150 m depth, cobbles and boulders are expected.

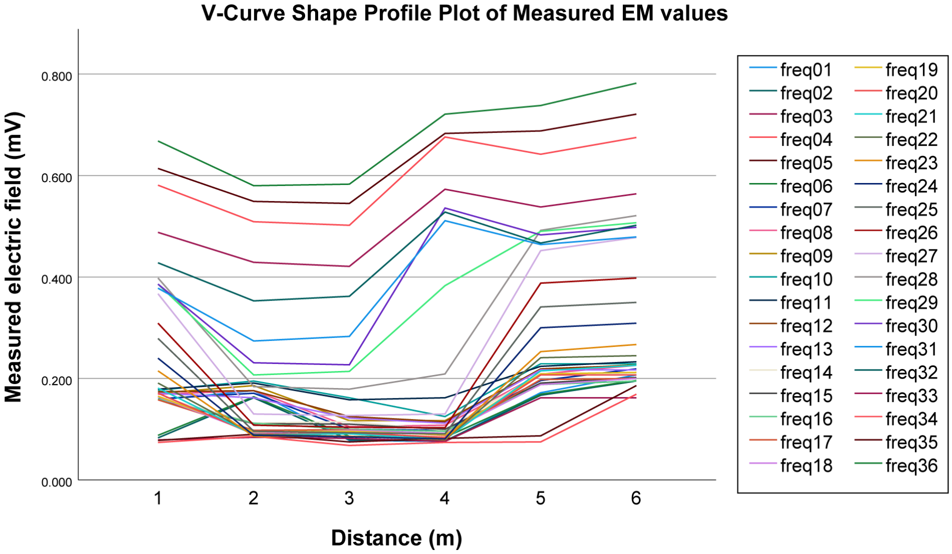

Fig. 12: Measured electric potential values with distance (Profile-2)

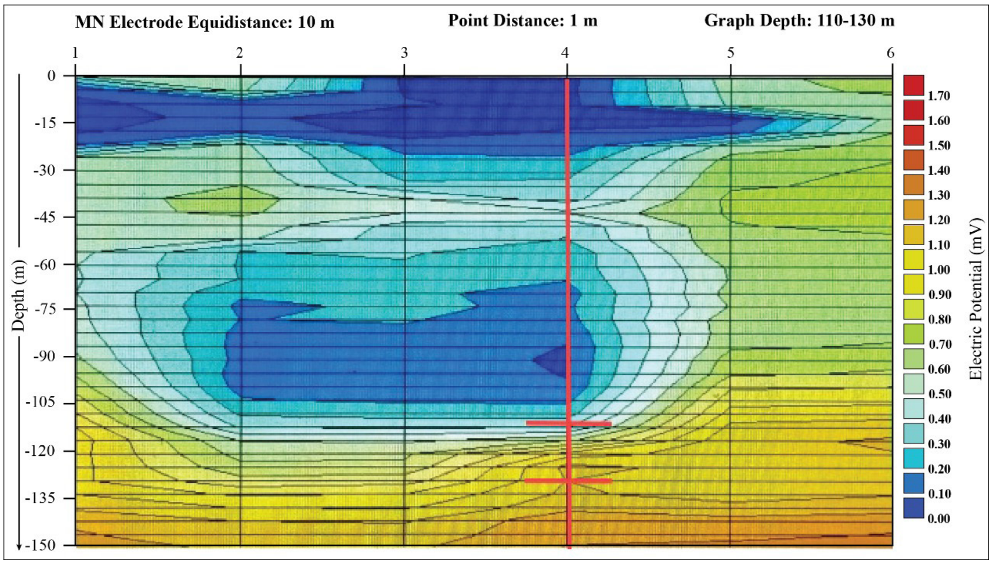

Fig. 13: Iso-Resistivity Profile Map (Profile-2)

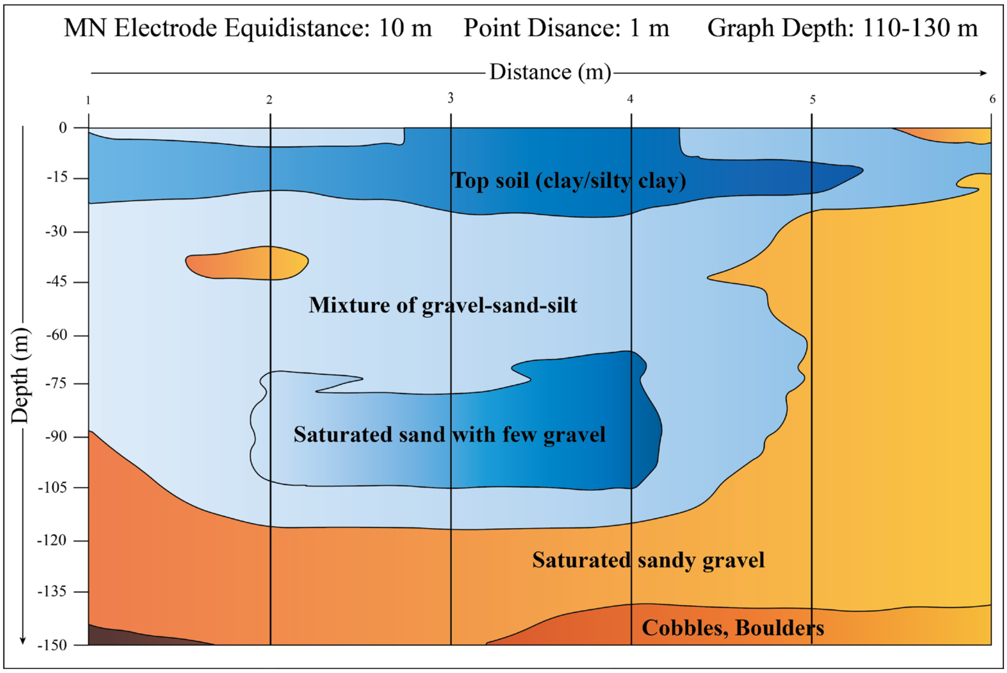

Fig. 14: Lithological Description (Profile-2)

Survey Profile-3

From iso-resistivity profile map, 2-3 subsurface layers can be delineated: saturated, partially saturated and unsaturated geological formations (Fig. 16 and Fig. 17). Clay/silty clay is expected at the top layer up to about 5 m depth. Saturated sand and gravel is expected as second layer up to about 270 m depth. From 270 m to 300 m depth, saturated silt-sand-gravel layer is expected.

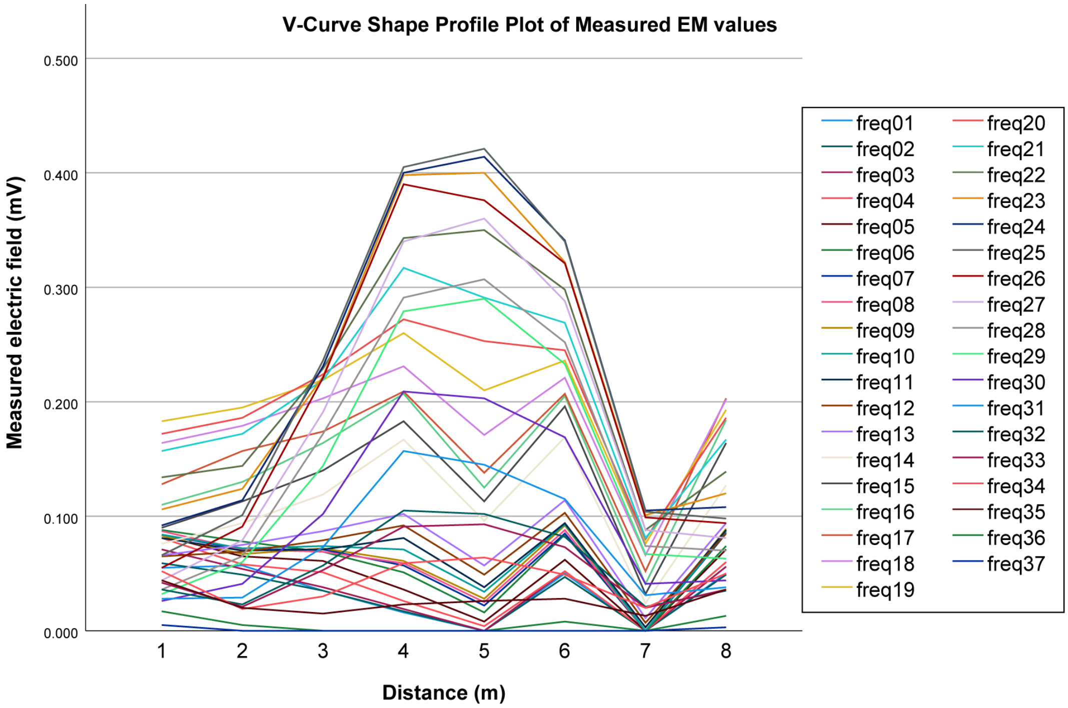

Fig. 15: Measured electric potential values with distance (Profile-3)

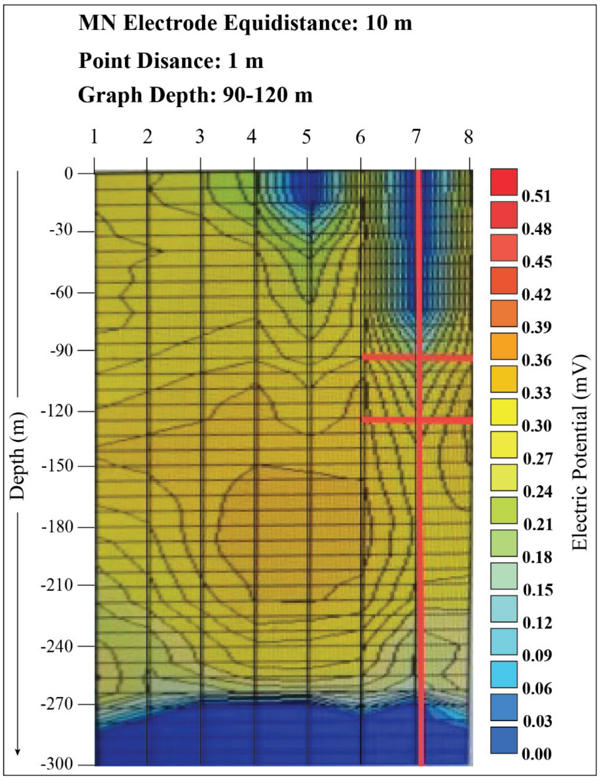

Fig. 16: Iso-Resistivity Profile Map (Profile-3)

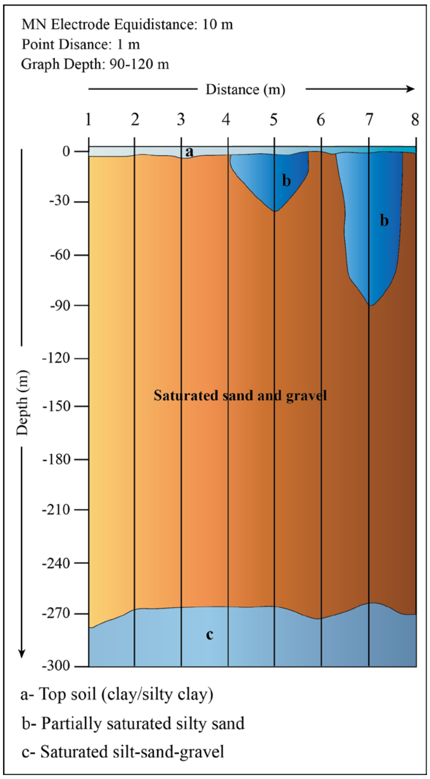

Fig. 17: Lithological Description (Profile-3)

Summary

Profile 1 (Fig. 10 and Fig. 11)

- Anomaly: Low-resistivity zone from 15–60 m depth (Chainage 9 m from start).
- Lithology: Saturated unconsolidated sediments.

Profile 2 (Fig. 13 and Fig. 14)

- Anomaly: Saturated layer from 15–130 m (Chainage 4 m from start).

Profile 3 (Fig. 16 and Fig. 17)

- Anomaly: Saturated zone beneath 15 m depth (Chainage 7 m from start).

Discussions

The main objective of this study was to identify water bearing zones natural electromagnetic methods. From the iso-resistivity profile map, three sub-surface layers were delineated, namely, unsaturated, partially saturated and unsaturated layers (on the basis of their hydrogeological parameters). All of the three iso-resistivity profiles exhibit a consistent shallow water table occurring between 10 m to 15 m depth as indicated by low electric potential values (<0.3 mV). This depth correlates with the nearby borehole logs. Similarly, the study conducted by (Shrestha et al., 2018) indicates that the water level depths in Saptari District for shallow aquifer varies from 1 m to 11 m and 5 m to 27 m for deep aquifers (Fig. 18). However, to optimize well yield and to enhance hydraulic efficiency, recommended drilling depths were selected based on the presence of coarse-grained, saturated layer present at variable depth of 50 m to 120 m within the aquifer system. The transmissivity varies from 15 m^2/day to 8000 m^2/day (Fig. 19). These layers, interpreted as fluvial sand and gravel deposit reflects the heterogeneous nature (both vertical and lateral heterogeneity) of fluvial depositional system. Prioritizing these high-permeable zones for screen installation ensures sustainable groundwater extraction by minimizing drawdown and maximizing well efficiency.

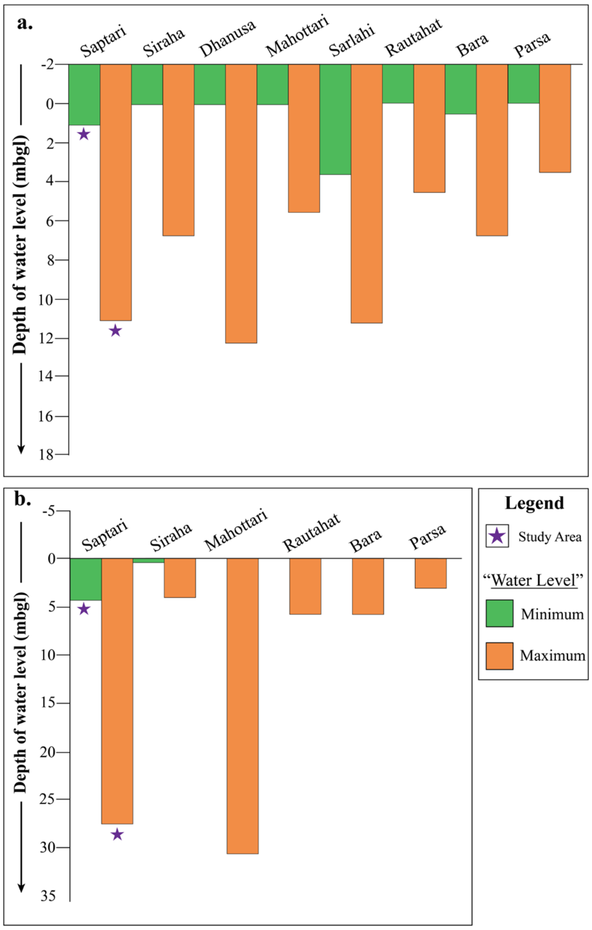

Fig. 18: Water Level Depths (a) Shallow Aquifer and (b) Deep Aquifer (after Shrestha et al., 2018)

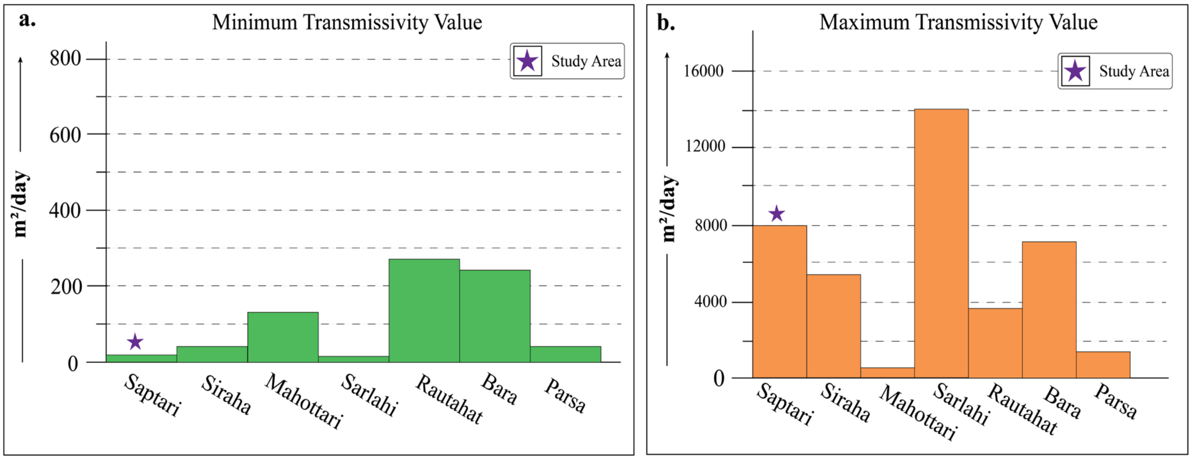

Fig. 19: Minimum and Maximum Transmissivity (after Shrestha et al., 2018)

Likely, many national and international researchers have worked in assessing the quality and quantity of groundwater potential in the Nepal Himalaya using non-invasive geophysical approaches. Shallow aquifer potential mapping was carried out by Thapa et al. (2019) where they conducted five 2D Electrical Resistivity Tomography surveys in Saptari District. They found out variation in lithological formation, including a patchwork of clay, silty clay, sand, gravel and boulder materials, with varying groundwater table (5-15 m depth). The findings of the present study show close resemblance in context of depth of water table and lithological composition. Similarly, Gautam et al. (2000) mapped subsurface karst structure with gamma ray and electrical resistivity profiles in Pokhara valley and inferred network of three linear subsurface channels orienting in NNE-SSW directions. Shah and Shrestha (2017) conducted geo-electrical sounding survey in the various part of the Lekhnath area of Pokhara Valley, Kaski District and determined aquifer thickness varying from 34 m to more than 200 m. The average calculated porosity of the aquifer material was 17.32%.

AQUIFER CHARACTERISTICS

A study by Pathak (2016) in Siwalik foothills of east Nepal revealed groundwater table to be deep at the Bhabar Zone, while the aquifer nearby the river and in Middle Terai is relatively shallow. Interpretation of iso-resistivity profile revealed the present study area to constitute mixed lithological composition, characteristic of both the Bhabar zone (gravel-boulders) and Middle Terai (silt-clay-sand-gravels). Also, the mapped aquifers (40–130 m depth) align with the hydrogeology of the Bhabar Zone, where coarse sediments enable deep percolation. Shallow aquifers (Profile 1) may represent local perched layers, while deeper zones (Profiles 2, 3) correlate with regional unconfined aquifers. Yield variations may be subjected to heterogeneity in sediment porosity and connectivity.

TECHNIQUE EFFICACY

The NEF method rapidly identified water-bearing zones with high resolution (1 m spacing). Its advantages include:

- **Cost-effectiveness:** Eliminates artificial power sources (Paterson and Ronka, 1971).
- **Speed:** 150 m profiles surveyed in <4 hours. However, depth limitations (max 150 m) restrict mapping of deeper aquifers in the Terai, which can extend to 500 m (Sah and Shrestha, 2007). Anomalies also require validation via pumping tests to confirm yield estimates.

SOCIOECONOMIC IMPLICATIONS

Use of non-invasive Natural Electromagnetic Field (NEF) technique for aquifer mapping provides significant socio-economic benefits, especially reducing the cost associated with groundwater exploration in resource-constrained regions. Drilling of unsuccessful borehole possesses great financial loss for communities, private sectors and government. Accurate identification of productive aquifer zones before drilling, reduces the unnecessary risk and expenditure. In the present scenario, delineation of saturated zones at different depths provides a clear target for drilling, hence minimizing the risk of failure. This pre-drilling understanding of the sub-surface allows for optimized well and screen placement resulting in time and cost effectiveness. This approach not only saves cost and time but also aids in sustainable water resource management and enhances overall agricultural productivity.

Comparison with Regional Studies

- Very Low Frequency-Electro Magnetic surveys in Nepal's Terai consistently identify low-resistivity layers at 30–150 m (Sharma and Baranwal, 2005). This study's results corroborate Sah et al. (2002), highlighting the Bhabar Zone's role as a recharge corridor where rivers lose their water while passing through these areas. The Middle Terai represents marshy area with shallow groundwater depth and presence of artesian condition.

Conclusion

The Natural Electromagnetic Field technique efficiently delineates shallow aquifer units within the study area:

1. Three productive aquifers were mapped at 40–50 m, 90–120 m, and 110–130 m depths in Rajbiraj.
2. The method provides rapid, low-cost reconnaissance for drilling site selection but requires supplementary pumping tests for yield verification.
3. Future work should integrate seismic or ERT methods to resolve deeper structures and quantify anisotropy.

This approach supports sustainable groundwater management in the Terai, where aquifer resilience is threatened by climate variability and over-extraction (Molle et al., 2018).

Acknowledgement

The authors would like to express their gratitude to the peoples of Rajbiraj Municipality-09 and all other helping hands.

References

Alley, W. M., Healy, R. W., LaBaugh, J. W. and Reilly, T. E., 2002. Flow and storage in groundwater systems. Science, 296(5575), 1985–1990.

Cagniard, L., 1953. Basic theory of the magneto-telluric method of geophysical prospecting. Geophysics, 18(3), 605–635.

Gautam, P., Pant, S. R. and Ando, H., 2000. Mapping of subsurface karst structure with gamma ray and electrical resistivity profiles: a case study from Pokhara valley, central Nepal. Journal of Applied Geophysics, 45(2), 97–110.

Guru, B., Seshan, K. and Bera, S., 2017. Frequency ratio model for groundwater potential mapping and its sustainable management in cold desert, India. Journal of King Saud University-Science, 29(3), 333–347.

Heilig, B., Beggan, C. and Lichtenberger, J., 2018. Natural sources of geomagnetic field variations.

Molle, F., López-Gunn, E. and Van Steenbergen, F., 2018. The local and national politics of groundwater overexploitation. Water Alternatives, 11(3).

Paterson, N. R. and Ronka, V., 1971. Five years of surveying with the Very Low Frequency—Electro magnetics method. Geoexploration, 9(1), 7–26.

Pathak, D., 2016. Water availability and hydrogeological condition in the Siwalik foothill of east Nepal. Nepal Journal of Science and Technology, 17(1), 31–38.

Reynolds, J. M., 2011. An introduction to applied and environmental geophysics. John Wiley and Sons.

Sah, R. B., Paudyal, K. R. and Gurmaita, H. N., 2002. Natural sources of arsenic poisoning in groundwater of Terai plain. Nepal. Journal of SAN, 4, 1–12.

Sah, R. B. and Shrestha, R., 2007. Toxic contaminants in groundwater of Terai Plain. SAN, 6, 45–54.

Sah, R. B., 2015. Stratigraphy of Nepal (Vol. 10). Stratigraphic Association of Nepal (SAN).

Shah, S. and Shrestha, S. R., 2017. Study of groundwater potential in Lekhnath area of Pokhara Valley using resistivity method. Bulletin of Nepal Hydrogeological Association, 2.

Sharma, S. P. and Baranwal, V. C., 2005. Delineation of groundwater-bearing fracture zones in a hard rock area integrating very low frequency electromagnetic and resistivity data. Journal of Applied Geophysics, 57(2), 155–166.

Shrestha, S. R., Tripathi, G. N. and Laudari, D., 2018. Groundwater Resources of Nepal: An Overview (pp. 169–193). https://doi.org/10.1007/978-981-10-3889-1_11

Thapa, B. R., Shrestha, S. R., Okwany, R. O. and Neupane, M., 2019. Shallow aquifer potential mapping in the foothills of Churia in Eastern Gangetic Plain of Saptari District, Nepal. Applied Water Science, 9(4), 92. https://doi.org/10.1007/s13201-019-0971-3

Upadhyay, B. and Sah, R. B., 2012. Toxic contaminants in groundwater of Geta Area. SAN, 8, 13–18.

Waff, H., 2000. Electrical resistivity imaging of groundwater systems using natural and controlled source magnetotellurics. University of Oregon, Oregon, Pp20.

Yogi, L. N., Thalal, T. and Bhandari, S., 2025. The role of agriculture in Nepal's economic development: Challenges, opportunities, and pathways for modernization. Heliyon, 11(2).

CONTENT